

# Towards a biodegradable bioelectronic device on a soft, biodegradable substrate

Emily Kate Hall

A thesis presented for the degree of  
Doctor of Philosophy.



The  
University  
Of  
Sheffield.

Department of Physics and Astronomy  
University of Sheffield  
October 2020



*This thesis is dedicated to Georgina Cartwright.*

*Miss you Grandma.*



# Abstract

Poly(3,4-ethylenedioxythiophene) (PEDOT) complexed with chondroitin sulfate (CS) (PEDOT:CS) was prepared and drop-cast films were demonstrated to be conductive, with a best sheet resistance of  $4.7 \text{ k}\Omega\text{cm}^{-1}$ . Novel organic electrochemical transistors (OECTs) based on 1-ethyl-3-(3-dimethylaminopropyl) carbodiimide hydrochloride (EDC)-crosslinked PEDOT:CS films were demonstrated with a maximum transconductance of  $50.5 \mu\text{S}$ . The OECTs saw an increase in output currents and ON/OFF ratios following 3-days submersion in water, thought to be a result of increased ionic conduction within the swollen matrix.

EDC-crosslinked hyaluronic acid (HA) hydrogels were prepared. They were demonstrated to be fully degradable, via hydrolysis, over a 4-day period in a pH 7.4 buffer at  $37^\circ\text{C}$ . The elastic moduli of the hydrogels increased with increasing concentration of EDC used in the crosslinking step. The moduli were found to be between 2 and 50 kPa which were within the range of elastic moduli reported in the literature for the CNS. A simple prototype HA gel with a grafted PEDOT:CS layer was also prepared and forms the basis of a fully degradable OECT.

Interest in organic bioelectronic devices to interface between biological systems and synthetic electronic systems is growing rapidly, especially for use in the central nervous system (CNS). Most organic electronic materials used in organic bioelectronic devices, such as PEDOT:poly(styrene sulfonate) (PEDOT:PSS), are not biodegradable and have poor long-term biocompatibility. The use of biomolecules, such as CS, as alternative counter-ions for PEDOT offer away of overcoming these limitations. The biocompatible, biodegradable, and mechanically appropriate device presented in this thesis could be developed further for use in the CNS and for the treatment of spinal cord injuries, of which there were 930,000 cases worldwide in 2016.



# Acknowledgements

First and foremost I would like to thank my supervisor Professor Mark Geoghegan for his support, encouragement, and useful scientific discussions throughout my PhD. Even after his move to Newcastle University, he continued to make time to meet in person, discuss experimental updates, and quiz my knowledge of 80's pop music. I would also like to thank Dr Jenny Clark who stepped into the role as my Sheffield-based supervisor after Mark left. She invited me into her group with open arms, and provided essential support throughout the writing of this thesis during the COVID-19 pandemic. My thanks also go to Dr Martin Grell for useful discussions about organic electronics. Nawal Alghamdi and Zahrah Alqahtani from Martin's group were also a great help in collecting electronic data in Sheffield - thank you!

My visits to the University of Cambridge were crucial to progressing my research and my thanks go to Professor Roisin Owens for allowing me to visit her labs in the Department of Chemical Engineering and Biotechnology, Dr Janire Saez for her time spent helping me run experiments, and the rest of the Bioelectronic Systems Technology group for being so welcoming. I would like to also thank Professor Ruth Cameron in the Department of Materials Science and Metallurgy at Cambridge for her discussions about soft materials for use in the human body at the start of my PhD that paved the way towards my work on soft hydrogels. Further thanks go to Professor Fabio Biscarini at the University of Modena and Reggio Emilia (UNIMORE), Italy, for letting me to visit and work in his bioelectronic labs. His expertise was invaluable. Also, thanks go to Dr Marcello Berto and Martina Giordani for helping me with lab work whilst I was in Italy and the rest of the lab group for inviting me along for daily espresso and being so friendly. I also had the chance to undertake experiments at the Italian Institute of Technology (IIT) in Ferrara, Italy, with the help of Dr Stefano Carli who I'd like to thank for helping me with everything electrochemical impedance spectroscopy related.

Special thanks go to my physics pals Dr Jamie Blakeman, Dr Ellie Dougherty, Emilia Hudzik, and Dr Stephanie Burg for supporting me through this crazy PhD journey and for all the Thursday pub trips. Even more special thanks go to my best friends in the world Faith, Liss, Harriet, Antonia, and Alice who have been by my side for 15 years now and I hope will be there for many more years to come.

My parents, Sally and David Hall, and my sister, Eleanor, have always been there for me through everything and have always been encouraging and supportive. My family is one of the most important things in my life, and I would not have been able to do this without them.

Will, if I had not come to Sheffield and do a PhD, we never would have met and I would have missed out on so many silly trips to IKEA, movie nights, and windy walks in the Peaks. This PhD has been hard at times but you have been my rock throughout. I am so excited to share whatever comes next with you.



# Contents

<b>Abstract</b>	<b>i</b>
<b>Acknowledgements</b>	<b>ii</b>
<b>List of Figures</b>	<b>xi</b>
<b>List of Tables</b>	<b>xvi</b>
<b>1 Introduction</b>	<b>1</b>
1.1 The human nervous system . . . . .	1
1.1.1 Nerve cells . . . . .	2
1.1.2 Formation and transmission of nerve impulses . . . . .	4
1.1.3 Synapses . . . . .	7
1.1.4 Central nervous system . . . . .	9
1.1.5 Spinal cord injuries . . . . .	11
1.1.6 Treating spinal cord injuries . . . . .	13
1.2 Organic bioelectronics . . . . .	14
1.2.1 Field-effect transistors . . . . .	15
1.2.2 Electrolyte-gated organic field-effect transistors . . . . .	15
1.2.3 Organic electrochemical transistors . . . . .	17
1.2.4 Introduction to poly(3,4-ethylenedioxythiophene) (PEDOT) . . . . .	19
1.3 Biomaterials . . . . .	21
1.3.1 Biocompatibility . . . . .	21

1.3.2	Biodegradability . . . . .	22
1.3.3	Mechanical Properties . . . . .	22
1.4	Hydrogels as biomaterials . . . . .	25
1.4.1	Hyaluronic acid and chondroitin sulfate . . . . .	26
1.4.2	Crosslinking hydrogels - EDC-crosslinking . . . . .	27
1.5	Summary and thesis overview . . . . .	31
<b>2</b>	<b>Experimental Techniques</b>	<b>33</b>
2.1	Introduction . . . . .	33
2.2	Infra-red (IR) spectroscopy . . . . .	33
2.2.1	Harmonic and anharmonic oscillators . . . . .	34
2.2.2	IR absorption . . . . .	34
2.2.3	Characterising samples using IR spectroscopy . . . . .	35
2.2.4	Fourier transform IR spectroscopy . . . . .	36
2.3	Ultra-violet (UV) spectroscopy . . . . .	37
2.3.1	Electronic transitions . . . . .	38
2.3.2	UV spectroscopy for organic electronic applications . . . . .	39
2.4	Electrochemical impedance spectroscopy (EIS) . . . . .	39
2.4.1	Impedance . . . . .	39
2.4.2	Nyquist and Bode plots . . . . .	40
2.4.3	Equivalent circuits . . . . .	42
2.4.4	Applications of EIS . . . . .	42
2.5	Mechanical testing techniques . . . . .	44
2.5.1	Elastic modulus . . . . .	44
2.5.2	Poisson's ratio . . . . .	45
2.5.3	Universal mechanical testing rig . . . . .	46
2.5.4	Indentation testing . . . . .	46
<b>3</b>	<b>Synthesis and characterisation of poly(3,4-ethylenedioxythiophene):biomolecule com-</b>	

<b>plexes and their devices</b>	<b>48</b>
3.1 Introduction . . . . .	48
3.1.1 Using PEDOT:PSS in organic bioelectronics . . . . .	48
3.1.2 Alternatives to PEDOT:PSS . . . . .	51
3.1.3 Device requirements . . . . .	54
3.2 Experimental Methods . . . . .	55
3.2.1 Materials . . . . .	55
3.2.2 Synthesis of PEDOT complexed with chondroitin sulfate (PEDOT:CS) and hyaluronic acid (PEDOT:HA) by oxidative polymerisation . . . . .	55
3.2.3 Forming films of PEDOT:CS and PEDOT:HA . . . . .	56
3.2.4 Determining the thickness of the drop-cast PEDOT:CS and PEDOT:HA film samples using atomic force microscopy (AFM) . . . . .	57
3.2.5 Crosslinking films using EDC crosslinking . . . . .	58
3.2.6 Electronic characterisation of PEDOT:CS and PEDOT:HA . . . . .	58
3.2.7 Proof of concept: OECT characterisation of PEDOT:CS and PEDOT:HA . . . . .	59
3.3 Results and discussion . . . . .	60
3.3.1 Synthesis of PEDOT:CS and PEDOT:HA by oxidative polymerisation . . . . .	60
3.3.2 Forming films of PEDOT:CS and PEDOT:HA . . . . .	65
3.3.3 Electronic characterisation of PEDOT:CS and PEDOT:HA . . . . .	72
3.3.4 Proof of concept: Transistor characterisation of PEDOT:CS and PEDOT:HA . . . . .	79
3.4 Summary and further work . . . . .	82
<b>4 Optimising a PEDOT:biomolecule organic electrochemical transistor</b>	<b>84</b>
4.1 Introduction . . . . .	84
4.1.1 Synapstors . . . . .	85
4.1.2 Tubistors . . . . .	86
4.1.3 Understanding and optimising a PEDOT:biomolecule OECT . . . . .	88
4.2 Experimental methods . . . . .	88
4.2.1 Materials . . . . .	88

4.2.2	OECT characterisation . . . . .	89
4.2.3	Sample preparation for UV spectroscopy and EIS . . . . .	90
4.2.4	UV spectroscopy . . . . .	90
4.2.5	Electrochemical impedance spectroscopy . . . . .	90
4.2.6	Synapstor preparation and characterisation . . . . .	91
4.2.7	Scaffold preparation by lyophilisation . . . . .	91
4.3	Results and discussion . . . . .	92
4.3.1	OECT device characterisation and optimisation . . . . .	92
4.3.2	UV spectroscopy . . . . .	96
4.3.3	Electrochemical impedance spectroscopy . . . . .	98
4.3.4	Degradation of PEDOT:CS films and OECT devices . . . . .	100
4.3.5	Synapstor preparation . . . . .	104
4.3.6	Lyophilisation of PEDOT:CS and PEDOT:HA . . . . .	106
4.4	Summary and future work . . . . .	108
<b>5</b>	<b>Creating biocompatible, degradable, and soft hydrogels from biomolecules</b>	<b>111</b>
5.1	Introduction . . . . .	111
5.1.1	Hydrogels and their uses in the body . . . . .	112
5.1.2	Summary and requirements of hydrogels for use in the central nervous system . . . . .	115
5.2	Experimental methods . . . . .	116
5.2.1	Materials . . . . .	116
5.2.2	Synthesis of chondroitin sulfate and hyaluronic acid hydrogels by EDC-crosslinking	116
5.2.3	General multi-step submersion method for hydrogel preparation . . . . .	118
5.2.4	Infra-red spectroscopy . . . . .	118
5.2.5	Acidification of HA for film preparation . . . . .	118
5.2.6	Swelling properties of chondroitin sulfate and hyaluronic acid hydrogels . . . . .	119
5.2.7	Degradation experiments . . . . .	119
5.2.8	Mechanical testing . . . . .	120

5.2.9	Combination of HA hydrogel with PEDOT:CS and PEDOT:HA . . . . .	121
5.3	Results and discussion . . . . .	122
5.3.1	Synthesis of chondroitin sulfate and hyaluronic acid hydrogels by EDC-crosslinking	122
5.3.2	Swelling properties of CS and HA hydrogels . . . . .	128
5.3.3	Degradation of hyaluronic acid hydrogels . . . . .	134
5.3.4	Mechanical properties of hyaluronic acid hydrogels . . . . .	135
5.3.5	Combination of HA hydrogels with PEDOT:CS . . . . .	142
5.4	Summary and future work . . . . .	143
<b>6</b>	<b>Summary and future work</b>	<b>146</b>
6.1	Summary . . . . .	146
6.2	Future Work . . . . .	149
	<b>Bibliography</b>	<b>152</b>
	<b>Appendix A</b>	<b>163</b>



# Abbreviations and Symbols

$\epsilon$	linear strain
$\lambda_{max}$	maximum absorption wavelength
$\nu$	frequency (as it relates to spectroscopy)
$\nu$	Poisson's ratio (as it relates to mechanical testing)
$\omega$	frequency (as it relates to impedance)
$\sigma$	normal stress
$\Theta$	phase angle
$ Z $	length of impedance vector
$A$	area
$a$	radius of indenting cylinder
$C$	capacitance
$d$	indentation depth
$D$	degree of swelling
$E$	elastic modulus
$E$	energy (as it relates to spectroscopy)
$E^*$	reduced elastic modulus
$F$	normal (applied) force
$g_m$	transconductance
$h$	Planck constant
$I_{DS}$	source-drain current
$I_{GS}$	gate current/leakage
$I(\omega, t)$	current as a function of frequency
$I$	current
$j$	imaginary number, square root of $-1$
$k$	spring constant, Hookes Law
$L_0$	original length
$L$	length
$L$	inductance
$m_{t=0}$	mass of the hydrogel at $t = 0$
$m_d$	dry mass of hydrogel
$m_s$	swollen mass of hydrogel
$m_t$	mass of the hydrogel at t
$m_w$	wet mass of hydrogel
$\phi$	phase difference

$R$	resistance
$R_{CT}$	charge transfer resistance
$R_S$	solution resistance
$R_{\square}$	sheet resistance
$V_{DS}$	source-drain voltage
$V_G$	gate voltage
$V(\omega, t)$	voltage as a function of frequency
$V$	voltage
$W/L$	width to length ratio
$W_s$	percentage water uptake of hydrogel matrix itself
$W_w$	percentage water uptake of hydrogel (including water in pores)
$x$	distance, Hookes Law
$X$	reactance
$Z_{imaginary}$	imaginary impedance
$Z_{real}$	real impedance
$Z(\omega)$ or $Z$	impedance
AFM	atomic force microscopy
APS	ammonium persulfate
$Ca^{2+}$	calcium ion
CNS	central nervous system
Coll	collagen
CS	chondroitin sulfate
CV	cyclic voltammetry
DBSA	dodecylbenzenesulfonic acid
DMSO	dimethyl sulfoxide
DNA	deoxyribonucleic acid
DS	dextran sulfate
ECM	extracellular matrix
EDC	1-ethyl-3-(3-dimethylaminopropyl)carbodiimide hydrochloride
EDOT	3,4-ethylenedioxythiophene
EGOFET	electrolyte-gated organic field-effect transistor
EGOS	electrolyte-gated hybrid nanoparticle/organic synapstor
EIS	electrochemical impedance spectroscopy
FET	field-effect transistor
FTIR	Fourier transform infra-red
FTO	fluorine doped tin oxide
GABA	$\gamma$ -aminobutyric acid
GG	guar gum
GOPS	3-glycidoxypropyltrimethoxysilane
$H^+$	proton
HA	hyaluronic acid
hep	heparin
HOMO	highest occupied molecular orbital
IIT	Italian Institute of Technology
IR	infra-red

IUPAC	International Union of Pure and Applied Chemistry
K <sup>+</sup>	potassium ion
LUMO	lowest unoccupied molecular orbital
MOSFET	metal-oxide-semiconductor field-effect transistor
MWCO	molecular weight cut off
Na <sup>+</sup>	sodium ion
NHE	normal hydrogen electrode
NHS	<i>N</i> -hydroxysuccinimide
NMR	nuclear magnetic resonance
NOMFET	nanoparticle organic memory field-effect transistor
NPCs	neuronal progenitor cells
OECT	organic electrochemical transistor
OEM	organic electronic material
OFET	organic field-effect transistor
OLEDs	organic light emitting diodes
P3HT	poly(3-hexylthiophene)
PANI	poly(aniline)
PBS	phosphate buffered saline
PDMS	polydimethylsiloxane
PEDOT	poly(3,4-ethylenedioxythiophene)
PEDOT:CS	PEDOT complexed with CS
PEDOT:HA	PEDOT complexed with HA
PEDOT:PSS	poly(3,4-ethylenedioxythiophene) complexed with poly(styrene sulfonate)
PEG	poly(ethylene glycol)
PFPE-DMA	dimethacrylate-functionalised perfluoropolyether
PLGA	poly(L-lactide-co-glycolide)
PNS	peripheral nervous system
PSS	poly(styrene sulfonate)
RFID	radio frequency identification
SCI	spinal cord injury
STP	short-term plasticity
T	transmittance
UNIMORE	University of Modena and Reggio Emilia
UV	ultraviolet
UV-vis	ultraviolet-visible
v	vibrational quantum number
W	Warburg impedance



# List of Figures

1.1	Simplified diagram of the human nervous system . . . . .	2
1.2	Diagram of neuron . . . . .	2
1.3	Diagram of sensory neuron . . . . .	3
1.4	Diagram showing the glial cells present in the CNS . . . . .	4
1.5	Establishing the resting potential of a neuron . . . . .	5
1.6	Potential difference across the membrane of an axon as an action potential is generated . . . . .	6
1.7	Diagram showing saltatory conduction in myelinated neurons . . . . .	7
1.8	Annotated diagram of a synapse . . . . .	8
1.9	Structures in the central nervous system . . . . .	10
1.10	Meninges that surround the spinal cord . . . . .	11
1.11	Structures within the spinal cord . . . . .	11
1.12	Illustration of e-dura device . . . . .	14
1.13	Schematic diagram of an organic field-effect transistor . . . . .	16
1.14	Schematic diagram of an electrolyte-gated organic field-effect transistor . . . . .	16
1.15	Schematic diagram of an organic electrochemical transistor . . . . .	17
1.16	Schematic of a PEDOT:PSS OECT . . . . .	18
1.17	Characteristics of a typical depletion mode organic electrochemical transistor . . . . .	19
1.18	Chemical structure of PEDOT . . . . .	19
1.19	Chemical structure of poly(styrene sulfonic acid) . . . . .	20
1.20	Structure of doped PEDOT stabilised by PSS. . . . .	20
1.21	Generic hydrogel structure . . . . .	25

1.22	Chemical structures of hyaluronic acid and chondroitin sulfate . . . . .	26
1.23	1-Ethyl-3-(3-dimethylaminopropyl)carbodiimide hydrochloride (EDC) . . . . .	28
1.24	EDC-crosslinking reaction scheme to form amides . . . . .	28
1.25	EDC-crosslinking reaction scheme to form esters . . . . .	29
1.26	Possible crosslinks forming between collagen, chondroitin sulfate, and a diamine . . . . .	30
2.1	Quantum mechanical harmonic and anharmonic oscillator models . . . . .	35
2.2	Characteristic IR bands . . . . .	36
2.3	Michelson interferometer . . . . .	37
2.4	Electronic energy level transitions . . . . .	38
2.5	Phase shift in an AC signal . . . . .	40
2.6	Generic Nyquist plot . . . . .	41
2.7	Generic Nyquist plot labelled . . . . .	41
2.8	Generic Bode plot . . . . .	42
2.9	Example equivalent circuit . . . . .	43
2.10	Visual representation of a compressive elastic deformation . . . . .	44
2.11	Typical stress-strain curve . . . . .	45
2.12	Various indenter geometries for mechanical testing . . . . .	46
2.13	Contact mechanics model used for elastic modulus calculations using a cylindrical probe . . . . .	47
3.1	Preparing the PEDOT:biomolecule samples for AFM . . . . .	57
3.2	Photo of a substrate used in electronic testing . . . . .	59
3.3	Experimental set up for electronic characterisation of PEDOT:biomolecule films . . . . .	59
3.4	Experimental set up for transistor characterisation of PEDOT:biomolecule films . . . . .	60
3.5	PEDOT:CS aqueous suspension . . . . .	61
3.6	Discoloured PEDOT:CS samples . . . . .	63
3.7	Discoloured solvents following PEDOT:HA washing . . . . .	64
3.8	Drop-cast thin films of PEDOT:CS 1:1 and PEDOT:CS 1:2 . . . . .	67
3.9	Horizontal profile of PEDOT:CS film . . . . .	68

3.10	Horizontal profile of PEDOT:HA film . . . . .	69
3.11	AFM scans of PEDOT:CS and PEDOT:HA films . . . . .	70
3.12	Crosslinked PEDOT:CS drop-cast films . . . . .	71
3.13	I/V plots for uncrosslinked PEDOT:CS 1:1 . . . . .	73
3.14	I/V plots for more samples of uncrosslinked PEDOT:CS 1:1 . . . . .	74
3.15	I/V plots for PEDOT:HA 1:1 . . . . .	76
3.16	I/V plots for PEDOT:CS 1:1 synthesised with half the required mass of APS . . . . .	77
3.17	Delaminated gold on the glass substrate. . . . .	78
3.18	Output characteristics of a PEDOT:CS based OECT device . . . . .	80
3.19	Transfer characteristics of a PEDOT:CS based OECT device . . . . .	81
3.20	Transconductance of a PEDOT:CS based OECT device . . . . .	82
4.1	Tubistor . . . . .	87
4.2	Photo of the quartz substrates used in OECT characterisation . . . . .	93
4.3	Transfer curves for a PEDOT:CS 1:1 based OECT . . . . .	93
4.4	Transfer curves with transconductances . . . . .	94
4.5	Demonstration of gate leakage . . . . .	95
4.6	UV spectra of PEDOT:PSS from literature . . . . .	97
4.7	UV spectra of PEDOT:CS dispersions . . . . .	97
4.8	UV spectra of crosslinked PEDOT:CS films . . . . .	98
4.9	Nyquist plot EIS data for PEDOT:CS . . . . .	99
4.10	Bode plot and phase angle EIS data for PEDOT:CS . . . . .	99
4.11	Transfer curves (degradation experiments) . . . . .	100
4.12	Nyquist plot from EIS data for PEDOT:CS (degradation experiment) . . . . .	102
4.13	Bode plot from EIS data for PEDOT:CS (degradation experiment) . . . . .	102
4.14	Phase angles from EIS data for PEDOT:CS (degradation experiment) . . . . .	103
4.15	UV spectra of crosslinked PEDOT:CS 1:1 films (degradation experiments) . . . . .	104
4.16	UV spectra of crosslinked PEDOT:CS 1:2 films (degradation experiments) . . . . .	105

4.17	Laser ablation pattern . . . . .	106
4.18	Sample post-laser ablation . . . . .	106
4.19	GOPS crosslinked PEDOT:CS scaffolds . . . . .	107
4.20	Freeze-dried uncrosslinked PEDOT:CS and PEDOT:HA samples . . . . .	108
5.1	Sample preparation for mechanical testing . . . . .	120
5.2	Sketch of mechanical tester . . . . .	121
5.3	HA hydrogel with drop-cast PEDOT:CS aqueous dispersion . . . . .	122
5.4	Hyaluronic acid films . . . . .	125
5.5	Stacked IR spectra of HA hydrogels synthesised with different EDC solution concentrations	127
5.6	Stacked IR spectra of HA hydrogels synthesised with different EDC solution concentrations (close up) . . . . .	129
5.7	Relative peak transmittance vs. EDC solution concentration . . . . .	129
5.8	Disintegrating CS hydrogel samples during swelling tests . . . . .	130
5.9	Degree of swelling of chondroitin sulfate hydrogels . . . . .	131
5.10	Water uptake of chondroitin sulfate hydrogels . . . . .	131
5.11	Degree of swelling of hyaluronic acid hydrogels . . . . .	133
5.12	Water uptake of hyaluronic acid hydrogels . . . . .	133
5.13	Degradation profiles of hyaluronic acid hydrogels . . . . .	134
5.14	Force-distance plot . . . . .	136
5.15	Elastic moduli of hyaluronic acid hydrogels as a function of EDC concentration . . . . .	137
5.16	Force-distance plot with 0.02 N applied force . . . . .	138
5.17	Indentation depth and elastic moduli of HA gels undergoing multiple probing cycles . . .	140
5.18	Elastic moduli of hyaluronic acid hydrogels as a function of EDC concentration (subset) .	141
5.19	Elastic moduli of hyaluronic acid hydrogels as a function of EDC concentration under 0.02 N applied force . . . . .	141
5.20	Elastic moduli of hyaluronic acid hydrogels as a function of EDC concentration under 0.05 N applied force . . . . .	141
5.21	HA hydrogel with PEDOT:CS drop-cast layer . . . . .	142

6.1	IR spectra of uncrosslinked HA film . . . . .	163
6.2	IR spectra of crosslinked HA film (0.026 mol dm <sup>-3</sup> EDC) . . . . .	164
6.3	IR spectra of crosslinked HA film (0.052 mol dm <sup>-3</sup> EDC) . . . . .	164
6.4	IR spectra of crosslinked HA film (0.26 mol dm <sup>-3</sup> EDC) . . . . .	165
6.5	IR spectra of crosslinked HA film (0.52 mol dm <sup>-3</sup> EDC) . . . . .	165
6.6	IR spectra of crosslinked HA film (1.0 mol dm <sup>-3</sup> EDC) . . . . .	166
6.7	IR spectra of crosslinked HA film (1.3 mol dm <sup>-3</sup> EDC) . . . . .	166



# List of Tables

1.1	ASIA Impairment Scale . . . . .	12
1.2	Elastic moduli of various common materials . . . . .	23
1.3	Elastic moduli of structures in the central nervous system . . . . .	24
3.1	Elastic moduli of structures in the central nervous system . . . . .	51
3.2	Reagents in PEDOT:biomolecule syntheses . . . . .	56
3.3	Horizontal profile data for PEDOT:CS 1:1 drop-cast film . . . . .	69
3.4	Horizontal profile data for PEDOT:HA 1:1 drop-cast film . . . . .	70
3.5	Sheet resistances of PEDOT:CS drop-cast films . . . . .	75
3.6	Sheet resistances for PEDOT:HA drop-cast films . . . . .	76
3.7	Sheet resistances for PEDOT:CS drop-cast films (half APS) . . . . .	77
3.8	ON/OFF ratios for a PEDOT:CS 1:1 based OECT) . . . . .	81
4.1	Composition of samples for freeze-drying . . . . .	92
4.2	Characteristics of PEDOT:CS OECTs after submersion in water . . . . .	101
5.1	Ethanol to EDC solution preparations . . . . .	117
5.2	EDC solution concentrations . . . . .	118



# Chapter 1

## Introduction

Spinal cord injuries (SCIs) can be devastating to sufferers with many victims experiencing some level of paralysis. In the USA alone, there were around 288,000 people with SCIs in 2018 [1]. Global estimates vary as the availability of data varies from country to country, but it is known that more than 75% of sufferers of traumatic SCIs are male [2]. Throughout history, SCIs and paralysis have been considered terrible and often permanent ailments. However, there are a number of treatments that show promising results, such as physiotherapy, surgical interventions to minimise trauma, and electrical stimulation of the spinal cord. Additionally, some researchers are looking into using organic bioelectronics in the spinal cord to treat and manage the pain related to SCIs, and other neurological problems [3–5].

The aim of this project was to create a novel, biodegradable, organic bioelectronic device, namely an organic electrochemical transistor (OECT), that could be suitable for use in the spinal cord and used in the treatment of SCIs in future. This chapter introduces the biology of the human nervous system and more specific information on the spinal cord, spinal cord injuries (SCIs), and their current treatments. The chapter then moves on to introduce organic bioelectronics, biomaterials, and hydrogels, lending context to the development of the novel device development described by this thesis.

### 1.1 The human nervous system

The human nervous system can be split into two categories; the peripheral nervous system (PNS) and the central nervous system (CNS). Both of these systems have different roles to play in the control and homeostasis of the human body. The human CNS is comprised of the brain and the spinal cord, whereas the PNS encompasses all the other neurons in the body [6, 7] as shown in figure 1.1. The PNS is involved in the detection of a stimulus (such as light or temperature) by a sensory organ (such as the eyes or skin) which then triggers a cascade of events sending a signal along sensory neurons to the CNS. The CNS then triggers a response to the stimulus signal by sending out a signal down motor neurons to an effector (e.g. a muscle group) which elicits the desired action (such as blinking or moving a hand away from a hot surface).

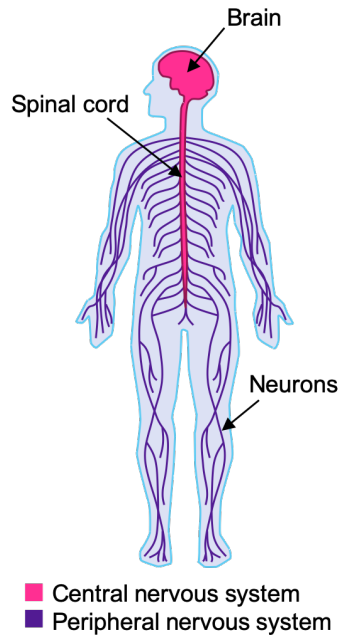


**Figure 1.1:** A simplified diagram of the human nervous system.

### 1.1.1 Nerve cells

The nervous system is made up of many individual nerve cells, known as neurons, as well as other cells known as glia [6–8]. The typical structure of a neuron is shown in figure 1.2. There are three main parts of a neuron cell; the cell body, the axon, and the axon terminals. The cell body contains the nucleus of the cell and is covered in protrusions extending outwards called dendrites. A single neuron cell can have vast and complex networks of dendrites (known as dendritic trees) which receive up to thousands of input signals [8]. These signals may be excitatory or inhibitory resulting in the generation of an action potential or not, respectively. Action potentials, the impulses that fire down a neuron, are explained in more detail in section 1.1.2.

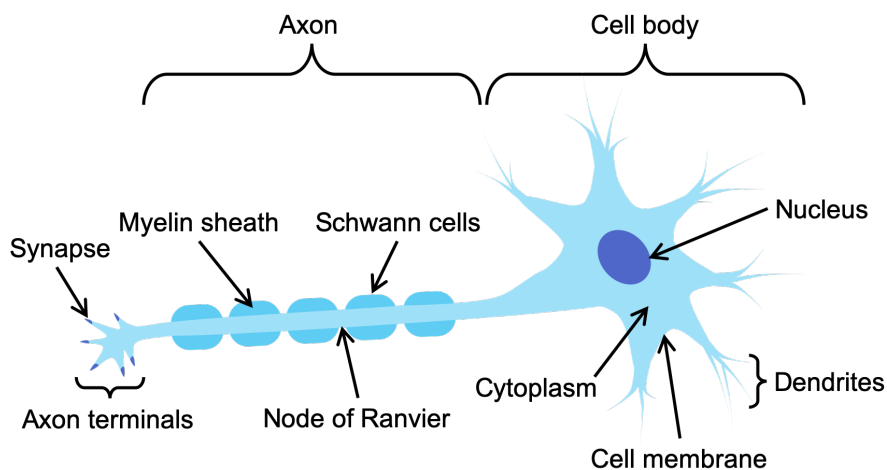


**Figure 1.2:** A diagram showing an individual neuron with the major structures labelled.

The axon of a neuron extends outwards from the cell body. The end of the axon splits into smaller

branches, the ends of which are called axon terminals. The axon terminals interface with other cells at junctions called synapses which are the sites where a signal from one pre-synaptic neuron is transmitted over to the next neuron along (the post-synaptic neuron). Synapses are explained in detail in section 1.1.3.

Many axons are covered in a fatty layer of insulation known as the myelin sheath. The myelin sheath insulates the axon and allows nerve signals to be carried rapidly from one end of the axon to the other [6, 8]. The myelin sheath is not continuous but covers sections of the axon, with short gaps between each section of sheath called the Nodes of Ranvier [6]. Myelinated axons transmit action potentials (the electrical impulses of the nervous system) faster than unmyelinated axons due to a process called saltatory conduction (see section 1.1.2) where the electrical impulse can ‘jump’ between the Nodes of Ranvier [8]. The myelin sheath is generated by Schwann cells in the PNS (as labelled on figure 1.2), whereas it is generated by oligodendrocytes in the CNS. These are examples of types of glial cells found in the nervous system (more details on glial cells follow this section). The role of the myelin sheath is extremely important in the normal control of the human body and problems with the myelin sheath can be devastating. Multiple sclerosis, which occurs as a result of de-myelination of the CNS, can leave a patient with muscle weakness and co-ordination issues, and there is no known cure [6, 9].

Depending on the specific role of the neuron, the structure of the cell may vary. For example, figure 1.2 shows the structure more typical of a motor neuron cell. These have a different structure to a sensory neuron (figure 1.3) where the distinction between the axon and dendrites is not as pronounced. A single protrusion leaves the cell body and splits in two to form two branches; one branch goes to the spinal cord to communicate with the CNS, and the other branch goes towards sensory receptors to receive sensory input [6]. Both of the branches and the single protrusion from the cell body are myelinated.

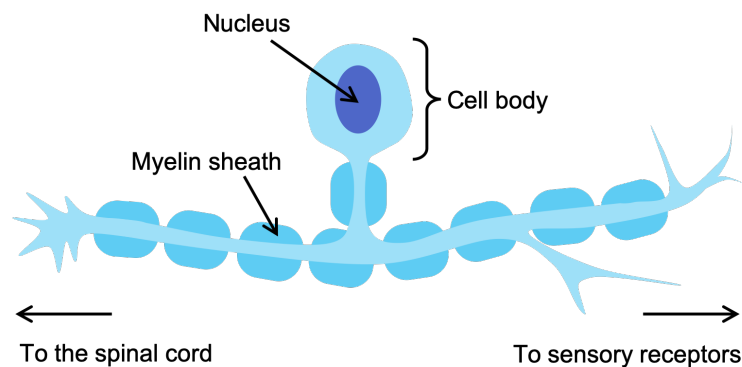


**Figure 1.3:** A diagram showing an individual sensory neuron with the major structures labelled.

## Glial cells

Glial cells are the other type of cell found alongside nerve cells in the human nervous system. In general, glial cells act to support and protect the neuronal cells in the CNS and PNS [7]. Schwann cells are the main type of glial cell present in the PNS, along with satellite cells [6]. Schwann cells produce myelin that forms the myelin sheath in the PNS, as well as acting to support nerve regeneration. Satellite cells help regulate the chemical environment surrounding sensory neurons. On the other hand, there are three main types of glial cell in the CNS (figure 1.4); oligodendrocytes, astrocytes, and microglia [7, 8]. Oligodendrocytes are responsible for the myelination of the CNS and also provide stability to the system.

Astrocytes are star-shaped cells which are the most common glial cell in the CNS. Their role is to support and maintain the blood-brain barrier and regulate the chemical surroundings of neurons. They also act as glucose storage facilities for neurons, and are thus highly important for the metabolism of the CNS. Finally, the microglia act as the immune system of the CNS, and help to clear dead cells and other waste materials. There are also ependymal cells, another CNS glial cell, that are found surrounding the spinal cord and brain which are involved in the circulation of cerebrospinal fluid.

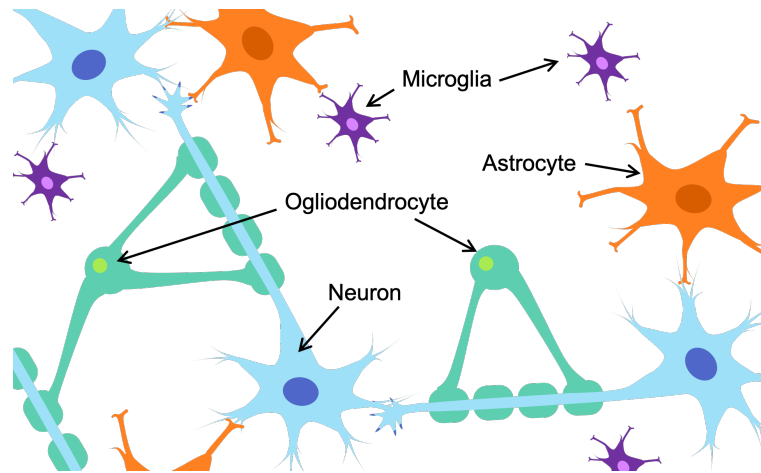


**Figure 1.4:** A diagram showing the glial cells present in the central nervous system, including astrocytes, oligodendrocytes, and microglia. Neurons are also shown.

Glial cells also play a role in protecting the nervous system after trauma by forming scar tissue around the site of an injury [8]. Such a physical barrier, although useful for keeping away harmful bacteria etc, also can stop neuronal regrowth which is why injuries of the nervous system can have devastating outcomes such as paralysis. Glial scarring is discussed in more detail in section 1.1.5.

## 1.1.2 Formation and transmission of nerve impulses

### Resting Potential

Prior to describing how nerve impulses, i.e. action potentials, are formed and propagated, it is required to understand how neurons are found in their inactive state at resting potential. Embedded in the surface of the nerve cell, there are sodium-potassium pumps that actively pump positive sodium ions ( $\text{Na}^+$ ) out of the cytoplasm to the outside of the cell whilst simultaneously pumping positive potassium ions ( $\text{K}^+$ ) from outside the cell into the cytoplasm [6] as shown in figure 1.5.  $\text{Na}^+$  and  $\text{K}^+$  ions diffuse back down their concentration gradients, but  $\text{K}^+$  diffuse back out of the cell faster than  $\text{Na}^+$  can diffuse back into the cell. This leads to a net movement of positive ions out of the cell making the inside of the cell negatively charged relative to the outside of the cell across the cell membrane. The potential difference is known as the resting potential and is approximately  $-70 \text{ mV}$  [6].

### Action Potential

When a stimulus is detected by a receptor in a sensory organ, a cascade of events within the cell is triggered. Initially, there will be a change in permeability to  $\text{Na}^+$  and  $\text{K}^+$  in the cell membrane at the

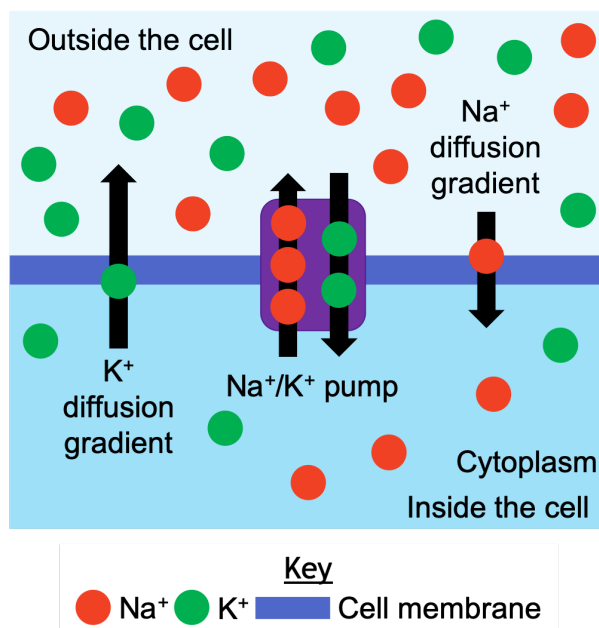


**Figure 1.5:** The diagram describes the process of establishing the resting potential in a neuron. The  $\text{Na}^+/\text{K}^+$  pump actively moves three  $\text{Na}^+$  out of the cell and two  $\text{K}^+$  ions into the cell. The large arrow labelled  $\text{K}^+$  diffusion gradient describes the faster diffusion of  $\text{K}^+$  back out of the cell than  $\text{Na}^+$  back into the cell (described by the small arrow on the right). This leads to the imbalance of ions seen in the diagram where there are many more positively charged ions outside of the cell than inside the cell, leading to a potential difference across the cell membrane where outside the cell has a net positive charge.

area of stimulation, which causes  $\text{Na}^+$  channels in that area to open [6].  $\text{Na}^+$  floods from the exterior of the cell into the cytoplasm down the concentration gradient that was established at resting potential. This influx of  $\text{Na}^+$  results in depolarisation across the membrane (i.e. the resting potential of the cell starts to become more positive from  $-70$  mV towards  $-65$  mV and  $-60$  mV and so on). If the depolarisation reaches a threshold voltage of around  $-55$  mV to  $-50$  mV, an action potential has been triggered and this can be considered the start of a nerve impulse. Note that if the threshold potential is not reached, no action potential is generated and the resting potential will be restored via ion diffusion. The influx of  $\text{Na}^+$  ions continues until the action potential reaches  $+40$  mV which in turn triggers the  $\text{Na}^+$  channels to close and  $\text{K}^+$  channels to open, causing  $\text{K}^+$  to flood out of the cytoplasm to outside of the cell. This process is called repolarisation as the potential across the membrane decreases [6]. The  $\text{K}^+$  then close and the  $\text{Na}^+/\text{K}^+$  pump restarts which works to restore the distribution of ions across the membrane, restoring the resting potential.

The formation of the action potential described above does not explain how a nerve impulse is carried along a neuron, but simply describes the changes in membrane potential in a specific area of the cell triggered by a stimulus.

When an action potential is set up across a localised area of the cell membrane, adjacent areas of the cell membrane are still at resting potential. This difference in potential results in a local current between the action potential and resting potential. The flow of  $\text{Na}^+$  towards the areas of resting potential triggers the  $\text{Na}^+$  channels in that area to open and cause depolarisation to occur until the action potential is reached. This results in the movement of the action potential and therefore the nerve impulse down the neuron.

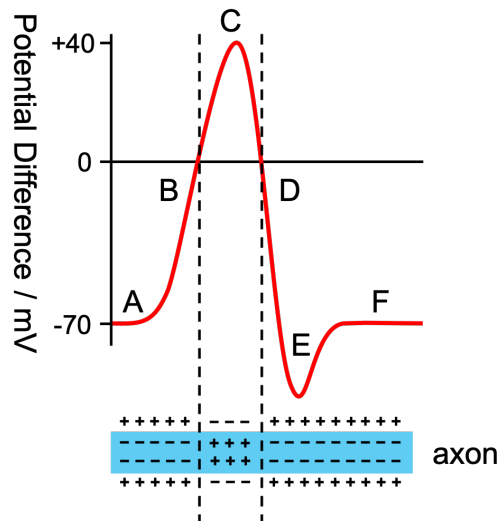


**Figure 1.6:** A simple plot of potential difference across the membrane of an axon as an action potential is generated. At point A, the cell is at resting potential ( $-70$  mV). As the potential across the axon increases to the threshold potential due to the influx of  $\text{Na}^+$  ions, depolarisation (B) occurs, reaching the action potential of  $+40$  mV at C. The potential then decreases again as  $\text{K}^+$  channels open allowing repolarisation across the membrane (D). Hyperpolarisation (E) occurs as the distribution of ions across the cell membrane leads to a more negative potential than resting potential (F), however this is brief (around 3 milliseconds), and resting potential is quickly re-established through the movement of ions across the membrane.

The illustration of the axon of a neuron below the plot depicts the change in net charge inside and outside the cell across the cell membrane when an action potential is generated.

Following the action potential, the length of time taken for the resting potential to be reestablished is called the refractory period, and during this time no new action potentials can be generated [6]. This means that the action potential can only travel in one direction down the neuron as the area behind the action potential will always be in recovery back to the resting potential.

If a stimulus is large, it will result in a greater frequency of impulses, not a larger action potential; i.e. another impulse will quickly follow the previous. As such, intensity of the stimulus is frequency modulated. For example, a low intensity stimulus will result in a low frequency of impulses down the neuron, whereas a very intense stimulus will give a very high frequency of impulses. Additionally, a high intensity stimulus will likely affect more than one neuron which will mean that there will be many impulses carried from many individual neurons to the CNS. The CNS can then interpret the many impulses as a very intense stimulus. All stimuli will result in an action potential of  $+40$  mV, as long as the initial threshold potential is reached. The size of the action potential does not change with intensity of stimulus.

### Saltatory Conduction

In a myelinated neuron, the myelin sheath (described in section 1.1.1) acts to insulate the axon. As a result,  $\text{Na}^+$  and  $\text{K}^+$  ions cannot pass through the cell membrane where it is insulated by the sheath. These ions can only pass from the cytoplasm of the neuron across the cell membrane at gaps in the myelin sheath at the Nodes of Ranvier. This means that the action potential ‘jumps’ along the neuron from one

node to the next in a process called saltatory conduction. The action potential is carried down the cell a lot quicker than in an unmyelinated neuron, which is advantageous to an organism as it results in faster responses within the body.

Saltatory conduction occurs down the axons of myelinated neurons, as demonstrated in figure 1.7. When an action potential is triggered, there is an influx of sodium ions into the axon only at a Node of Ranvier. The local current created around the node spreads in the direction of the action potential and triggers the sodium channels in the adjacent node to open. This allows the influx of  $\text{Na}^+$  ions to begin causing a change in potential across the membrane at that node, until the threshold potential is reached and another action potential is triggered [10]. The saltatory conduction continues down the neuron and appears to hop from one node to the next [8]. As previously mentioned, following the action potential, a refractory period occurs when no new action potentials can be established across the membrane. [6] This is also true in the case of saltatory conduction where no new action potentials can occur during the refractory period across the membranes at the Nodes of Ranvier. This means that the action potential can only travel in one direction down the neuron as the area behind the action potential will always be in recovery back to the resting potential.

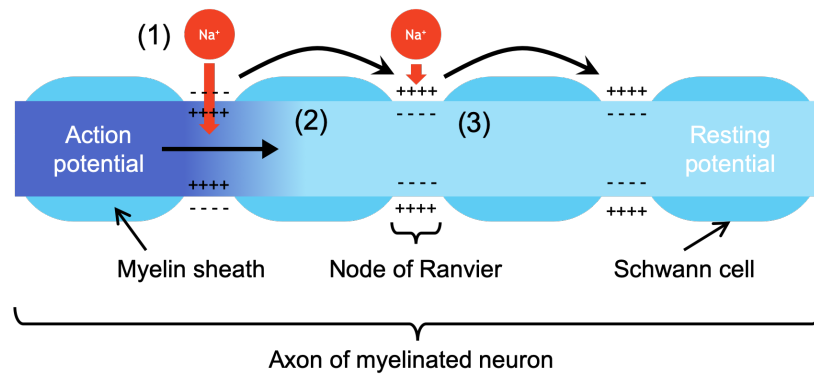


**Figure 1.7:** When an action potential is triggered, there is an influx of sodium ions into the axon only at a Node of Ranvier (1). The local current created around the node spreads in the direction of the action potential (2) and triggers the sodium channels in the adjacent node to open (3), which eventually triggers an action potential at this node. This repeats at each node giving the appearance of the action potential hopping from one node to the next. The directionality is caused by the refractory period following the action potential.

### 1.1.3 Synapses

As individual neurons are not in contact with each other, a nerve impulses must traverse this gap, or synapse, using an alternative system to trigger another action potential in the next neuron along.

As described in section 1.1.2, an action potential is generated and travels down a neuron by the depolarisation of the neuron cell membrane. When the action potential reaches the end of the axon of the presynaptic neuron, known as the synaptic knob, voltage-gated calcium ion channels open [6]. Calcium ions ( $\text{Ca}^{2+}$ ) flood into the synaptic knob and the influx of  $\text{Ca}^{2+}$  ions trigger vesicles containing chemical neurotransmitters to migrate towards the presynaptic membrane, fuse with the membrane, and release neurotransmitters into the synapse itself (the synaptic cleft) [6]. The neurotransmitters then diffuse down a concentration gradient towards the postsynaptic neuron where they bind to complementary ligand-gated

$\text{Na}^+$  channels in the postsynaptic membrane. The binding of the neurotransmitter molecules to the  $\text{Na}^+$  channels cause them to open and there is an influx of  $\text{Na}^+$  ions into the postsynaptic neuron [6]. The influx of the  $\text{Na}^+$  ions causes depolarisation across the postsynaptic membrane and once the threshold potential is reached, an action potential is generated and the propagation of the nerve impulse continues. This process is described by figure 1.8.

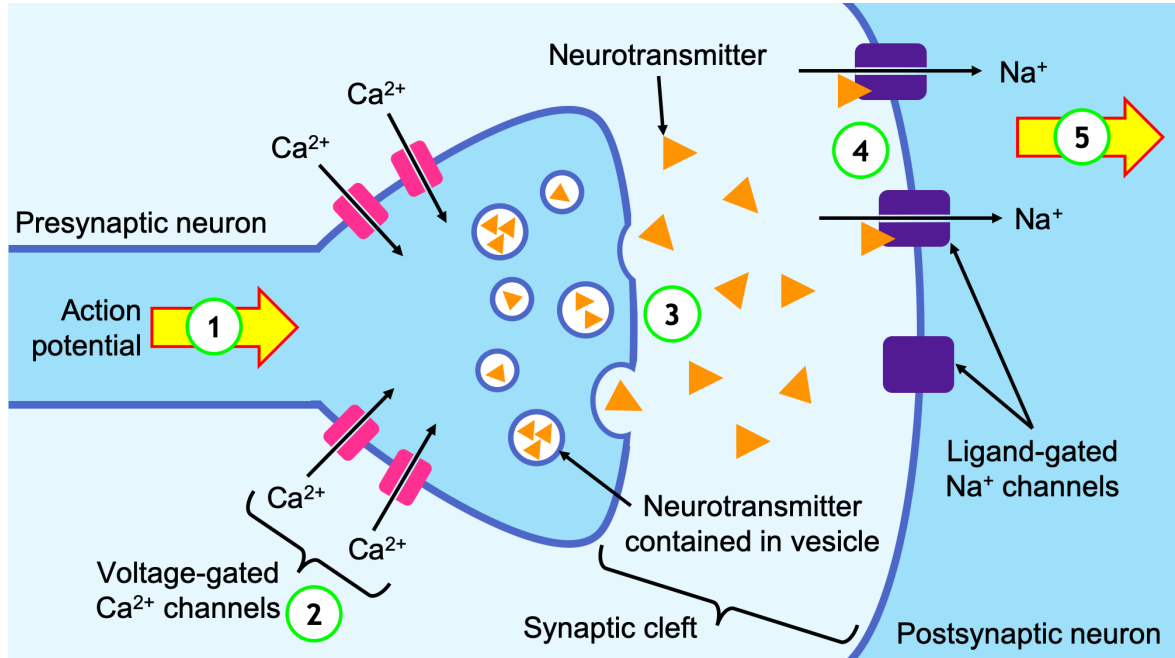


**Figure 1.8:** A simple diagram of a synapse with the presynaptic neuron on the left, and the postsynaptic neuron on the right. When the action potential (1) reaches the end of the presynaptic neuron, it triggers the opening of voltage-gated calcium channels (2). The influx of the  $\text{Ca}^{2+}$  ions then triggers vesicles containing neurotransmitter (orange triangles) to fuse with the presynaptic membrane releasing neurotransmitter into the synaptic cleft (3). The molecules of neurotransmitter diffuse across the synaptic cleft and bind with the complementary ligand-gated  $\text{Na}^+$  channels (4) on the post-synaptic membrane. This causes the  $\text{Na}^+$  channels open leading to an influx of  $\text{Na}^+$  ions into the postsynaptic neuron leading to the depolarisation of the postsynaptic membrane, and triggering an action potential (5).

Once there is no longer an action potential present in the presynaptic neuron, the release of neurotransmitter into synaptic cleft stops. To stop the continual generation of new action potentials in the postsynaptic neuron, the neurotransmitter present in the synaptic cleft requires clearing. The neurotransmitter can be reabsorbed back into the presynaptic neuron, it can be broken down by specific enzymes, or simply diffuse away from the synapse and be absorbed by glial cells. Once there is no more neurotransmitter present, the ligand-gated  $\text{Na}^+$  channels can close (as they are no longer bound to the complementary neurotransmitter) and the postsynaptic neuron returns to resting potential.

The presence of synapses in the nervous system interrupt the flow of action potentials and thus slow down the overall speed of nerve impulses as chemical diffusion of neurotransmitter across the synaptic cleft is a slower process than the electrical impulse along the neuron itself. The presence of synapses is, however, advantageous as they act to further ensure that nerve impulses only travel in one direction.

## Neurotransmitters

Chemical neurotransmitters play a key role in the human nervous system as they allow the propagation of neuronal impulses across synapses. There are a number of different types of neurotransmitter present in the human nervous system but all can be broadly categorised as excitatory or inhibitory neurotransmitters.

Excitatory neurotransmitters bind to the post-synaptic membrane and trigger the opening of ion channels, and thus trigger an action potential. On the other hand, when inhibitory neurotransmitters bind to the post-synaptic membrane, it does not trigger the firing of an action potential in the post-synaptic neuron [6]. Examples of excitatory neurotransmitters include acetylcholine, and glutamate, whereas  $\gamma$ -aminobutyric acid (GABA) and glycine are examples of inhibitory neurotransmitters.

## Synaptic plasticity

Synaptic plasticity refers to how synapses can change their behaviour over time in response to changes in their activity. Changes in synaptic plasticity are usually a result of how much neurotransmitter is released into a synapse and/or a change in how the postsynaptic neurons respond to a neurotransmitter [6]. This synaptic plasticity within the nervous system is important for the formation and retention of memories and is important for learning.

Synaptic plasticity operates on multiple timescales; long- and short-term. Long-term synaptic plasticity refers to changes in the synapse that last for minutes to hours or more and are usually related to learning and memory [6]. Short-term plasticity (STP) happens on a much faster timescale, from milliseconds to minutes, and is thought to be more related to simpler processing tasks [11–13].

STP acts to either enhance or depress a response across a synapse in the post-synaptic neuron. An action potential in the presynaptic neuron will trigger the release of neurotransmitter into the synapse. As each action potential triggers the release of neurotransmitter, there will be an increase in the amount of neurotransmitter in the synaptic cleft that builds up over a short time. The greater concentration of neurotransmitter released results in a short-term enhanced response in the post-synaptic neuron. If repeating action potentials keep triggering the release of neurotransmitter across a synapse, there can then be a depressive response in the post-synaptic neuron. This is because there is a depletion of available neurotransmitter in the pre-synaptic neuron as it cannot be replaced or recovered at a high enough rate to keep up with the frequency of the incoming action potentials.

STP behaviour is of interest to many in the field of organic bioelectronics who are looking to develop neuromorphic devices which could be used to interface directly with neurons and the human nervous system. An example of such a device is a synapstor which is explained in more detail in chapter 4.

### 1.1.4 Central nervous system

The CNS in the human body acts to receive information from the rest of the body in the form of nerve impulses, and controls and coordinates all bodily functions and responses. It is made up of the brain and the spinal cord, which itself runs from the brain stem down to the base of the spine [7], as shown in

figure 1.9. The spinal cord is protected by the vertebrae of the spinal column. Between the vertebrae are disks of cartilage which help cushion the spine and provide flexibility. There are 31 pairs of spinal nerves that emerge from the spinal cord between the vertebrae. Each nerve emerges from the spinal cord as two branches known as roots, one from the anterior and the other from the posterior. The spinal cord only reaches three quarters down the spinal column, but a bundle of nerves called the *cauda equina* extends further. The *cauda equina* carries nerve impulses to and from the legs into the spinal cord and CNS. The spinal cord is usually split into four regions; the cervical region, the thoracic region, lumbar region, and the sacral region [8]. The cervical region of the spinal cord supplies nerves to the upper part of the body including the back of the head, neck, shoulders and arms, and the diaphragm. The thoracic section of the spinal cord supplies the chest and some parts of the abdomen, with the lumbar region supplying the lower back and certain parts of the thighs and legs. Finally, the sacral region connects with nerves in the buttocks, the legs and feet, and the genitals.

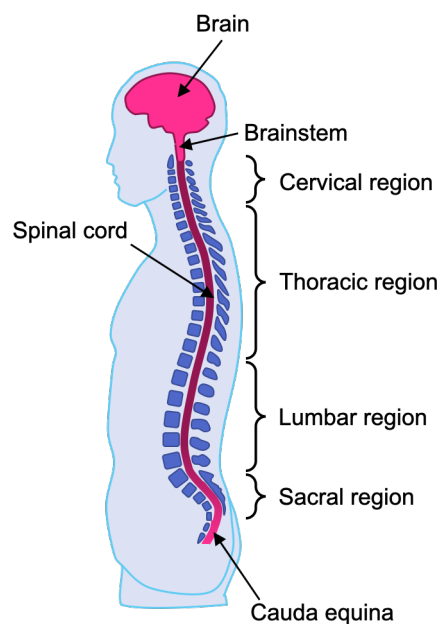


**Figure 1.9:** The structures present in the CNS, including the brain and the spinal cord.

The spinal cord is covered by three membrane layers known as meninges; the dura mater (outer most membrane), the arachnoid mater, and the pia mater (innermost membrane) [14]. These meninges (see figure 1.10) encapsulate the spinal cord in cerebrospinal fluid which cushions the spinal cord from shock damage and transport nutrients and waste products around the CNS.

The spinal cord itself is made up of two main types of tissue; grey and white matter (figure 1.11), each playing a different role [6, 7]. The butterfly shaped centre of the cord is made up of grey matter with the ventral or anterior horns containing motor nerve cells that transmit information from the CNS to skeletal muscles responsible for movement. The dorsal or posterior horns contain sensory neurons which transmit sensory impulses from around the body to the CNS. The white matter that surrounds the central grey matter is made up of columns of nerve fibres (axons) that carry sensory information to the brain from the rest of the body (ascending tracts) and columns that carry nerve impulses from the brain to the muscles (descending tracts). The white matter is named as such due to its white colour which is a result of the fatty myelin sheath insulating layer described previously [8].

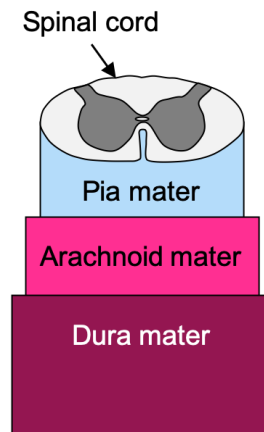


**Figure 1.10:** There are three meninges that surround the spinal cord; the pia mater, the arachnoid mater, and the dura mater.

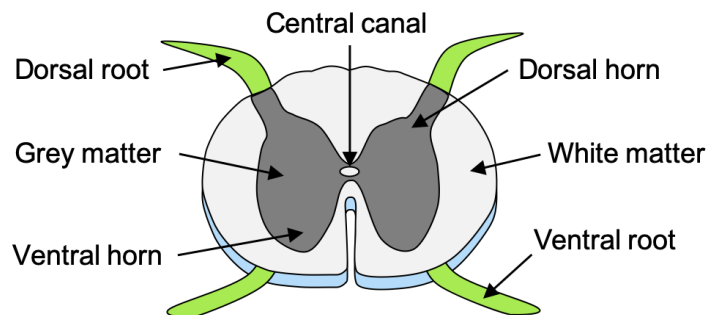


**Figure 1.11:** A labelled cross section of the spinal cord.

The spinal cord is the first part of the CNS to receive information from sensory neurons around most of the body and channels these signals up to the brain. Likewise, the spinal cord acts as the main conduit from the brain to the rest of the body allowing responses to sensory information to keep the human body alive and moving. Moreover, the spinal cord is responsible for coordinating certain reflexes such as the knee jerk reflex, via relay neurons without input from the brain [6]. Having considered the role of the spinal cord within the human body, it is clear to see that a traumatic injury or disease of the spinal cord that disrupts its normal functionality would cause large detrimental effects to the function and control of rest of the body.

### 1.1.5 Spinal cord injuries

Spinal cord injuries (SCIs) are typically categorised as non-traumatic or traumatic meaning that they are caused by disease or an external physical force/impact, respectively [2, 8]. Global estimates of the prevalence of SCIs vary as the availability of data varies from country to country. Traumatic SCIs appear to have increased in incidence in modern times, however this could be due to increased availability of data. In 2007, there were estimated total 180,000 new cases of traumatic SCI globally [15], and more recent data shows that in 2016 there were 930,000 cases [16]. The main causes of traumatic SCI globally are falls and road injuries [16]. The incidence of SCIs is higher in the male population as data shows that more than 75% of sufferers of traumatic SCIs are male [2].

The action of an SCI is often through mechanical trauma leading to compression, torsion, or complete severance of the spinal cord itself [17, 18]. This is referred to as the primary injury, and results in damage to the neurons and the oligodendrocytes in the spinal cord [2, 17]. The primary injury also results in the disruption of the blood-spinal cord barrier which can lead to haemorrhaging bringing an influx of inflammatory cells triggering the inflammation of the spinal cord [2]. This inflammation can often lead to further injury as the spinal cord expands to fill the space in the spinal canal and compresses the spinal cord further at the site of injury [17, 18]. The secondary injuries have more complex pathologies and cause extensive neuronal and oligodendrocytic damage, mostly due to lack of blood supply [2, 17]. The inflammation of the spinal cord subsides over time and cystic cavities form due to loss of tissue volume [2]. Glial scarring also occurs in a process called gliosis. The function of the glial scar tissue is to protect the spinal cord and wider CNS after injury by reforming the blood-spinal cord barrier that forms a barrier against infectious microorganisms and to seal off the boundary between neuronal and non-neuronal tissue. Glial scar formation also helps encourage the revascularisation of the injury site which helps the healing process around the injury [2]. The drawback however is that the formation of glial scar tissue also greatly restricts the regrowth of neurons meaning the spinal cord cannot heal and reform a connection following SCI [2, 18].

The severity of an SCI is measured by the ASIA impairment scale (table 1.1) that grades the level of function that remains in various parts of the body as a result of an SCI. This scale runs from the least severe grade E with no neurological deficit or sensory loss up to the most severe grade A with complete loss of motor and sensory function below the level of injury [19].

**Table 1.1:** The American Spinal Injury Association (ASIA) Impairment Scale [19].

Category	Description
A (Complete)	No motor or sensory function is preserved in the sacral segments S4–S5.
B (Incomplete)	Sensory function preserved but not motor function is preserved below the neurological level and includes the sacral segments S4–S5.
C (Incomplete)	Motor function is preserved below the neurological level, and more than half of key muscles below the neurological level have a muscle grade less than 3.
D (Incomplete)	Motor function is preserved below the neurological level, and at least half of key muscles below the neurological level have a muscle grade of 3 or more.
E (Normal)	Motor and sensory function are normal.

The position of injury on the spinal cord indicates what level of functionality will be lost as a result of that SCI. As previously stated, the thoracic spinal cord supplies nerves to the chest and some of the abdomen, so an SCI above this region will result in loss of function in the chest, abdomen, and regions of the body below this point. A SCI lower down the spinal cord may result in loss of function in the legs only, for example. Paraplegia describes paralysis from the chest or waist down. Tetraplegia or quadraplegia refers to paralysis below the cervical spinal cord or the first thoracic vertebra that results in some degree of loss of function in arms and legs, respectively. Other effects of paralysis include loss of bowel and bladder control depending on the position of the injury. SCIs can have significant impact on mental as well as physical health, with many sufferers of traumatic SCIs reporting symptoms of depression and anxiety [1].

### 1.1.6 Treating spinal cord injuries

There are no known cures for SCIs. There are, however, a number of ways to manage and minimise the extent of the damage during primary injury stage [2, 18, 20]. Typically, this involves minimising compression in the region of the SCI, initially through completely immobilising the spinal column by the use of a spine board and a cervical collar during transfer to hospital. Surgery is a major method of decompressing the spinal cord, and allows realignment of the spinal column [2, 20]. There are also a large range of pharmacological interventions that may be carried out during the early stages of SCIs to minimise inflammation [18].

Beyond treating the initial injury, rehabilitation is the main focus of treating SCIs [17] and physical therapies make up a large part of this rehabilitation [2]. Strength and mobility training are typically important and can be used to train patients to be able to recover some lost function as a result of an SCI. Mobility training has been shown to trigger cellular signalling changes that encourage axon regeneration in animal models [2]. Virtual or augmented reality therapies have been shown to reduce the neuropathic pain that SCI patients often experience [21]. In one study [22], it was shown that complete paraplegic SCI patients could actually recover voluntary motor control of muscles below the point of injury through use of a immersive virtual reality training program with complementary walking training using an exoskeleton. This led to half the patients in the study being reclassified as having incomplete paraplegia.

Scaffolds and hydrogels designed for use in the CNS have been shown to encourage the regrowth of neural cells and tissues [8, 18, 23]. These structures mimic the environment in the body in which native cells grow, and can support cell regeneration. Many examples of scaffolds and hydrogels as experimental treatments *in vitro* and in animal models are summarised in chapter 5. Cell-based therapies are also of great interest to researchers as a way of restoring functionality to those suffering from SCIs. Implantation of stem cells into the site of an SCI has resulted in improvements in ASIA impairment scores in human test subjects with patients regaining some sensory and motor functionality [23]. Furthermore, the use of biomaterial scaffolds in SCI treatments can be combined with stem cell-based treatments and have had some successes in animal testing [8, 18, 23].

Another approach to treating SCIs is through the use of bioelectronics. Electrical spinal cord stimulation has been shown to reduce pain in SCI patients [24], and can be used to stimulate motor function in non-functioning muscles [25] helping patients regain bladder and bowel control, for example. Electronic stimulation combined with physical training can produce even more impressive results with recovery of functionality in the limbs of paralysed test subjects [26], including allowing paralysed human patients to walk again unaided [5]. In 2015, the development of an e-dura was reported [27]. The e-dura was a soft neuroprosthesis that mimicked the shape and elasticity of the dura mater and contained an array of electrodes and chemotrodes (microfluidic channels that delivers drugs locally), as shown in figure 1.12. The device was shown to restore locomotion in rats after a paralyzing SCI. The e-dura was different to typical electrostimulation devices as it directly interfaced the spinal cord under the dura mater whereas prior to the development of the device, stimulating electrodes were typically attached to the skin for transcutaneous application of stimulation [26]. The electrodes of the e-dura provided continuous electrochemical stimulation to the spinal locomotor circuits below a thoracic SCI. By contrast, the chemotrodes (microfluidic channels) delivered serotonergic replacement drug therapies to the site of the SCI. Side effects of serotonergic agents on the autonomic nervous system can cause dysfunction, which if untreated, can lead to effects such as tachycardia, hypertension, and diarrhoea. Together the electrical and chemical

stimulation allowed the paralysed rats to walk on their hind legs again on a treadmill whilst their body weight was supported.

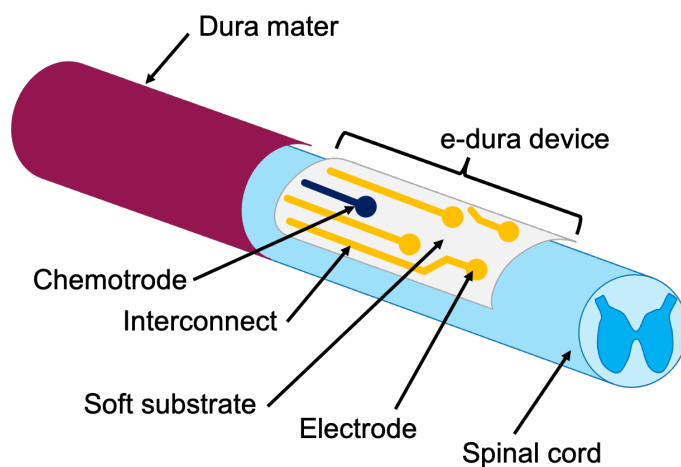


**Figure 1.12:** Illustration of the e-dura device described by [27], showing the positioning of the device under the dura mater of the spinal cord, as well as the electrodes and chemotrode on the e-dura itself.

The e-dura device was scaled and developed for use in non-human primate test subjects [28] however the experiments differed to those for the rat models. The purpose of the experiments in the non-human primates was to demonstrate the translation of a experimental soft bioelectronic device in animals to use in humans. It was shown that the scaled e-dura device could illicit reflex responses in the forelimbs when applying electrical stimulatory signals.

Organic bioelectronics are of interest for use in the treatment of SCIs and in the spinal cord in general [4, 29–33]. For example, micropatterned poly(pyrrole) and poly(pyrrole)-coated nano-fibres have been shown to influence the direction of neuron growth indicating that they could be used to help guide neuron regrowth through an SCI [29]. In addition, poly(3,4-ethylenedioxythiophene):poly(styrene sulfonate) (PEDOT:PSS) based organic electrochemical transistors (OECTs) have been used to record brain and neuronal activity [31, 33, 34], offering a route for use in the spinal cord.

## 1.2 Organic bioelectronics

Organic bioelectronics is a field of research encapsulating the use of organic electronic devices in biological systems [34]. The use of such devices may be to regulate the function of an organ or biological process such as neural implants in the brain, monitor the function of a biological system such as glucose monitoring in the blood stream of diabetics, to deliver drugs and chemical therapies to specific localised tissues, or a combination of all three [29, 30, 34]. There are a number of different types of organic electronic devices with different architectures including organic field-effect transistors (OFETs), electrolyte-gated organic field-effect transistors (EGOFETs), and organic electrochemical transistors (OECTs). All three types operate by the modulation of a current from a source to a drain electrode through an organic material through the application of a potential bias at a gate electrode.

### 1.2.1 Field-effect transistors

To understand how OFETs, EGOFETs, and OECTs operate, it is useful to understand how conventional field-effect transistors (FETs) function.

FETs are a type of transistor that use an electric field to control the current flowing between a source and a drain electrode through a semiconductor [31]. They are three terminal devices consisting of a source, drain, and gate electrode. The application of a voltage to the gate electrode imposes an electric field that alters the conductivity of the material between the source and the drain electrode, thus controlling the flow of current between the two terminals. Typically, FETs only use one type of charge carrier; n-type FETs have electron charge carriers, and p-type FETs make use of holes as charge carriers [31]. There are also examples of ambipolar FETs that use two types of charge carrier. The density of the charge carriers influences the conductivity of the channel between the source and the drain and thus amount of current flowing between the two terminals. FETs can operate in one of two modes; depletion mode or enhancement mode. In depletion mode, the application of a gate voltage ‘depletes’ the amount of charge carriers available in the semiconductor and thus decreases the current flowing between the source and the drain electrode. This leads to the FET eventually turning ‘off’ and no current flows [35]. For this reason, depletion mode devices are often referred to as ‘normally-ON’ FETs. On the other hand, enhancement mode devices begin in an ‘off’ state where no current can flow between the source and drain electrodes and application of a voltage bias at the gate allows current to flow between the two terminals [35]. The most common FET is the metal-oxide-semiconductor field-effect transistor (MOSFET) and it is considered to form the basis of modern electronics [31, 36].

Organic field-effect transistors (OFETs) form the basis of a lot of organic electronic research. These are FETs that use organic semiconductors as the semiconductor layer. Typically the devices make use of  $\pi$ -conjugated organic semiconductors such as poly(3-hexylthiophene) (P3HT) [35]. The source/drain electrodes and the organic semiconducting material is separated from a gate electrode by an insulating dielectric layer [30] (figure 1.13). As with conventional FETs, the electric field generated by the gate electrode modulates the availability of the charge carriers in the organic semiconductor by drawing charge carriers towards/away from the dielectric layer, and thus modulates the source-drain current. When first developed OFETs were often used as sensors for gases and vapours, but have been demonstrated to detect molecules in aqueous environments [30], and are used in radio frequency identification (RFID) tags [37]. The change in current upon exposure to different concentrations of analyte at fixed gate and source-drain voltages can be used to create calibration curves, which can then be used to measure the concentration of the analyte in an unknown sample [35]. For example OFET-based sensors have been used to selectively detect the different enantiomers of menthol [38], a molecule often used in food flavourings.

### 1.2.2 Electrolyte-gated organic field-effect transistors

Instead of a dielectric layer as in the OFET, EGOFETs are gated through an electrolyte. The gate and the organic electronic material (OEM) are in direct contact with the electrolyte (figure 1.14) and thus the modulation of the source-drain current is due to the field effects of electrical double layers at the gate-electrolyte interface and the electrolyte-OEM interface [35, 39] (figure 1.14). The OEMs used in EGOFETs are usually organic semiconducting polymers [39] such as P3HT [36], however there have also been examples of graphene-based EGOFETs [40]. Pentacene is also a common organic layer used

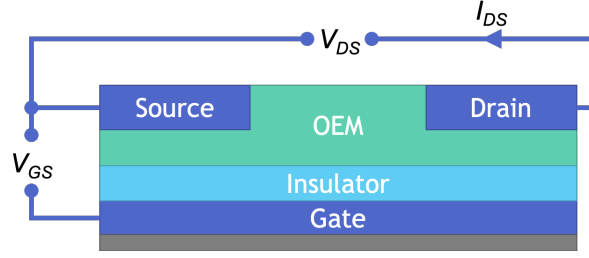


**Figure 1.13:** Schematic diagram of an organic field-effect transistor (OFET) showing the gate electrode separated from the source, drain, and organic electronic material (OEM), by an insulator layer. In the case of an OFET, the OEM is an organic semiconductor.  $V_{DS}$  refers to the potential difference between the source and drain, whereas  $V_{GS}$  refers to the potential difference across the gate and source.  $I_{DS}$  shows the current flowing when the device is switched on.

in EGOFETs [35]. The effect of changing the voltage at the gate electrode depends on the type of organic semiconductor used in the device. When the gate electrode is negatively biased, it results in the accumulation of positive ions at the gate-electrolyte interface, which in turn results in an accumulation of anions at the electrolyte-OEM interface [36, 39, 40]. This accumulation of anions results in the accumulation of holes in the top layer of the OEM which, in the case of the p-type semiconductor, makes OEM more conducting resulting in a greater source-drain current.

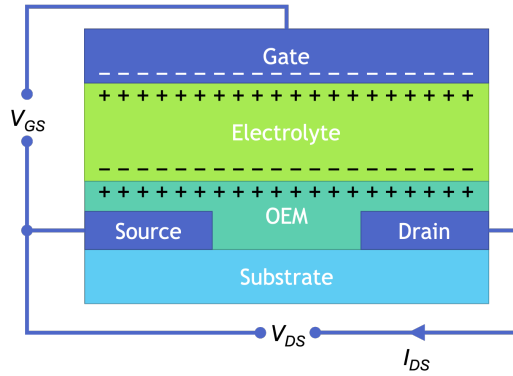


**Figure 1.14:** Schematic diagram of an electrolyte-gated organic field-effect transistor showing the gate electrode separated from the source and the drain electrodes, and the organic electronic material (OEM). Electrical double layers form at the gate-electrolyte interface and at the electrolyte-OEM interface.  $V_{DS}$  refers to the potential difference between the source and drain, whereas  $V_{GS}$  refers to the potential difference across the gate and source.  $I_{DS}$  shows the current flowing when the device is switched on.

The accumulation of ions at the interfaces is in the form of electrical double layers [35, 36, 39, 40]. As the device operates in electrolyte solution, there is a bulk concentration of solvated anions and cations. When the gate is negatively biased, an electrical double layer form at the interface between the gate and the electrolyte. This consists of a dense layer of cations at the interface called the Helmholtz layer, which is made up of a single layer of solvent molecules and solvated cations. The diffuse layer contains solvated cations at a greater concentration than found in the bulk of the electrolyte, and decreases in concentration the further away one moves from the gate into the bulk of the solution. An equivalent double layer is formed at the electrolyte-OEM interface with a double layer of anions. An electrical field is established across the interfaces which, in turn, prevents the flow of electric current across the interfaces, thus allowing the electrical double layer to be described as a capacitor [36]. The capacitance

of the electrical double layers is typically very high, around  $10 \mu\text{F cm}^{-2}$  [35], due to their very small thickness (on the order of a few angstroms) [36]. This allows EGFETs to operate at very low voltages (less than 1V) [36, 40] which makes them ideal for biological sensing applications. Typically, EGFET biosensors operate via the inclusion of a biorecognition element. This is often in the form of enzymes or antibodies embedded in the organic semiconductor surface. There have been many reported examples of EGFET-based biosensors including deoxyribonucleic acid (DNA) and dopamine sensors [30, 36, 41]. Clinically relevant EGFET devices have also been realised. In 2020, Sailapu *et al.* [42] published a paper describing an ultrasensitive EGFET biosensor that could detect HIV-1 p24 antigens in fM concentrations, making the device suitable for early diagnosis of HIV. Furthermore, there have been examples of directly interfacing EGFET devices with neural tissues for stimulation and measurement applications [43, 44].

### 1.2.3 Organic electrochemical transistors

OECTs have a similar basic configuration to EGFETs, however they operate via a different principle. OECTs operate by ions penetrating and doping/dedoping the OEM, instead of forming electrical double layers at interfaces as in EGFETs with no penetration of the OEM.

OECTs were first developed by White *et al.* in the 1980s [45]. The researchers demonstrated that by applying a potential bias at a gate electrode separated from a poly(pyrrole) film by an electrolyte solution, the conductivity of the poly(pyrrole) could be modulated. OECTs operate via the doping and dedoping of an organic electronic material (OEM) [31, 34, 36] such as PEDOT:PSS. A gate electrode is separated from the OEM by an electrolyte solution, as seen in figure 1.15. By applying a voltage bias at the gate electrode, ions can be driven in or out of the OEM from or to the electrolyte [34]. In turn, this dopes or dedopes the OEM, altering its conductivity. The changes in conductivity of the OEM therefore can modulate the current that flows between the biased source and drain electrodes [31]. The key characteristic that distinguishes OECTs from other devices is that the doping state of the OEM changes across the entire volume of the material as oppose to just at the interface [31].

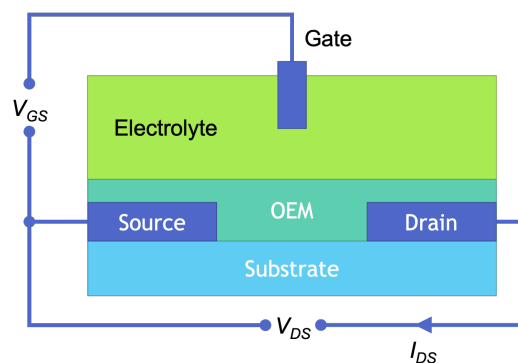


**Figure 1.15:** Schematic diagram of an organic electrochemical transistor showing the gate electrode separated from the source and the drain electrodes, and the OEM.  $V_{DS}$  refers to the potential difference between the source and drain, whereas  $V_{GS}$  refers to the potential difference across the gate and source.  $I_{DS}$  shows the current flowing when the device is switched on.

The OEM of choice for most OECTs is PEDOT:PSS due to its high conductivity and favourable charge transfer properties [30, 33, 46]. PEDOT:PSS is also easily processable, and stable under aqueous condi-

tions and in air. PEDOT itself is a semi-conducting polymer which when doped is a p-type conductor which means that the charge carriers in PEDOT are holes. The positive holes are electronically balanced by the negative charges of sulfonate anions on the PSS [31]. This material is discussed more extensively in section 1.2.4.

PEDOT:PSS based OEETs operate in depletion mode [30, 31, 33, 46]. This means that when there is no voltage applied at the gate electrode, the PEDOT is fully doped allowing current to flow between a biased source and drain electrode [30, 31]. This is also known as the “ON” state. This state is shown in figure 1.16 on the left where the gate voltage ( $V_G$ ) is less than or equal to zero volts. As a voltage bias is applied to the gate electrode, ions from the electrolyte are driven into the bulk of the PEDOT:PSS and act to counterbalance the negative charges on the PSS instead of the positive holes in the PEDOT, thus dedoping the PEDOT rendering it non-conductive [30, 46]. No current can flow through the channel between the source and drain, and thus the OEET is said to be “OFF”. This can be seen on the right of figure 1.16.

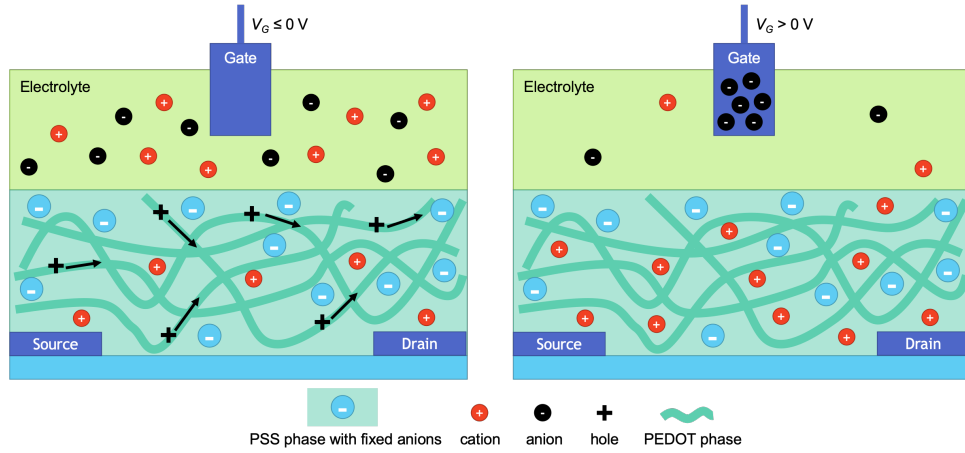
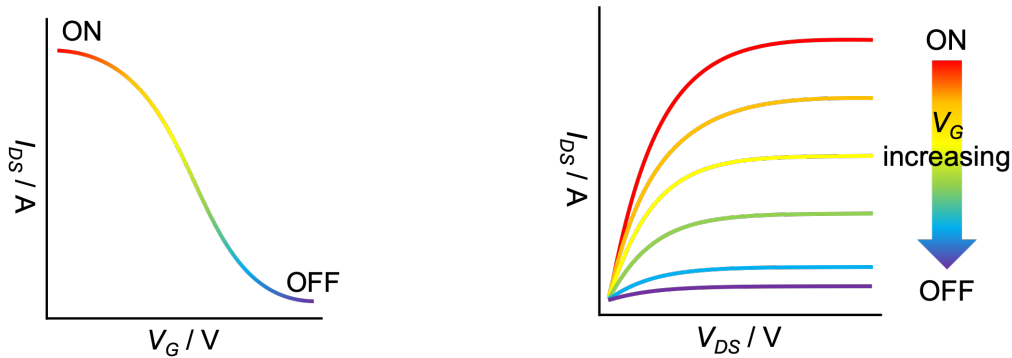


**Figure 1.16:** A PEDOT:PSS based OEET [30].

One of the advantages of OEETs is that the dedoping or doping occurs through the entire volume of the OEM opposed just at the interface like in ‘traditional’ FETs [31]. The result of this is that a small change in gate voltage leads to a large change in source-drain current meaning that the devices are highly sensitive and can operate at low voltages, making them ideal for use in biological sensing applications. On the other hand, the volumetric nature of the OEET responses results in slow response times on the order of a few microseconds [31]. This is attributed to the ionic contribution to the operation of the OEET [47]. Ion diffusion through the OEM is usually the rate limiting factor of OEET devices. This is due, in combination, to the capacitance of the channel and the resistance of the electrolyte [30, 31].

Transfer curves and plots of output characteristics are useful tools in demonstrating how OEETs (and other transistors) operate. Figure 1.17 shows a transfer curve for a typical depletion mode OEET and the output characteristics for the same. These plots can also be used to assess the properties of the OEET. OEETs can transduce small changes in the voltage at the gate electrode into large changes in the source-drain current, thus the greater the gradient of a transfer curve, the larger the change in source-drain current for any given gate voltage. The gradient of the transfer curve, i.e. the first derivative  $\delta I_{DS}/\delta V_G$ , is called the transconductance ( $g_m$ ) and is typically very high for OEET devices [31]. The transconductance of OEETs scale with thickness of the OEM, whereas this is not the case with FETs, and therefore thickness of the OEM is a parameter that can be tuned to tune the device performance

[30]. Other elements of the device geometry can also be changed to tune the device performance such as the source and drain electrode design, as the width to length ratio of the channel is directly related to the transconductance of the devices [31].



(a) A transfer curve for a typical depletion mode OEET. (b) Output characteristics for a depletion mode OEET.

**Figure 1.17:** The transfer (a) and output (b) characteristics of a typical depletion mode OEET device. In both plots, it can be seen that as the gate voltage ( $V_G$ ) increases, there is a decrease in source-drain current ( $I_{DS}$ ) as the PEDOT (or other OEM) is dedoped, resulting in the device moving from an ON state to an OFF state. Additionally, the output characteristics plot (b) shows how increasing the gate voltage ( $V_G$ ) causes the source-drain current to ( $I_{DS}$ ) to decrease, no matter the source-drain voltage ( $V_{DS}$ ), due to the dedoping of the PEDOT or other OEM.

As OEETs transduce signals between ionic (ions in the electrolyte) and electronic currents (current flow through the OEM), this often makes them the interface of choice between biological signals and synthetic electronics, making them a favoured bioelectronic device for many applications. The low operation voltages and the ability to function in water/electrolytes makes them ideal for use as sensors [48].

#### 1.2.4 Introduction to poly(3,4-ethylenedioxythiophene) (PEDOT)

Poly(3,4-ethylenedioxythiophene) (PEDOT, figure 1.18) is a semiconducting polymer which is usually found in its oxidised (or doped) conducting form, stabilised by poly(styrene sulfonate) (PSS, figure 1.19). Together the material is often referred to as PEDOT:PSS.

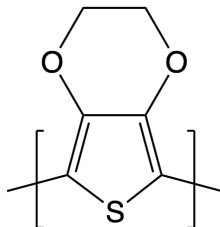


**Figure 1.18:** The chemical structure of neutral poly(3,4-ethylenedioxythiophene).

The PEDOT molecule has a conjugated  $\pi$ -electron system which is the source of the semiconducting behaviour seen in pristine undoped PEDOT. In the context of PEDOT:PSS and other conducting polymers, doping and dopants refer to the oxidation state of the PEDOT molecules and materials that change that oxidation state. This is unlike in solid-state physics where a dopant refers to neutral atoms (impurities) introduced into a pure crystalline lattice to alter the conductivity of the crystalline material [49].

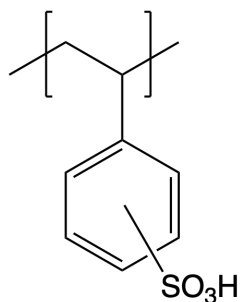


**Figure 1.19:** The chemical structure of neutral poly(styrene sulfonic acid), when stabilising PEDOT there is a loss of protons to form PSS (the sulfonate form of the molecule).

Upon synthesis, PEDOT is typically found in its conducting, doped form. When doped (or oxidised), PEDOT is a p-type conductor, which allows a hole current to flow when a voltage bias is applied [31]. The positive holes are electronically balanced by the negative charges of sulfonate anions on the PSS which provides stability to the PEDOT in water [31, 50]. This can be seen in figure 1.20. PEDOT:PSS is both ionically and electronically conductive which makes it suitable for a range of applications including bioelectronic applications [31, 50, 51]. PSS was originally added to PEDOT to improve its water processability which resulted in the production of commercial grade PEDOT:PSS aqueous dispersions [49, 51]. The PSS is usually present in excess in the dispersions, typically in a ratio of 1:2.5 up to 1:6 PEDOT:PSS [49].

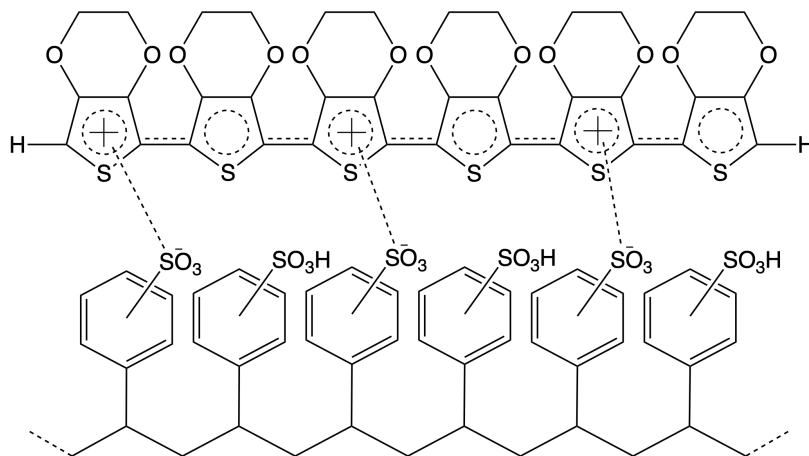


**Figure 1.20:** Doped, conducting PEDOT stabilised by PSS. The positive holes are stabilised by the sulfonate anions shown here by the dotted lines between the positive hole charges on the PEDOT and the negatively charged sulfonate groups on the PSS.

A key advantage of PEDOT is that it forms transparent thin films in its oxidised state [31]. This has led to it being used widely as an anti-static coating and to form transparent electrodes in organic light emitting diodes (OLEDs) and in organic solar cells [31, 52].

There are two main methods to synthesise PEDOT:PSS; oxidative polymerisation and electropolymerisation. Both these methods result in PEDOT in its oxidised conductive state with the PSS present forming a complex. It is important to polymerise the 3,4-ethylenedioxythiophene (EDOT) monomer in the presence of the complexing polymer counter-ion as PEDOT is insoluble in most solvents including water [52]. Oxidative polymerisation is a chemical polymerisation reaction in solution, and is the more

common method used to synthesise PEDOT:PSS as it is a one-pot reaction that is easily scalable. The oxidation of the PEDOT occurs via chemical means in the solution during the reaction, and the result is an aqueous dispersion of PEDOT:PSS. Aqueous dispersions of PEDOT:PSS can be used to form thin films through a variety of methods including spray-coating, spin-coating and drop-casting, among others [30, 52]. On the other hand, the electropolymerisation method causes the polymerisation reaction to occur directly on an electrode surface, and does not require any chemical oxidants as the PEDOT is oxidised by the electrode submerged in the reaction solution [30, 52].

An overview of a number of different bioelectronic devices based on PEDOT:PSS is presented in chapter 3, including an alcohol sensor [53] and OECTs for the detection of the heartbeat [54, 55].

## 1.3 Biomaterials

Organic bioelectronic devices for use *in vivo* (and any material or device that is to be implanted into the body) can be described as a biomaterial. Biomaterials are defined by the International Union of Pure and Applied Chemistry (IUPAC) as a “material exploited in contact with living tissues, organisms, or microorganisms” [56]. Biomaterials have been used in human society for centuries for different purposes, from glass eyes, prosthetic limbs, and false teeth, to more modern innovations such as breast implants, contact lenses, and cardiac pacemakers. An important consideration when using biomaterials is how they will interact with human tissues. There are three main requirements for biomaterials implanted into the body; the biomaterials must be biocompatible, biodegradable, and have appropriate mechanical properties [57]. Biomaterials can be fabricated by a range of synthesis routes, and their properties can be tuned by design. This section will speak broadly of the requirements of a biomaterial in the human body and how these requirements relate to the requirements of the organic bioelectronic device presented in this thesis.

### 1.3.1 Biocompatibility

Biocompatibility is a key consideration when developing a biomaterial as it is imperative that there is minimal immune response from the host body which could interfere with the intended action of the biomaterial [57]. IUPAC defines biocompatibility as the “ability to be in contact with a living system without producing an adverse effect” [56].

The human immune system works to detect and remove foreign material from the body to help protect itself from the effects of poisons, harmful bacteria, and viruses. When a biomaterial is implanted into the body, the immune system will detect the foreign object and trigger an inflammatory response that could result in rejection of the implanted biomaterial [57]. The level of response can be minimised by careful choice of compatible material. For a bioelectronic device placed in the CNS, this is incredibly important as a non-compatible material could result in a severe inflammatory response resulting in neuronal cell death and the formation of glial scar tissue [8] (see section 1.1.5 for more on glial scarring). Significant neuronal cell death could severely impact the normal functioning of the CNS, which in turn can result in severe disability and death [8, 58]. In addition, the bioactivity or ability of cells to grow and proliferate on a biomaterial must be considered, especially in tissue engineering and scaffold applications [57]. For bioelectronic applications, it is important to consider bioactivity as the bioelectronic device will likely be

interfacing with cells and tissues so that the device can sense or stimulate cells as required.

### 1.3.2 Biodegradability

Not all biomaterials implanted in to the body are intended to be permanent. For example, many tissue scaffolds are designed to support cell regrowth until they are no longer required and the native cell scaffold (the extracellular matrix or ECM) can grow and replace it [57, 59]. Additionally, it is likely that even with a permanent implant, there will be some wear and tear with small amounts of the biomaterial being released from the intended site of action. A biodegradable biomaterial must have the “capability of being degraded by biological activity” [56]. This could be degradation by the action of enzymes or some other cell-mediated process or hydrolysis. The products of biodegradation must themselves be biocompatible and non-toxic to the human body. Furthermore, the degradation products must be easily metabolised and excreted from the body without causing damage or interfering with other tissues, organs, and bodily processes [57]. It should be noted that if the biomaterial degrades solely due to hydrolysis without any contribution by living elements, it is not strictly considered to be biodegradation, but simply hydrolysis or hydrolytic degradation [56]. Additionally, the lifetime of a biomaterial or implanted device must be considered as the biodegradation of the implanted material must happen over a specific time-frame [59]. Depending on the function of the implant, the degradation may take place over hours, days, weeks, months, or years. The implanted biomaterial must be able to maintain functionality at a tolerable level over the period of degradation until such a time where it is deemed acceptable to no longer work as effectively. This is known as bio-stability. Biodegradable bioelectronic devices are not common in the literature, as the majority of organic electronic materials are not degradable [60].

### 1.3.3 Mechanical Properties

Finally, the implanted biomaterial must have mechanical properties that match the mechanical properties of the tissues with which the material will interact [57]. This means that if the biomaterial is being implanted into a harder tissue, the biomaterial must also be hard. Equally, if the biomaterial is implanted into a soft environment, it also has to be soft. Mismatching the mechanical properties of implanted material with the site of implantation can lead to an immune response and scarring around the site of implantation which would cut off the implant or device from the tissues with which it is supposed to interact. In the case of a bioelectronic device in the CNS, there would probably be glial scar formation, cutting off the device from its target tissues or cells, rendering the device useless [8, 58].

This requirement to match mechanical properties was demonstrated very well in the work of Minev *et al.* [27] (previously discussed in section 1.1.6). When designing the e-dura device, the scientists were sure to pick a material that could resemble the mechanical properties of the spinal cord as closely as possible. Careful choice of polydimethylsiloxane (PDMS) as the soft base for the e-dura meant that the mechanical properties of the e-dura device more closely matched the mechanical properties of neural tissues compared to typical stiff plastic neuroprotheses. In experiments described in the paper, a stiffer plastic implant (polyimide film) and a softer implant (PDMS-based) were implanted into rat spinal cords and the motor skills of the rats was observed over 6 weeks. The rats with the stiffer implants showed deterioration in movement around 1-2 weeks post-implantation which continued until the end of the experiment. By contrast, the rats with the soft implant showed no deterioration in motor skills and were indistinguishable

from the control group with no implants. Additionally, cellular markers typical of a foreign body immune response were detected in the site around the stiff implant, but no significant difference in levels of these markers was seen around the soft implant site compared to the control. This showed that there was a large immune response with the stiff implant, but no significant response seen with the soft implant. This acts as a demonstration showing that mismatching the mechanical properties of an implanted material with the tissue it interacts with can trigger a measurable immune response and has visible effects on the efficacy of the implant.

## Introduction to elastic modulus

One of the most common ways of quantifying the mechanical properties of a material is measuring the elastic modulus,  $E$ . The elastic modulus of a material quantifies how much that material deforms elastically under stress. It is defined as the ratio of normal stress ( $\sigma$ ) over linear strain ( $\epsilon$ ) [61], as shown in equation 1.1. This elastic modulus, which is also sometimes referred to as the Young's modulus, describes linear elastic deformation and is applicable for tensile and compressive stress. Stress is usually defined as an applied force ( $F$ ) over an area ( $A$ ) (see equation 1.2). On the other hand, strain describes the deformation of the material as a result of the applied stress quantifying it as the change in length of the material sample in one dimension ( $\Delta L = L - L_0$ ) divided by the original length ( $L_0$ ) of the material sample in that dimension. This is shown in equation 1.3. Elastic deformation is non-permanent and the material will return to its original shape once the stress has been removed. On the other hand, plastic deformation is a permanent deformation. Elastic modulus is measured in units of pascals (Pa).

$$E = \frac{\sigma}{\epsilon} \quad (1.1)$$

$$\sigma = \frac{F}{A} \quad (1.2)$$

$$\epsilon = \frac{\Delta L}{L_0} = \frac{L - L_0}{L_0} \quad (1.3)$$

The elastic moduli of a number of common materials are shown in table 1.2. These demonstrate the variation in elastic moduli from very hard materials such as diamond down to human skin.

**Table 1.2:** The elastic moduli of various common materials and tissues in the human body.

Material	Elastic modulus
Diamond (films)	800 - 950 GPa [62]
Aluminium	106.85 GPa [63]
Bone	13.5 - 30.1 GPa [64-66]
Expanded polystyrene foam	6.3 - 32.3 MPa [67]
Skin	129±88 kPa [68], 4.2 - 8.5 MPa [69]

Methods of measuring the elastic modulus of a material and the theory behind these measurements are discussed more extensively in chapter 2.

## Elastic modulus of the central nervous system

There are a variety of different tissue types within the CNS meaning that caution must be taken when reporting the elastic modulus of the various structures within the CNS. For example, when the elastic modulus of the spinal cord is reported, it must be specific as to exactly what tissues were sampled otherwise there is the question of whether the protective meninges were intact or removed. Other considerations include whether a human sample was used or a sample from another animal species, whether the measurements were *in vivo* (the tissue was still *in situ*) or *in vitro* (the tissue was removed from the body and tested), and whether the measurement was undertaken on a live animal or taken post-mortem. These variations in technique and sample types result in variations in the reported elastic moduli of CNS tissues and structures, however there is general consensus that the CNS is very soft and thus has a low elastic modulus compared to other tissues and structures in the body such as bone [64–66]. A summary of the elastic moduli measured for the brain and spinal cord is given in table 1.3.

**Table 1.3:** A summary of the elastic moduli of the structures in the CNS.

Tissue type	Elastic modulus	Comments
Human brain	3 - 10 kPa	No specification on grey vs. white matter [70]
Pig brain	$5.7 \pm 1.6$ - $23.8 \pm 10.5$ kPa	Mixture of grey and white matter [71]
Human spinal cord	1.02 - 1.37 MPa	Cadaver samples, <i>in vitro</i> characterisation [72]
Human spinal cord	1.40 MPa	Intact pia mater, cadaver samples, <i>in vitro</i> characterisation [73]
Human spinal cord	89 kPa	Incised pia mater, cadaver samples, <i>in vitro</i> characterisation [73]
Rabbit spinal cord	$16 \pm 5$ kPa	With pia mater, cadaver samples, <i>in vitro</i> characterisation [74]
Rabbit spinal cord	$5 \pm 2$ kPa	Without pia mater, cadaver samples, <i>in vitro</i> characterisation [74]
Bovine spinal cord	$1.19 \pm 0.13$ MPa	Measured 3 hours after slaughter, was seen to increase with increase time post-mortem [75]
Cat spinal cord	230 kPa	<i>In vivo</i> measurements on anaesthetised live animal [76]
Puppy spinal cord	265 kPa	<i>In vivo</i> measurements on anaesthetised live animal [77]

Any organic bioelectronic device that is intended for use in the spinal cord must have a similarly low elastic modulus to ensure minimal immune response to allow it to operate effectively. Consideration of the whole device is therefore required. Typically, organic electronic devices make use of hard substrates such as glass during development. The elastic modulus of glass varies with manufacturing and materials used but typically it is around 70 GPa [78], which is around 10,000 times greater than the values reported for the spinal cord. There is, therefore, a requirement to lower the elastic modulus of the organic bioelectronic device if it were to be used in the CNS.

## 1.4 Hydrogels as biomaterials

One approach to lowering the elastic modulus of an organic bioelectronic device would be to use a soft substrate. Hydrogels offer a route for this approach. Hydrogels are three-dimensional crosslinked polymer networks that significantly swell in water [79–81]. The generic structure of a hydrogel can be seen in figure 1.21 which shows the polymer strands crosslinked to form a porous structure. Hydrogels may be crosslinked physically using polymer entanglements and/or other physical attractions such as ionic attractions and hydrogen bonding [80]. Alternatively, chemical crosslinks using covalent bonding may be used to form chemical hydrogels [80, 81].

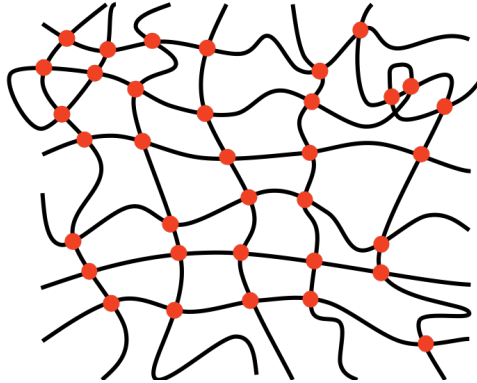


**Figure 1.21:** The generic structure of a hydrogel showing the polymer strands in black with the crosslinks indicated by the red circles.

Hydrogels have a large number of applications as biomaterials due to their ability to retain significant volumes of water [79, 81]. The structure of a hydrogel is typically a highly crosslinked matrix with pores through which water and other species can move. Such an interconnected and porous network has similarities to the extracellular matrix (ECM) which itself is an extensive interconnected network of pores in which cells sit, although hydrogel pores and those of the ECM are of different length scales, typically on the order of many micrometers and tens of nanometers respectively [80, 82–84]. Additionally, the vast array of materials that can be used to form a hydrogel and the variation of crosslinking methods can offer a large level of control. This allows the synthesis and manufacture of a hydrogel that has ideal properties suited to its intended end use and that fulfils the three main requirements of a biomaterial (biocompatible, biodegradable, and mechanically appropriate). For example, by changing the degree of crosslinking through the gel, the mechanical properties may be tuned to give a higher or lower elastic modulus as required. This flexibility in material and properties make hydrogels ideal candidates for use within the CNS.

Hydrogels have been used as biomaterials for more than half a century [85]. In 1959, the first soft contact lenses were administered to clinical patients in Prague [86]. It was shown that the soft contact lenses could correct eyesight, and caused minimal discomfort to patients. These soft contact lenses were one of the first examples of using hydrogels as biomaterials with clinical success [87]. Nowadays, hydrogels are common biomaterials. There is a large amount of interest in hydrogels prepared from naturally occurring materials, such as hyaluronic acid (HA) and chondroitin sulfate (CS), due to their biocompatibility and biodegradability properties [81, 85, 88]. These are especially popular for use in the CNS for their compatibility which can act to minimise immune responses that otherwise could lead to glial scar formation and related detrimental effects [70, 89–94]. Hydrogels for use in the CNS are

discussed in chapter 5.

### 1.4.1 Hyaluronic acid and chondroitin sulfate

Hyaluronic acid (HA) and chondroitin sulfate (CS) are linear polysaccharides that occur naturally in the body (figure 1.22). They are specifically categorised as glycosaminoglycans and are thought to perform a range of biological roles. CS is formed from the alternating monosaccharides *N*-acetylgalactosamine and glucuronic acid, and HA is formed from glucuronic acid and *N*-acetylglucosamine.

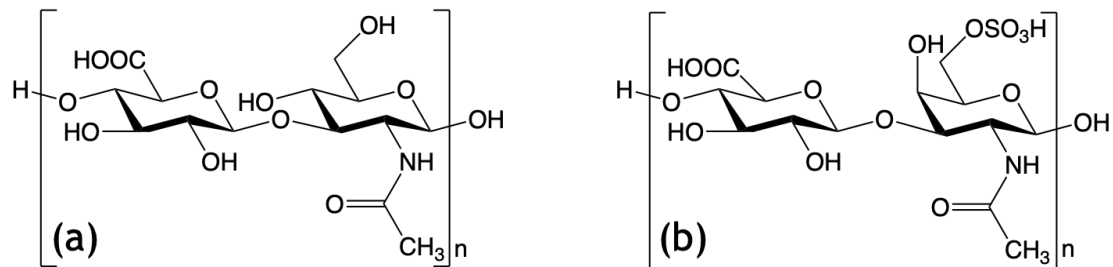


**Figure 1.22:** Chemical structures of hyaluronic acid (a) and chondroitin sulfate (b).

CS is found in abundance in cartilaginous ECM in joints [95], and is also found in the CNS. The role of CS within the CNS is as a biological marker that acts to guide the growth of neurons during mammalian development [96]. On the other hand, it is thought to play a role in glial scar formation as a result of SCIs [97], which could limit applications in the treatment of SCIs as typically glial scar formation is to be avoided. Similarly, HA is found throughout the ECM throughout the CNS. It is a major constituent of the ECM of the brain [8] and it is thought to play a role in a massive range of biological processes [98] including healing, guiding cell differentiation, and signalling functions.

As CS and HA are both found naturally in the human body, they are considered to be inherently biocompatible, meaning that they are of interest to researchers working on biomaterials. Additionally, as these materials are naturally derived, the body has metabolic pathways through which these materials can be broken down. Hyaluronidase and chondroitinase ABC work to break down HA [99, 100] and CS [101] respectively. This means that there is a predetermined biodegradation route in the body and thus the molecules are biodegradable.

Presently, HA is a very popular component of moisturisers and other skin treatments [102]. A product search of hyaluronic acid on Boots.com (a popular UK pharmacy, health and beauty retailer) returned 331 results, 310 of which are under the category of beauty and skin care (on the date of the search 11/08/2020) [103]. The popularity of HA as a moisturising ingredient in skin care is due to its ability to absorb large amounts of water [102], giving a plumped and hydrated appearance to skin. The hygroscopic properties of HA also make it attractive for researchers developing hydrogels, along with its inherent biocompatibility and biodegradability. A number of hydrogels synthesised from HA are discussed in chapter 5 [89, 94] and are found extensively throughout the literature, designed for a range of applications including *in vitro* tissue scaffolds [83, 104], dermal tissue regeneration [105], cartilage regeneration [106], and the treatment of SCIs [70, 89, 92, 94], among others.

CS, on the other hand, can be found in a number of joint-care supplements and osteoarthritis treatments. It has been found that taking CS can decrease the pain and discomfort in the joints of those suffering

from osteoarthritis and there is evidence that it may slow further deterioration in the joints of sufferers [107–109]. Although a lot of CS hydrogel research focuses on cartilage repair [110–113], there has been some work towards the use of CS hydrogels in the CNS. For example, Karumbaiah *et al.* [100] found that sulfated-CS hydrogels could be used to facilitate tissue repair in lesions created by traumatic injury to the CNS. Sulfated-CS hydrogels were prepared by photocrosslinking sulfated-CS that had had been methacrylated. The authors exploited the ability of CS to direct the differentiation of neural stem cells and showed that the hydrogels encouraged self renewal and growth of neural stem cells better than control experiments. This work was preceded by experiments in which sulfated-CS was crosslinked with poly(ethylene glycol) via Michael addition [114]. This experiment was also undertaken with sulfated-HA, and both the CS and the HA gels were determined to have similar mechanical properties. It was shown that both gels supported neural cell growth, but CS outperformed HA. This was determined by the fact that the length of neurites grown in the CS hydrogels were consistently significantly longer than those grown in the HA gels. Similarly, Liu *et al.* [115] demonstrated that implanting methacrylated-CS hydrogels containing neural stem cells into the sites of SCIs in rats encouraged the cells to differentiate into neuronal cell types and minimised the formation of glial cells (which form the scarring leading to loss of functionality in SCI victims), thus encouraging functional recovery.

CS and HA are both naturally found in the human body, and are therefore inherently biocompatible. Additionally, they are both biodegradable *in vivo* due to the presence of specific enzymes that have the role of breaking down the molecules. CS and HA both require crosslinking to form hydrogels. There are a range of crosslinking methodologies previously reported in the literature for CS and HA hydrogels including photocrosslinking methacrylated HA [89, 112], various click chemistries [84, 92, 116], and disulfide crosslinks [117], among others [118], however a popular method for crosslinking glycosaminoglycans is the use of carbodiimide crosslinking using 1-ethyl-3-(3-dimethylaminopropyl)carbodiimide hydrochloride (EDC) [83, 90, 100, 111, 119, 120].

#### 1.4.2 Crosslinking hydrogels - EDC-crosslinking

There are a range of methods to crosslink a material to form a hydrogel including physical entanglements, hydrogen bonding, and covalent crosslinks. Typically the amount of crosslinking in a hydrogel determines its properties. For example, a gel with low levels of crosslinking can typically swell in water more than one with a larger number of crosslinks, as the matrix will contain larger and smaller pores respectively [83, 121]. This is well demonstrated in the paper by Grover *et al.* [121], where the authors describe a collagen tissue scaffold where the degree of swelling (that is to say the mass of the swollen structure relative to the dry mass) reduced when EDC-crosslinking was introduced. Additionally, the pores within the scaffold decreased in size upon crosslinking, whilst the tensile strength of the matrices increased from uncrosslinked to crosslinked. It should be noted that the uncrosslinked scaffolds could not be fully mechanically characterised due to low failure stresses and difficulty in handling the materials. This example from Grover *et al.* [121] highlights how crosslinking has a direct effect on the resulting properties of a hydrogel.

Carbodiimide crosslinkers, such as 1-ethyl-3-(3-dimethylaminopropyl)carbodiimide hydrochloride (EDC) (figure 1.23), are typically used to mediate the formation of amide bonds between carboxylic acids and primary amines under aqueous conditions [121, 122]. It is often used with biological molecules such as proteins and carbohydrates. The EDC molecule is toxic but it is water soluble [83]. This means that

EDC, and the by-product of EDC-crosslinking which is also water soluble, can easily be removed from a hydrogel or other reaction mixture by washing.

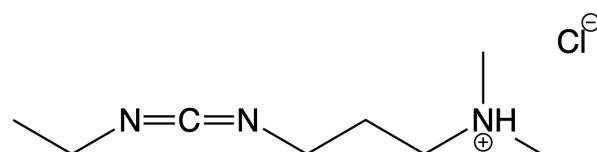


**Figure 1.23:** The chemical structure of 1-ethyl-3-(3-dimethylaminopropyl)carbodiimide hydrochloride (EDC).

It has been shown that the EDC can facilitate crosslinking between carboxylic acid and hydroxyl groups [120] to form ester bonds, and thus EDC-crosslinking could be used to form ester bonds between CS and/or HA molecules to form crosslinked hydrogel networks. EDC is known as a ‘zero-length’ crosslinker as none of the EDC molecule ends up in the final crosslinking bond [122].

Typically, in the case of amide formation, the EDC-coupling reaction is usually reported to proceed as follows [123] described by figure 1.24. The EDC molecule reacts with a carboxylic acid to form an unstable *O*-acylisourea intermediate. If this then reacts with water, hydrolysis occurs, returning the original carboxylic acid and an isourea by-product from the EDC. If the intermediate instead undergoes nucleophilic attack by a primary amine, an amide bond is formed linking the original carboxylic acid and the amine. Again, an isourea by-product is formed from the spent EDC.

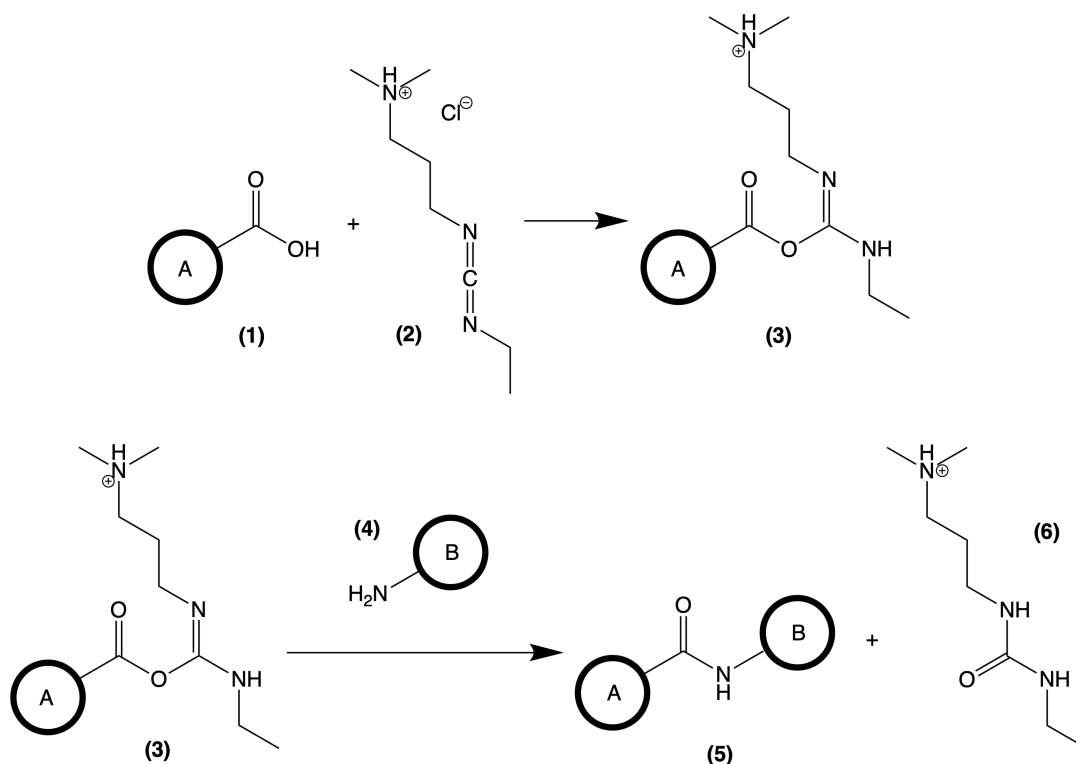


**Figure 1.24:** EDC-crosslinking reaction scheme between molecule A and molecule B to give an amide bond: (1) Molecule A contains a carboxyl group that reacts with EDC (2) to form an unstable *O*-acylisourea intermediate (3). This intermediate can then undergo nucleophilic attack by the primary amine on molecule B (4) to form an amide bond between molecule A and B (5) and an iso-urea by-product (6).

Tomihata *et al.* [120] described EDC-coupling between carboxyl and hydroxyl groups, and used infra-red (IR) spectroscopy that showed that the EDC molecule mediates the formation of acid anhydrides. It is not clear whether the acid anhydride formation is inter- or intra-molecular, however it is likely that the *O*-acylisourea intermediate, described in figure 1.24, is formed allowing acid anhydride formation to occur [124]. The reaction then proceeds by the acid anhydrides reacting with alcohol groups on other molecules to form ester bonds, as shown in figure 1.25.

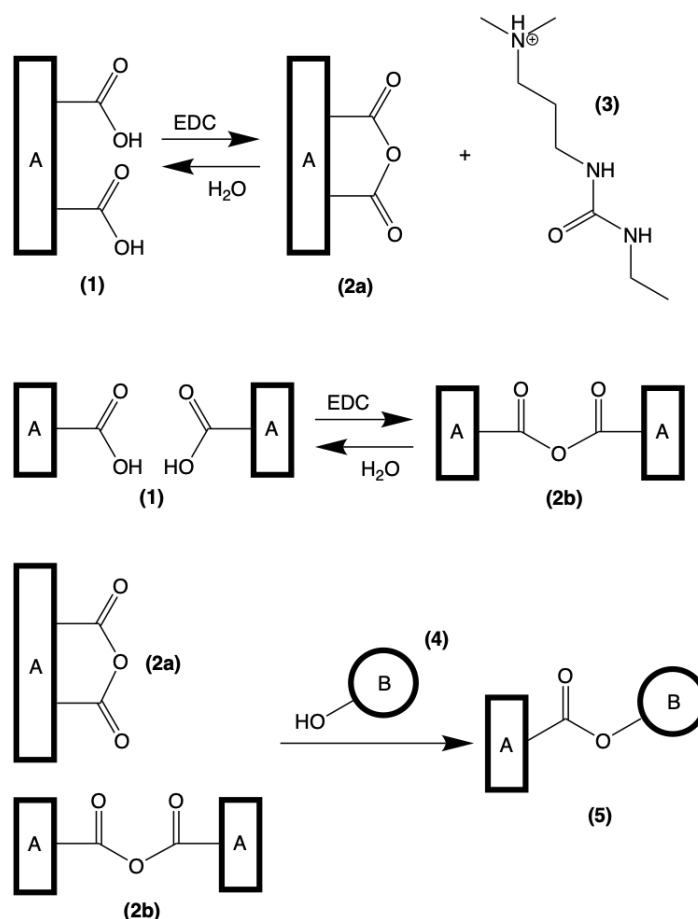


**Figure 1.25:** EDC-crosslinking reaction scheme between molecule A and molecule B to give an ester bond: (1) Initial acid anhydride formation is mediated by EDC – intra (2a) - or intermolecular (2b) (unclear which). A water soluble isourea by-product (3) is also formed. Nucleophilic attack of acid anhydride by hydroxyl group of molecule B (4) follows, giving the final formation of an ester linkage (5).

*N*-hydroxysuccinimide (NHS) is sometimes used in conjunction with EDC to facilitate the EDC-coupling reaction. It is thought to increase the reaction efficiency by reacting with the carboxylic acid group to form a more stable NHS-ester intermediate than the *O*-acylisourea intermediate that forms in reactions with no NHS present [123]. The addition of NHS to a EDC reaction mixture is optional, and it is not always utilised.

For biomaterial applications, EDC-crosslinking has been used for many years. In 1995, Olde Damink *et al.* [125] reported the successful synthesis of crosslinked collagen matrices using EDC-crosslinking. Collagen was freeze dried to give a porous structure that was then submerged in an EDC or EDC and NHS solution. The pH of the reaction was controlled by the addition of 0.1 M  $HCl_{(aq)}$  or 0.1 M  $NaOH_{(aq)}$  throughout. The resulting crosslinked matrices were rinsed thoroughly and lyophilised a second time. The crosslinks

formed by this method in collagen were amide bonds, as in this case, the EDC-mediated reaction was between carboxylic acid groups and amines. It was observed that the modulus of the crosslinked collagen increased with level of crosslinking for high strains, but decreased with level of crosslinking for low strains. It was suggested that this was due to the structure of collagen itself, and the spatial limitations of the fibres for crosslinking.

Both HA and CS have previously been reported to undergo EDC-crosslinking to form hydrogels. Hanthamrongwit *et al.* [119] investigated a collagen based gel containing CS as a potential artificial skin substitute. EDC-crosslinking was used to attach CS, sometimes in the presence of diamines, to collagen gels that were themselves prepared from pH-altered collagen solutions. These reactions formed amide crosslinks. The addition of the diamines (diaminobutane or diaminohexane) was to increase the number of available reactive groups during crosslinking as the diamines could react with the collagen or the CS once the appropriate carboxylic acid group had been activated by EDC. This meant that amide bonds could form directly between collagen and CS, collagen and collagen, collagen and diamine, and CS and diamine. The different linkages are summarised in figure 1.26. This diversity of crosslinking meant that there was more variation in crosslink length and type throughout the gels, which could give diversity of properties.

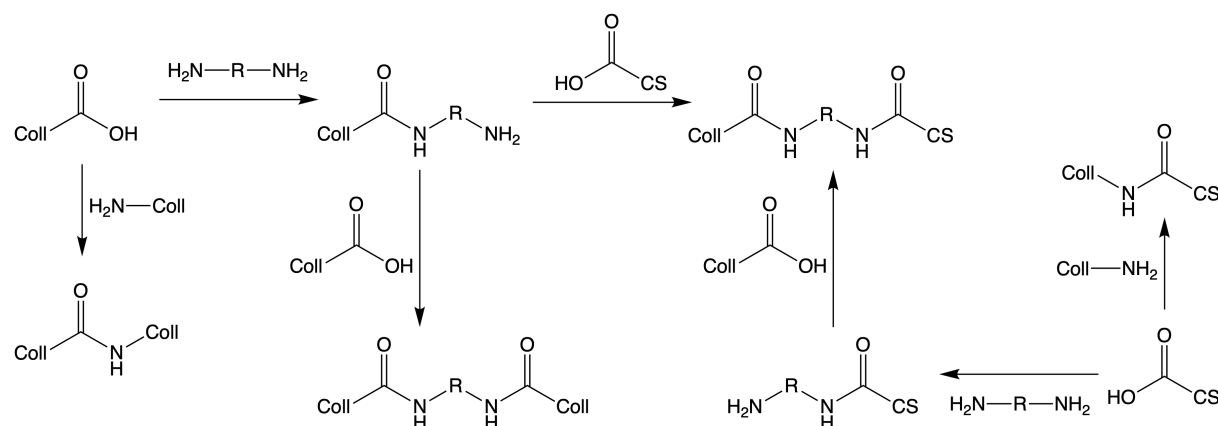


**Figure 1.26:** The range of possible EDC-mediated crosslinking bonds that could form between collagen (Coll), chondroitin sulfate (CS), and a generic diamine ( $\text{H}_2\text{N-R-NH}_2$ ) as summarised by Hanthamrongwit *et al.* [119].

Tomihata *et al.* [120] used EDC to crosslink HA films via intermolecular ester bonding between carboxylic acid and hydroxyl groups. Pectin films were also crosslinked in this way, demonstrating the ability of EDC to mediate crosslinking via ester bonds. The films were characterised via IR spectroscopy to confirm this. Furthermore, similar to the use of diaminobutane in the work of Hanthamrongwit *et al.* [119], lysine, an amino acid that contains a second amino group, and its methyl ester were also used during crosslinking to give amide crosslinks. The degradation of the various HA films was recorded and demonstrated that the addition of the lysine methyl-ester prolonged the lifetime of the HA gels in pH 7 buffered solution at 25 °C to over two weeks, versus the HA films prepared without lysine which completely degraded under the same conditions in roughly 7 days. This was attributed to the need for the presence of enzymes to quickly degrade amide bonds, whereas ester bonds can undergo fairly fast hydrolysis.

More recently, Li *et al.* [126] synthesised interpenetrating collagen-HA-CS networks for use in brain tissue engineering and related therapies for traumatic brain injury. These were prepared by freeze-drying collagen to form scaffolds, which were then submerged in CS or HA or combined CS and HA solutions

for four hours. The solutions also contained EDC, NHS, adipic acid dehydrate, and 2-morpholinoethane sulfonic acid hydrate. Prior to being added to the collagen scaffold, these solutions were stirred for 4 hours and refrigerated at 4 °C for a minimum of 12 hours. The reaction was quenched, and the reaction mixture rinsed. The mixed networks were freeze dried again. The elastic moduli of the collagen, collagen-CS, collagen-HA, and collagen-CS-HA interpenetrating networks were 14.6 kPa, 16.3 kPa, 16.8 kPa, and 27.9 kPa respectively. These materials were assessed for the viability, differentiation, and proliferation of various clinically relevant neural cells, and it was determined that the collagen-HA and collagen-CS-HA networks were the most promising candidates to be used in brain tissue engineering applications in the future.

These examples demonstrate EDC-coupling is a facile and steadfast method of crosslinking materials to form hydrogels, including hydrogels containing CS and HA. The ability of EDC to mediate the formation of ester bonds, which are hydrolytically degradable, make it an ideal method of crosslinking CS and HA to create a hydrogel that is biodegradable, and biocompatible. Furthermore, EDC-coupling can be applied to other systems requiring crosslinking, such as the PEDOT:chondroitin sulfate/hyaluronic acid (PEDOT:CS/PEDOT:HA) films presented in chapters 3 and 4.

## 1.5 Summary and thesis overview

This chapter has introduced the human nervous system and SCIs demonstrating that such injuries to the CNS can be devastating, life-changing events. Treatments for SCIs are limited however organic bioelectronics is an area of interest to researchers demonstrated by the e-dura device [27] example given in section 1.1.6. The field of organic bioelectronics covers a wide range of devices and applications. OECTs were highlighted as a device architecture favoured by researchers for *in vivo* applications due to their low operating voltages and ability to transduce small ionic signals into electronic signals [31]. This means that they can act as an interface between biology and man-made technology. Furthermore, the requirements of a biomaterial used in the body were introduced and emphasised the need for an implanted material to be biocompatible, biodegradable, and mechanically appropriate. Hydrogels were also introduced as these materials offer a route to fulfilling the criteria for biomaterials.

The aim of this project is to develop a degradable OECT device that, in future, could be used in the spinal cord, therefore consideration of the requirements for such a device is needed. If intended for use in the human body, such devices must fulfil the requirements of a biomaterial; biocompatibility, biodegradability, and appropriate mechanical properties.

In the OECT device, there must be an organic electronic material (OEM) that is biocompatible, biodegradable, mechanically appropriate to the elastic modulus of the spinal cord, and importantly for a bioelectronic device, conductive. The OEM must also be able to form a thin film that does not dissolve or immediately breakdown in electrolyte or water. This is so the material can be characterised, and fit the architecture of a typical OECT. There is, however, the requirement that this material does break down in a controlled way over time so that it can be considered degradable. Additionally, this material must be able to function as the OEM in an OECT, i.e. that a current through this material can be modulated by changing the doping status of the material. This would provide the proof of concept that such a material could be used in an OECT type device. Additionally, there is a requirement to design a material that could be used as a substrate for the OECT devices to make them suitable for implantation

in to the CNS. This is because many substrates used during testing and development of OECTs, such as glass slides, would be unsuitable for use in the CNS due mechanical mismatch. The biocompatibility and biodegradability of the substrate material would also have to be carefully considered. Hydrogels are of great interest to researchers in the field of biomaterials due to their hydrated, porous structures which make them ideal materials for providing surfaces on which cells can grow [80, 81]. The control given to the properties of a hydrogel through material and crosslinking type allows them to be designed to give the most desirable properties, including the three key properties of a biomaterial; biodegradability, biocompatibility, and appropriate mechanical properties, making hydrogels ideally suited for use as a soft substrate for the OECT.

**Chapter 2** describes a number of experimental techniques and theories used in the work in this thesis including electrochemical impedance spectroscopy (EIS), ultra-violet and infra-red spectroscopy, and mechanical testing.

In **chapter 3**, the focus of the work is development of a biocompatible and conductive material based on poly(3,4-ethylenedioxythiophene) (PEDOT) complexed with chondroitin sulfate/hyaluronic acid (PEDOT:CS/PEDOT:HA) and proving that these materials can function in an OECT. Additionally, a crosslinking method that favours degradation will be presented, however the degradation of the device is not discussed until chapter 4. It is shown that PEDOT complexed with chondroitin sulfate (PEDOT:CS) or hyaluronic acid (PEDOT:HA) can be synthesised via an oxidative polymerisation method as demonstrated by Mantione *et al.* [127]. These materials can be drop-cast and were shown to be conductive, with a best sheet resistance of  $4.7 \text{ k}\Omega\text{cm}^{-1}$  for PEDOT:CS which was comparable to similar untreated PEDOT:PSS films. Crosslinking of the PEDOT:CS and PEDOT:HA films using 1-ethyl-3-(3-dimethylaminopropyl)carbodiimide hydrochloride (EDC) was demonstrated and the materials were tested for their transistor characteristics. An OECT using PEDOT:CS as the organic electronic material was successfully tested and characterised with a peak transconductance of  $50.5 \mu\text{S}$ . This provided the proof of concept that such materials could be used in OECT devices.

The next step in the development of the biocompatible and biodegradable OECT was to optimise and understand the behaviour of PEDOT:CS in more detail. Work towards optimising the transistor behaviour of the OECT is presented in **chapter 4** through changes in electrode geometry. Furthermore, an examination of the degradation of the device was undertaken, and ultraviolet (UV) spectroscopy and electrical impedance spectroscopy (EIS) were used to understand PEDOT:biomolecules in more detail. In addition, experiments towards creating synapstors (bioelectronic devices that mimic the short term plasticity of synapses [13, 44, 128–133]) from PEDOT:CS were undertaken, as well as lyophilisation experiments to create 3D scaffolds from PEDOT:CS and PEDOT:HA as a step towards creating tubistors (3D scaffolds made from conducting polymers that demonstrate transistor-type behaviour [134]).

**Chapter 5** describes the preparation of CS and HA hydrogels, and the swelling properties are presented. The mechanical properties of the HA hydrogels were found to be tunable by the amount of EDC used in during their preparation, and the gels were found to have elastic moduli that were comparable to those of the spinal cord. The degradation profile of the HA hydrogels was also determined, and demonstrated that they were hydrolytically degradable under simulated physiological conditions. Finally, initial experiments combining HA hydrogels with PEDOT:CS are also reported.

The final chapter of this thesis, **chapter 6**, provides a summary of the work presented in this thesis and points towards future experiments.

## Chapter 2

# Experimental Techniques

### 2.1 Introduction

This thesis covers a broad research area thus a broad range of experimental techniques and theories have been used to collect and interpret data, respectively. The methods used for each individual experiment are detailed in the relevant results chapter, but a wider overview of the analysis techniques and the theory behind them is presented here. The experimental methods used in this thesis can be broadly categorised into electronic, spectroscopic, and mechanical testing techniques.

Electronic testing was used to characterise crosslinked and uncrosslinked films of PEDOT:biomaterial dispersions for their conductivity and, in the case of crosslinked PEDOT:chondroitin sulfate (PEDOT:CS) films, assess their performance in an organic electrochemical transistor (OECT) architecture. The electronic testing techniques are reported and discussed in detail in chapters 3 and 4 and will not be discussed here.

Spectroscopic techniques such as infra-red (IR) spectroscopy and ultra-violet (UV) spectroscopy were used to assess the level of crosslinking in hyaluronic acid (HA) hydrogels and to assess the electronic properties of PEDOT:CS aqueous dispersions and films upon crosslinking and degradation, respectively. Electrochemical impedance spectroscopy (EIS) can be used to assess complex impedance of a material versus frequency. In the case of the work presented in this thesis, EIS was used to follow the ionic and ohmic contributions to the conductivity of the PEDOT:biomolecule materials.

Mechanical testing was undertaken on HA hydrogels to determine their elastic moduli for comparison with the elastic moduli of the spinal cord.

### 2.2 Infra-red (IR) spectroscopy

In the broadest definition, spectroscopic techniques are used to probe the relationship between a material and electromagnetic radiation [135]. This makes spectroscopic techniques incredibly powerful tools in the characterisation of all matter. IR spectroscopy is used to examine the interaction of infra-red radiation

with solid, liquid, or gaseous samples. This spectroscopic technique is typically used to identify functional groups present on molecules in a sample, making it a popular analysis technique in synthetic chemistry. Furthermore, IR spectroscopy has applications outside of scientific research laboratories in food safety, forensic science, and the restoration of artworks.

During IR spectroscopy, the sample is exposed to a broad spectrum of IR radiation (approximately 4000 to 400  $\text{cm}^{-1}$  in the mid-IR region for typical laboratory spectrometers). The sample then absorbs that radiation at specific frequencies that relate to the vibrational frequencies of a part of the sample molecule [135, 136]. An IR spectrum is obtained that shows peaks at these frequencies. The height of the peaks equate to the relative absorbance of the sample (or transmittance through the sample depending on the axes) at each of the frequencies to which the sample was exposed [136, 137].

### 2.2.1 Harmonic and anharmonic oscillators

As IR spectroscopy is concerned with vibrations in sample molecules, it is useful to understand vibrational energy in molecules. In general terms, the total energy of a molecule is made up of electronic, vibrational, and rotational contributions, however in the case of IR spectrometry only vibrational contributions are of interest. (Rotational transitions can be probed in the far IR regions of the spectrum, however for ease, only vibrational contributions are discussed here.) In the quantum mechanical harmonic oscillator model of molecular vibration, vibrational energy is quantized into vibrational energy levels. Each energy level can be described by a quantum number  $v$ , where  $v$  is an integer, and the vibrational energy levels are equidistant from one and other [136, 137]. The ground state of the vibrational energy levels is at  $v=0$  and the energy level may only change by  $\Delta v = \pm 1$ . This model is simple and not that realistic as it does not account for the fact that dissociation will occur at a certain potential energy [137]. The anharmonic oscillator model is more realistic in describing the vibrational energy levels of a molecule. The energy requirement to jump from one level to the next becomes smaller as the vibrational quantum number increases (see figure 2.1). Additionally, at a certain potential energy the two nuclei described in the model will dissociate which can be seen in figure 2.1 by the increasing internuclear distance beyond that of the harmonic oscillator model.

Changes in energy levels are triggered by the absorption of a photon which has an energy that perfectly matches the energy gap between the two levels [137]. This energy change is described by equation 2.1, where  $\Delta E$  is the change in energy,  $h$  is the Planck constant, and  $\nu$  is the frequency. This concept is true for any energy level transition, be it electronic, vibrational, or rotational, and is the basis on which all spectroscopic methods rely.

$$\Delta E = h\nu \tag{2.1}$$

### 2.2.2 IR absorption

For an absorption to be IR active, the dipole moment of the molecule must change during the vibration [135–138]. This is known as the selection rule for IR spectroscopy. The dipole moment of a molecule is a result of the differences in partial charges on the constituent atoms however, as an approximation, the electronegativity of a molecule's constituent atoms can be used to estimate the dipole [136, 137]. For

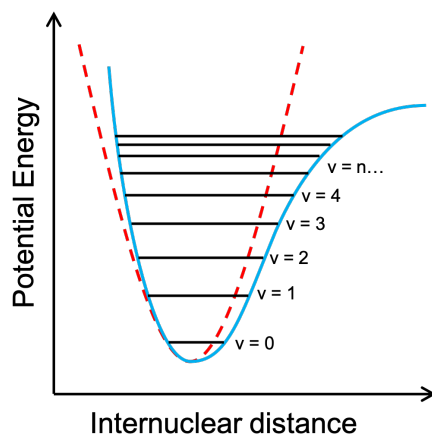


**Figure 2.1:** The quantum mechanical harmonic (red, dashed line) and anharmonic (blue, solid line) oscillator models for vibrational energy levels. The energy levels indicated on the potential energy curve are for the anharmonic oscillator model and can be seen to become closer together as quantum number,  $v$ , increases [137].

example, there is a large difference in the electronegativity of carbon and oxygen of a carbonyl group giving the bond a large dipole [136]. When the bond vibrates (stretching mode), there is an increase in dipole moment meaning that this molecular vibration is IR active. The larger the change in dipole moment, the greater the absorption seen in the IR spectrum [136, 137].

Molecules have a number of normal or fundamental vibrational modes, and the number of these vibrations is known as the number of degrees of freedom possessed by the molecule. Linear polyatomic molecules with  $N$  atoms have  $3N - 5$  vibrational degrees of freedom, whereas non-linear polyatomic molecules with  $N$  atoms have  $3N - 6$  vibrational degrees of freedom [136, 137]. Some of these vibrational modes will have the same frequency as the movements are equivalent, and thus are described as degenerate. The vibrations themselves may be a stretch (changing bond lengths) or a bend (changing bond angles), and can be symmetric or asymmetric.

The energy of the IR radiation frequency that is absorbed by a sample molecule must match the energy gap between the ground and excited vibrational energy level, and must have the same frequency of one of these normal modes of vibration and results in a change in dipole moment [136, 137].

### 2.2.3 Characterising samples using IR spectroscopy

When measuring an IR spectrum, the frequency of the absorbed IR radiation will not be seen by the detector and thus appear as a peak in the spectrum acquired. These peaks at different frequencies can then be used to identify the sample. There are characteristic vibrational frequencies for specific bond types and functional groups, which can be used to identify these bonds and groups within a sample [135–138]. Some of these characteristic frequencies are shown in figure 2.2. For example, the carbonyl stretching band can be found between  $1800\text{ cm}^{-1}$  and  $1650\text{ cm}^{-1}$ , however the exact frequency of the stretch is determined by the surrounding groups and atoms meaning that different types of carbonyl groups have slightly different frequencies [136, 137, 139]. Typically the carbonyl stretching band for carboxylic acids can be found as a strong peak centred between  $1720\text{ cm}^{-1}$  and  $1650\text{ cm}^{-1}$ , whereas

the carbonyl stretch for an aldehyde or ketone is typically found centred around  $1710\text{-}1685\text{ cm}^{-1}$  and  $1685\text{-}1666\text{ cm}^{-1}$  respectively [139]. The fingerprint region of a typical IR spectrum is labelled on figure 2.2 and occurs between  $1500\text{ cm}^{-1}$  and  $500\text{ cm}^{-1}$  [136]. This region of the IR spectrum is typically highly complex, and can be difficult to extract useful information from, especially in the case of an unknown sample. The complex absorption bands can be used to identify a compound if a reference spectrum is available and the two spectra can be compared. The fingerprint region is named as such as this area in the IR spectrum is individual to a particular compound, like a human finger print is individual to a certain person [136].

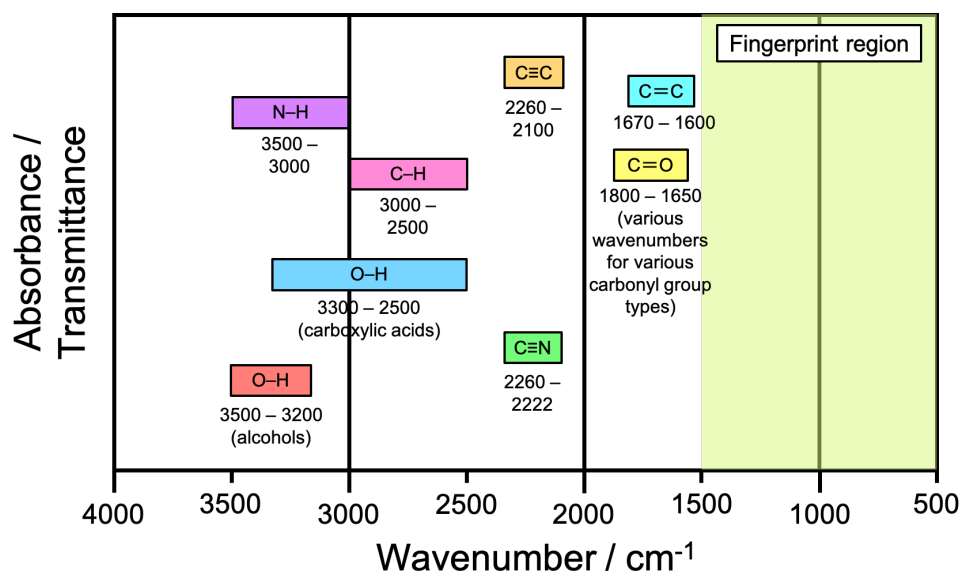


**Figure 2.2:** Characteristic IR bands for a variety of bond types [135–139].

The exact position of any peak in an IR spectrum is affected by the state of the sample being probed (solid, liquid, solution, paste, gas etc) and hydrogen bonding within the sample [136, 137]. This can make it more challenging to identify characteristic bands in the spectra however, as IR spectroscopy is a well established technique, there are many texts and reference tables that can be used to aid identification of molecular structures from the IR spectra [136].

#### 2.2.4 Fourier transform IR spectroscopy

Fourier transform IR spectroscopy (or FTIR spectroscopy) is probably the most popular IR spectroscopy technique used in laboratories today [138]. FTIR is named as such as it requires a Fourier transformation step to extract the spectral data from interferograms, the raw data that FTIR spectrometers collect.

FTIR exploits the fact that waves of electromagnetic radiation of identical frequency can overlap. This is known as interference. IR radiation passes through an interferometer, then through a sample into a detector to obtain an FTIR spectra [136]. In the case of FTIR spectrometry that uses a Michelson interferometer [136–138], a single IR radiation beam is split using a beam splitter with one beam reflected onto a stationary mirror, and the other beam from the splitter is reflected on a moving mirror (figure 2.3). The reflected beams recombine at the beam splitter and are directed through the sample. The radiation passes through the sample into a detector.

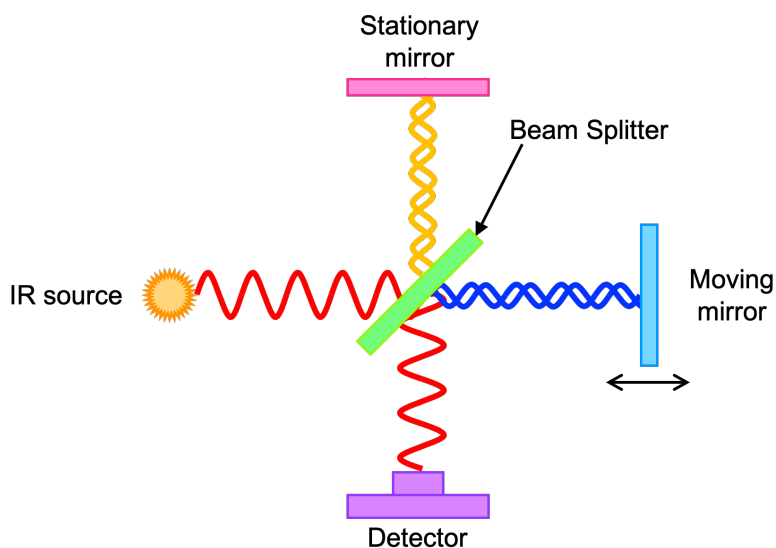


**Figure 2.3:** A sketch of a Michelson interferometer based FTIR spectroscopy set up [136, 138]. During measurements, the sample would sit in front of the detector.

Due to the moving mirror, the path-length of the one of the split beams changes causing a phase shift which means when the beams recombined, the interference of the IR radiation changes over time as the mirror moves [136, 138]. As a broad spectrum of IR radiation is being examined simultaneously, the level of interference of different wavelengths varies with the mirror distance/time. This yields a complex interferogram of time versus detector signal that can be converted in to the ‘single beam’ by Fourier transform that shows the frequency response of the whole instrument including the sample. By forming the ratio of the single beam of a background measurement of the instrument itself without the sample present with the single beam with the sample present, the FTIR spectrum of the sample can be produced [137]. The Fourier transform step and combination of the single beams is usually an automatic process completed by FTIR software on a computer.

The advantage of FTIR spectroscopy over older IR spectroscopy methods is the speed of the data collection and production of a spectrum [135, 136]. Older IR spectrometers typically exposed a sample to specific wavelengths of the IR radiation incrementally which was a slow process and were often not very sensitive [136].

IR spectroscopy has been presented as a useful tool for inspecting the chemical structure of molecules in a sample. In this thesis, this technique is used to determine whether chemical crosslinks have been formed in HA hydrogel samples by identifying the presence of a carbonyl peak around  $1700\text{ cm}^{-1}$  in the IR spectra indicating the formation of ester bonding. Discussion of these experiments can be found in chapter 5.

## 2.3 Ultra-violet (UV) spectroscopy

Where IR spectroscopy was concerned with the vibrational energy levels of a molecule, UV spectroscopy or UV-visible (UV-vis) spectroscopy can be used to probe the electronic energy levels of a molecule.

### 2.3.1 Electronic transitions

A molecule can absorb electromagnetic radiation that excites an electron from the highest occupied molecular orbital (HOMO) to the lowest unoccupied molecular orbital (LUMO). The energy of the absorbed radiation must match the energy gap between the two energy levels (equation 2.1) [140]. All molecules contain bonding and anti-bonding electron orbitals. In saturated molecules, these are  $\sigma$  and  $\sigma^*$  orbitals respectively. In unsaturated molecules, there are  $\pi$  and  $\pi^*$  orbitals in addition to the  $\sigma$  and  $\sigma^*$  orbitals. Furthermore, some molecules have electrons that are not involved in bonding known as n-electrons. Typically, the orbitals increase in energy as follows:  $\sigma$  (bonding),  $\pi$  (bonding), n (non-bonding),  $\pi^*$  (anti-bonding), and  $\sigma^*$  (anti-bonding) [141]. The possible electronic transitions between molecular orbitals can be seen in figure 2.4. The gap between the  $\pi$  and  $\pi^*$  energy levels in molecules with conjugated  $\pi$ -systems is significantly smaller than in a molecule with single isolated  $\pi$ -bonds [140]. In general,  $\sigma \rightarrow \sigma^*$  transitions are not typically seen in the UV region of the spectrum [135]. The species that show these transition types are usually organic molecules [135]. Other electronic transitions can also be followed with UV-vis spectroscopy.

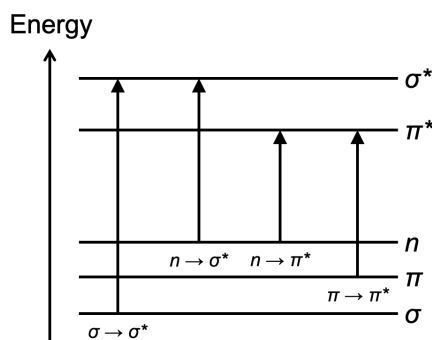


**Figure 2.4:** Electronic energy level transitions that are possible during UV spectroscopy [141]. The energy gaps are not to scale.

Similar to IR spectroscopy where the radiation excites a molecule from a lower vibrational energy level to a higher vibrational energy level, UV radiation is absorbed and excites an electron from a lower energy level to a higher energy level (the HOMO to the LUMO). The wavelength of the absorbed radiation will then be absent in the radiation measured by the detector leading to a peak in the resulting spectrum [135]. The majority of UV-vis spectrometers expose samples to wavelength ranges between 200 nm and 1100 nm with the UV-vis spectrum running from 100 nm to 800 nm [140]. Different types of electronic transition occur at different wavelengths and can be characteristic of the chemical environment in the molecule. Usually the maximum absorption wavelength ( $\lambda_{max}$ ) is the quantity of interest in UV spectroscopy, and can be related to a particular bond type within a molecule [135, 141]. For example, the  $\lambda_{max}$  for carbonyl groups is typically seen between 186-280 nm [135, 141]. The exact wavelength of a peak for a particular bond type varies with the chemical structure of the molecule, solvent choice, and hydrogen bonding within the sample [135, 141].

UV-vis spectroscopy can be used to follow the concentrations of species in solution as the absorbance of the sample at a given wavelength scales with the concentration of the absorbing species in solution [135, 140, 141]. Other applications include following reaction kinetics, and the degradation of dyes [140].

### 2.3.2 UV spectroscopy for organic electronic applications

UV spectroscopy is used in the field of organic electronics to probe the electronic transitions between the electronic states of conducting polymers.

In  $\pi$ -conjugated polymers, there are electrons delocalised along the polymer chain as a result of the alternating carbon-carbon double and single bonds. These electrons allow charge transfer along the molecule, and give these molecules their semiconducting or conducting properties. By doping these materials, a charge transfer to/from the polymer chain occurs and a p- or n-type doped polymer can be obtained [142]. Poly(3,4-ethylenedioxythiophene) (PEDOT), for example, is a p-type conducting material when doped, with polaronic and bipolaronic charge carriers [143]. The presence of the polarons and bipolarons in PEDOT alters the electronic energy levels within the PEDOT molecules [142]. This means that electronic transitions attributed to the presence of polarons and bipolarons can occur when exposed to the correct wavelength of electromagnetic radiation. These transitions can be detected by UV-vis spectroscopy and give indications to the conductivity of the PEDOT as conductivity scales with the amount of polarons and bipolarons present in the sample [144]. This fact was exploited in this thesis to assess the electronic properties of PEDOT:CS aqueous dispersions and films upon crosslinking and degradation. These experiments are detailed in chapter 4.

## 2.4 Electrochemical impedance spectroscopy (EIS)

Like optical spectroscopy, EIS is a non-destructive analysis technique. It is used to examine the complex impedance of an electrochemical system [145–147]. EIS has applications in a huge range of fields including battery science, bioelectronics, material sciences including corrosion testing, biological sciences, and sensors [148]. During EIS, a sinusoidal voltage is applied to a circuit at a range of frequencies and the impedance to the resulting current is measured [145–148]. This analysis technique can be used to examine the type of response in an electrochemical system where high frequencies relate to short term responses such as chemical reactions, and lower frequencies relate to longer term responses such as diffusion [146]. EIS can also be used to quantify the total impedance of a system at a specific frequency which is useful in biological applications as certain frequencies are of biological interest. For example, neuroprotheses often operate at around 100 Hz and thus the impedance of a specific electrode material at this frequency can be measured and compared with other electrode materials [149].

### 2.4.1 Impedance

Where resistance concerns direct current and voltages, impedance can be considered the alternating current equivalent of resistance. Depending on the specific phenomena impeding the current, a phase shift between the applied alternating voltage and the current can occur (figure 2.5) [145, 146].

The impedance,  $Z(\omega)$ , as a function of frequency  $\omega$ , is defined as the ratio of voltage,  $V(\omega, t)$ , to the current,  $I(\omega, t)$ , at each frequency. This can be described by equation 2.2 where  $\phi$  is the phase difference [146].

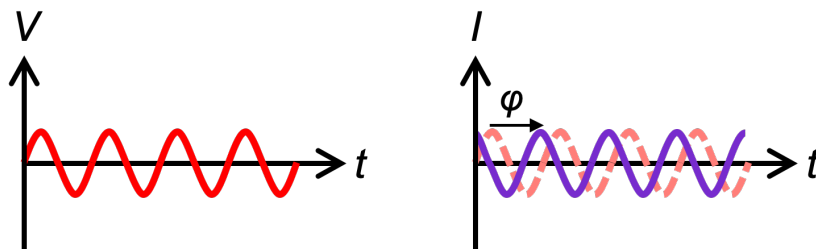


**Figure 2.5:** An alternating potential signal (left, red) can produce a phase-shifted alternating current signal (right, purple) as a result of impedance through a sample.

$$Z(\omega) = \frac{V(\omega t)}{I(\omega t)} = \frac{|V| \sin(\omega t)}{|I| \sin(\omega t + \phi)} \quad (2.2)$$

Impedance is presented as a complex number as it is easier to use imaginary numbers than manipulate trigonometric ratios. Sines and cosines can be converted to imaginary numbers using Euler's formula. It should be noted that usually  $i$  is used to describe the square root of  $-1$ , however in the case of impedance  $j$  is used to avoid confusion with current which is usually denoted by  $I$ .

As the impedance ( $Z$ ) depends on the specific phenomena occurring within the system, impedance can also be described as being made up of real and imaginary contributions where the real impedance ( $Z_{real}$ ) is the resistance ( $R$ ) contribution and the imaginary impedance ( $Z_{imaginary}$ ) is the reactance ( $X$ ) contribution (equation 2.3). The reactance,  $X$ , refers to the inductive and capacitive contributions to the overall impedance of a system. Capacitors and inductors induce phase shifts in the current and the impedance of these simple electronic components depend on the frequency and are, therefore, mathematically described using imaginary numbers [145–147]. The impedance for these components are given by equations 2.4 and 2.5 for capacitors and inductors respectively, where  $C$  is the capacitance and  $L$  is the inductance. On the other hand, resistors do not induce phase shifts and the impedance of these components is simply the resistance ( $R$ ) (equation 2.6) [145–147].

$$Z = R + jX \quad (2.3)$$

$$Z_C(\omega) = \frac{1}{j\omega C} \quad (2.4)$$

$$Z_{ind}(\omega) = jL\omega \quad (2.5)$$

$$Z_R(\omega) = R \quad (2.6)$$

## 2.4.2 Nyquist and Bode plots

One of the most useful methods of displaying information about the impedance of a electrochemical system is to use a Nyquist plot. Nyquist plots are named after Harry Nyquist, a researcher at Bell

Laboratories, who first developed the technique of displaying information in the 1930s. EIS can be used to generate Nyquist plots for an electrochemical system and consists of the real impedance ( $Z_{real}$ ) on the x-axis and imaginary impedance ( $Z_{imaginary}$ ) on the y-axis [145–147]. Each point on a Nyquist plot is taken at a different frequency so the total impedance at any given point can be represented by a vector of length  $|Z|$  and the angle between the vector and the x-axis is the phase angle  $\Theta$  (figure 2.6)[145].

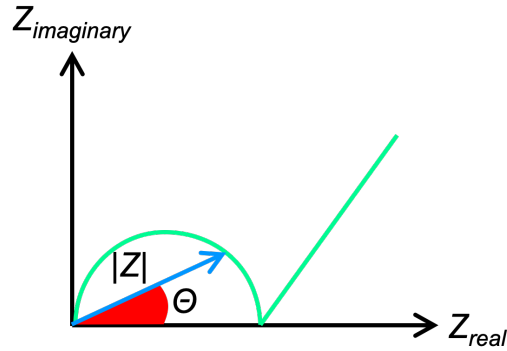


**Figure 2.6:** A generic Nyquist diagram with the data plotted in green with a vector of length  $|Z|$  in blue at angle  $\Theta$  from the x-axis in red.

Characteristic features and plot shapes in the Nyquist diagrams can give a range of information about an electrochemical system including indications of processes and phenomena that are occurring in a sample such as diffusion of ions and charge transfer events. There are many different shapes that a Nyquist plot can take. For example, a common shape that Nyquist plots take when plotting EIS data is a semi-circle followed by a linear section as seen in figure 2.7. The semi-circle indicates that a charge transfer process is occurring [145]. The points where the semi-circle meets the x-axis on the plot is where the contribution of the imaginary impedance to the total impedance is zero. This means that the total impedance is only a result of real contributions, i.e. resistance. The left hand point where this occurs is usually referred to as the solution resistance ( $R_S$ ), and the right hand point is the charge transfer resistance ( $R_{CT}$ ), as seen in figure 2.7. The solution resistance ( $R_S$ ) is related to the transport properties of the electrolyte whereas the charge transfer resistance ( $R_{CT}$ ) relates to the electrochemical reactions occurring at the electrodes [145, 146]. The linear section that follows the semi-circle is a result impedance from diffusion of electroactive species in the system [145, 146]. As the plot is at  $45^\circ$  angle to the x-axis in the example Nyquist plot, this particular impedance is known as the Warburg impedance.

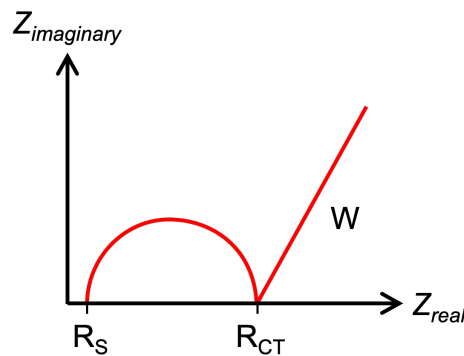


**Figure 2.7:** A generic Nyquist diagram with the data plotted in red with the charge transfer resistance ( $R_{CT}$ ), solution resistance ( $R_S$ ), and Warburg impedance ( $W$ ) labelled.

Other shapes that the Nyquist plot may take include a flatter semi-circle indicating more complex phenomena than a single charge transfer process, and requires more detailed analysis [145, 146]. Alternatively, multiple loops in the Nyquist plot indicates that multiple events are occurring requiring multiple time-constants to describe the phenomena [146].

Another plot that can be used to show EIS results is a Bode plot (figure 2.8). A Bode plot displays the impedance ( $Z$ ) (real, imaginary, or total) as a function of frequency, and also often shows the phase angle  $\Theta$ . The shape of Bode plots do not hold as much information about the events occurring in an electrochemical system, but can be used to directly assess the impedance at a specific frequency.

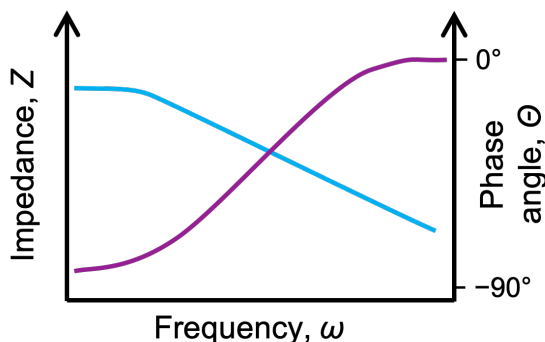


**Figure 2.8:** A generic Bode diagram with the impedance data ( $Z$ ) plotted in blue and the phase angle in purple ( $\Theta$ ).

### 2.4.3 Equivalent circuits

EIS data can be used to produce equivalent circuit models which describe the behaviour of the electrochemical system under investigation. An electrochemical system can mimic the behaviour of simple electronic components which means that any electrochemical system can be described by combinations of the mathematical expressions given for various components as highlighted in section 2.4.1 [145]. For example, a simple equivalent circuit that is often used as a starting point for many models is a resistor in series with a second resistor and capacitor that are in parallel (figure 2.9). This circuit offers an approximation of the impedance behaviour of a simple electrochemical reaction [145]. In such a simple electrochemical system with a highly conductive ionic solution, the first resistor models the solution resistance. The second resistor and capacitor in parallel describe the charge transfer resistance and double layer capacitance behaviour, respectively, occurring at the electrode interface.

Equivalent circuit modelling is very useful as it allows the contributions of different phenomena in a electrochemical system to be examined separately. EIS allows the user to identify characteristics of a system and produce such a equivalent circuit model.

### 2.4.4 Applications of EIS

As previously referenced, EIS has a range of applications in a range of different fields and some of those applications are outlined below.

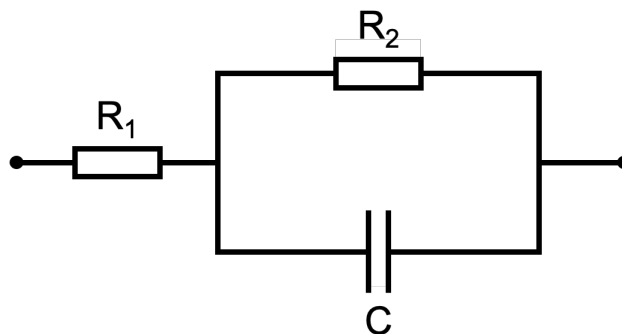


**Figure 2.9:** An example equivalent circuit with a resistor ( $R_1$ ) in series with a second resistor ( $R_2$ ) and capacitor ( $C$ ) that are in parallel.

In chapter 4, EIS is used to identify the contributions of ionic and ohmic activity to the overall conductivity of the PEDOT:biomolecule materials. The shapes of the Nyquist plots are used to indicate how the system changes prior to and after PEDOT:biomolecule crosslinking. This type of analysis is useful in the field of organic bioelectronics as it gives an indication of how a conducting polymer is performing in a system [150]. Using EIS to separate out the contributions of ionic and ohmic effects allows the experimentalist to identify what aspects of the sample material need tuning to achieve maximum conductivity (or indeed minimal impedance). Also within the field of organic bioelectronics, EIS has been used to determine the suitability of conducting polymer coatings for microelectrode arrays with coatings that reduce the impedance across the array by a greater amount being more suited to neural recording and stimulation [151]. In other biology-related applications, EIS can be used to measure the concentration of bacteria in medium and has been used to detect antigen-antibody binding events [148, 152]. Additionally, as the technique scans across a range of frequencies, it can be used to probe the impedance of a device at any given frequency within that range. As previously mentioned, this is useful for neuroprostheses as they often operate at around 100 Hz and thus the impedance of a specific electrode material at this frequency can be measured and compared with other electrode materials [149]. Furthermore, the proliferation of electronically active cells on a surface can be followed with EIS as the impedance of the system increases with increasing cell growth [134].

Energy storage researchers use EIS to study batteries. By producing equivalent circuits from EIS data to describe the phenomena occurring within batteries, it can be understood why batteries fail after repeated cycling or may be used to identify the most appropriate electrolyte for a certain battery system by choosing the system showing the lowest impedances [148].

Corrosion testing is one of the most popular applications of EIS, especially in industrial settings. EIS can be used to assess the level of corrosion on a metal surface as corrosion changes impedance of the test sample. The charge transfer resistance mentioned in section 2.4.2 is the quantity that is most often noted for corrosion experiments as there are only resistive (ohmic) contributions to the impedance and thus fewer variables affect its value [148].

## 2.5 Mechanical testing techniques

The phrase “mechanical properties” refers to a fairly broad array of quantities that describe how a material acts under a load. In this thesis, the quantity used to describe the mechanical properties of biomaterials and the central nervous system is the the elastic modulus (or Young’s modulus).

### 2.5.1 Elastic modulus

The elastic modulus of a material quantifies linear elastic deformation and is applicable for tensile and compressive stress. Elastic deformation is non-permanent and the material will return to its original shape once the stress has been removed. On the other hand, plastic deformation is a permanent deformation. As outlined in the introduction (chapter 1), the elastic modulus ( $E$ ) is defined as the ratio of normal stress ( $\sigma$ ) over linear strain ( $\epsilon$ ) [61, 153, 154]. Stress is usually defined as an applied force ( $F$ ) over an area ( $A$ ) ( $\sigma = F/A$ ), whereas strain describes the deformation of the material as a result of the applied stress. Strain is quantified as the change in length of the material sample in one dimension ( $\Delta L = L - L_0$ ) divided by the original length ( $L_0$ ) of the material sample in that dimension ( $\epsilon = \Delta L/L$ ) [61, 153–155].

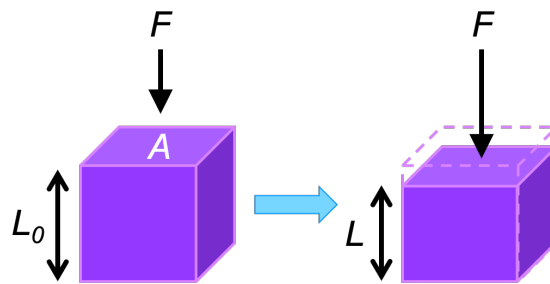


**Figure 2.10:** Visual representation of a compressive elastic deformation - a force ( $F$ ) is applied over an area ( $A$ ) which causes the compression of the material and length  $L_0$  to change to length  $L$ .

In practice, the stress-strain relationship for a particular material can be plotted to give a stress-strain curve (figure 2.11).

In the elastic regime, the stress-strain relationship is linear and follows Hooke’s law, so the elastic modulus may be extracted directly from the gradient of the plot [153–155]. Hooke’s law (equation 2.7) describes how the extension of a spring by a distance ( $x$ ) is linearly proportional to the force ( $F$ ) needed to extend the spring to that length, where  $k$  is a constant describing the stiffness of that spring.

$$F = kx \tag{2.7}$$

Hooke’s law can be applied to the elastic deformation of a material instead of a spring, yielding the equation describing the elastic (or Young’s) modulus (equation 2.8).

$$\sigma = E\epsilon \tag{2.8}$$

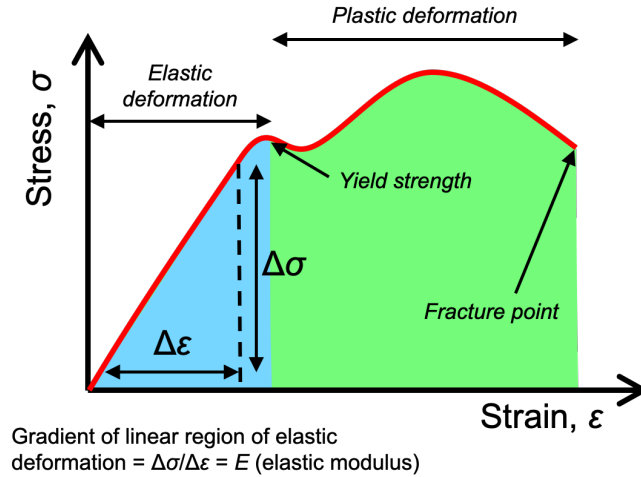


**Figure 2.11:** Typical stress-strain curve showing regions of both elastic and plastic deformation, and the eventual mechanical failure of a sample at the fracture point. The yield strength indicates the point at which the sample enters the plastic regime.

## 2.5.2 Poisson's ratio

The Poisson's ratio ( $\nu$ ) of a material is another quantity that is used to describe the mechanical properties of a material. The Poisson's ratio is a measurement of how a material expands or contracts along an axis perpendicular to the axis of compression or tension [154, 156]. Typically, when a material is stretched along the longitude direction (axially), the material tends to contract in the transverse direction (laterally). The opposite is also typically true, when a material is compressed along the longitude direction (axially), the material tends to expand in the transverse direction (laterally). There are a few exceptions to these behaviours where a tensile force axially results in an expansion of the material laterally, as oppose to a contraction. Equally, a compressive force axially results in an contraction of the material laterally as oppose to a expansion in these exceptional cases. These materials are called auxetics [156, 157].

The actual value of the Poisson's ratio is the ratio of the strain along the transverse direction ( $\epsilon_{trans}$ ) over the strain along the axial direction ( $\epsilon_{axial}$ ), given by equation 2.9, all as a result of an applied stress in the axial direction.

$$\nu = \frac{\epsilon_{trans}}{\epsilon_{axial}} \quad (2.9)$$

If the transverse strain of a material is along the x-axis, and the axial strain is along the z-axis, then the strains are defined by equations 2.10 and 2.11 where x and z are the original lengths of the sample in the transverse and axial directions.

$$\epsilon_{trans} = \frac{dx}{x} \quad (2.10)$$

$$\epsilon_{axial} = \frac{dz}{z} \quad (2.11)$$

The value of Poisson's ratio is usually between 0 and 0.5 for an isotropic, elastic material, however auxetic materials have negative values [156, 157]. Incompressible materials such as rubber have Poisson's ratios of

0.5 [154, 156]. Hydrogels are also considered to be incompressible, and a Poisson's ratio of 0.5 is assumed [158].

### 2.5.3 Universal mechanical testing rig

Typically, the simplest method of characterising the elastic modulus of a material is to use a universal mechanical testing rig. These instruments are usually uniaxial, so can apply force onto a sample along one axis at a constant rate and can be set up to run compression or tensile experiments. Universal testing rigs are available in a range of different sizes from large industrial machines capable of applying forces on the order of meganewtons, to smaller laboratory bench-top devices [155]. The testing rigs apply a force to a given sample and produce load-displacement data which can be trivially converted to stress-strain plot (as seen in figure 2.11), allowing the user to easily obtain the elastic modulus of the sample.

### 2.5.4 Indentation testing

Indentation testing is another common method of mechanically characterising materials. Instead of applying a force across a cross-sectional area of a sample, a compressive force is applied to a small localised area of a sample and indents that area. Indentation testing is advantageous for hydrogel mechanical characterisation as the hydrated gels can be difficult to handle and thus can be difficult to attach to universal testing rigs [155]. Depending on the nature of the gel, it may also be problematic to form a consistent geometry for testing with a universal rig. Indentation testing can be used across a range of scales from large indenters (centimetres) in metal testing to nanoindentation experiments using atomic force microscopy (AFM) techniques. Furthermore, there are a number of different indenter geometries that may be used, such as spheres, cones, and cylinders (figure 2.12).

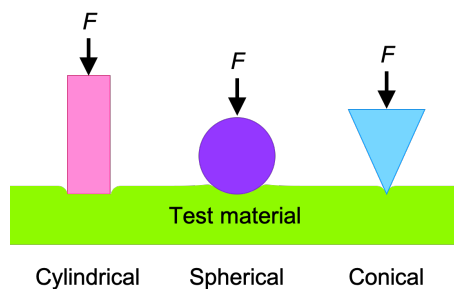


**Figure 2.12:** Various indenter geometries for mechanical testing.

### Contact mechanics

The theories of contact mechanics are used to determine the elastic modulus from indentation experiments. Contact mechanics describes the deformation of solids in contact with each other, and can be used to determine areas of contact between two surfaces, depths of indentation, and elastic moduli. Different indenter geometries require different contact mechanical solutions. Additionally, the theories presented here assume no adhesion between the material under investigation and the indenting probe. Adhesive contact can be described by a number of theories that are outside the scope of this thesis.

Indentation testing with a flat-ended cylinder is used to determine the elastic moduli of crosslinked HA hydrogels in chapter 5. Contact mechanics dictates that assuming non-adhesive contact between a rigid, flat-ended cylinder, and an elastic half space (figure 2.13), the relationship between the indentation depth ( $d$ ) and the normal force ( $F$ ) is given by equation 2.12 where  $a$  is the radius of the indenting cylinder [159, 160]. This yields the reduced elastic modulus ( $E^*$ ) which can be converted into the elastic modulus ( $E$ ) of the sample using equation 2.13 [160], where  $\nu$  was the Poisson's ratio of the sample or indenter.

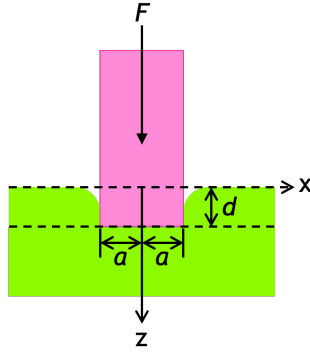


**Figure 2.13:** A diagram of the contact mechanics model used for elastic modulus calculations, showing a rigid flat-ended cylinder (pink), with radius  $a$ , indenting an elastic half space (green) to a depth of  $d$  due to a normal force ( $F$ ).

$$F = 2aE^*d \quad (2.12)$$

$$\frac{1}{E^*} = \frac{(1 - \nu_{sample}^2)}{E_{sample}} + \frac{(1 - \nu_{indenter}^2)}{E_{indenter}} \quad (2.13)$$

Spherical and conical probe solutions are also possible, with the latter probe type being popular in nanoindentation techniques. Nanoindentation techniques are very popular in the characterisation of soft materials such as hydrogels and biological tissues as nanoindentation is sensitive to very small indentation depths on the order of nanometres. There are a number of specially designed nanoindenter machines available which can be used in wet environments making them useful for hydrated materials such as hydrogels and biological samples. On the other hand, AFM can be used in a similar way where the AFM tip can be used as the indenting probe [158]. The limitation of nanoindentation techniques is that they can lead to overestimation of the elastic modulus as result of inaccurate measurements of the depth of indentation due to incorrect detection of the onset of contact with the surface of the sample [161].

## Chapter 3

# Synthesis and characterisation of poly(3,4-ethylenedioxythiophene):biomolecule complexes and their devices

### 3.1 Introduction

Typically, doped poly(3,4-ethylenedioxythiophene) complexed with poly(styrene sulfonate) (PEDOT:PSS) is the organic electronic material (OEM) used in many examples of OECTs and other bioelectronic devices for use in the body. PEDOT:PSS itself was introduced in section 1.2.4. This introduction will describe its uses in organic bioelectronics. It will also provide a review of PEDOT stabilised with alternative materials to PSS, and why these might be used, leading into the experimental work which will be discussed later in this chapter.

#### 3.1.1 Using PEDOT:PSS in organic bioelectronics

PEDOT:PSS is a popular material for use as the organic electronically conducting polymer in a number of organic electronic devices due to its desirable properties: PEDOT:PSS is highly conductive (with conductivities up to  $3000 \text{ S cm}^{-1}$ , depending on specific formulation and if any treatments have been applied), possesses favourable charge transfer properties, it conducts both ionically and electronically, has easy processability, is stable under aqueous conditions, can form transparent thin films, and studies have shown a lack of cytotoxicity in biocompatibility testing [46, 150, 162, 163]. These reasons, as well as the commercial availability of PEDOT:PSS, make it the material of choice for use in organic electronic devices for uses both in and out of biological systems. One of the most common applications for organic bioelectronic devices are sensors. Typically, these sensors make use of PEDOT:PSS as the OEM in the channel of some type of organic field-effect transistor (OFET), OECT, or electrolyte-gated organic

field-effect transistor (EGOFET), or as the electrodes themselves in such devices [31, 46, 150, 163]. One example of such an application is the alcohol sensor developed by Bihar *et al.* [53] which can be used as a disposable breathalyser. This sensor was an OECT device that used ink-jet printed PEDOT:PSS electrodes on paper, making the production of these devices facile and cheap. A collagen-based gel containing enzyme alcohol dehydrogenase and nicotinamide adenine dinucleotide, which together act to facilitate a reaction producing acetaldehyde and electrons from ethanol, was deposited across the channel of the device. When a user blows over the device, ethanol carried on the breath gets exposed to the gel and reacts producing electrons which decreases the conductivity of the source-drain channel, decreasing the source-drain current output. This decrease in conductivity can be compared to a calibration curve which allows the user to determine the breath alcohol level. The paper reports successful testing on subjects that consumed alcohol showing that the performance of the simple OECT breathalyser was comparable to a commercially available breathalyser. In the alcohol sensor, PEDOT:PSS was used for the electrodes, however more typically PEDOT:PSS is found in the channel, like in the case of the glucose sensor reported by Liu *et al.* [164] in 2008. PEDOT:PSS was utilised as an organic electronic material (OEM) in an organic thin film transistor, and was used to immobilise glucose oxidase enzyme which converts glucose into gluconic acid and hydrogen peroxide. The hydrogen peroxide and PEDOT:PSS react, and thus the output current of the device changes, allowing measurements of the concentration of the glucose to be made against a calibration curve of the output current.

Since 2008, there have been developments in the use of organic electronics to detect glucose concentrations, such as the work by Kanakamedala *et al.* [165] who developed an OECT glucose sensor based on PEDOT:PSS alone without the need for the addition of an enzyme. Additionally, Bihar *et al.*, who reported the alcohol sensor discussed above, have also developed an organic bioelectronic device for sensing glucose concentrations utilising ink-jet printed PEDOT:PSS in combination with glucose oxidase [166]. This device is reported to be completely metal free, and stable in storage for a month which offers easy manufacture and use for patients and medical professionals. The creation of organic bioelectronic glucose sensors such as those mentioned above has real-world value. Such glucose sensors remove the need for invasive blood glucose monitoring in diabetic patients who require regular information on their glucose levels. Usually, the glucose concentration of a patient is measured using a pin-prick blood test where a small needle is used to draw blood from the finger and dropped onto a handheld sensor. This process can be painful and time consuming. On the other hand, organic bioelectronic glucose sensors can accurately measure glucose concentrations in aqueous solutions, such as saliva removing the need for pin-prick testing.

PEDOT:PSS based organic bioelectronic devices are not only used as sensors to specific molecules. OECTs can be used to detect small potential changes that occur in the body as a result of the heart beating, for example. Campana *et al.* [54] developed a highly sensitive OECT device that could be used to measure the electrocardiograph of a human heartbeat. The device was made up of gold contacts and a PEDOT:PSS channel on a bioresorbable scaffold made of poly(L-lactide-co-glycolide) (PLGA). It could be placed on the skin and using the tiny changes in the potential of the skin when the heart beats, the electrocardiograph could be recorded and the characteristic PQRST wave form seen. The PLGA introduced biocompatibility and biodegradability to the device, which therefore could be used in future applications inside the body, in other electronically active systems such as the central nervous system (CNS), without the need for invasive removal surgeries.

Hempel *et al.* [55] also demonstrated a PEDOT:PSS OECT device for measuring electrophysiological

signals. Unlike Campana *et al.*, these OEECTs were examined in direct contact with HL-1 cardiomyocytes (cardiac cells) which spontaneously beat. The changing extracellular potentials of the HL-1 cells meant that the spontaneous signals could be measured by the OEECT. This example shows that OEECTs can be used effectively to measure electrical signals within the body, such as the action potentials seen in the CNS. OEECTs based around PEDOT:PSS are of interest for use in the CNS. For example, a flexible electrophysiology array designed to record electronic signals in the leg muscles of a rat was developed by Lee *et al.* [167] and was based on OFETs and PEDOT:PSS OEECTs. This array was produced as an alternative to the hard and invasive microneedle arrays used to record brain activity that are standard in the field of electrophysiology. The soft conformable array was successfully demonstrated to measure the electrophysiological signals in the muscles of rats when muscle contraction was activated with blue light. The flexibility afforded by the parylene substrate and the PEDOT:PSS and gold thin film circuitry allowed the device to directly contact the three-dimensional muscle surface. This was unlike harder arrays that cannot bend and conform to give perfect contact between the electrodes measuring biological signals and the biological surface.

Despite the wide use of PEDOT:PSS in organic bioelectronics, there are drawbacks to using the material as a conducting polymer in devices for implantation into the body. One of the biggest issues is the acidic nature of the PSS [127]. There is usually a greater amount of PSS than PEDOT in PEDOT:PSS preparations, often in a 1:2.5 up to 1:6 ratio [49]. PSS contains some residual sulfonate protons ( $H^+$ ) as it is derived from poly(styrene sulfonic acid) [168]. The excess of PSS compared to PEDOT results in a highly acidic environment. Typically, PEDOT:PSS aqueous dispersions have pH values below 3, which is incompatible with the human physiological pH of 7.4. An acidic environment could result in cell death in delicate tissues such as in the spinal cord. This issue boils down to the biocompatibility of PEDOT:PSS. The long-term biocompatibility of PEDOT:PSS in the body is not well studied [169, 170]. This is important if a device is to be present in the human body for a long period of time.

Linked to the compatibility, considerations towards the degradation of PEDOT:PSS is important. PEDOT:PSS degradation *in vivo* or *in vitro* appears to have not been studied [127]. However, concerns about the degradation and release of acid protons from the PSS have been aired. A review paper by Feig *et al.* [60] highlighted the need for degradable OEMs for use in organic bioelectronics to improve the therapeutic outcomes and environmental impact of such technologies. In addition to the acidity of PEDOT:PSS being of concern for biocompatibility, there are also concerns for device performance. This has been explored in the field of organic semiconductor devices. The acidic protons from the PSS in PEDOT:PSS have been shown to degrade and reduce the performance of layered organic semiconductor devices. Studies have shown that introducing an alternative polyelectrolyte material or other counterion can improve the lifetimes of PEDOT:PSS based organic semiconductor devices [171]. This may be applicable to organic bioelectronic devices as well.

Furthermore, PEDOT:PSS does not have the most desirable mechanical properties for use in the body, especially in soft environments such as the CNS (0.0003 - 1.40 MPa [70, 72–76], more details in section 1.3.3). Back in 2003, it was reported that PEDOT:PSS spun microfibres were found to have Young's moduli of  $1.1 \pm 0.3$  GPa [172], however this is not particularly useful value when considering organic bioelectronic devices such as OEECTs as they tend to be formed of thin films of PEDOT:PSS. Thin films of PEDOT:PSS were reported by Lang *et al.* [173] to have Young's moduli that varied with levels of relative humidity with a Young's modulus of  $2.8 \pm 0.5$  GPa at 23% relative humidity,  $1.9 \pm 0.02$  GPa at 40% relative humidity, and  $0.9 \pm 0.2$  GPa at 55% relative humidity. This showed that at low relative

humidities, PEDOT:PSS was brittle but became more plastic with increased moisture. Using a buckling method, multiple OEMs had their Young’s moduli characterised by Tahk *et al.* [174] and showed that PEDOT:PSS had a Young’s modulus of  $2.26\pm 0.05$  GPa which was consistent with the values reported by Lang *et al.*. Of the OEMs tested in the experiments detailed in this paper, PEDOT:PSS had the second lowest Young’s modulus with poly(aniline) (PANI) being softest with a value of around 0.03 GPa, however this was attributed to the organic solvent used with PANI acting as a plasticiser. A 2019 study by Dazou *et al.* [175] also found the Young’s modulus of pristine PEDOT:PSS films to be of a similar magnitude at 1.15 GPa.

Table 3.1 summarises the elastic moduli measured for various structures within the central nervous system (CNS). These values are discussed in more detail in chapter 1, however it is clear that there is a discrepancy between PEDOT:PSS and CNS tissues. PEDOT:PSS has a Young’s modulus on the order of giga-Pascals, whereas the soft tissues of the CNS are in the kilo-Pascal to mega-Pascal region. Mismatched mechanical properties between tissues and implants can lead to rejection of the implant by the body, and it being cut off by scar tissue meaning it cannot function as intended.

**Table 3.1:** A summary of the elastic moduli of the structures in the CNS. More detail is given on these values in chapter 1.

Tissue type	Elastic modulus / MPa	References
Brain	$0.3 \times 10^{-3} - 1.0 \times 10^{-3}$	[70]
Human spinal cord	1.02 - 1.37	[72]
Human spinal cord	0.089 - 1.40	[73]
Rabbit spinal cord	$(0.5\pm 0.2) \times 10^{-3} - (1.6\pm 0.5) \times 10^{-3}$	[74]
Bovine spinal cord	$1.19\pm 0.13$	[75]
Cat spinal cord	0.23	[76]

In summarising the mechanical properties of PEDOT:PSS, Kayser *et al.* [176] reported that PEDOT:PSS and PEDOT were brittle and not stretchable. This is relevant for how the materials actually work within the body, as the body is a dynamic environment which deforms and changes shape as a person moves and grows. With this in mind, any implanted material must have properties enabling it to continue to function as the body moves etc.

The structure of grains of PEDOT:PSS in aqueous dispersions has been shown to consist of a PEDOT centre surrounded by a PSS shell [176]. This provides the stabilisation required in solution. However, the PSS shell is considered to be a major contributor to the high elastic moduli reported. This is suggested to be due to strong ionic interactions between PEDOT and PSS [174, 176].

Alternative stabilising materials for PEDOT, instead of PSS, may offer more biocompatible and mechanically appropriate alternatives to PEDOT:PSS for use in organic bioelectronics that also may offer a route to a degradable material.

### 3.1.2 Alternatives to PEDOT:PSS

To improve the biocompatibility of PEDOT for applications in the human body, there have been a number of different approaches attempted including altering the EDOT monomer to give alternative chemical

functionality, and using alternative stabilising materials instead of PSS [127, 177, 178]. A number of biomolecules have been explored as alternatives to PSS for PEDOT. As stated earlier, PEDOT:PSS has some potential biocompatibility issues therefore using native biomolecules as alternatives to PSS has been explored as a possible route to improving biocompatibility [127, 177, 178]. Additionally, the use of a biomolecule introduces a possible route for degradation of a PEDOT based material, as many biomolecules can be enzymatically degraded *in vivo* [60].

There have been multiple approaches to producing PEDOT stabilised with biomolecules. Oxidative polymerisation of EDOT in the presence of biomolecules to form PEDOT:biomolecule aqueous dispersions as well as electrochemical polymerisations have been demonstrated.

In 2008, Asplund *et al.* [169] published a paper describing the electropolymerisation of PEDOT with fibrinogen, hyaluronic acid (HA), and heparin (hep) to form PEDOT:fibrinogen, PEDOT:HA, and PEDOT:hep, respectively, for use as potential new materials for use in neural electrodes. HA is a glycosaminoglycan found in the extracellular matrix and is described in more detail in chapter 1. Hep is another glycosaminoglycan found in the body and acts as an anticoagulant. Fibrinogen is a protein found in the blood of humans and other vertebrates and is involved in blood clotting. EDOT was electropolymerised from aqueous solutions of these three biomolecules onto platinum disks at a current of 4  $\mu\text{A}$  for various time periods between 100 to 2000 seconds to give PEDOT:biomolecule films of varied thicknesses. The films were electrochemically characterised via cyclic voltammetry (CV) and electrochemical impedance spectroscopy (EIS). The PEDOT:fibrinogen was difficult to electropolymerise due to the fibrinogen being adsorbed onto the metal surface during polymerisation, leading to poor conductivity in PEDOT:fibrinogen films. By contrast, the PEDOT:HA and PEDOT:hep showed similarities in conductivity and film structure to PEDOT:PSS, with PEDOT:hep being investigated further for its stability under biologically relevant conditions. The PEDOT:hep was found to be less stable over the course of the experiment than PEDOT:PSS suggesting that the choice of counter-ion for doped PEDOT has an effect on its overall stability over time [179]. This suggested that the PEDOT:hep was degradable, which is a key aim of the work described in this thesis, and supports the assumptions made later in this chapter that the use of a biomolecule paves the way for a degradable PEDOT:PSS alternative.

In addition, Asplund *et al.* [180] assessed the biocompatibility of PEDOT:HA and PEDOT:hep *in vitro*, and the biocompatibility of PEDOT:hep *in vivo* in Sprague-Dawley rats. The biocompatibility of a material is typically tested by standard cytotoxicity screenings on L929 fibroblast cells (a type of cell that is involved in producing the extracellular matrix) and SH-SY5Y neuroblastoma cells (a research cell line used as models for neuron function and differentiation). The additional experiments on PEDOT:hep consisted of implanting PEDOT:hep-coated platinum electrodes into rat brains. These experiments shows that the PEDOT:hep implants showed no significant difference to the platinum control implants with regards to inflammatory response or distance of neuronal cells from the implants, and large immune responses were present for both implant type. The immune responses were thought to be due to the imbalance in mechanical properties of the hard implant versus the soft rat brain, so this result may not pertain to the biocompatibility of the PEDOT:hep itself, but does highlight the need for appropriate matching mechanical properties for implants into tissues.

More recently, doped PEDOT stabilised with chondroitin sulfate (CS) was prepared via electropolymerisation onto platinum microelectrodes intended for use as neural implants [181, 182]. The control of film thickness afforded by electropolymerisation is useful, but chemical approaches to PEDOT:biomolecule

synthesis are more likely to be used in the long run due to the scalability of such a process [30]. PEDOT:biomolecule aqueous dispersions can be used to form thin films via spray coating, spin-coating, and drop-casting, like PEDOT:PSS [30, 178].

There have been many examples of PEDOT:biomolecules synthesised via oxidative polymerisation and all of the syntheses follow a similar methodology; a solution of biomolecule is prepared, and EDOT added to it along with an oxidising agent and a catalyst. This mixture is stirred until the reaction reaches completion, and in some cases, the resulting aqueous dispersion is purified.

DNA-stabilised PEDOT (PEDOT:DNA) was synthesised by oxidative polymerisation [183] and demonstrated improved conductivity (approximately  $1 \text{ S cm}^{-1}$ ) compared to similarly prepared PEDOT:PSS (approximately  $0.15 \text{ S cm}^{-1}$ ), suggesting that not only can the introduction of biomolecules into PEDOT dispersions improve biocompatibility but also potentially offer improvements to the electronic properties compared to PEDOT:PSS. Another example of this is, in a 2015 study, PEDOT stabilised with sulfated cellulose was found to have an electrical conductivity 38 times greater than that of PEDOT:PSS [184].

Films prepared from aqueous dispersions of PEDOT with dextran sulfate (PEDOT:DS) was reported to have conductivities up to  $19.6 \text{ S cm}^{-1}$  [185]. This was achieved through careful tuning of the PEDOT:DS ratio, a low reaction temperature, and an ethylene glycol treatment. However even without the addition of ethylene glycol, conductivities of up to  $19.2 \text{ S cm}^{-1}$  were reported for some samples. In the case of PEDOT:PSS, there is usually a 2-3 order of magnitude increase in conductivity when treated with ethylene glycol which was not the case with the PEDOT:DS. These high conductivities were accompanied by evidence of greater compatibility with L929 cells than PEDOT:PSS, giving further evidence that biomolecule alternatives to PSS may be more appropriate for use in conjunction with PEDOT for use in biological applications.

Synthesis of PEDOT with guar gum (GG) has also been demonstrated via oxidative polymerisation [186]. This was then used to form a conductive hydrogel (or iongel) by freeze-drying an isolated powder of PEDOT:GG and introducing an ionic liquid to form a gel. This material demonstrated both electronic and ionic conductivity which is of interest for biomedical and energy storage uses.

Mantione *et al.* synthesised PEDOT with chondroitin sulfate (PEDOT:CS), hyaluronic acid (PEDOT:HA), and heparin (hep) in various ratios via oxidative polymerisation [168]. The synthesised aqueous suspensions were spin-cast into thin films and the conductivity measured with a four-point probe. It was shown that PEDOT:CS in a 85:15 ratio demonstrated the highest conductivity at  $0.075 \text{ S cm}^{-1}$ , closely followed by PEDOT:HA in the same ratio with a conductivity of  $0.071 \text{ S cm}^{-1}$ . The level of conductivity achieved by PEDOT:CS and PEDOT:HA in the 85:15 ratio was comparable to films of PEDOT:PSS with no extra treatments. The PEDOT:hep dispersions did not yield films with conductivities as high as the CS and HA dispersions. This was suggested to be a result of low dispersion stability and the presence of large aggregates compared to the CS and HA dispersions. Furthermore, it was proposed that the HA dispersions had lower conductivities compared to the CS dispersions as HA contains no sulfonate groups, analogous to the sulfonate groups found on PSS. In addition, the biocompatibility of PEDOT:CS, PEDOT:HA, and PEDOT:hep films were assessed. It was demonstrated that all of the PEDOT:biomolecule materials evaluated displayed no cytotoxicity towards L929 cell lines and thus all were assessed for functional biocompatibility with SH-SY5Y neuroblastoma cells and the human astrocytoma cell line CCF-STTG1 which acted as a model for human astrocytic cells. These experiments determined that all of the PEDOT:biomolecule materials assessed did not interfere with the physiological functions of the cells, and

had additional neuroregenerative properties compared to PEDOT:PSS which would be useful in the case of treating injuries to the CNS. PEDOT:CS was also shown to have a neuroprotective effect on some SH-SY5Y cells that were exposed to hydrogen peroxide, which usually induces cell death. The biocompatibility demonstrated in this study did not only show that PEDOT:CS, PEDOT:HA, and PEDOT:hep were as biocompatible as PEDOT:PSS, supporting the work by Asplund *et al.* [180], but that there were additional advantages to using the PEDOT:biomolecule materials compared to PEDOT:PSS with regards to CNS functional biocompatibility which would be useful in creating a device for use in the CNS and the treatment of injuries such as SCIs.

Despite a fairly large range of research around the synthesis of PEDOT:biomolecule complexes, there has been little research into using these materials in bioelectronic devices, or other applications. This presents an opportunity to explore use of these PEDOT:biomolecule materials in bioelectronic devices such as OECTs.

PEDOT:biomolecules demonstrate a natural, inherently biocompatible approach to the problems surrounding PEDOT:PSS for use in bioelectronics. Using a naturally occurring biomolecule from the human body removes compatibility concerns and can allow devices to be used in the body with minimal immune response, which could impact device performance. Using PEDOT:biomolecules in such a device also offers a degradability not found in PEDOT:PSS based devices, as biomolecules can be enzymatically degraded in the body [60]. This is advantageous as a degradable device could remove the need for potentially dangerous and invasive surgeries for device removal. Additionally, using alternative biomolecule counter-ions could offer tuning of the mechanical properties of PEDOT via choice of biomolecule, making it more suitable for uses in devices in soft environments such as the CNS [127, 178]. This highlights that there is the potential to develop an organic bioelectronic device based on PEDOT with biomolecule counter-ions that could offer a biodegradable, biocompatible, and more mechanically appropriate route to bioelectronic devices in the body. Furthermore, such a device would be ideal for use in the CNS and specifically in the delicate spinal cord. A more biocompatible approach may encourage new nerve growth over a SCI, and the electronic measurements could offer insight into how nerve cells in the spinal cord function following SCIs. In the future, this could lead to being able to use organic bioelectronic measurements to control exoskeletons or other aids to help paralysis victims regain the ability to walk after a traumatic SCI, similar to the work on the e-dura by Courtine *et al.* [5, 27] described in the introduction chapter (chapter 1).

### 3.1.3 Device requirements

The aim of this project is to develop a biocompatible, biodegradable, and mechanically appropriate OECT device that could be used in the spinal cord in future, therefore consideration of the requirements of such a device is needed.

In this OECT device, there must be an organic electronic material (OEM) that is biocompatible, biodegradable, mechanically appropriate to the elastic modulus of the spinal cord, and importantly for a bioelectronic device, conductive. The OEM must also be able to form a thin film that does not dissolve or immediately breakdown in electrolyte or water. This is so the material can be characterised, and fit the architecture of a typical OECT. There is, however, the requirement that the material breaks down in a controlled way over time so that it can be considered degradable. Additionally, the material must

be able to work as the OEM in an OEET, i.e. that a current through the material can be modulated by changing the doping status of the material via changing a gate potential through an electrolyte. This would provide the proof of concept that such a material could be used in an OEET type device.

In this chapter, the development of a biocompatible and conductive material based on PEDOT complexed with CS or HA (PEDOT:CS or PEDOT:HA) is presented. Following the experimental methods, it is shown that PEDOT:CS and PEDOT:HA can be synthesised via an oxidative polymerisation method as demonstrated by Mantione *et al.* [127]. It will be demonstrated that these materials can be drop-cast and are conductive, with sheet resistances of  $4.7 \text{ k}\Omega\text{cm}^{-1}$  for PEDOT:CS which was comparable to similar untreated PEDOT:PSS films. Additionally, 1-ethyl-3-(3-dimethylaminopropyl)carbodiimide hydrochloride (EDC) crosslinking is presented. This crosslinking technology favours degradation, however the degradation of the device will not be discussed until chapter 4. Finally, the successful preparation and testing of an OEET using PEDOT:CS as the OEM will be demonstrated and characterised with a peak transconductance ( $g_m$ ) of  $50.5 \mu\text{S}$ . This provided the proof of concept that such materials could be used in OEET devices.

## 3.2 Experimental Methods

### 3.2.1 Materials

Chondroitin sulfate A sodium salt from bovine trachea, hyaluronic acid sodium salt from *Streptococcus equi*, 3,4-ethylenedioxythiophene, ammonium persulfate, N-(3-Dimethylaminopropyl)-N'-ethylcarbodiimide hydrochloride, ethanol, and phosphate buffered saline tablets were supplied from Merck (formerly Sigma Aldrich). Iron (III) sulfate hydrate (Reagent grade, Alfa Aesar) was purchased from Fisher Scientific. SnakeSkin Dialysis Tubing (10K MWCO) was purchased from Thermo Scientific.

Deionised water was acquired from the lab purifier.

### 3.2.2 Synthesis of PEDOT complexed with chondroitin sulfate (PEDOT:CS) and hyaluronic acid (PEDOT:HA) by oxidative polymerisation

#### Oxidative polymerisation method

The method used was based on the oxidative polymerisation method reported by Mantione *et al.* [168].

To prepare a 2% (w/w) PEDOT:CS or PEDOT:HA aqueous dispersion in a 1:1 ratio by mass, CS or HA (0.20 g) was stirred in water (20.0 g, 1.11 mol) until completely dissolved to give a viscous solution. This took around five minutes for CS solutions, and up to an hour for HA solutions. Following this, 3,4-ethylenedioxythiophene (EDOT, 0.20 g, 1.41 mmol) was added to the solution and stirred for 15 minutes. Ammonium persulfate (APS, 1.5 equivalents, 0.48 g, 2.10 mmol) and a catalytic amount of iron (III) sulfate was then added to the mixture. The reactions were stirred for 48 hours at room temperature to produce 2% (w/w) aqueous dispersions of PEDOT:CS or PEDOT:HA as appropriate.

Dispersions of PEDOT:CS and PEDOT:HA of other ratios were also prepared. For consistency, all

aqueous dispersions were prepared to 2% (w/w). The method used was identical to the one described above but alternative masses of EDOT and CS or HA were used. Additionally, the mass of APS was altered with the mass of EDOT to give 1.5 molar equivalents each time. The masses used are given in table 3.2. The same mass of water (20.0 g, 1.11 mol) was used for each synthesis.

**Table 3.2:** Masses of the reagents used in the synthesis of PEDOT:CS and PEDOT:HA in various mass ratios.

Ratio of PE-DOT:biomolecule	Mass of EDOT / g	Mass of CS or HA / g	Mass of APS / g
1:1	0.20	0.20	0.48
1:2	0.13	0.27	0.31
1:3	0.10	0.30	0.24
1:4	0.08	0.32	0.13

## Purification

A washing regimen based on work by Wang *et al.* [187] was used to purify the aqueous dispersions of PEDOT:CS/PEDOT:HA. Up to half by volume of each discoloured PEDOT:CS or PEDOT:HA aqueous dispersion sample was kept aside as a comparison point for each washed sample. The PEDOT:CS or PEDOT:HA aqueous dispersion was shaken for five minutes with an equal volume of acetone, and the phases were allowed to settle out. The organic layer was then pipetted off. This was repeated twice more with acetone, followed by three washes with equal volumes of ethanol. On the final wash with ethanol, the PEDOT:CS or PEDOT:HA aqueous dispersion mixed with the ethanol was poured over filter paper, collecting the solid PEDOT:CS or PEDOT:HA which was then air dried in a heated cabinet for five minutes. The solids were then scraped off the filter paper, and dried in the vacuum oven for 30 minutes at 50 °C under vacuum. The mass of the dry material was then recorded and the appropriate mass of water to give 2% (w/w) solids was added to it in a glass vial. The sample was shaken thoroughly for five minutes to resuspend the solid PEDOT:CS or PEDOT:HA. In some cases an additional sonication step was introduced to distribute the solids. The samples were then stored in the refrigerator until required.

An alternative purification method was also employed after the washing method was determined to be inappropriate. Aqueous dispersions of PEDOT:CS and PEDOT:HA were dialysed using SnakeSkin dialysis tubing with a 10K molecular weight cut off (MWCO) in deionised water for 96 hours. The water was changed four times during this period. The samples were then stored in glass vials and sonicated for ten minutes prior to storage.

### 3.2.3 Forming films of PEDOT:CS and PEDOT:HA

#### Spin-cast film formation

PEDOT:CS 1:1 2% (w/w) aqueous suspension was spin-coated onto the glass slides for one minute at 1000 rpm. The sample was then allowed to air dry for 30 minutes and were then dried in a vacuum oven for one hour at 50 °C.

## Drop-cast film formation

To prepare a drop-cast film of PEDOT:CS or PEDOT:HA, a small volume of aqueous dispersion was dropped onto a clean glass slide substrate using a pipette. The volume of sample varied depending on the size of film required, but for method development purposes *ca.* 10  $\mu\text{l}$  of sample was used. Multiple drying regimes were attempted; (1) dried in the heated glassware drying cabinet for ten minutes, (2) dried under a nitrogen stream until dry, and (3) air dried.

Following these experiments, most drop-cast films were prepared via air drying or drying in the heated cabinet. The technique used is stated in the experimental relevant to sample preparation and discussed in the results and discussion sections. Additionally, some samples were sonicated for up to 20 minutes prior to drop-casting.

### 3.2.4 Determining the thickness of the drop-cast PEDOT:CS and PEDOT:HA film samples using atomic force microscopy (AFM)

#### Sample preparation

Drop-cast PEDOT:CS and PEDOT:HA samples were prepared by drop-casting a small volume (10  $\mu\text{l}$ ) of PEDOT:CS (1:1) and PEDOT:HA (1:1) aqueous dispersion on clean silicon wafers or clean glass slides and allowing to air dry for 30 minutes on the bench top, followed by 30 minutes in the heated cabinet. This gave silicon wafers and glass slides with small circular drop-cast films of PEDOT:CS and PEDOT:HA.

For the AFM measurements, a razor blade was used to cleanly score through the centre of the drop-cast films perpendicular to the substrate to form a straight edged valley through the centre of the sample down to the substrate surface, as shown in figure 3.1. By measuring the depth of the valley from the top to the substrate base, the thickness of the film may be determined.

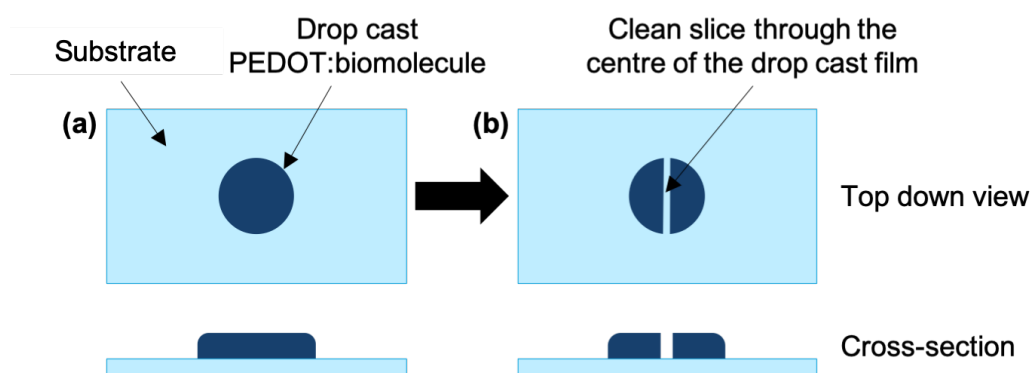


**Figure 3.1:** Preparing a PEDOT:biomolecule sample for AFM; (a) the drop-cast PEDOT:biomolecule film is sliced down the centre to give (b) a central valley that reaches the substrate which can be clearly seen in the sketch of the sample cross-section.

## Atomic force microscopy

AFM measurements were made using an Asylum Research (Oxford Instruments, Abingdon, UK) MFP-3D microscope in contact mode by Dr Jamie Blakeman at the University of Sheffield. MLCT cantilevers (Bruker AFM Probes, Camarillo, CA, USA) were used to capture height and deflection images using the D arm, which has a nominal spring constant of 60 pN/nm. Spring constants were confirmed to be within manufacturer's tolerances using the thermal tune method [188]. Scans were conducted across the prepared sample edge into the valley described in figure 3.1. The scan area was  $50\ \mu\text{m} \times 50\ \mu\text{m}$  at a resolution of  $256\ \text{line} \times 256\ \text{points}$ . Height images were processed in Gwyddion [189], with basic flattening presets applied. Cross sections of the height image were designated in three equally spaced parts of the height scan and the average heights of the sample, the substrate and the resulting difference calculated for each cross section.

### 3.2.5 Crosslinking films using EDC crosslinking

The method of EDC crosslinking PEDOT:CS and PEDOT:HA films was originally adapted from methods used by Tomihata *et al.* [120] for crosslinking CS and HA hydrogel films. The typical method for crosslinking the PEDOT:biomolecule films is as follows, however this was altered as required to use different concentrations of EDC solution. For example, an EDC crosslinking solution ( $0.26\ \text{mol dm}^{-3}$ ) was prepared by dissolving EDC (0.25 g, 0.0013 mol) in water ( $1.0\ \text{cm}^3$ , 0.0055 mol) and ethanol was added ( $4.0\ \text{cm}^3$ , 0.069 mol) to create a mixture of EDC solution and ethanol in a 20:80 ratio. One crosslinking mixture was prepared for each substrate with a PEDOT:CS or PEDOT:HA film.

The PEDOT:CS or PEDOT:HA films on substrates were then entirely submerged in the crosslinking mixture for typically 24 hours, however some samples were exposed to the crosslinking mixture for less time (see results and discussion). The substrates with the films on them were then carefully removed from the crosslinking mixture and rinsed in deionised water by submersion for up to  $3 \times$  five minutes with fresh water each time. It was at this point that there was an issue with delamination of the films, however those that did not delaminate were then air dried either in a heated cabinet for up to 24 hours, or air dried with no additional heat or ventilation for 24 hours.

Some samples were then dried further in the vacuum oven at  $50\ ^\circ\text{C}$  for 30 minutes to one hour, however this tended to lead to delamination of the films.

### 3.2.6 Electronic characterisation of PEDOT:CS and PEDOT:HA

For the characterisation of the electronic properties of PEDOT:CS and PEDOT:HA films, substrates prepared by colleagues, Nawal Alghamdi and Zahrah Alqahtani, were used. These substrates consisted of a glass base with five sets of gold contacts with a small channel down the middle of each (shown in figure 3.2). They were prepared following the method reported by Talal Althagafi [190].

To form a continuous film over the substrate channel, a small volume of the PEDOT:biomolecule aqueous dispersion of interest (10  $\mu\text{l}$ ) was drop-cast over a channel gap of the substrate as seen in figure 3.2. The samples were then slowly air dried on the bench top for up to 24 hours, but typically between 30 minutes and 2 hours. Following this, some samples were then dried further in the vacuum oven at  $50\ ^\circ\text{C}$  for 30

minutes to one hour, however this tended to lead to delamination of the films so was not repeated on all samples.

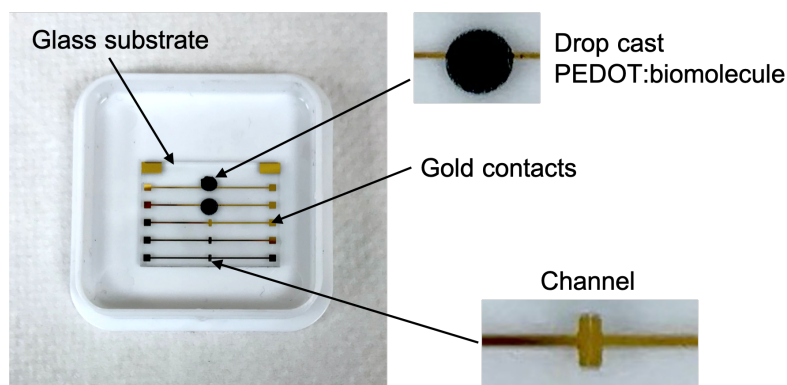


**Figure 3.2:** A photo of one of the substrates used during electronic testing of PEDOT:biomolecule samples with the gold contacts, channel, and substrate clearly highlighted. There are single drop-cast films of different samples over individual channels so each can be characterised.

Both uncrosslinked and crosslinked samples were tested for their conductivity. The crosslinked samples were crosslinked using the method outlined above. The concentration of the EDC solution used is reported with each specific sample in the results and discussion section of this chapter.

The current-voltage relationship of the PEDOT:CS and PEDOT:HA drop-cast films were determined by applying sweeps of potential differences across the sample (0 to +1 V, and -1 V to +1 V) using the OFET Analyzer (Keithley 2400 Source Meter) and recording the current. This set up is summarised in figure 3.3. These measurements were completed with the help of Nawal Alghamdi and Zahrah Alqahtani.

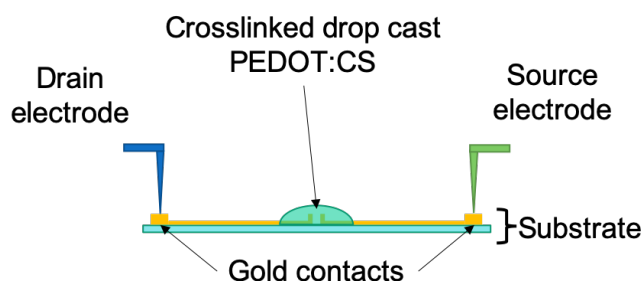


**Figure 3.3:** A schematic diagram of the experimental set up for electronic characterisation of PEDOT:biomolecule films; the source and drain electrodes are connected to the OFET Analyzer which applies the potential difference across the sample.

### 3.2.7 Proof of concept: OECT characterisation of PEDOT:CS and PEDOT:HA

For transistor characterisation, the PEDOT:CS film samples required crosslinking for testing. The samples were prepared on the same substrates as the above in the same way, and then crosslinked using the EDC crosslinking method outlined above.

To prove that PEDOT:CS could be used in an OECT, a tungsten wire gate electrode was introduced to the experimental set up used for the electronic characterisation as seen in figure 3.4. Phosphate buffered

saline (PBS, 0.1 M) solution was prepared from PBS tablets and was carefully pipetted (4  $\mu\text{l}$ ) onto the PEDOT:CS film to be used as the electrolyte, being sure that the PBS filled the gap between the gate electrode and the PEDOT:CS sample. Additional PBS was added 4  $\mu\text{l}$  at a time as required if the PBS evaporated.

The output characteristics of the PEDOT:CS OECT were measured by sweeping the potential differences between the source and drain from  $-0.8\text{ V}$  to  $+0.8\text{ V}$  in 0.1 V intervals using the OFET Analyzer (Keithley 2400 Source Meter) at gate voltages of  $-0.6\text{ V}$  to  $+0.6\text{ V}$  in 0.2 V intervals and the source-drain current and source-gate current was recorded. Again, these measurements were carried out with the help of Nawal Alghamdi and Zahrah Alqahtani.

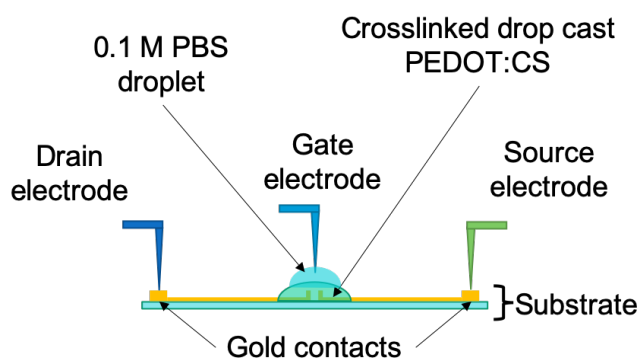


**Figure 3.4:** A schematic diagram of the experimental set up for transistor characterisation of PEDOT:biomolecule films; the source, drain, and gates electrodes were all connected to the OFET Analyzer. The transistor is gated through PBS as the electrolyte.

### 3.3 Results and discussion

The aim of this project is to develop a biocompatible, biodegradable, and mechanically appropriate OECT device that with further development could be suitable for use in the spinal cord and used in the treatment of SCIs. Such an OECT device must contain an organic electronic material (OEM) that is biocompatible, biodegradable, mechanically appropriate to the elastic modulus of the spinal cord, and conductive. PEDOT complexed with CS and PEDOT complexed with HA were chosen as candidates to fill these requirements.

#### 3.3.1 Synthesis of PEDOT:CS and PEDOT:HA by oxidative polymerisation

As discussed in the introduction to this chapter, alternative PEDOT complexing polymers could offer biocompatibility, biodegradability, and more favourable mechanical properties to an OECT device for implantation into the body than an OECT device based on PEDOT:PSS. For this reason, CS and HA were chosen as potential alternatives to PSS to act as a counter-ion for PEDOT for use in an OECT. Mantione *et al.* [168] reported their synthesis in 2016, however little further work has appeared in the literature on these materials. An introduction to CS and HA can be found in chapter 1.

Mantione *et al.* [168] assessed the biocompatibility of PEDOT:CS and PEDOT:HA and showed that they

displayed no cytotoxicity towards any of the cell lines tested. Their work also showed that the materials were functionally biocompatible with SH-SY5Y neuroblastoma cells and the human astrocytoma cell line CCF-STTG1, and had additional neuroregenerative properties compared to PEDOT:PSS which would be useful in the case of treating injuries to the CNS. PEDOT:CS was also shown to have a neuroprotective effect on some SH-SY5Y cells when experimentalists tried to trigger hydrogen peroxide induced cell death. This evidence combined with the fact that CS and HA are both glycosaminoglycans that naturally occur in the body, especially in the extracellular matrix (ECM) of the CNS, shows that they are biocompatible. This allows the first requirement of biocompatibility to be fulfilled for the OEM in the OECT. In addition, CS and HA are studied in chapter 5 as materials to form crosslinked hydrogels that could be appropriate for use in the CNS.

Initially, using the Mantione *et al.* [168] methodology as a guide, a 2% (w/w) aqueous dispersion of PEDOT:CS in a 1:1 ratio by mass was synthesised. Upon observing the reaction over the course of the 48 hour stir, the colour of the solutions changed from a transparent, slightly yellow colour to a dark blue-black dispersion as seen in figure 3.5. In the first hour of the reaction, the solutions changed from transparent and slightly yellow to cloudy yellow to opaque grey. Over the following 24 hours, the solution changed to the characteristic blue-black colour of PEDOT:PSS indicating the presence of conducting PEDOT in the reaction mixture. However an additional 24 hours of stirring to bring total reaction time to 48 hours was required as Mantione *et al.* indicated that full conversion of the reactants occurred over 48 hours.



**Figure 3.5:** An example of a PEDOT:CS aqueous suspension displaying a clear dark blue-black colour, indicating the presence of conducting doped PEDOT.

It was also observed that over the course of the reaction, the viscosity of solution changed. Over the first hour of stirring, there was a noticeable increase in solution viscosity making the solution difficult to stir with the magnetic stirrer. After another hour of stirring, the viscosity was observed to decrease to that similar of water in appearance, and the resulting dispersion after 48 hours of stirring appeared to have a similar viscosity. These observations match those made by Mantione *et al.* [168] who prepared similar PEDOT:biomolecule dispersions and saw decreasing viscosity over a 48 hour reaction time as well as a colour change over the course of the reaction from clear to dark blue.

The initial increase in viscosity of the reaction solution was likely the result of a decrease in pH that caused the protonation of the carbonyl group on CS. This would have increased the number of intermolecular hydrogen bonds between CS molecules in the solution, resulting in the formation of a physical hydrogel-like structure. The decrease in viscosity of the solution over the course of the reaction could then be attributed to the disruption of these intermolecular hydrogen bonds as the negative charges move to

stabilise the positively charged PEDOT species instead of forming intermolecular hydrogen bonds. This was suggested by Mantione *et al.* [168] who postulated that as the reaction proceeds, the negative charges on the CS molecules move to stabilise the positively charged PEDOT species produced by the polymerisation reaction in solution. In turn, this decreases the amount of CS available to form hydrogen bonds thus resulting in the decreasing viscosity over the course of the oxidative polymerisation reaction. This assertion was supported in the Mantione *et al.* paper [168] by evidence of similar observations of decreasing viscosity in a dispersion polymerisation reaction when preparing poly(vinyl acetate) latexes using poly(vinyl alcohol) as stabilizer [191].

PEDOT:HA in a 1:1 ratio by mass was also prepared in the same way and similar observations were made. The only difference was that the initial HA solution was much more viscous than the CS solution of the same concentration. The viscosity of the PEDOT:HA reaction solution decreased over the course of the polymerisation to the same water-like consistency as the PEDOT:CS aqueous dispersion.

As both PEDOT:CS and PEDOT:HA 1:1 aqueous dispersions were successfully synthesised, other ratios of PEDOT to biomolecule were then produced. Multiple ratios of PEDOT:CS (1:1, 1:2, 1:3, and 1:4) and PEDOT:HA (1:1, 1:2) were prepared so the effect of the amount of biomolecule in the suspension could be examined later. This was achieved by keeping the total mass of EDOT monomer and CS or HA constant. This meant that all the resulting PEDOT:CS or PEDOT:HA aqueous suspensions were the same concentration of 2% (w/w). The amount of ammonium persulfate (APS) was altered in conjunction with the amount of EDOT, so the ratio of EDOT to APS was constantly 1:1.5 molar equivalents. Mantione *et al.* [168] did not specify whether the dispersion concentration was kept constant at 2% (w/w) for the various ratios of PEDOT:biomolecules. Comparisons between PEDOT:CS/PEDOT:HA of ratios other than 1:1 and the literature samples must be made carefully.

The reactions of the various different ratios of PEDOT to CS or HA proceeded similarly to the 1:1 ratios with comparable colour changes and viscosity changes over the course of the 48 hour reaction time. In spite of this, it was noted that the colour changes described in the initial 1:1 syntheses appeared to happen more slowly with increasing concentration of biomolecule. This was likely to be a result of the changing mass of APS, which acts as the initiator in the reaction, that scales with the mass of EDOT monomer. Less APS initiator will result in fewer EDOT monomer units being oxidised to form the radical cations which combine and deprotonate to give a dimer. This oxidation, combination, and deprotonation process repeats to give longer chains, and the polymerisation continues. Due to a lower level of this initiator, the polymerisation reaction will not proceed at the same rate thus the colour change indicating the presence of conductive PEDOT will not happen as quickly. Additionally, the slower colour change may be due to the increased biomolecule concentration increasing the viscosity of the reaction solution which makes the mixing of the reactants the limiting factor in the rate of reaction as opposed to less initiator. It should be noted that in the case of the PEDOT:CS samples in a 1:4 ratio, the reactions were left to stir for 96 hours, as opposed to the usual 48 hours. This was to ensure that the reactions were complete as the colour changes indicating reaction completion did not occur over the first 24 hours.

## Purification

Following multiple successful syntheses of PEDOT:CS and PEDOT:HA aqueous dispersions, some discolouration was observed in a number of samples; some were orange and some were a yellow/green colour,

see figure 3.6. The discoloured samples also tended to not be fully suspended - i.e. the solid particles sank. This was not an expected result, and Mantione *et al.* did not report such observations.



(a) Orange discolouration in the aqueous phase. (b) Yellow/green discolouration in the aqueous phase.

**Figure 3.6:** PEDOT:CS aqueous samples that showed discolouration in the aqueous phase, as well as solid particles that are no longer suspended and have settled at the bottom of the sample vial.

Both the orange and green colours in the aqueous phase of the samples could be explained by an excess of iron ions from the iron (III) sulfate that was used as a catalyst for the oxidative polymerisation reaction. Iron (II) sulfate and iron (III) sulfate can give green and orange solutions in water, respectively.

Firstly, all the syntheses were checked that the correct amount of each reagent was used. New syntheses of PEDOT:CS 1:1 were undertaken using an even smaller catalytic amount of iron sulfate and still showed discolouration. Following this, new syntheses utilising fresh reagents straight from the manufacturer were unsuccessful as these new samples also saw discolouration in the aqueous phase implying that the issue was not due to old reagents. Following these failed experiments, a purification step following synthesis was introduced. Multiple papers reporting the syntheses of PEDOT complexed with biomolecules used similar oxidative polymerisation methodologies but followed up the synthesis with a purification step [183–185, 187, 192].

Initially, a washing regimen based on work by Wang *et al.* [187, 192] was used. In the Wang *et al.* paper [187], PEDOT:HA aqueous suspensions were synthesised using an oxidative polymerisation method by adding APS to a HA solution containing EDOT monomer. At the completion of the reaction, the aqueous suspension of PEDOT:HA was centrifuged with an equal volume of acetone and the sediment retained. The sediment was then washed and centrifuged with ethanol and then water, three times with each solvent. The sediment was then dried in a vacuum oven to yield a dry PEDOT:HA powder. For the PEDOT:CS and PEDOT:HA synthesised here, this purification methodology was adapted. This differed from the method given in the paper due to the lack of availability of a centrifuge. Up to half of each of the discoloured PEDOT:CS or PEDOT:HA aqueous dispersion samples were kept aside as a comparison point for each washed sample. The PEDOT:CS or PEDOT:HA aqueous dispersion was washed three times with acetone then ethanol. To make sure that the samples were thoroughly mixed and separated, each wash step consisted of vigorous shaking for at least ten minutes, and left to settle out for as long as required to give a sediment layer at the bottom of the vial. As well as the solid blue/black PEDOT:CS sediment, a fine white stringy material was also seen in samples. This material was suspected to be CS. Additionally, there was always some PEDOT material that did not fully settle out into the base of the vial and thus each wash step resulted in a loss of a small amount of PEDOT material when pipetting

off the liquid phase. Despite this, it appeared that the washing steps were removing the discolouration as exemplified in figure 3.7 where the discolouration in the spent solvents involved in the washes get progressively less discoloured with each washing step. This was mirrored by less discoloured samples through the washing.



**Figure 3.7:** The solvents collected from each washing step from a typical sample of discoloured PEDOT:HA aqueous suspension. The vial on the left contains the combined acetone liquid phases from the first two washes. The yellow discolouration is very prominent in this solvent. The centre sample contains the collected solvent following the third acetone wash which is a much paler yellow colour. The vial on the right contains the ethanol collected during the ethanol washes where no discolouration can be seen.

Following the ethanol washes, the sample was filtered and the solid PEDOT:CS or PEDOT:HA dried. The solids were then resuspended in water to give a 2% (w/w) aqueous dispersion. The resuspension of the PEDOT:biomolecule was challenging. The PEDOT:CS and PEDOT:HA solids tended to clump together and turn into a large gelatinous aggregate (roughly 1 to 2 cm in diameter) when exposed to water. To try and distribute the solids, the samples were shaken up to try and break up the large aggregations of material. This was successful to some extent in that it broke the larger aggregates into smaller pieces, and the PEDOT:CS and PEDOT:HA samples resembled aqueous dispersions more than previous. An additional sonication step was used to ensure the aggregates were fully distributed throughout the samples to give a 2% (w/w) aqueous dispersion. The discolouration was no longer present in the PEDOT:CS and PEDOT:HA aqueous suspensions following these washing steps, however the issues with loss of PEDOT material when pipetting off the liquid phase, and the presence of the white material during the ethanol wash meant that it was necessary to take another approach to purification that resulted in less loss of product and was simpler.

Dialysis of PEDOT:biomolecules aqueous suspensions was a common purification technique amongst the literature [183–185]. The popularity of the technique combined with its ease meant that dialysis was used as a purification step on the discoloured PEDOT:CS and PEDOT:HA samples. Aqueous dispersions of PEDOT:CS and PEDOT:HA were dialysed (10K MWCO) in deionised water for 96 hours. The water was changed four times during this period. The SnakeSkin dialysis tubing was chosen as it required no pre-treatment before use, so the aqueous dispersions could just be transferred directly into the tubing and immersed in water. Following the dialysis, the PEDOT:CS and PEDOT:HA aqueous samples were transferred into glass vials and it was clear that all the discolouration in the PEDOT:CS and PEDOT:HA samples was no longer present. The dialysis step allowed the small iron species, that were suspected to cause the discolouration, to move out of the sample whilst the PEDOT:CS and PEDOT:HA remained in the dialysis tubing. One drawback of this method of purification was that the solid particles in the

aqueous dispersions tended to aggregate, and so a sonication step was introduced to break down any larger aggregates prior to storage. The ease and effectiveness of the dialysis method followed by sonication was chosen as the purification methodology for all PEDOT:biomolecule aqueous suspensions.

### 3.3.2 Forming films of PEDOT:CS and PEDOT:HA

Through careful choice of counter-ion, biomolecule-based, biocompatible PEDOT:PSS alternatives were synthesised and purified. To assess the materials for their electrical properties and for their end use in an OECT, the PEDOT:CS and PEDOT:HA were required to be formed into films. The following section discusses film formation and the methods used to achieve a uniform film for testing. Film formation for PEDOT-based materials is important. Typically in a bioelectronic device, a thin film of OEM forms the channel through which a current is modulated. It is important that this thin film is homogeneous and continuous in nature to give the best electronic properties.

Usually to get a thin film of PEDOT:PSS, spin-coating is used. Spin-coating is used to coat a substrate by dropping a small volume of material onto the surface, and the sample is spun and the centrifugal force spreads the material to give a film. Any excess material flies off the substrate as it spins, and if the solvent is volatile enough, a dry film is given. Often the films are heated to drive off any excess solvent still present in the film. This method is used as it can control the thickness of the film produced by simply altering spin speed, and it is very fast and facile. Spin-coating can achieve homogeneous continuous films that are ideal for testing and end uses as they are reproducible.

Drop-casting is an alternative method of film formation that involves simply dropping a volume onto the surface that you wish to form a film on, and allowing it to dry over time. This drying step may be controlled over set temperatures, or make use of a vacuum to speed up drying. Drop-cast films are typically harder to reproduce exactly. Drop-casting forms thicker films than spin-cast films as more material is involved in the film formation, however there is evidence in some cases that drop-cast films perform better in OECT devices than spin-cast films [193]. This is due to the volumetric nature of OECT responses where doping and dedoping of the organic electronic material occurs across the entire volume of the channel (unlike in EGFETs where doping/dedoping only occurs at interfaces). In an OECT, a thicker channel yields larger transconductances than thinner channels [194].

Another consideration for film formation was crosslinking. For use in an OECT, there is a requirement for the PEDOT:CS and PEDOT:HA films to be crosslinked as the OEM is in direct contact with an electrolyte. If the films are not crosslinked in some way, the PEDOT:CS and PEDOT:HA will dissolve and resuspend leaving delaminated uneven films. The crosslinking also relates to the lifetime of the film. Crosslinking is extremely important with regards to the degradation of the PEDOT:biomolecule for use in the biodegradable OECT device. The type and extent of crosslinking allows control of the degradation of the films. Mantione *et al.* [168] formed crosslinked spin-cast, thin films of PEDOT:CS, PEDOT:HA, and PEDOT:Hep using 3-glycidoxypropyltrimethoxysilane (GOPS) as the cross-linker. The use of GOPS is popular in PEDOT:PSS crosslinking due to the facile nature of the method and the strong bonds formed between the sulfonate groups on PSS and the GOPS molecule [53, 150, 195, 196]. In spite of the popularity of crosslinking using GOPS, the PEDOT:biomolecule samples here were not crosslinked using this method as the crosslinks that are formed are not easily degradable. Instead EDC crosslinking was used as the resulting ester crosslinks can be hydrolysed leading to degradable films.

### Spin-cast PEDOT:CS and PEDOT:HA films

The first attempts to form PEDOT:CS and PEDOT:HA thin films were based on the methods of Mantione *et al.* [168]. A small volume of 2% (w/w) aqueous suspension of PEDOT:CS 1:1 was carefully pipetted into the centre of a clean glass substrate and spun at 1000 rpm for 60 seconds. The coated glass substrate was then allowed to air dry for 30 minutes, followed by one hour in a vacuum oven at 50 °C. Mantione *et al.* [168] used these same parameters to form thin films of PEDOT:CS and PEDOT:HA on glass coverslips, however they added GOPS as a crosslinker, dodecylbenzenesulfonic acid (DBSA) to improve film formation, and ethylene glycol to enhance conductivity to the aqueous suspensions.

In the case of the experiments undertaken here, no continuous thin film was formed. From initial inspections, it was clear that no continuous film had formed, and this was confirmed under inspection under the microscope where only a few single particles of PEDOT:CS could be seen on the glass substrate. It is likely that the lack of additives to the aqueous dispersion changed the film forming properties compared to those of Mantione *et al.* [168]. As the pristine properties of the PEDOT:CS films synthesised here were to be assessed, no crosslinker or other additives were added to the spin-coating material. Furthermore, the solvent used for spin-coating was water which could also have supplemented to the poor film formation as water is not very volatile and thus does not quickly evaporate on spinning to leave behind the solid film. The high water content also contributed to the low viscosity of the PEDOT:CS aqueous dispersion as well as unfavourable interactions with the hydrophobic glass surface. All of these factors resulted in the failure of PEDOT:CS spin-coating in comparison to the films prepared by Mantione *et al.* [168]. It should be noted that Mantione *et al.* did not seem to address the addition of ethylene glycol, GOPS crosslinker, or DBSA with regards to the film formation, or later the conductivity.

As a result of these issues with spin-casting, an alternative casting approach was taken.

### Drop-cast PEDOT:CS and PEDOT:HA films

An alternative approach was taken by drop-casting. Drop-casting offered a route to forming a continuous film more appropriate for testing, but formed thicker films. There was some variation in the appearance of the drop-cast films with the drying technique used. A set of drop-cast films were prepared on the same glass slide using different drying techniques allowing comparison of the methods on the resulting film, and this slide is shown in figure 3.8.

As expected, all the films produced experienced the coffee ring effect [197] to some extent. The effect is so called as it is often seen when a coffee spillage dries. The coffee ring effect describes how aqueous suspensions of solid particles move via capillary flow during evaporation of the aqueous phase, forming a ring-shaped deposit around the edge of the droplet. The capillary flow is triggered by the differing rates of water evaporating at different points on the droplet. This flow pulls the small particles to the outer edge of the sample causing a build-up of particles at the edge of the sample upon evaporation. As both the PEDOT:CS 1:1 and 1:2 samples were aqueous suspensions of solid particulates, the coffee ring effect was seen. It was noted that the only observable difference between all the films of PEDOT:CS 1:1 and PEDOT:CS 1:2 was that the 1:1 ratio films appeared darker in colour. This was attributed to the greater quantity of PEDOT in these samples relative to the CS, as both samples were of 2% (w/w) solids.

It appeared that both air drying and heating the samples caused the largest gathering of material on the

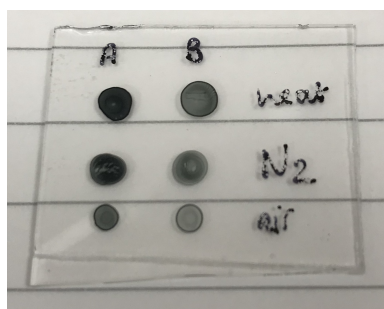


**Figure 3.8:** Drop-cast films of PEDOT:CS 1:1 (column A) and PEDOT:CS 1:2 (column B), dried using different techniques. The top row of films were dried for ten minutes in the heated glassware drying cabinet, the middle row of films were dried under a nitrogen stream, and the bottom row of films were air dried on the bench top for one hour.

outer edge of the film, whereas the using a stream of nitrogen during drying avoided this ringing effect. This is likely due to the nitrogen stream moving the particles of PEDOT:CS around during drying, not allowing them to gather at the film edges giving a more even appearance to the films. On the other hand, the centre of the PEDOT:CS 1:1 and PEDOT:CS 1:2 films both started to pull away from the substrate in the nitrogen dried samples, which would not be ideal for testing purposes. This delamination occurred in a number of PEDOT:CS test films that were nitrogen dried. It is suggested that once the majority of the water had been driven out of the sample by the nitrogen flow, the force of the gas on the damp sample could have caused partially adhered particles on the substrate surface to be pulled off leading to delamination as the film dried further. In addition, the nitrogen dried films did not appear to be as homogeneous in the centre of the films as the heated or air dried films which can be seen in figure 3.8. As homogeneity is considered important for a thin film in an OECT, as well as the delamination problems, the nitrogen drying step was deemed inappropriate.

Following these experiments, most drop-cast films were prepared via air drying or drying in the heated cabinet. There were also some issues with delamination of PEDOT:CS and PEDOT:HA drop-cast samples using these drying techniques. Delamination occurred more often with the samples dried in the heated cabinet. For this reason in later experiments the drying technique was carefully chosen to give the film the best chance to avoid delamination and cracking, and the methods used for the sample preparations are indicated clearly in the experimental methods. It was observed that in a number of films appeared lumpy and heterogeneous, and these poor quality films tended to be formed from an aqueous dispersion that had been stored for a long time prior to casting. The poor film quality was suspected to be due aggregation of PEDOT:CS and PEDOT:HA particulates during storage. Prior to casting, a sonication step was introduced to re-disperse any aggregates present in the PEDOT:biomolecule aqueous dispersions. The sonicated samples were then drop-cast and the appearance of the films improved.

Additionally, it was noted that PEDOT:HA drop-cast films all tended to take longer to dry compared to PEDOT:CS drop-cast films. This was probably because that HA has a greater capacity to swell in water than CS, and thus this hydrophilicity causes the films to hold onto water better than CS.

In future development work, a surfactant, such as DBSA, could be added to the aqueous suspensions when casting the films to improve the quality of the films, in a similar way to the addition of DBSA to PEDOT:PSS aqueous suspensions to give higher quality films. Mantione *et al.* [168] utilised DBSA when spin-casting the PEDOT:CS, PEDOT:HA, and PEDOT:Hep films in their experiments.

One drawback of using a drop-casting method was that the resulting films appeared to be fairly thick, especially compared to spin-cast thin films of other materials. This was of concern for electronic testing purposes as the sheet resistance was to be the value used to assess the conductivity of materials. The sheet resistance relies on the assumption that the material being tested is a thin film thus the thickness of PEDOT:CS and PEDOT:HA drop-cast films needed to be determined. For the purposes of these experiments, the thin film must be significantly smaller than the width of the channel ( $30\ \mu\text{m}$ ) used in the sheet resistance testing.

### Determining the thickness of drop-cast PEDOT:CS and PEDOT:HA films using atomic force microscopy

To understand the effect thickness of the PEDOT:biomolecule films had on properties later in these studies, atomic force microscopy (AFM) was used to determine the thickness of the films.

Small films of PEDOT:CS 1:1 and PEDOT:HA 1:1 were drop-cast on clean silicon wafers and dried. The films were prepared so they resembled films that would be used in electronic testing which is discussed later in this section. This meant that the films were very small in area. The films were carefully sliced into with a very sharp razor blade to give a clean step through the centre of the films to the glass substrate, as described in the section 3.2.4. Scans of the PEDOT:CS and PEDOT:HA samples were performed on the glass substrate and the silicon substrates. The substrate type made no difference to the final data, and the two types were only used due to availability.

Three horizontal profiles were taken from each PEDOT:CS and PEDOT:HA sample scan to give three cross-sections of the step created by the razor blade. The difference between the mean height of the sample and the mean height of the substrate in the horizontal profile gave the thickness of the film, and from the three thicknesses a mean thickness was generated. Two typical horizontal profiles of each data set can be seen in figures 3.9 and 3.10.

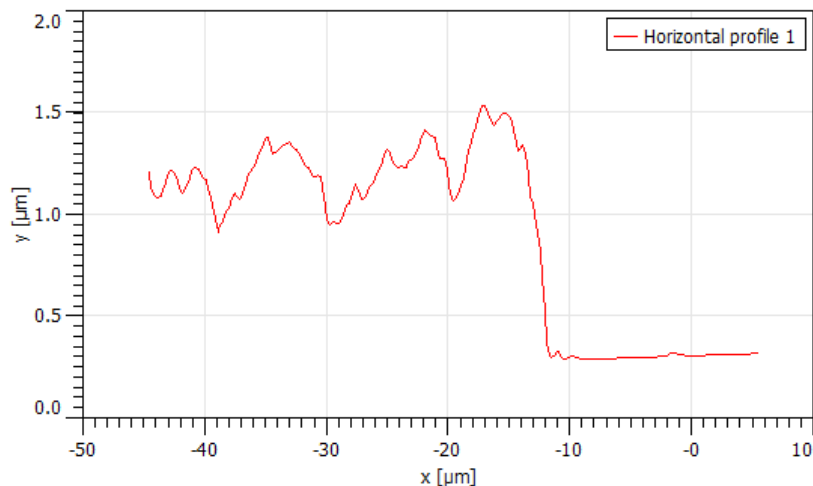


**Figure 3.9:** Horizontal profile of the PEDOT:CS 1:1 drop-cast film on silicon taken using AFM. The large step in the profiles shows the large step between the sample film surface and the substrate. Two more horizontal profiles for the sample were taken at different points to generate a mean film thickness.

The mean thickness  $\pm$  standard deviation of the PEDOT:CS (table 3.3) and PEDOT:HA (table 3.4) sam-

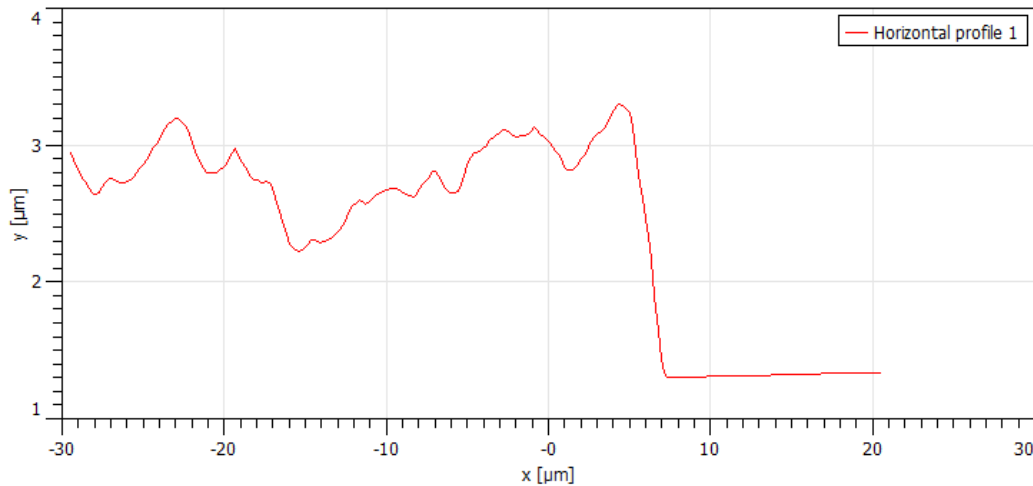


**Figure 3.10:** Horizontal profile of the PEDOT:HA 1:1 drop-cast film on glass taken using AFM. Again, two more horizontal profiles for the sample were taken at different points to generate a mean film thickness.

**Table 3.3:** Horizontal profile data for PEDOT:CS 1:1 drop-cast film

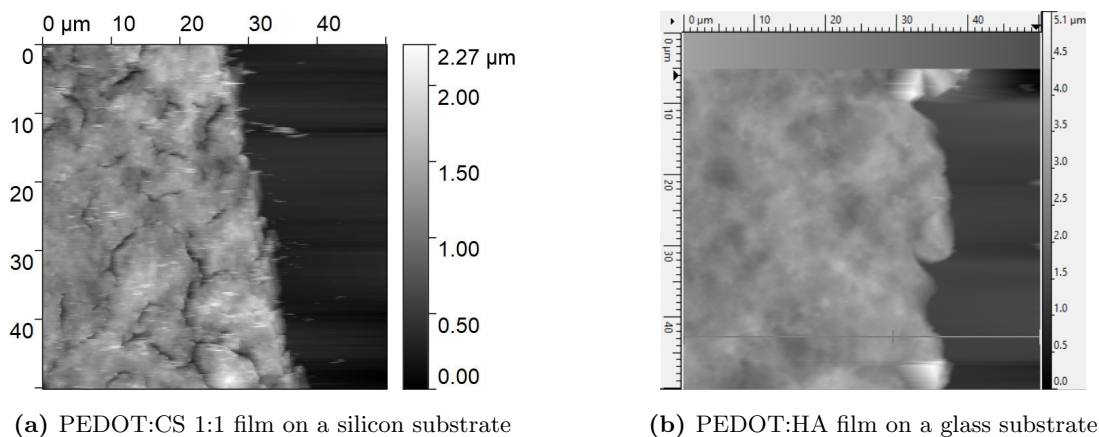
Horizontal profile	Mean sample height / nm	Mean substrate height / nm	Difference / nm
1	1217	301	916
2	1273	210	1063
3	1180	376	804

ples were  $928 \pm 106$  nm and  $1469 \pm 47$  nm, respectively. No mention of thickness for any of the PEDOT:glycosaminoglycan spin-coated films was found in the Mantione *et al.* paper [168], so no comparison could be made. From these data, it was clear that there was a marked difference in film thickness between PEDOT:CS and PEDOT:HA. As no vacuum oven was used to fully dry the films it was likely that some water still remained in the samples leading to some swelling. HA is highly hydrophilic and may not have dried out as completely as the PEDOT:CS leading to an increase in film thickness. This was supported by observations during data collection where in one sample, a small amount of PEDOT:HA was scraped from the surface of the PEDOT:HA during a scan. This also suggests that PEDOT:HA was a soft material, however no quantifiable data were collected at this time.

Additionally, height images of the films surfaces (figure 3.11) were captured and a clear difference in morphology could be seen between the two. The PEDOT:CS film appeared drier and contained small cracks over a rough surface. On the other hand, the PEDOT:HA film appeared more homogeneous and was suspected to not be as dry as the PEDOT:CS film lending it a swollen appearance, which lent support to the suggestion that the PEDOT:HA film was more hydrated than the PEDOT:CS film. Nevertheless, the height of the films were found to be around 3% of the width of the channels used in sheet resistance testing and thus could be considered thin films.

**Table 3.4:** Horizontal profile data for PEDOT:HA 1:1 drop-cast film

Horizontal profile	Mean sample height / nm	Mean substrate height / nm	Difference / nm
1	2790	1321	1469
2	2797	1271	1526
3	2829	1417	1412

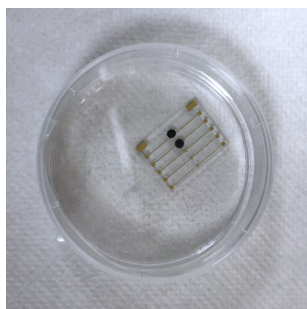
**Figure 3.11:** Image generated by AFM on the PEDOT:CS 1:1 and PEDOT:HA drop-cast films on silicon and glass substrates respectively. On the left is the rough film surface, and on the right (black) is the substrate.

### Crosslinking drop-cast PEDOT:CS and PEDOT:HA films

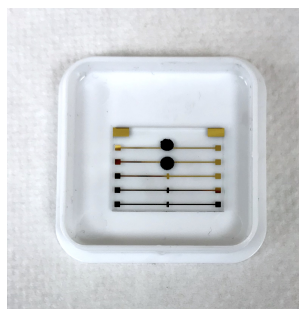
Following the successful formation of the PEDOT:CS and PEDOT:HA films, the next stage in creating a biocompatible, biodegradable OECT device suitable for use in the spinal cord was to crosslink the PEDOT:CS and PEDOT:HA. A crosslinking step is important on two levels; firstly crosslinking is required to secure the PEDOT:CS and PEDOT:HA in a film when it comes in contact with aqueous solutions, and secondly, the crosslinking is a major consideration in the degradation of the PEDOT:CS and PEDOT:HA and can be used to ensure a controlled degradation.

OECT devices function via gating through an electrolyte. CS and HA are water soluble thus a crosslinking step is required so that the PEDOT:CS and PEDOT:HA do not start to dissolve and disintegrate when used in an OECT. Crosslinking steps are common in PEDOT:PSS devices, often using GOPS, to form insoluble films [53, 150, 195, 196]. GOPS crosslinking forms strong insoluble films however in the case of the work presented here, the aim was to create degradable OECT device, and thus another crosslinking method was required.

Here, EDC crosslinking was chosen as the crosslinking method. EDC crosslinking is explained in more detail in chapter 1, however to summarise EDC crosslinking mediates the formation of ester bonds between carboxylic acid groups and hydroxy groups on the CS and HA molecules. These ester bonds are hydrolytically degradable and thus ensure degradability of the PEDOT:CS and PEDOT:HA in the OECT. The simple degradation route of EDC crosslinked materials also allows easier study of this degradation, as the hydrolysis of the ester bonds requires no enzymes or other materials. The EDC molecule does not form part of the crosslinks, and any spent EDC is washed away as a by-product following crosslinking.



(a) Submerged in a crosslinking solution.



(b) Crosslinked sample following the rinse step.

**Figure 3.12:** PEDOT:CS 1:1 drop-cast films on the substrates used for electronic characterisation, (a) during submersion in the crosslinking solution, and (b) following the rinse step after crosslinking, thus its damp appearance.

Additionally, EDC crosslinking is the crosslinking method of choice for the CS and HA hydrogels discussed in chapter 5. These hydrogels could be used as substrates for the OECT devices, intended to improve the biocompatibility and the mechanical properties of the device. The consistency of crosslinking method in both the OEM of the OECT and the hydrogel that may act as the substrate in the spinal cord could make synthesis simpler in future.

PEDOT:CS and PEDOT:HA films were crosslinked by submerging the films in solutions of EDC in an 80:20 mixture of ethanol and water for 24 hours during initial experiments. This crosslink method was consistent with the method used for the CS and HA hydrogels in chapter 5. When the drop-cast PEDOT:CS and PEDOT:HA films were removed from the crosslinking solution, they were immersed in water as a rinse step to remove any unreacted EDC and by-products. This step also acted as a test to see whether crosslinking was successful, as an uncrosslinked film would immediately start to delaminate and disperse through the water, whereas a crosslinked PEDOT:CS or PEDOT:HA film did not. Figure 3.12 shows the crosslinking process on PEDOT:CS 1:1 drop-cast films on the substrates used for electronic testing (see section 3.3.3).

It was considered that 24 hours of crosslinking time may not be necessary for the small amount of PEDOT:CS and PEDOT:HA in the films. The 24 hour crosslinking period was originally chosen to reflect the EDC crosslinking method developed for the CS and HA hydrogels covered in chapter 5. These hydrogels contained a significantly greater mass of CS or HA than the small amount present in a PEDOT:CS or PEDOT:HA drop-cast film and thus a longer crosslinking period was appropriate. An experiment was undertaken where a drop-cast PEDOT:CS 1:1 film was submerged in a EDC solution-ethanol mixture as outlined in the general experimental method (section 5.2.3), but instead of leaving immersed for 24 hours, the sample was immersed for only two hours. Concurrently, another PEDOT:CS 1:1 drop-cast film was submerged in an equivalent crosslinking solution for 24 hours. Both samples were removed from their crosslinking solutions following the assigned crosslinking periods. As expected, upon rinsing, the 24 hour sample did not dissolve and rinsing was completed, demonstrating successful crosslinking. The two hour sample was submerged in water for rinsing and also did not dissolve or delaminate in any way. This implied that two hours was ample time for crosslinking to occur in these small film samples. This was not quantitative proof of crosslinking but provided evidence that the 24-hour crosslinking period may not be necessary, which would speed up the processing of these films in the future. To gain quantitative insight into the crosslinking, IR spectroscopy could be used to identify

the formation of crosslinking ester bonds in the CS and HA portions of the PEDOT:biomolecule films. By following the height of the emerging ester peak in the IR spectra over the crosslinking period, this technique could also be used to probe the speed of crosslinking and whether the full 24-hour crosslinking period were necessary.

In the majority of cases, PEDOT:CS and PEDOT:HA drop-cast films were crosslinked in EDC solutions of high concentrations (typically  $0.26 \text{ mol dm}^{-3}$ ,  $1 \text{ cm}^3$ ). This would have provided a great excess of EDC and may have led to incomplete crosslinks giving dangling ends with incomplete formation of ester bonds. This would likely alter the degradation time, and thus in future experiments, examination of the effect of EDC concentration in the crosslinking of the PEDOT:CS and PEDOT:HA films should be completed, especially with regards to the effect on degradation and electronic properties.

The choice of EDC crosslinking for the PEDOT:CS and PEDOT:HA begins to fulfil the requirement of a degradable OECT device. The degradation of PEDOT:CS and PEDOT:HA will not be examined in this chapter, but will be covered in chapter 4.

### 3.3.3 Electronic characterisation of PEDOT:CS and PEDOT:HA

Previously, the synthesis and formation of films of PEDOT:CS and PEDOT:HA have been discussed. As these materials are for use in a bioelectronic device, the electronic properties are important. For quantifying the properties of a thin film of electronic material, sheet resistance is a useful parameter to measure to give the resistance of the film. A smaller sheet resistance indicates a more conductive material.

The aim of this particular work was to show that PEDOT:CS and PEDOT:HA were conductive, and therefore were candidates for use in an OECT. Additionally, by quantifying the sheet resistance, comparisons could be made between PEDOT complexed with CS and with HA and the effect of crosslinking the PEDOT:CS and PEDOT:HA films on the electrical properties could be probed. To show that PEDOT:CS and PEDOT:HA films are electronic conductors, there was a requirement to show linear Ohmic responses. This means that the responses must follow Ohm's law, given by equation 3.1 where  $R$  is the resistance,  $V$  is the voltage, and  $I$  is the current. In the case of voltage-current plots, this means that they should be linear. These plots could then be used to determine the sheet resistance of a film and thus give a quantitative value for comparison with PEDOT:PSS and with each other.

$$R = V/I \tag{3.1}$$

The choice of substrate for measuring the sheet resistance was standard for the method of measurement used in Sheffield. (The substrates were prepared in Sheffield by Nawal Alghamdi and Zahrah Alqahtani following methods outlined by Talal Althagafi [190].) The substrates consisted of gold electrodes patterned onto glass substrates, as seen in figures ?? and 3.2. The channel of these substrates had a width of 1 mm and a length of  $30 \mu\text{m}$  giving a width to length ratio ( $W/L$ ) of 33.3.

Initially, uncrosslinked PEDOT:CS 1:1 samples were prepared by drop-casting PEDOT:CS aqueous suspension over the channel area of the substrate and the electronic properties probed. (electronic properties of the PEDOT:CS film was determined by applying sweeps of potential differences across the sample (typ-

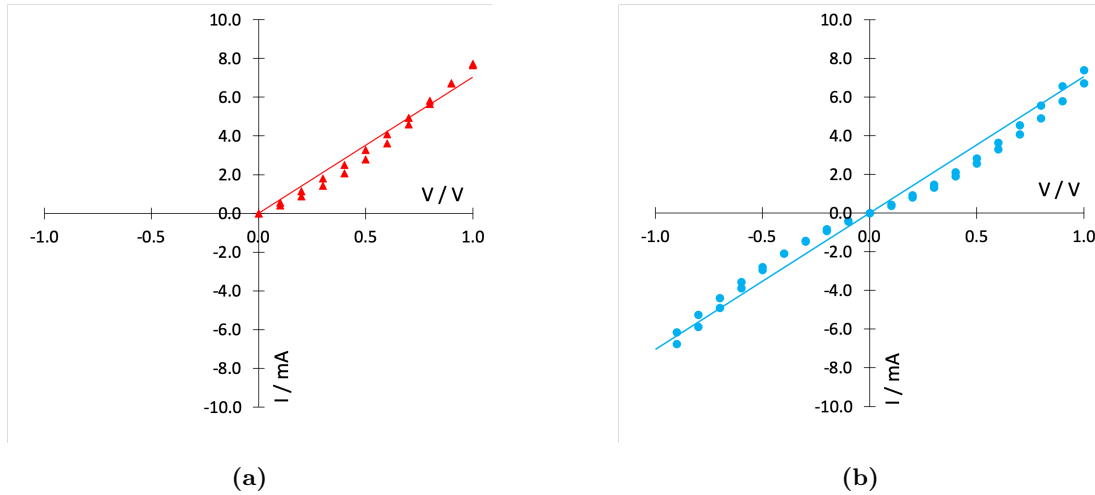


**Figure 3.13:** I/V plots for uncrosslinked PEDOT:CS 1:1

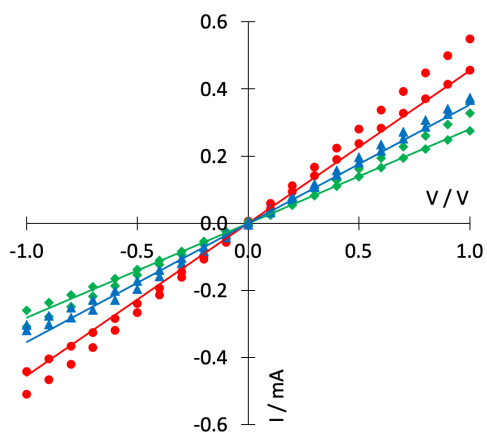
ically from  $-1$  V to  $+1$  V) and measuring the current.) The results showed linear Ohmic behaviour in the voltage-current plots (figure 3.13) and confirmed that PEDOT:CS 1:1 was conductive. PEDOT:CS and PEDOT:HA films had previously been shown to be conductive by experiments by Mantione *et al.* [168].

Following this confirmation of conductivity, a library of other samples were tested using this same method and gave Ohmic responses, see figures 3.14, 3.15, and 3.16. Note there was some slight variation in drying techniques between samples (see experimental section 3.2.3). In addition, crosslinked samples were tested. These samples were drop-cast and dried, following by crosslinking, as outlined in the experimental methods.

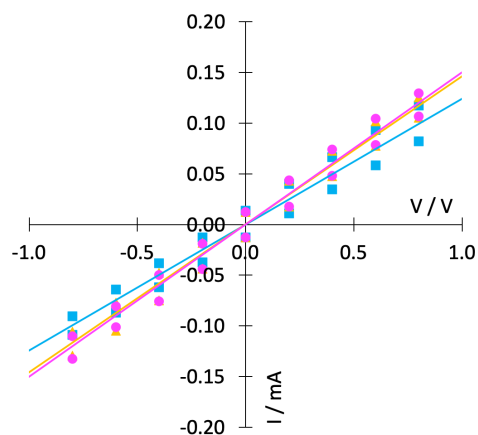
The plots showed linear behaviour and so followed Ohm's Law given in equation 3.1, thus the reciprocal of the gradient of the linear fit gives the resistance,  $R$ . Resistance depends on the area and length of the material in question, but as the samples used were thin films, sheet resistance was used. To obtain the sheet resistance,  $R_{\square}$ , the measured resistance  $R$  was multiplied by the ratio of the width ( $W$ ) of the channel to the length ( $L$ ), see equation 3.2. The channel of the substrates had a width of 1 mm and a length of  $30 \mu\text{m}$  ( $W/L = 33.3$ ). It should be noted that the thickness of the drop-cast films, as determined by AFM, was much smaller than the dimensions of the channel and thus the films could be considered thin and thus sheet resistances could be calculated.

$$R_{\square} = \frac{W}{L}R \quad (3.2)$$

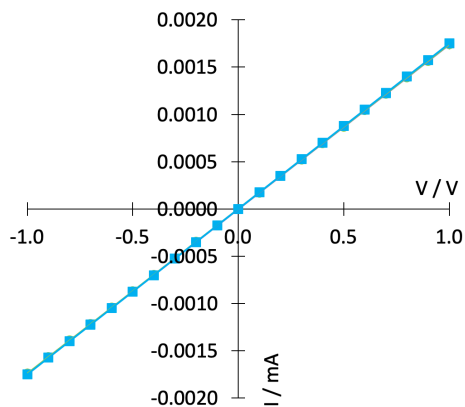
The sheet resistances were calculated for each PEDOT:CS and PEDOT:HA ratio tested. As each sample was scanned three times, a mean sheet resistance for each sample was calculated. Table 3.5 gives the sheet resistances calculated for a number of different PEDOT:CS samples. All of these samples were not crosslinked. The error given is standard deviation. Table 3.6 shows the sheet resistance values calculated for a PEDOT:HA film before and after a crosslinking step, and table 3.7 shows the sheet resistances for drop-cast samples of PEDOT:CS 1:1 that was synthesised using half the required mass of APS compared to the other samples, both before and after an EDC crosslinking step. These experiments and results are discussed following the tables and figures below.



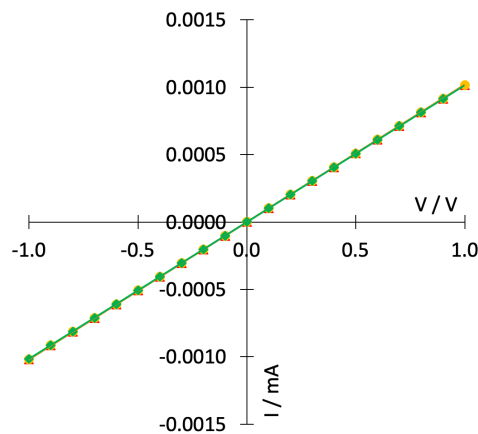
(a) PEDOT:CS 1:1, no dialysis.



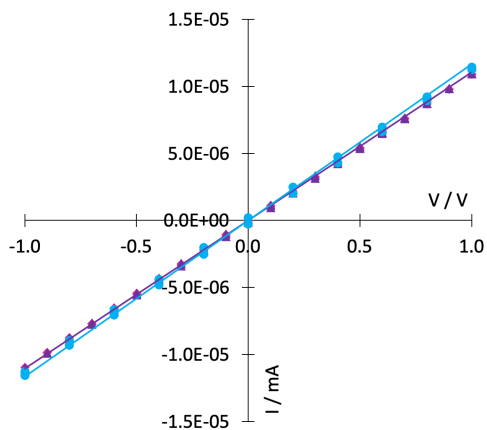
(b) PEDOT:CS 1:1, no dialysis.



(c) PEDOT:CS 1:1, discoloured sample, dialysed.



(d) PEDOT:CS 1:1, dialysed.



(e) PEDOT:CS 1:2, dialysed.

**Figure 3.14:** I/V plots for uncrosslinked PEDOT:CS samples. These plots correspond to the sheet resistances reported for samples in table 3.5.

**Table 3.5:** Sheet resistances calculated for various uncrosslinked PEDOT:CS drop-cast films. The letter labels refer to the plots seen in figure 3.14.

<b>PEDOT:biomolecule</b>	<b>Mean sheet resistance <math>\pm</math> standard deviation / <math>\text{M}\Omega\text{cm}^{-1}</math></b>	<b>Comments</b>
PEDOT:CS 1:1	$(4730 \pm 3.30) \times 10^{-6}$	No discolouration in sample, no dialysis
PEDOT:CS 1:1 (a)	$(95.5 \pm 18.5) \times 10^{-3}$	No dialysis
PEDOT:CS 1:1 (b)	$0.239 \pm 0.021$	No dialysis
PEDOT:CS 1:1 (c)	$19.1 \pm 0.048$	Discoloured sample, dialysed
PEDOT:CS 1:1 (d)	$32.7 \pm 0.050$	Dialysed
PEDOT:CS 1:2 (e)	$(2.98 \pm 0.0843) \times 10^3$	Dialysed

Upon first inspection of table 3.5, it is striking that samples of the same type, synthesised by the same method - i.e. PEDOT:CS 1:1 - showed such variation in sheet resistance. For example PEDOT:CS 1:1 had reported sheet resistances of  $4.73 \text{ k}\Omega\text{cm}^{-1}$  which is comparable to some pristine PEDOT:PSS films (Jönsson [198] reported sheet resistances of  $1.9 - 2.9 \text{ k}\Omega\text{cm}^{-1}$ ), however another PEDOT:CS 1:1 sample had a sheet resistance nearly 7000 times that ( $32.7 \pm 0.050 \text{ M}\Omega\text{cm}^{-1}$ ). The sample-to-sample variation for the same sample type appeared to correlate with whether the sample was dialysed (dialysed samples showed larger sheet resistance). There was also variation in the sheet resistances within the dialysed (or not dialysed) PEDOT:CS 1:1 samples which was probably a result in slight variation in film thicknesses within the sample sets. The data presented here are insufficient to verify the statistical validity of these trends. (More data could have been collected to probe these trends however this was limited by issues with compatibility between the EDC crosslinking methodology and the substrates. This is discussed in more detail at the end of this section.) Therefore, further work, unfortunately beyond the scope of this project, is needed. It is clear, however, that the electronic properties of PEDOT:biomolecule films are highly sensitive to a number of variables. Care needs to be taken when synthesising and preparing samples.

The sheet resistance of the PEDOT:CS samples increased markedly with the increased ratio of CS to PEDOT from 1:1 to 1:2 (table 3.5). This was expected as the overall concentration of the PEDOT:CS aqueous dispersions was maintained at 2% (w/w), so increasing the ratio of CS in the sample decreased the amount of PEDOT present. Less PEDOT resulted in less conductive material and thus higher sheet resistances. Although the sheet resistance increased with increased biomolecule to PEDOT ratio, the larger amount of biomolecule present could be advantageous with mind towards biocompatibility and degradation. Of course, a device based on PEDOT:CS needs to be conductive or it would not function, but other studies suggest that a greater amount of biomolecule would improve biocompatibility which in turn could lead to better outcomes with regard to minimisation of scar tissue and immune response which would result in better contact between the device and the tissues of interest [127]. This could be a trade off later in the design of a device for use within the CNS or other parts of the body based on PEDOT:CS.

When comparing the lowest sheet resistance data for PEDOT:CS and for PEDOT:HA in tables 3.5 and 3.6 respectively, PEDOT:CS performs better than PEDOT:HA as a conductive material due to its

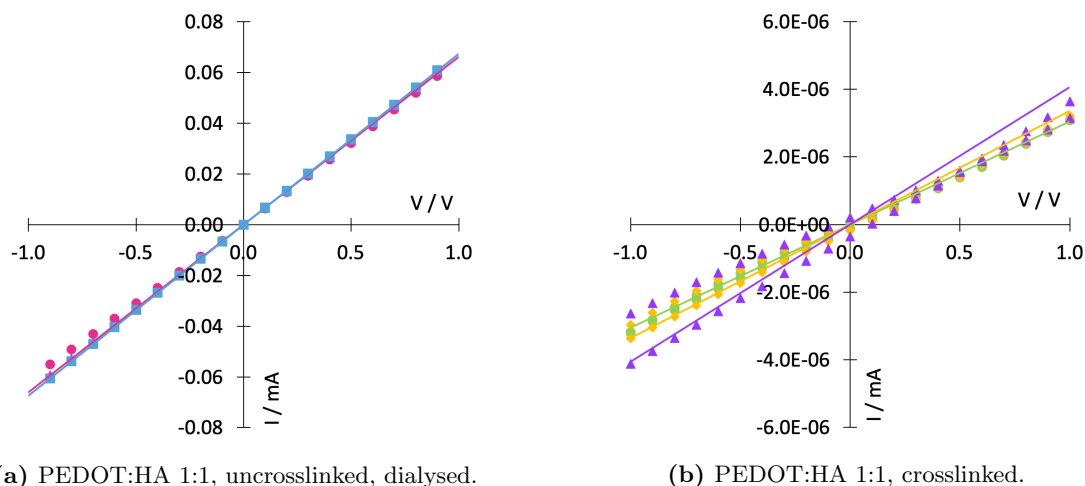


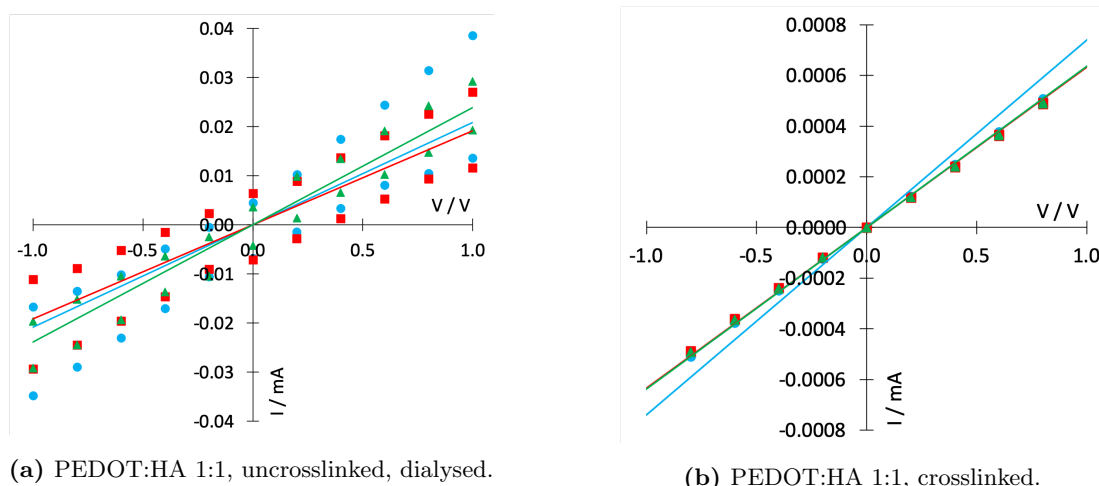
**Figure 3.15:** I/V plots for PEDOT:HA 1:1 samples.

**Table 3.6:** Sheet resistances calculated for PEDOT:HA drop-cast films

PEDOT:biomolecule	Mean sheet resistance $\pm$ standard deviation / $\text{M}\Omega\text{cm}^{-1}$	Comments
PEDOT:HA 1:1 (uncrosslinked)	$(498 \pm 4.50) \times 10^{-3}$	Dialysed
PEDOT:HA 1:1 (crosslinked)	$(9.67 \pm 1.12) \times 10^3$	0.26 mol $\text{dm}^{-3}$ EDC solution

lower sheet resistances. This conclusion is consistent with the results previously reported by Mantione *et al.* [168] who reported higher conductivities for PEDOT:CS than PEDOT:HA in all ratios. It was proposed that the CS was a more effective counter-ion to the doped PEDOT due to the presence of sulfate moieties which are analogous to the sulfonate groups found on PSS [168]. On the other hand, the large variations in the PEDOT:CS 1:1 data makes direct comparison more challenging. As previously stated, the best (smallest) PEDOT:CS 1:1 sheet resistance is around 7000 times greater than the worst (largest) PEDOT:CS 1:1 sample. If one were to pick the worst reported sheet resistance of PEDOT:CS 1:1 and compare it with the equivalent PEDOT:HA 1:1 (uncrosslinked) sample, it would appear that the PEDOT:HA performed better. This inconsistency again demonstrates the variation within the data for each PEDOT:biomolecule type which could be a result of slight variations in thickness in the PEDOT:biomolecule films but also seems to correlate with the dialysis status of the sample. Further data should be collected to determine the statistical validity of these trends; however this is outside the immediate scope of this project.

A number of PEDOT:CS 1:1 samples were prepared with half the mass required of ammonium persulfate (APS), and none of the resulting aqueous suspensions were dialysed. When comparing all the PEDOT:CS 1:1 samples with the full mass of APS that were NOT dialysed with PEDOT:CS 1:1 with half the mass of APS, the PEDOT:CS 1:1 (half APS) sample gave a sheet resistance of  $1.58 \pm 0.141 \text{ M}\Omega\text{cm}^{-1}$  which was approximately 6.5 times larger than the largest sheet resistance for PEDOT:CS 1:1 (full mass of APS, not dialysed) sample ( $240 \pm 21 \text{ k}\Omega\text{cm}^{-1}$ ). The sample with half the mass of APS gave a greater sheet resistance than a PEDOT:CS 1:1 sample synthesised with the full mass of APS. This was an expected result as the APS acted as the oxidising agent in the synthesis of PEDOT:biomolecules. As previously stated, the APS oxidises the EDOT monomer to form radical cations which then combine and deprotonate to



(a) PEDOT:HA 1:1, uncrosslinked, dialysed.

(b) PEDOT:HA 1:1, crosslinked.

**Figure 3.16:** I/V plots for PEDOT:CS 1:1 synthesised with half the required mass of APS.

**Table 3.7:** Sheet resistances calculated for PEDOT:CS drop-cast films, synthesised with half the required mass of APS compared to all the other samples presented here.

PEDOT:biomolecule	Mean sheet resistance $\pm$ standard deviation / $M\Omega\Box^{-1}$	Comments
PEDOT:CS 1:1 (uncrosslinked)	$1.58 \pm 0.141$	Half mass of APS, no dialysis.
PEDOT:CS 1:1 (crosslinked)	$50.0 \pm 3.50$	Half mass of APS, 0.26 mol $dm^{-3}$ EDC solution, no dialysis.

start the polymerisation reaction. The oxidation, combination, and deprotonation process repeats to give polymerised PEDOT. If there is half the mass of APS present in the reaction mixture upon preparation of PEDOT:biomolecules, there will be a limitation on the rate at which the polymerisation can occur which will likely lead to less conducting PEDOT present in the final sample.

Another observation across the data set was that there were 20,000-fold and 31-fold increases in the sheet resistances of the PEDOT:HA 1:1 and the PEDOT:CS 1:1 (half mass of APS), respectively, from an uncrosslinked sample to a crosslinked sample. The crosslinking of the PEDOT:biomolecule is important for the use of the material in the OECT device, and with regards to the degradation as required by the requirements of this project. This increase in sheet resistance is likely due to the change in film structure upon crosslinking. Håkansson *et al.* [195] reported that upon crosslinking PEDOT:PSS films with GOPS the conductivity of the PEDOT:PSS decreased. This was found to be a result of a change in the morphology of the material due to the reaction between the GOPS and the PSS that surround the highly conducting PEDOT:PSS particles. Similarly, crosslinking the PEDOT:CS and PEDOT:HA will result in a tighter matrix than an uncrosslinked PEDOT:CS film leading to lower levels of ionic conductivity, and thus higher sheet resistances. In addition, there could also be a chemical change in the PEDOT due to the EDC crosslinking methodology used. There was speculation in a 2012 paper by Jimison *et al.* [199] that a specific reaction can occur where EDC directly attacks PEDOT, however this was not proven and would require further experimentation. Quantification of the level of crosslinking in the films would provide insight into changes in the electronic behaviour following the EDC crosslinking step. A spectroscopic

method such as NMR spectroscopy could be used to track how the crosslinking method changes the PEDOT:biomolecule samples chemically which could help prove or disprove these hypotheses. In spite of the increased sheet resistance, the crosslinking is a necessary step in the development of the material for use in the OECT. The crosslinking step is required so that the degradation of PEDOT:biomolecule material can be controlled, as well as avoiding delamination or dissolution of the OEM layer when the OECT device is exposed to electrolyte. The role of crosslinking and degradation in PEDOT:biomolecules drop-cast films is assessed in more detail in chapter 4.

The data presented in this section does not give the full picture on the sheet resistance of PEDOT:CS or PEDOT:HA. A full library of PEDOT:biomolecule aqueous dispersions was synthesised as described in the experimental methods; PEDOT:CS 1:1, 1:2, 1:3, and 1:4, as well as PEDOT:HA 1:1 and 1:2. All of these samples were prepared for testing, however not all preparations were successful, as alluded to earlier in this discussion. There were some problems with delamination of materials following the drying step for the PEDOT:CS 1:3 and 1:4 aqueous dispersions. Even when dried slowly, the PEDOT:CS samples with larger ratios of CS shrunk and pulled on the gold contacts causing them to crack, rendering them unusable. Additionally, there were some issues with compatibility of the substrates manufactured in-house with the EDC crosslinking methodology later in the project. When the substrate was placed in contact with the EDC crosslinking mixture (80:20 ethanol to EDC solution), the gold contacts would delaminate from the glass substrate, as seen in figure 3.17. This also hampered attempts to gather data for the crosslinked PEDOT:biomolecule samples. The delamination was thought to have occurred due to poor gold adhesion to the glass substrates as a result of poor chromium adhesion layer deposition. Further substrates were prepared but there were issues with the evaporator used to deposit the chromium adhesion layer and the gold onto the glass substrate which meant that the equipment did not deposit the required thicknesses of each material leading to further delays and poor substrate quality.

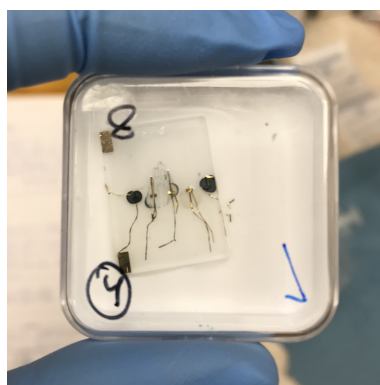


**Figure 3.17:** Photo of one of the glass substrates prepared for testing with PEDOT:CS and PEDOT:HA samples, however severe delamination of the gold electrodes occurred during the crosslinking step, and rendered the sample unusable.

Consideration of the method of data collection itself is also necessary when looking at these results. The gold standard method of sheet resistance measurement is using a four-point probe. In their work on PEDOT:CS and PEDOT:HA, Mantione *et al.* [168] used a four-point probing method to determine the conductivity of the films of PEDOT:biomolecule. Four-point probing is advantageous over two terminal sensing techniques as the voltage and current electrodes are separated to give two voltage and two current electrodes (hence four-point probing) which eliminates any contribution contact resistance makes to the measured resistance of a sample. Contact resistance is the resistance contribution from the interfaces of

electrical connections, in contrast to the intrinsic resistance of the material under investigation. For this work, a two-point probing method was used. Despite not being the gold-standard, it was still considered appropriate as the main aim of this work was to prove that PEDOT:CS and PEDOT:HA were conductive and to gain an indication of their properties given varied ratios and the effect of crosslinking.

Through this section, it has been demonstrated that PEDOT:CS and PEDOT:HA are both conductive materials, supporting the work by Mantione *et al.* [168] and that the sheet resistance of the materials appears to be sensitive to crosslinking. These materials offer an alternative to PEDOT:PSS with regards to biocompatibility and degradation, and thus were put forward for OECT characterisation. As previously stated, there is a lack of literature on using PEDOT:biomolecules in bioelectronic devices. This is an area that could be exploited with regards to creating devices for use in the CNS due to the advantages of using biocompatible and biodegradable PEDOT:CS or PEDOT:HA. To that end, initially a proof of concept is required to show that PEDOT:CS and PEDOT:HA can be used in a biologically relevant OECT.

### **3.3.4 Proof of concept: Transistor characterisation of PEDOT:CS and PEDOT:HA**

The aim of this project was to develop a biocompatible, biodegradable, and mechanically appropriate OECT. The PEDOT:CS and PEDOT:HA both fulfil the requirements of being biocompatible and biodegradable through the choices of biomolecule counter-ions for the PEDOT, and the EDC crosslinking creates hydrolytically degradable ester crosslinks. The next stage was to show that these materials could be used in an OECT device.

PEDOT:CS and PEDOT:HA 1:1 samples were prepared using the same substrates and techniques as in the simple electronic testing. The first requirement of an OECT device based on PEDOT:biomolecule is to examine how the current through PEDOT:CS can be modulated through application of a gate voltage through an electrolyte. In the introduction chapter (chapter 1), the functioning of the nervous system and generation and propagation of action potentials within the CNS and peripheral nervous system (PNS) was discussed. Sodium and potassium ions were shown to be very important within these systems and their functioning, thus phosphate buffered saline (PBS) was used at the electrolyte in these experiments as it provided an ample source of biologically relevant ions including sodium and potassium, as well as providing an electrolyte of physiological pH (7.4).

The output characteristics for the PEDOT:CS 1:1 OECT can be seen in figure 3.18. As the gate voltage is increased, the source-drain current decreased, demonstrating depletion mode transistor characteristics.

Unfortunately no data were obtained for PEDOT:HA. This is not to say that PEDOT:HA would not work in a OECT device, but at this time no data were collected. Again, this was due to substrate issues (as outlined in the previous section), with the gold contacts delaminating from the substrates around the PEDOT:HA 1:1 sample upon drying. This was exacerbated by newly prepared samples suffering gold delamination during crosslinking (as seen in figure 3.17). The delamination occurred when the substrate came into contact with the ethanol and EDC solution mixture during the crosslinking step in sample preparation. As previously mentioned, attempts were made to mitigate this issue by preparing new substrates however this was unsuccessful and the problem continued to occur.

From these data, the transfer characteristics of the PEDOT:CS based OECT were extracted (figure 3.19).

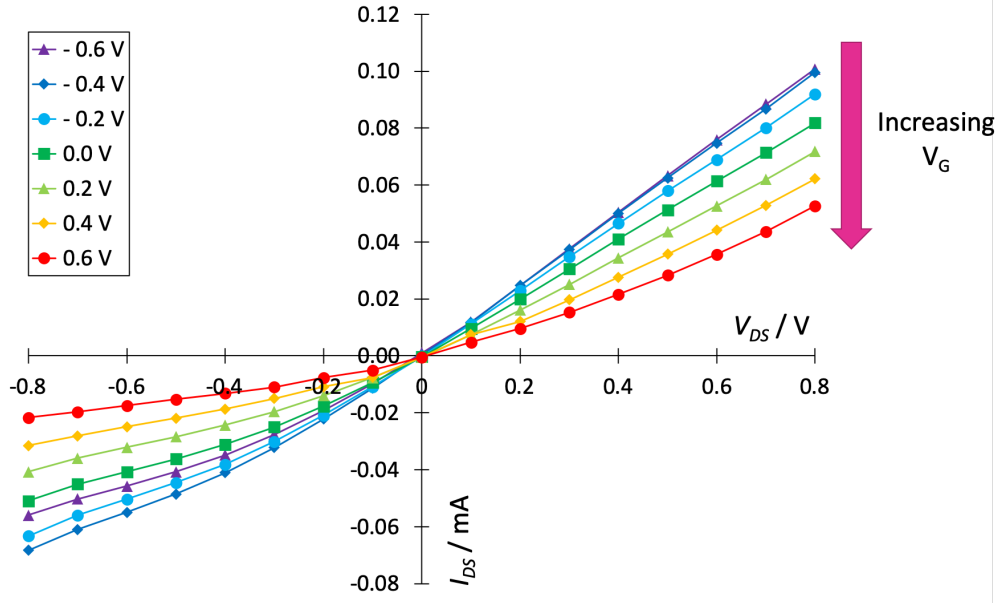


**Figure 3.18:** The output characteristics showing that PEDOT:CS 1:1 can function as an OEFT. Each data set describes a different gate voltage ( $V_G$ ).

To quantify the relationship between the output current of the OEFT and the input voltage, the transconductance is calculated from the transfer characteristics. The transconductance ( $g_m$ ) was defined as the change in source-drain current ( $I_{DS}$ ) over the change in gate voltage ( $V_{GS}$ ), as described by equation 3.3. The transconductance of the material changes with the gate voltage and with the source drain voltage, as can be seen in figure 3.20.

$$g_m = \frac{\delta I_{DS}}{\delta V_{GS}} \quad (3.3)$$

Typically, the maximum transconductance of an OEFT device is the reported value and for this PEDOT:CS 1:1 OEFT that value was  $50.5 \mu\text{S}$  ( $V_{GS} = -0.2 \text{ V}$ ,  $V_{DS} = 0.8 \text{ V}$ ). This is an order of magnitude smaller than more optimised OEFT type devices reported in the literature that tend to have transconductances on the order of millisiemens [31], whereas EGFETs have transconductance values on the order of microsiemens [131]. This could suggest that the PEDOT:CS device is operating as an EGFET as opposed to an OEFT, however it also could be simply that the OEFT has not been optimised and the maximum transconductance value could be increased through more careful device design or chemical treatments to improve conductivity in future.

From the output and transfer characteristics compiled, it can be seen that the changing gate voltage up to  $0.6 \text{ V}$  does not appear to switch the OEFT off. That is to say at the limits of the gate voltages measured here, the source-drain current ( $I_{DS}$ ) never reaches zero, except in the case of the source-drain voltage of  $0 \text{ V}$  which is expected. This implies that the PEDOT:CS is never completely dedoped within in the range of gate voltages investigated. This could be rectified by extending the range of voltages explored up to  $1 \text{ V}$ , however this could not be taken further due to concerns about water hydrolysis. Additionally, as long as there is a large enough difference between the maximum current ON state and the minimum current OFF state, the behaviour can be exploited as an OEFT. The ON/OFF ratio is a useful characteristic to note here. This is the ratio of the current when the device is on, and producing its

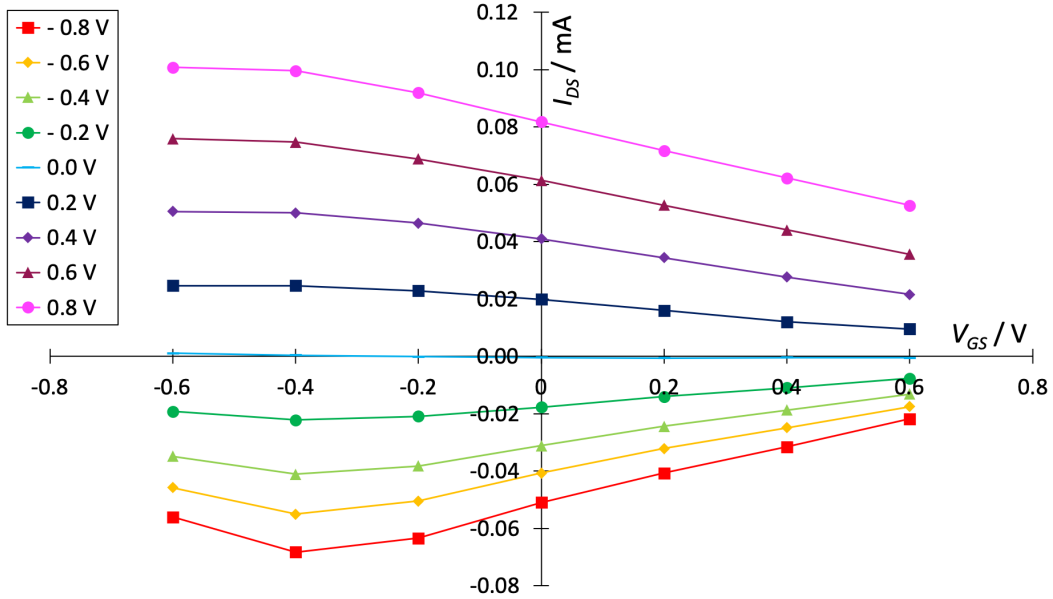


**Figure 3.19:** The transfer characteristics of the PEDOT:CS 1:1 OEET. Each data set is for a different source-drain voltage ( $V_{DS}$ ) as described by the key.

maximum source-drain current (at  $V_G = -0.6$  V), divided by the off current, in this case, the minimum source-drain current (at  $V_G = 0.6$  V). These ON/OFF ratios are reported in table 3.8.

**Table 3.8:** Calculated ON/OFF ratios of the PEDOT:CS 1:1 based OEET.

Source-drain voltage ( $V_{DS}$ / V)	ON/OFF ratio
-0.8	2.6
-0.6	2.6
-0.4	2.6
-0.2	2.5
0.2	2.6
0.4	2.3
0.6	2.1
0.8	1.9

The ON/OFF ratios reported here were all around two, which is not very large at all for OEET devices. In a 2019 paper, Lingstedt *et al.* [200] assessed the effect of dimethyl sulfoxide (DMSO) treatments on the output characteristics of PEDOT:PSS based OEETs. DMSO is known to greatly enhance the conductivity of PEDOT:PSS films. In the paper, even the worst performing OEET had an ON/OFF ratio of around 70. This is obviously significantly larger than the ON/OFF ratios reported here, and suggests that the PEDOT:CS based OEET was not competitive in terms of performance compared to PEDOT:PSS devices at this time.

Nevertheless, OEET proof of concept was successful for the PEDOT:CS 1:1 material, and showed that this biocompatible, degradable alternative to PEDOT:PSS functioned in an OEET. This has not previously been established in the literature and was the first step in developing an OEET device that in future could be used in the CNS. In spite of the successful proof of concept, the device required tuning and further assessment to give the most useful output properties. PEDOT:PSS is a well understood material

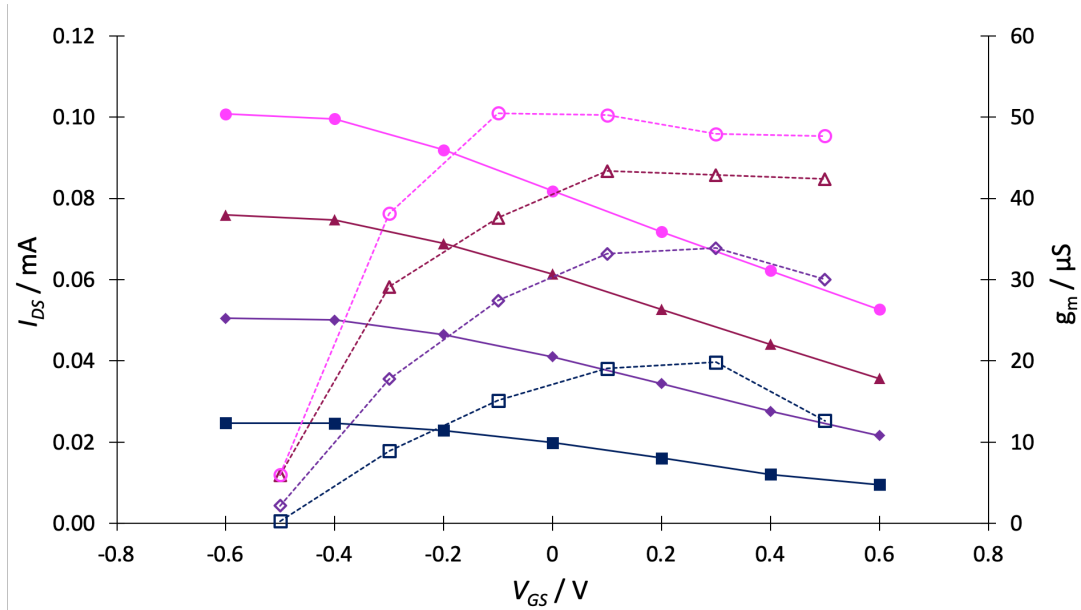


**Figure 3.20:** The transfer characteristics (solid line) of the PEDOT:CS 1:1 OEET for  $V_{DS}$  of 0.2 V (solid dark blue square), 0.4 V (solid purple diamond), 0.6 V (solid maroon triangle), and 0.8 V (solid pink circle). The related transconductance values (dashed line) for each  $V_{DS}$  are given on the second axis with the equivalent unfilled shape data points.

that has been assessed and optimised for use in OEET devices through careful design. For example, PEDOT:PSS devices have been optimised by changing the electrode design to maximise the  $W/L$  ratio or adding additives such as ethylene glycol for improved conductivity. Similar optimisations are required of the PEDOT:CS device developed here.

The next step in the development of the biocompatible and biodegradable OEET was to optimise and understand how the PEDOT:CS was functioning in the OEET by altering the PEDOT:CS ratio, changing the substrate design, and examining the degradation of the device to indicate how it would perform when implanted into the body. This is explored in chapter 4.

### 3.4 Summary and further work

This chapter has described the initial proof of concept for a biocompatible, biodegradable OEET device based on PEDOT complexed with CS or HA. The use of these materials is novel in a transistor set up and offers a route to creating a device that could be used in the central nervous system, and perhaps in SCI treatment. The biocompatibility issues with PEDOT:PSS have been mitigated by choosing CS and HA as alternative counter-ions for PEDOT. These glycosaminoglycans are found naturally in the human body, especially in the CNS. To prove this biocompatibility definitively, further work involving direct exposure to cell lines would be required, however evidence from literature has previously demonstrated that PEDOT:CS and PEDOT:HA are biocompatible with fibroblast and neuroblastoma cells [168, 180]. Drop-casting was established as a suitable method for forming films of PEDOT:CS and PEDOT:HA, as this method gave continuous films, which were fairly homogeneous after altering the method to include a sonication step. By crosslinking the PEDOT:CS and PEDOT:HA films via EDC crosslinking, a route

for degradation has been achieved as the ester bonds formed are hydrolytically degradable. Additionally, within the body enzymatic degradation of the CS and HA would occur as these materials are naturally occurring and thus can be broken down by chondroitin ABC lyase and hyaluronidase. It was demonstrated that PEDOT:CS and PEDOT:HA are conductive, and thus may be used in an OECT. There was a range of sheet resistances measured, and it was noted that the crosslinked samples exhibited greater sheet resistances than uncrosslinked samples. This will be investigated further in chapter 4. Finally, it was demonstrated that PEDOT:CS could be used in an OECT device and had a maximum transconductance of  $50.5 \mu\text{S}$ . This acted as a proof of concept as a starting point for optimisation. Improvements to device performance may be achieved by changing the design of the electrodes used to increase the  $W/L$  ratio, and adding additives such as ethylene glycol for improved conductivity. Also, the effect of dialysis on the electronic properties should be more closely examined as dialysis appears to have a significant effect on the sheet resistance of the PEDOT:biomolecule films.

Once an optimised device is achieved, it will be time to consider about how the device could be used in the spinal cord or more broadly within the body. It may be possible to calibrate the OECT response with various concentrations of biologically relevant ions, such as  $\text{Na}^+$ . This could then be used to detect influxes of  $\text{Na}^+$  ions in an area of the spinal cord which would indicate a neuron signal. Additionally, if these devices were considered for uses outside the CNS, they could be used to detect glucose concentrations in diabetic patients for diagnosis applications for example. To move more towards a use in the human body, the PEDOT:CS and PEDOT:HA devices should be assessed for compatibility with live cells on both a biocompatible level and to see how the presence of cells affects the functioning of the device.

## Chapter 4

# Optimising a PEDOT:biomolecule organic electrochemical transistor

### 4.1 Introduction

In chapter 3, poly(3,4-ethylenedioxythiophene):poly(styrene sulfonate) (PEDOT:PSS) was introduced as a popular material for use in bioelectronic devices. The drawbacks of using PEDOT:PSS within the body were also discussed highlighting issues with compatibility. PEDOT complexed with biomolecules offer a biocompatible alternative to PEDOT:PSS that may be more suitable for *in vivo* use. A number of PEDOT complexes with alternative biomolecule counter-ions have been demonstrated to show better biocompatibility over PEDOT:PSS, but there is little known about these materials in bioelectronic devices such as organic electrochemical transistors (OECTs).

OECTs are useful devices for use in the body due to their low operating voltages and ability to transduce small ionic signals into electronic signals and thus can act as an interface between biology and synthetic technology [31]. If intended for use in the human body, such devices must fulfil the following requirements: biocompatibility, biodegradability, and appropriate mechanical properties. These requirements ensure that a device can work effectively in the body as intended with minimal immune response. In order to achieve these requirements, a biocompatible alternative to PEDOT:PSS should be used.

In the previous chapter, PEDOT:CS and PEDOT:HA aqueous dispersions were successfully synthesised by oxidative polymerisation, and demonstrated that they could form drop-cast thin films. These films were electronically characterised and were seen to show conductivity, with a best recorded sheet resistance of  $4.7 \text{ k}\Omega\text{cm}^{-1}$  for PEDOT:CS (1:1). For transistor characterisation, the PEDOT:CS and PEDOT:HA films required crosslinking which was achieved using EDC-coupling methods. The PEDOT:CS (1:1) crosslinked film was then used in a simple organic electrochemical transistor (OECT) set up, demonstrating depletion mode behaviour and a maximum transconductance of  $50.5 \mu\text{S}$ . This acted as a proof of concept that an OECT device could use a biocompatible, degradable material that would be suited to *in vivo* applications.

The next step in the development of the biocompatible and biodegradable OECT was to optimise and understand the behaviour of PEDOT:CS in more detail. Work towards optimising the transistor be-

haviour of the OECT is presented in this chapter through changes in electrode geometry. Furthermore, an examination of the degradation of the device was undertaken, and ultraviolet (UV) spectroscopy and electrical impedance spectroscopy (EIS) were used to understand the high sheet resistances observed for the crosslinked PEDOT:biomolecules in chapter 3. In addition, experiments towards creating synapstors (bioelectronic devices that mimic the short-term plasticity of synapses [13, 44, 128–133]) from PEDOT:CS were undertaken. Moreover, lyophilisation experiments to create 3D scaffolds from PEDOT:CS and PEDOT:HA were performed as a step towards creating tubistors (3D scaffolds made from conducting polymers that demonstrate transistor-type behaviour [134]).

Organic bioelectronics is a vast research area covering many potential applications. The PEDOT:CS based OECT device discussed in this thesis is intended to be developed for use in the central nervous system (CNS) for spinal cord injury (SCI) treatment in future. This is one particular application of bioelectronics within the nervous system. Another is the synapstor.

### 4.1.1 Synapstors

The term synapstor, a contraction of synapse and transistor, appears to have been coined by Alibart *et al.* [129] in 2012. They are bioelectronic devices that can mimic the short-term plasticity (STP) effect seen across biological synapses. The possibilities afforded by synapstors has not been fully realised. If a synapstor were developed that were able to interface directly with neurons, it could be used as an artificial synapse which could offer direct neuron to silicon communication technology. Such interfacing would be revolutionary in the treatment of injuries and diseases of the nervous system (for example, spinal cord injuries (SCIs)).

Synapses and STP were introduced in detail in section 1.1.3. Synapses are junctions between individual nerve cells. Action potentials (nerve signals) cannot jump from one neuron to the next, so there has to be an alternative method for these signals to be passed on. When an action potential reaches a synapse, it triggers a cascade of events that release neurotransmitters into the synaptic cleft. The neurotransmitters diffuse across the cleft and bind to the post-synaptic membrane, triggering an action potential in the next neuron. STP behaviour acts to increase or decrease the scale of response across the synapse. When an action potential triggers the presynaptic neuron to release neurotransmitter in to the synapse, every incoming action potential will cause it to release more and more into the synaptic cleft. This results in an increase in the amount of neurotransmitter in the synaptic cleft which builds up over a short time. The greater concentration of neurotransmitter released results in a greater number of neurotransmitter molecules binding with the post-synaptic membrane, enhancing the response in the post-synaptic neuron in the short-term. If there are repetitive incoming action potentials in the presynaptic neuron, however, there can be a diminished or depressive response in the post-synaptic neuron due to the depletion of neurotransmitter in the pre-synaptic neuron. This depletion occurs as neurotransmitter cannot be replaced or recovered at a high enough rate in the pre-synaptic neuron to keep up with the frequency of the incoming action potentials. The result is that if there is a high frequency input in the pre-synaptic neuron, there is a low frequency output in the post-synaptic neuron due to the availability of neurotransmitter.

STP mimicking devices have been of interest to researchers in the field of neuromorphic computing for a number of years. Alibart *et al.* [128, 129] demonstrated a nanoparticle organic memory field-effect

transistor (NOMFET) that displayed STP. The aim of the work was to develop a device for neuromorphic computing that could imitate a facilitating or depressing biological synapse. The timescales and frequency of the STP behaviour in the NOMFET could be altered and tuned through changing the size of the gold nanoparticles embedded in a pentacene conductive layer. Desbief *et al.* continued work on the NOMFET [130], and developed a electrolyte-gated hybrid nanoparticle/organic synapstor (EGOS) [44] taking the concepts of NOMFET architecture further. These EGOS devices also exhibited STP behaviour and were interfaced with neuronal cell lines which had no reported effect on the STP behaviour. Furthermore, EGOSs based on 2,7-dioctyl [1]benzothieno[3,2-b][1]benzothiophene that use PEDOT:PSS electrodes were also shown to demonstrate STP [131].

STP behaviour was realised in a PEDOT:PSS OECT by Gkoupidenis *et al.* [13] in 2015. The device architecture was simple with gold electrodes (source, drain, and gate) patterned onto a glass substrate and a thin PEDOT:PSS film to act as a channel material. A polydimethylsiloxane (PDMS) well was filled with KCl solution to act as the electrolyte. A pulsing voltage with set time gaps between each pulse was applied to the gate electrode which acted as the presynaptic signal. The source-drain output current was recorded to detect the equivalent to postsynaptic activity. A depressive response could be obtained when the time gap between the pulses was less than a critical value. The STP behaviour detected here was attributed to the doping and dedoping of PEDOT:PSS. If the time gap was greater than the critical value, there was enough time for the cations driven in to the PEDOT:PSS to move back into the electrolyte prior to the second pulse. On the other hand, if the time gap between the pulses was inadequate to allow this charge equilibrium to reestablish, cations would build up in the PEDOT:PSS, dedoping it cumulatively and thus giving a depressive output signal. The same author described STP behaviour in OECTs based on PEDOT:poly(oxolane) [132], as well as long-term plasticity which is of interest to researchers working towards neuromorphic computing.

A synapstor type device has also been used as an ultra-sensitive sensor to detect changes in dopamine concentrations in solution [133]. Dopamine functions as a neurotransmitter in the brain and is often cited as the happiness chemical in popular culture; the release of dopamine in the body relates to reward and pleasure behaviours [201]. Decreased dopamine concentrations in the extracellular fluid of the brain is related to the development of Parkinson's disease and thus detection of this decrease could be used to diagnose Parkinson's earlier than the onset of symptoms. The device was based on two PEDOT:PSS electrodes on a PDMS substrate, with the larger of the two electrodes acting as the pre-synaptic neuron by being pulsed with voltage square waves, and the smaller electrode acting as the post-synaptic neuron detecting the current. The response from the device was modulated by the presence of different concentrations of dopamine in a solution in contact with the electrodes, thus correlation plots could be obtained. The device did not respond when exposed to ascorbic acid and uric acid which are other common molecules found in the extracellular fluid of the brain, showing that the device was selective to dopamine. This sensor exemplified that synapstors and other bioelectronic architectures that exhibit STP have potential applications in implantable devices for use in the nervous system, and this work has been developed further in a recent paper from the same author [202].

#### 4.1.2 Tubistors

The principles that have guided the research in this thesis require that a device for use in the body must be biocompatible, biodegradable, and mechanically appropriate. In chapter 5, the use of a hydrogel

substrate is developed as an approach to improve the outcomes of the device if implanted into the body whilst maintaining the planar geometry of the OEET. An alternative approach is to create 3-dimensional transistor devices.

Much of the field of organic bioelectronics produces research on planar device architectures such as the OEET. Traditional planar devices may not be as effective at mimicking the cellular environment that they are exposed to if implanted *in vivo*. This can lead to devices that, if not carefully designed, are attacked by the immune system and rejected from the body. On the other hand, a bioelectronic device prepared from an organic electronic material in such a way to give porous scaffold that mimics the structure of the extracellular matrix (ECM) could offer an alternative to devices with planar geometries.

Pitsalidis *et al.* [134] demonstrated a 3D scaffold prepared from PEDOT:PSS with integrated gold electrodes that allowed it to act as an electrochemical transistor for simultaneous cell culturing and monitoring purposes. Tubistors were so named as they were prepared by lyophilisation of PEDOT:PSS in a T-shaped tube mold to form a transistor in a tube (figure 4.1) where the scaffold forms the channel of the device. Gold electrodes were inserted into the mould via the side port of the tube prior to freeze-drying so they may act as source-drain electrodes during tubistor operation. The tubistor was gated through a sodium chloride solution electrolyte and the gate electrode was inserted into the tube (not in contact with the scaffold).

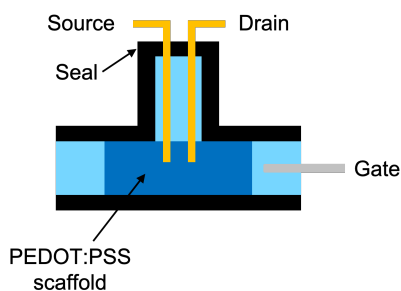


**Figure 4.1:** Schematic diagram of a tubistor structure [134].

The tubistor devices are thought to function in the same way as OEETs via the doping and dedoping of the PEDOT:PSS by ions from the electrolyte being driven in and out of the polymer by the modulation of the gate electrode voltage. Typically the tubistors demonstrated transconductance values of greater than 12 mS, but the response times to switch on and off were slow at around 1.5 seconds. Cell seeding on the scaffolds yielded a significant decrease in device performance, but a slight recovery in transconductance was observed once any cells that were not attached to the scaffolds were rinsed away prior to the growth stage. The scaffolds were determined to be compatible with the cells, as the cells grew to completely cover them.

These 3D PEDOT:PSS scaffolds were also prepared in alternative molds meaning that they can be shaped freely, not confining them to a specific architecture for a specific application. The tubistors were prepared in such a way as to be appropriate for cell culturing studies. If, however, a scaffold could be shaped to fit in a lesion in a SCI for example, there is the possibility that these devices could be used to monitor or even guide cell growth as a potential treatment. Furthermore, if the scaffold were prepared from a degradable material such as PEDOT:CS, the scaffold would not require any invasive surgeries to remove it following its useful lifetime. As such, later in this chapter lyophilisation of PEDOT:CS and PEDOT:HA is reported and subsequent crosslinking attempts are described.

### 4.1.3 Understanding and optimising a PEDOT:biomolecule OECT

Following on from the work presented in chapter 3, the aim of this chapter is to develop and improve the performance of the PEDOT:biomolecule OECT device and examine its degradation.

First, the use of interdigitating electrodes to improve device performance was investigated and although no significant improvements were observed, the experiments acted as an opportunity to further demonstrate the use of PEDOT:CS in an OECT. Further characterisation of the PEDOT:CS itself using UV spectroscopy and electrochemical impedance spectroscopy (EIS) was carried out to probe the electronic and ionic conductivity of the material and examine changes that occurred following EDC-crosslinking and the effect of degradation. From these analysis techniques, it was observed that non-conducting undoped PEDOT was present in the samples following the EDC-crosslinking step which explained the increased sheet resistances upon crosslinking seen in chapter 3.

Next, as the OECT devices were intended to be degradable, the stability of the devices was investigated by submerging the OECT devices in water for 3 days and repeating transistor characterisation. The OECT devices demonstrated a marked increase in performance following the 3-day submersion with two- to four-fold increases in transconductance and increased output currents. EIS and UV spectroscopy demonstrated that following the 3-day submersion in water the PEDOT was present in its doped conducting form with both ionic and electronic conductivity occurring within the film.

Finally, experiments are presented using PEDOT:CS outside the scope of a planar OECT device. Experiments towards creating synapstors from the PEDOT:CS were undertaken by testing the laser ablation technique used by Giordani *et al.* [133] to pattern PEDOT:CS films on PDMS substrates. Additionally, the lyophilisation of PEDOT:CS and PEDOT:HA is reported and subsequent crosslinking attempts are described as a step towards creating 3D scaffolds that can demonstrate transistor-type behaviour such as those prepared by Pitsalidis *et al.* [134]).

## 4.2 Experimental methods

All of the work preparing and characterising the OECT and synapstor devices presented in this chapter was carried out at the University of Modena and Reggio Emilia (UNIMORE), Italy, with the help of Dr Marcello Berto and Martina Giordani. The UV spectroscopy and electrochemical impedance spectroscopy on PEDOT:biomolecule samples was carried out at the Centre for Translational Neurophysiology of the Italian Institute of Technology (IIT) in Ferrara, Italy, with the help of Dr Stefano Carli.

The PEDOT:biomolecule scaffold preparation and characterisation was carried out in the Department of Chemical Engineering and Biotechnology at the University of Cambridge with the help of Dr Janire Saez of the Bioelectronic Systems Technology group.

### 4.2.1 Materials

PEDOT:CS 1:1, 1:2, 1:3, and PEDOT:HA 1:1 aqueous suspensions (2% (w/w)) were prepared to the methods outlined in chapter 3. Quartz substrates patterned with interdigitated gold electrodes were pro-

vided by Dr Marcello Berto at UNIMORE. Polydimethylsiloxane (PDMS) Sylgard 184 was purchased from Dow Chemicals, Delaware. Ethanol, *iso*-propanol, *N*-(3-dimethylaminopropyl)-*N*'-ethylcarbodiimide hydrochloride (EDC), phosphate buffered saline tablets, (3-glycidyloxypropyl)trimethoxysilane (GOPS) and ethylene glycol were supplied from Merck (formerly Sigma Aldrich). Deionised water was obtained from the in-lab supplies at UNIMORE, IIT, and the University of Cambridge, as appropriate.

## 4.2.2 OECT characterisation

### Sample preparation

Two different PEDOT:CS 1:1 samples were used in OECT characterisation. One was prepared 6 weeks prior to testing and is referred to here as PEDOT:CS 1:1 (old). The other was prepared 1 week prior to testing and is referred to here as PEDOT:CS 1:1 (new). Quartz substrates were provided by Dr Marcello Berto at UNIMORE.

PEDOT:CS 1:1 (old), PEDOT:CS 1:1 (new), PEDOT:HA 1:1, and PEDOT:CS 1:3 aqueous suspensions (2% (w/w)) were used in the OECT characterisation experiments. The PEDOT:CS and PEDOT:HA samples were sonicated at room temperature for ten minutes before drop-casting 5  $\mu$ l of aqueous suspension onto the centre of the quartz substrates covering the channel region. The samples were air dried for five minutes, and then dried in an oven at 50 °C for one hour.

A crosslinking mixture was prepared from ethanol (24 cm<sup>3</sup>) and EDC solution (0.043 mol dm<sup>-3</sup>, 6 cm<sup>3</sup>). The crosslinking mixture was then distributed into individual vials (6 cm<sup>3</sup> per vial). One drop-cast PEDOT:CS or PEDOT:HA sample on a quartz substrate was submerged in each crosslinking mixture overnight. Following the overnight crosslinking period, the samples were carefully rinsed in water, and dried in the oven for two hours at 60 °C.

### Transistor characterisation

Each quartz substrate had a test pattern with four pairs of electrodes with channels between them. This meant that each sample was tested at least four times (at least once across each set of electrodes). The OECT characterisation was carried out using an Agilent B2912A Source Measure Unit inside a Faraday cage. A constant potential bias (-0.4 V) across the sample was maintained between the source and drain electrodes ( $V_{DS}$ ), and a platinum wire was used as the gate electrode. The samples were gated through PBS (50 mM) as the electrolyte solution, and the source-gate voltage ( $V_{GS}$ ) was varied to observe the OECT behaviour. The gate voltage was swept from 0.0 V to 1.0 V and back down to 0.0 V in steps of 0.001 V. The sweeps were repeated at least 10 times with 20 seconds between each sweep. The 10th sweep was considered as the true behaviour of the OECT device, as multiple sweeps were required to ensure the devices were stable. There was little variation observed between sweeps thus the devices were considered stable.

To examine device degradation, the drop-cast PEDOT:CS 1:1 (new) sample was left submerged in water for 3 days, and then dried in the oven for two hours at 50 °C. OECT characterisation was then carried out on this sample again.

### 4.2.3 Sample preparation for UV spectroscopy and EIS

For the aqueous phase UV spectroscopy, PEDOT:CS 1:1 and 1:2 aqueous dispersions (2% (w/w)) were diluted in water (50  $\mu\text{l}$  water to 250  $\mu\text{l}$  dispersion).

For the film samples, the PEDOT:CS 1:1 and PEDOT:CS 1:2 suspensions were sonicated for 15 minutes prior to drop-casting. PEDOT:CS 1:1 and PEDOT:CS 1:2 aqueous suspensions (2% (w/w)) were drop-cast on to fluorine doped tin oxide (FTO) glass and spread with a pipette to form even films across the surface (approximately 1 cm  $\times$  3 cm). This was repeated four times for each PEDOT:CS sample giving a total of eight samples. The samples were air dried for 30 minutes, then dried in the oven at 100  $^{\circ}\text{C}$  for ten minutes. All eight samples were carefully submerged in a crosslinking mixture comprising of ethanol (24  $\text{cm}^3$ ) and EDC solution (0.087 mol  $\text{dm}^{-3}$ , 6  $\text{cm}^3$ ) for one hour. The samples were then carefully rinsed in water, and air dried for 30 minutes.

### 4.2.4 UV spectroscopy

UV spectroscopy was undertaken on diluted PEDOT:CS 1:1 (new) and PEDOT:CS 1:2 dispersions, and PEDOT:CS 1:1 (new) and PEDOT:CS 1:2 crosslinked film samples on FTO glass. UV spectra of PEDOT:CS 1:1 (new) and PEDOT:CS 1:2 crosslinked film samples on FTO glass were measured again, following 3 days of submersion in water.

UV absorption spectra were collected with a JASCO V 750 and V 570 UV-vis spectrophotometers.

### 4.2.5 Electrochemical impedance spectroscopy

For EIS, Kapton tape was used to isolate an approximately 1  $\text{cm}^2$  area of the PEDOT:CS drop-cast film samples on FTO glass. This allows only the 1  $\text{cm}^2$  exposed area of PEDOT:CS film to contact the buffer solution during electrochemical characterisation, as well as ensuring none of the FTO glass was in contact with the buffer solution which could skew the results and not reflect the true electrochemical behaviour of the PEDOT:CS.

EIS were carried out using a Reference 600 potentiostat (Gamry Instruments) connected to a three-electrode electrochemical cell with a large-area Pt foil as a counter electrode and a Ag/3 M AgCl reference electrode (+0.197 V vs normal hydrogen electrode, NHE). The test sample acted as the working electrode, and the EIS was undertaken in saline solution (0.9% NaCl w/w in water). EIS was performed at 0 V by superimposing a voltage sine wave modulation (10 mV RMS amplitude) within the frequency range of 105-10<sup>-1</sup> Hz.

The samples were stored in water for 3 days and then EIS was repeated.

## 4.2.6 Synapstor preparation and characterisation

### Sample preparation

PDMS films were prepared on glass microscope slides. The microscope slides were cleaned prior to casting PDMS by sonication in ethanol and *iso*-propanol. The PDMS (PDMS:curing agent 9:1) was spin-cast on the glass substrates (3 minutes at 500 rpm) and cured in the oven for one hour at 120 °C. PEDOT:CS 1:1 (new) aqueous suspension (50 µl) was spin-coated (500 rpm for 5 seconds, then 1500 rpm for 20 seconds) on to the PDMS. This was repeated for six substrates to give six samples. The PEDOT:CS layer was then crosslinked by submerging all six samples overnight in a crosslinking mixture, prepared from EDC solution (0.043 mol dm<sup>-3</sup>, 6 cm<sup>3</sup>) and ethanol (24 cm<sup>3</sup>). The following day the samples were carefully rinsed with water and dried in the oven for approximately two hours at 50 °C.

Direct laser ablation with a short-pulsed Nd:YAG laser (centre wavelength 1064 nm, pulse width 10 ns, peak power 3 kW) with computer-aided design-driven laser scan marker ScribaR (Scriba Nanotecnologie S.r.l., Bologna, Italy) was used to pattern the spin-cast PEDOT:CS films on PDMS to create an electrode pattern in the PEDOT:CS film as seen in figure 4.17.

### Short-term plasticity characterisation

The electrolyte solution used in these experiments was PBS (50 mM, as in the OECT experiments). Each measurement was performed after a 180 second delay to allow the device to reach steady state. As shown in figure 4.17, the laser ablated pattern of the PEDOT:CS film gave two electrodes, E1 and E2. E2, acting as the presynaptic electrode, was pulsed with a square wave of -200 mV unipolar pulses at 500 Hz with a pulse width of 1 ms for a total time of 2 seconds (1 second of buffer time, and 1 second of measurement). The displacement current at E1 (post-synaptic electrode) was recorded to observe whether any STP depressing behaviour was observed.

## 4.2.7 Scaffold preparation by lyophilisation

### GOPS crosslinked scaffolds

A range of solutions were prepared from PEDOT:CS (1:1, 1:2, 1:3) and PEDOT:HA (1:1) 2% (w/w) aqueous dispersions as described by table 4.1.

Six 150 µl volumes of each prepared solution was pipetted into six individual wells of a 96 multiwell-plate, giving a total of six samples per solution. The multi-well plate was transferred to the freeze-dryer (Virtis SP Scientific AdVantage BenchTop Freeze Dryer) and the samples were lyophilised using the following protocol. The samples were frozen to -40 °C, cooling at a rate of -20 °C per hour. The ice was then sublimed from the samples and the scaffolds then dried for ten hours with the temperature increasing from -40 °C to 0 °C at a controlled rate of 1 °C per minute, under vacuum at 80 mtorr. The scaffolds were then annealed on a hot plate at 50 °C for 8 hours.

**Table 4.1:** Composition of solutions prepared for freeze-drying to form GOPS crosslinked PEDOT:biomolecule scaffolds.

Sample	Aqueous dispersion	Volume of aqueous dispersion / $\mu\text{l}$	Volume of GOPS / $\mu\text{l}$	Volume of ethylene glycol / $\mu\text{l}$
A	PEDOT:CS (1:1)	1000	20	100
B	PEDOT:CS (1:1)	1000	20	0
C	PEDOT:CS (1:2)	1000	20	100
D	PEDOT:CS (1:2)	1000	20	0
E	PEDOT:CS (1:3)	1000	20	100
F	PEDOT:CS (1:3)	1000	20	0
G	PEDOT:HA (1:1)	1000	20	100
H	PEDOT:HA (1:1)	1000	20	0

### EDC-crosslinked scaffolds

PEDOT:CS (1:1) and PEDOT:HA (1:1) 2% (w/w) aqueous dispersions (400  $\mu\text{l}$ ) were pipetted into the individual wells of a 96 multiwell-plate. The multi-well plate containing the samples was transferred into the freeze-dryer. The same lyophilisation protocol was used for these samples as for the GOPS crosslinked samples.

Unlike the GOPS crosslinked samples, these scaffolds contained no crosslinker during lyophilisation, so the EDC-crosslinking step was required after the PEDOT:CS and PEDOT:HA were freeze-dried. Following lyophilisation, a crosslinking mixture was prepared from EDC (0.10 g, 0.52 mmol) and an 75:25 ethanol:water mixture (10  $\text{cm}^{-3}$ ). The crosslinking solution (400  $\mu\text{l}$ ) was pipetted over the individual PEDOT:CS and PEDOT:HA scaffolds in the wells and left for 24 hours for crosslinking to occur. After 24 hours, attempts were made to pipette the crosslinking mixture out of the wells without disturbing the scaffolds. No further steps were taken to rinse or dry the material.

## 4.3 Results and discussion

### 4.3.1 OECT device characterisation and optimisation

Following on from the work presented in chapter 3, the aim of this chapter was to develop and improve the performance of the PEDOT:biomolecule OECT device. One such method to improve device performance was to alter the electrode geometry to maximise  $W/L$  ratios. For these experiments, this was achieved by using quartz substrates with interdigitating gold electrodes (gold thickness of 50 nm). The  $W/L$  ratio of these electrodes was 2000 compared to 33.3 for the electrodes used in chapter 3. A photo of the substrates can be seen in figure 4.2.

Additionally, the effect of the age of the PEDOT:CS sample used in the OECT was tested. An older PEDOT:CS 1:1 aqueous suspension, referred to here as PEDOT:CS 1:1 (old), that was synthesised six weeks prior to this testing was compared with a newer equivalent sample, PEDOT:CS 1:1 (new) that had

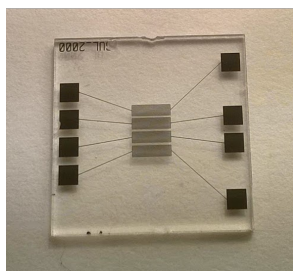


**Figure 4.2:** Photo of the quartz substrates used in OECT characterisation.

been prepared one week prior to testing. OECTs prepared from the older PEDOT:CS sample had previously demonstrated transistor behaviour when tested after synthesis. Unlike some PEDOT:biomolecule films on the glass substrates used in chapter 3, drop-cast samples on quartz substrates did not delaminate at any point during the experiments. The crosslinked samples were assessed for OECT behaviour. Each quartz substrate had a test pattern with four pairs of electrodes with channels between them. This meant that each sample was tested at least four times (at least once across each set of electrodes). The more recently synthesised PEDOT:CS 1:1 (new) sample demonstrated OECT behaviour within the given parameters. This is shown in figure 4.3. There were four pairs of electrodes on the substrates so four transfer curves were obtained for PEDOT:CS 1:1, however the data for one of the positions (in green on figure 4.3) demonstrated little modulation of the source-drain current. This was thought to be due to poor coverage of the channel with PEDOT:CS. The individual plots for each electrode position are also given in figure 4.4 with the related transconductance values also plotted.

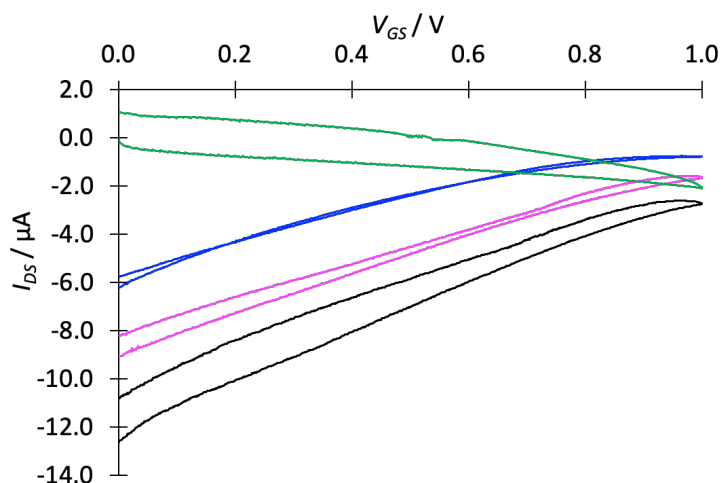
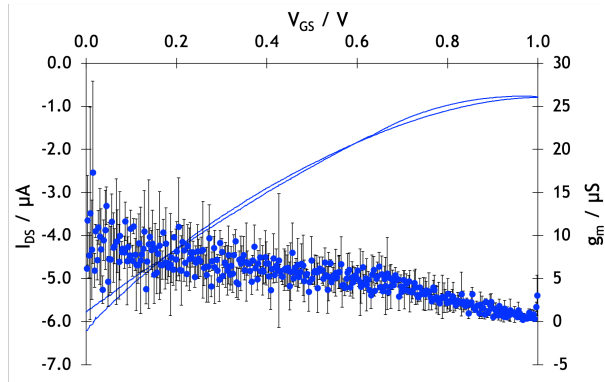
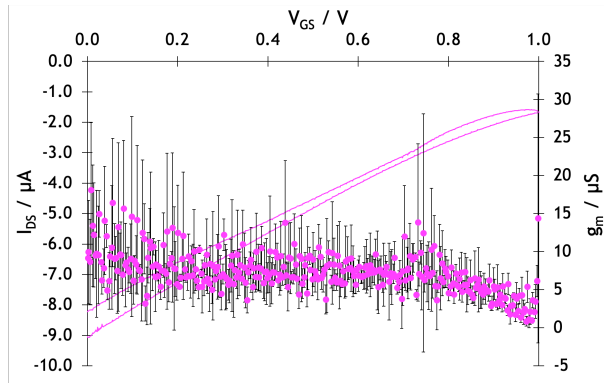


**Figure 4.3:** Transfer curves for a PEDOT:CS 1:1 based OECT. Each different coloured curve is from a different pair of electrodes on the quartz substrate ((a) blue, (b) pink, (c) black, (d) green).

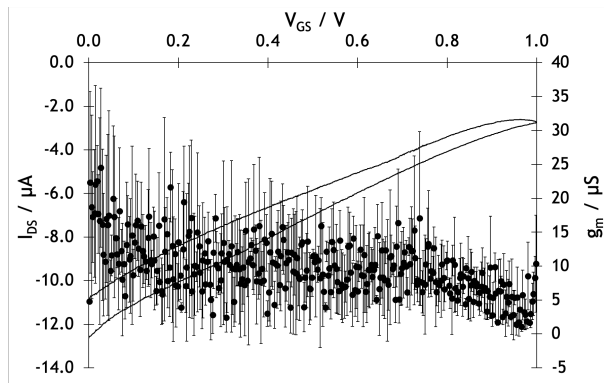
The maximum transconductance for these data was  $17.3 \mu\text{S}$ ,  $18.1 \mu\text{S}$ , and  $24.5 \mu\text{S}$  for data set a, b, and c from figure 4.3 respectively. The ON/OFF ratios were 7.9, 5.4, and 4.6 for data set a, b, and c from figure 4.3 respectively. The ON/OFF ratios were calculated from the upwards sweep of gate voltages as there was hysteresis seen in the curves, and no ON/OFF ratio was calculated for set of data in green on figure 4.3 (d). For comparison, the maximum transconductance obtained in the proof of concept testing in section 3.3.4 was  $50.5 \mu\text{S}$  however this value was obtained from an OECT operating at  $V_{DS}$  of 0.8 V. The maximum transconductance obtained for the equivalent  $V_{DS}$  of  $-0.4 \text{ V}$  was  $35.1 \mu\text{S}$ , and the ON/OFF ratio for the equivalent  $V_{DS}$  of  $-0.4 \text{ V}$  was 2.6. This new data showed no improvement in



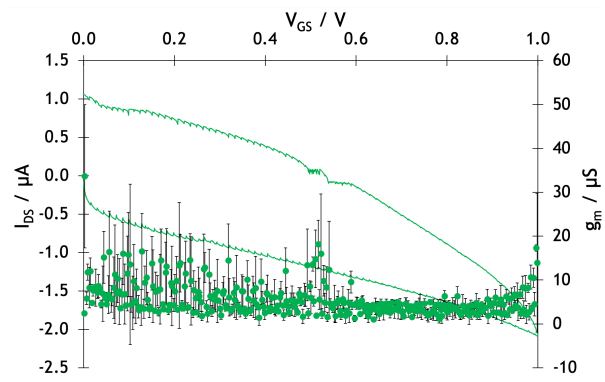
(a)



(b)



(c)



(d)

**Figure 4.4:** Individual transfer curves (lines) from figure 4.3 with the transconductances ( $g_m$ ) (points). The colours match the equivalent transfer curve on figure 4.3.

maximum transconductance, but did see an increase in the ON/OFF ratios. The increase in ON/OFF ratio, however, does not improve the device to the level of PEDOT:PSS OECTs which even in the worst cases can be around 70 [200]. The hysteresis in the source-drain current was attributed to asymmetry in the dedoping and doping processes involved in the operation of the OECT [131].

Additionally, it was observed that the OECT devices did not reach a fully OFF state (zero source-drain current in an ideal transistor) which was also observed in the previous measurements. It was expected from previous data (section 3.3.4) that a greater gate voltage ( $> +0.6$  V) was required to drive the OECT to a fully OFF state. These measurements probed a greater range of gate voltages up to 1.0 V and the phenomenon was still observed. There was, however, evidence that the source drain current ( $I_{DS}$ ) was reaching a plateau towards these higher gate voltages which indicated that the OFF state was beginning to be probed.

No transistor response could be obtained from the PEDOT:CS 1:3 sample or the PEDOT:HA 1:1 sample. It was suspected that the PEDOT:CS 1:3 ratio sample contained so little PEDOT relative to CS as the dispersions were also prepared to 2% solids that no response could be achieved. It was demonstrated that PEDOT:HA 1:1 was conductive in chapter 3. Although uncrosslinked PEDOT:HA had a best sheet resistance 100 times that of PEDOT:CS 1:1, it was expected to show OECT behaviour in these experiments. The HA is thought to act as a less effective counter-ion than CS to the doped PEDOT due to the lack of sulfate moieties which are analogous to the sulfonate groups found on PSS [168], leading to the lack of response. Additionally, the older of the two PEDOT:CS 1:1 samples (PEDOT:CS 1:1 (old)) did not give any transistor response. When tested, these samples saw large gate leakage ( $I_{GS}$ ) which was of the same magnitude as the source-drain current ( $I_{DS}$ ) (figure 4.5). This behaviour meant that the change in gate voltage was not modulating the source-drain current and therefore the sample was not acting like an OECT. The older PEDOT:CS 1:1 had previously been used in an OECT that demonstrated transistor behaviour when tested after immediately following synthesis. This result implied that the PEDOT:CS degraded in the aqueous dispersions over time, probably due to dissolution of CS resulting in dedoped material.

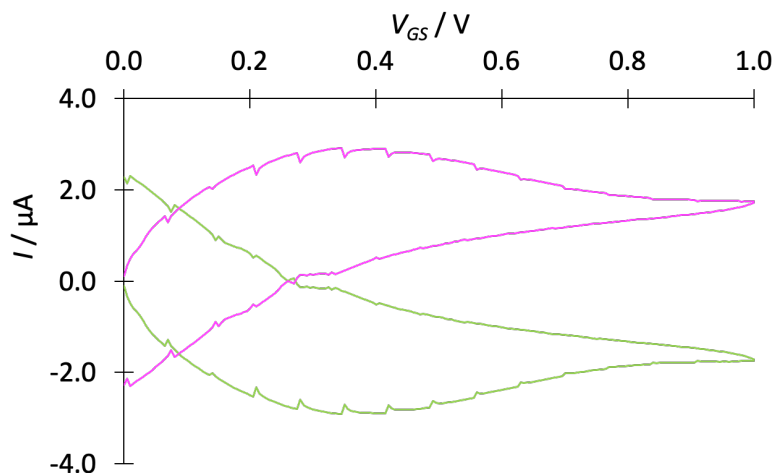


**Figure 4.5:** An example of the gate leakage phenomena observed for the old PEDOT:CS 1:1 sample and the PEDOT:CS 1:3 ( $I_{DS}$  = green line,  $I_{GS}$  = pink line).

From these data, it appeared that the interdigitating electrodes did not have any significant effects on the characteristics of the OECT devices, although an increase was seen in the ON/OFF ratios compared

to the original proof of concept data (section 3.3.4).

To summarise, PEDOT:CS 1:1 was demonstrated to function as the organic electronic material in an OECT device beyond the initial proof of concept. New quartz substrates with a  $W/L$  ratio of 2000 were used in these experiments, compared to 33.3 for the electrodes used in chapter 3. The transconductance did not see an overall increase although the ON/OFF ratios of the OECTs did increase two to three-fold compared to the original data collected on the substrates with a significantly smaller  $W/L$  ratio. In future, further different electrode configurations should be tested to work towards optimisation of the OECT devices. This would ideally consist of a greater number of interdigitating electrodes to maximise the  $W/L$  ratio. Additionally, further characterisation of the PEDOT:CS material itself would yield insight to allow further optimisation to be achieved. For this reason, UV spectroscopy and EIS was carried out on PEDOT:CS samples.

### 4.3.2 UV spectroscopy

For further optimisation of the device to be successful, it was important to understand the conductivity of the PEDOT:biomolecules. PEDOT:CS demonstrated conductivity exemplified by the best case sheet resistance for a drop-cast uncrosslinked film of  $4.7 \text{ k}\Omega\text{cm}^{-1}$ , however this value increased dramatically upon crosslinking. To try and understand the changes, UV spectroscopy and EIS were performed.

Mantione *et al.* [168] performed UV-visible-near IR spectroscopy on PEDOT:CS and PEDOT:HA of various ratios, among other PEDOT:glycosaminoglycan samples. The authors compared the UV spectra of these PEDOT:glycosaminoglycans with the UV spectra of PEDOT:PSS. In the PEDOT:PSS spectrum (as seen in figure 4.6), Mantione *et al.* [168] observed an absorption band centred around 800 nm which the authors attributed to PEDOT  $\pi - \pi^*$  interactions as well as a broad band centred at 1150 nm assigned as a polaron band. However, it is typical that a band centred around 1200 nm would be assigned as a bipolaron band in PEDOT:PSS UV-vis spectra with bands centred around 900 nm and 600 nm as the polaron band and undoped PEDOT band, respectively [144, 203–205]. The authors compared the PEDOT:PSS spectra with those for the PEDOT:glycosaminoglycans and observed a band centred at 700 nm that they assigned to PEDOT  $\pi - \pi^*$  interactions, similar to the PEDOT:PSS. On the other hand, the other band at 1150 nm was less intense. An additional typical PEDOT:PSS UV spectrum (taken from Gangopadhyay *et al.* [205]) can also be seen in figure 4.6.

UV spectroscopy was carried out on dilute samples of PEDOT:CS 1:1 and PEDOT:CS 1:2 (2% (w/w)) aqueous dispersions. PEDOT:CS samples of greater ratios and PEDOT:HA were not characterised. The spectra for PEDOT:CS 1:1 and 1:2 were very similar (figure 4.7), however this was expected as the only difference was the amount of CS in the sample. The UV spectroscopy undertaken here did not extend into the near-IR so comparison to the Mantione *et al.* [168] data beyond 900 nm was not possible. Additionally, the spectrometer did not probe the spectrum beyond 200 nm, so the spectra seen in figure 4.7 only display data between 200 and 900 nm. The PEDOT:CS spectra were both similar to a typical PEDOT:PSS UV spectrum taken from the literature [205] with a similar broad, but shallow, peak centred around 800 nm. Mantione *et al.* [168] attributed a similar band in the PEDOT:biomolecule UV-vis spectra around 800 nm to PEDOT  $\pi - \pi^*$  interactions, however it is suggested that the presence of this band should be attributed to PEDOT in the polaron state [144, 203–205]. The band centred about 825 nm in figure 4.7 was therefore attributed to PEDOT in the polaron state.

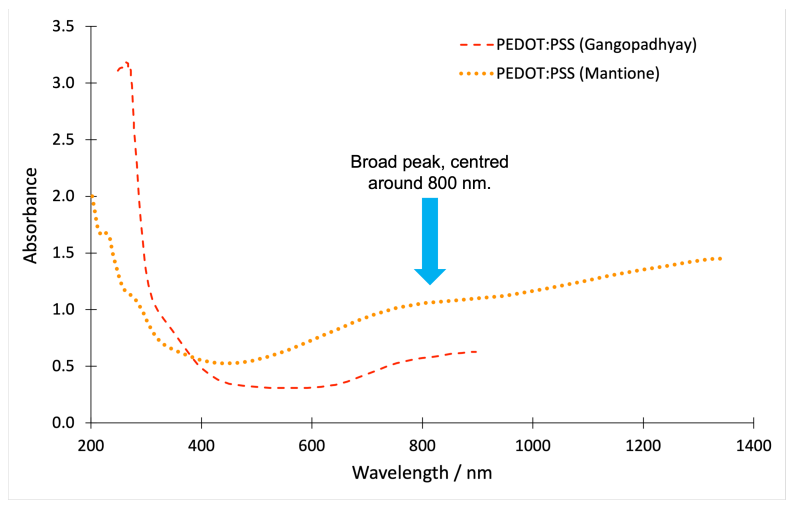


**Figure 4.6:** Typical PEDOT:PSS UV spectra from literature sources. The red dashed spectrum was taken from Gangopadhyay et al. [205] and the orange dotted spectrum was taken from Mantione et al. [168]

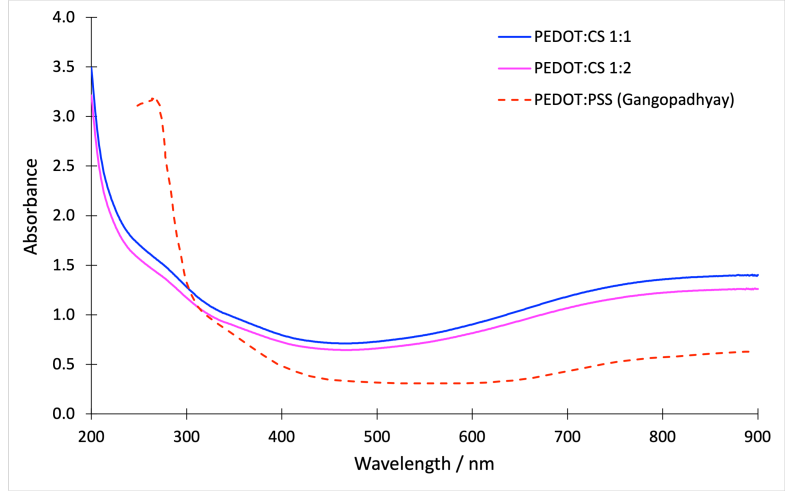


**Figure 4.7:** UV spectra of PEDOT:CS 1:1 aqueous dispersions (blue) and PEDOT:CS 1:2 aqueous dispersions (pink). In both, a broad band centred around 825 nm can be seen, forming a curved shape in the spectra at the higher wavelengths. A typical UV spectrum for PEDOT:PSS [205] is seen as the red, dashed plot as a comparison.

These UV spectra offered some insight into PEDOT:CS, however it was important to examine the materials in a crosslinked film to identify any evidence as to why the crosslinking affected the sheet resistances so dramatically. The UV spectra of crosslinked film samples of PEDOT:CS can be seen in figure 4.8.

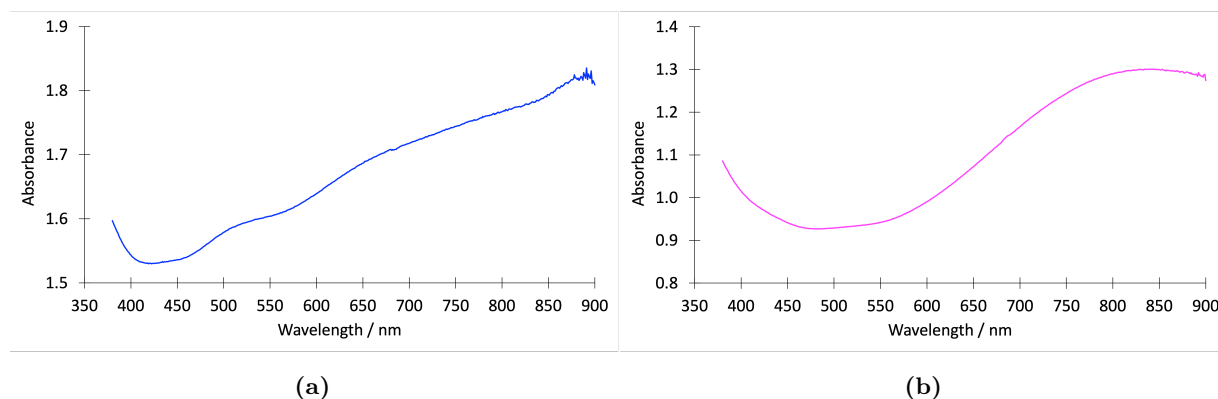


**Figure 4.8:** UV spectra of PEDOT:CS 1:1 crosslinked film (a, blue) and PEDOT:CS 1:2 crosslinked film (b, pink).

There were differences in the level of absorption for the two different PEDOT:CS samples, attributed to variation in film thickness. Both spectra had a broad peak centred around 825 nm again although it was challenging to identify for the PEDOT:CS 1:1 sample. In addition, there was a small ‘shoulder’ centred around 510 nm that was present in both spectra but was more clearly defined in the PEDOT:CS 1:1 sample. This was attributed to neutral undoped PEDOT [144, 203–205]. The change in doping state of the PEDOT in the PEDOT:CS films that occurred as a result of the crosslinking step would explain the increases in the sheet resistance upon crosslinking seen in chapter 3. If, following crosslinking, there is less doped PEDOT available in the samples, there will be less conductivity and thus a higher sheet resistance.

The EDC coupling methodology employed to crosslink these films was not known to have compatibility issue with PEDOT, however it is possible that EDC-crosslinking resulted in less CS available to act as a counter-ion for the positively charged doped PEDOT. It was assumed that the sulfate groups on the CS were responsible for the counter-ion effects as they would be analogous to sulfonate groups on PSS in PEDOT:PSS, however the carboxyl groups of the CS may also contribute. By crosslinking the CS using EDC, the carboxyl groups are utilised to form crosslinking ester bonds. If this is the case, it could lead to CS performing less effectively as a counter-ion, and therefore limit doping in the PEDOT.

To probe this behaviour further, EIS was completed on the PEDOT:CS crosslinked films.

### 4.3.3 Electrochemical impedance spectroscopy

EIS was introduced in the experimental techniques chapter as a analysis tool that can be used to examine the complex impedance of a material versus frequency. In the case of the work presented here, EIS was used to follow the ionic and ohmic (or electronic) contributions to the conductivity of the PEDOT:biomolecule materials.

EIS was undertaken on the crosslinked PEDOT:CS 1:1 sample prepared on fluorine doped tin oxide (FTO) glass and impedance data were collected. Unfortunately, it was not possible to complete EIS on

uncrosslinked samples as the technique required aqueous conditions which would have lead to sample dissolution. The EIS data supported the findings of the UV spectroscopy as it appeared that the crosslinked PEDOT:CS 1:1 was present in its non-conducting undoped form. This was illustrated by the dominating charge transfer event that was present in the Nyquist plot (figure 4.9). This was attributed to charge transfer between the sample film and the substrate. Additionally, the phase angle (figure 4.10) of the impedance was equal to zero in the low frequency domain which also indicated a lack of ionic conductance that is typical of conducting polymers. Finally, the ohmic resistance or real impedance ( $Z'$ ) was high (seen in figure 4.10) which indicated low conductivity. Both Nyquist and Bode plots were introduced in section 2.4.2 in the experimental techniques chapter.

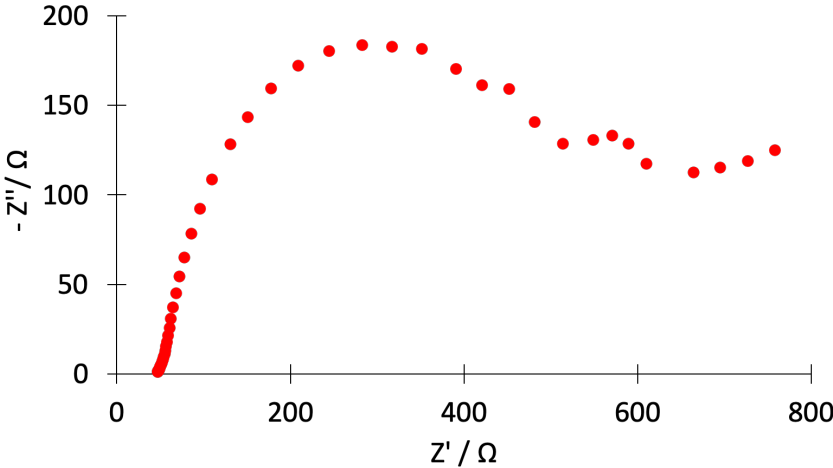


**Figure 4.9:** Nyquist plot produced from EIS data on PEDOT:CS 1:1 crosslinked film.

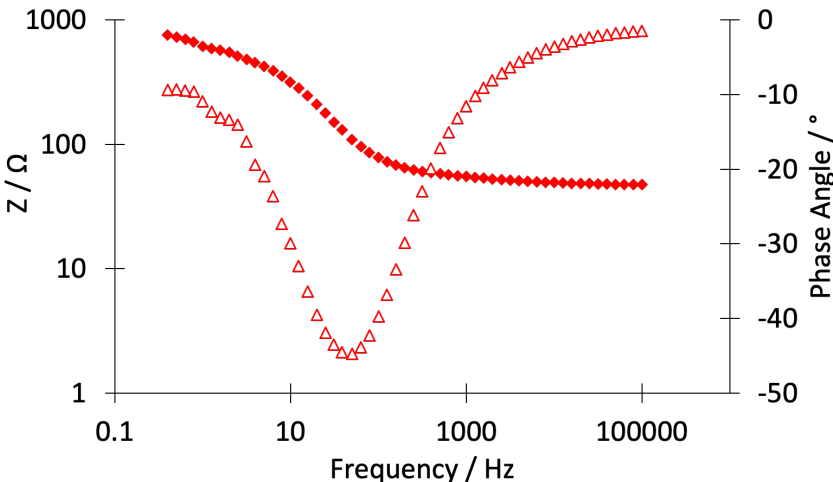


**Figure 4.10:** Bode plot (solid red diamonds) and phase angle (unfilled triangles) produced from EIS data on PEDOT:CS 1:1 crosslinked film.

It was observed during EIS that the PEDOT:CS films appeared to be purple in colour which also indicated the presence of PEDOT in its reduced non-conducting form as oppose to blue/black films which would indicate PEDOT was in its oxidised conducting form.

#### 4.3.4 Degradation of PEDOT:CS films and OECT devices

One of the aims of the work presented in this thesis was to develop a degradable OECT device. This was approached by using CS and HA as alternative counter-ions to PSS for PEDOT. CS and HA are both native to the human body and thus have their own biological degradation pathways through the action of enzymes. Additionally, the choice of EDC-crosslinking was taken as this method formed degradable ester crosslinks between the CS or HA molecules in the PEDOT:CS or PEDOT:HA films that formed the channel of the OECT. In chapter 3, PEDOT:CS 1:1 was successfully demonstrated to function as the organic electronic material in an OECT device. Experiments presented earlier in this chapter demonstrated this further, however until this point, the degradability of the devices had not been investigated.

Simple experiments were carried out to assess how the OECT device performance changed following 3 days of submersion in water. Concurrent experiments were carried out on PEDOT:CS films so that the effects could be assessed by UV spectroscopy and EIS. Additionally, these experiments acted to probe whether conductivity could be recovered through degradation of the ester crosslinks in the PEDOT:CS films. The degradation experiments were carried out on PEDOT:CS 1:1 OECT device samples, and the PEDOT:CS 1:1 and 1:2 films on FTO glass from UV/EIS experiments.

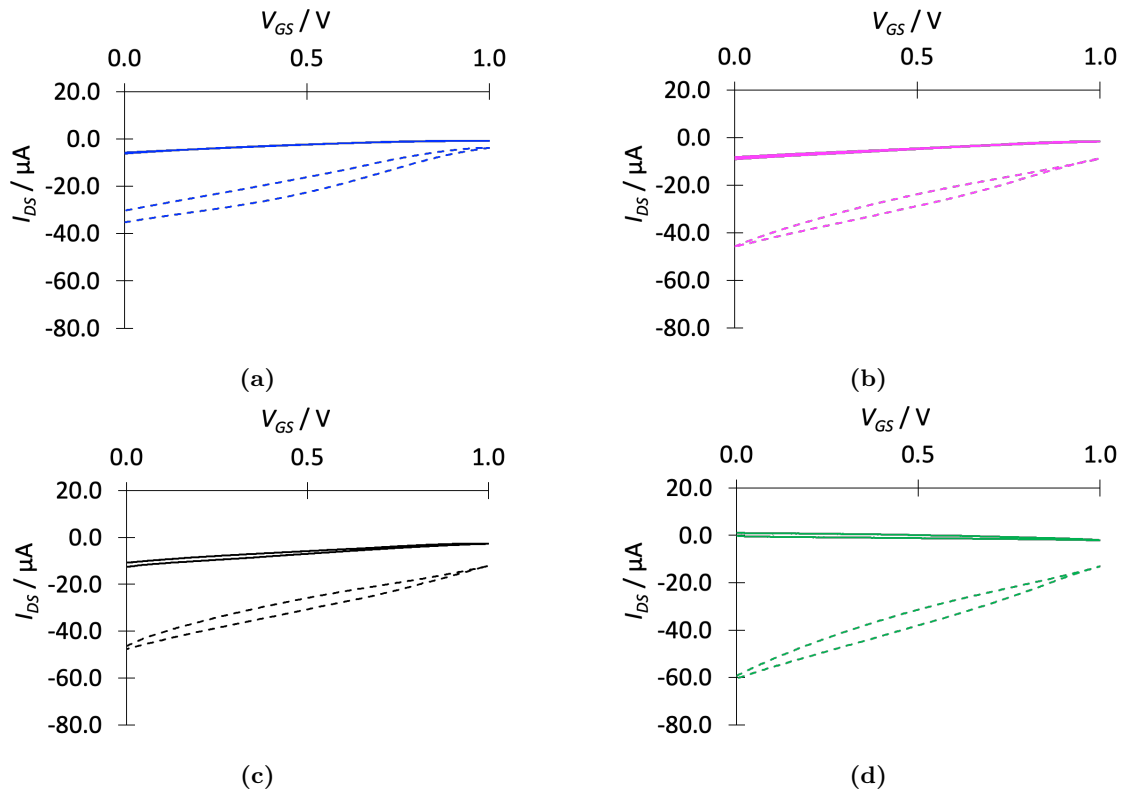


**Figure 4.11:** Transfer curves for PEDOT:CS 1:1 based OECTs with data prior to submersion in water (solid line) and following the submersion in water for 3 days (dashed line). The colours indicate matching data on figure 4.3.

Figure 4.11 shows that all of the OECTs demonstrated a marked increase in performance following submersion in water for 3 days, with the maximum output current ( $I_{DS}$ ) increased up to five-fold. Notably, the electrode position that did not previously show any transistor behaviour prior to the degradation experiment (in green on figure 4.3) began to demonstrate OECT behaviour following the 3 day submersion

in water. The maximum transconductance (table 4.2) increased across all of the OEET device electrode pairs compared to those from the same device prior to submersion in water for three days, whereas the ON/OFF ratios remained approximately similar.

**Table 4.2:** Characteristics of PEDOT:CS 1:1 OEETs after submersion in water for 3 days. The electrode positions correspond to the figure labels on figure 4.11.

Electrode position	Maximum transconductance / $\mu\text{S}$	ON/OFF ratio
(a)	53.1	9.4
(b)	78.0	5.2
(c)	70.8	3.8
(d)	90.5	4.5

A short-term increase in PEDOT:PSS-based transistor performance due to swelling has been observed [55]. A similar increase in performance was observed for the PEDOT:CS OEET with the degradation of the tightly bound matrix resulting increased swelling of the crosslinked film. Fewer crosslinks would lead to a more open porous structure within the PEDOT:CS film, leading to more facile ion diffusion increasing the conductivity. Additionally, this effect supported the assertion that the act of crosslinking the films in the first place decreased conductivity due to the formation of a tightly bound matrix. The swollen matrix (through either degradation of crosslinks, or simple swelling itself) resulted in a recovery of conductivity and improved device performance. EIS and UV spectroscopy was undertaken on the PEDOT:CS samples that had been submerged in water for 3 days to examine changes in the PEDOT:CS that caused this increase in OEET performance.

After 3 days submerged in water, EIS was repeated on the PEDOT:CS 1:1 (new) sample and the results can be seen in figures 4.12, 4.14, and 4.13. There was a shift in the charge transfer event seen in the Nyquist plot prior to the 3 day submersion. The large charge transfer no longer dominated the data and the Nyquist plot consisted of a much smaller semi-circle at much lower impedances (figure 4.12). The increasing linear section following the semi-circular shape in the plot was typical of capacitive behaviour, which indicated ionic conduction expected of conducting polymers. Furthermore, this result was supported by the change in the phase angle. There was a shift to a more negative angle (relative to zero) at low frequencies (figure 4.14) which suggested that diffusion of ions through pores was facilitated. Additionally, figure 4.13 shows that the ohmic resistance (the real part of impedance) decreased, signposting an increase in conductivity.

From the EIS data, it is clear that the 3 day submersion in water triggered ionic conduction within the PEDOT:CS sample that did not occur prior to the submersion. This supported the suggestion that the OEET performance improvements were a result of increased swelling of the crosslinked film like the short-term increase in PEDOT:PSS-based transistor performance due to swelling reported by *Hempel et al.* [55] The specific mechanism of the hypothesised swelling is not clear. It could be due to the breakdown of the crosslinking ester bonds in the CS, providing more flexibility in the sample and larger pores allowing movement of ions through the material, or swelling alone, or a combination of the two effects.

UV spectroscopy was also carried out on the crosslinked PEDOT:CS film samples following the 3-days submersion in water and changes were also observed in the spectra. Figure 4.15 shows the changing spectra for the crosslinked PEDOT:CS 1:1 film with the dark blue plot showing the original spectrum obtained. The cyan spectrum was for the same sample after the 3 day submersion in water when the

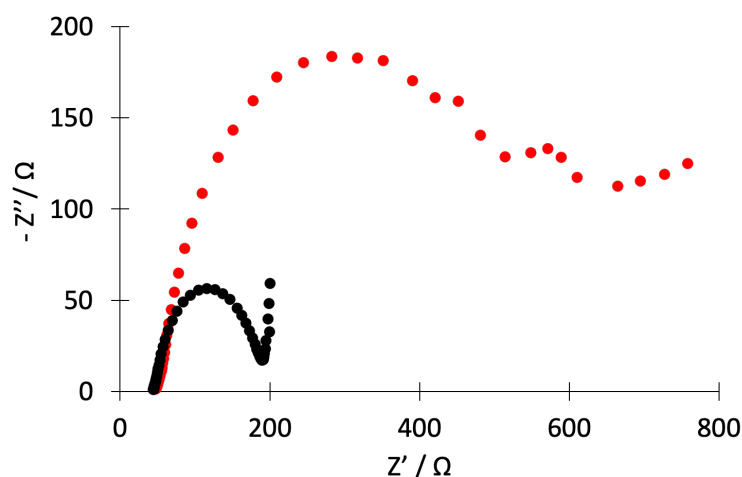


**Figure 4.12:** Nyquist plot produced from EIS data on PEDOT:CS 1:1 crosslinked film with the initial measurements in red, and the measurements following sample submersion in water in black.

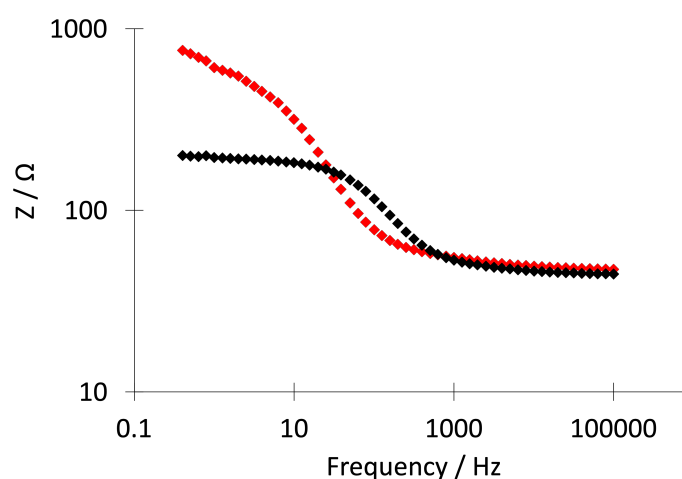


**Figure 4.13:** Bode plot produced from EIS data on PEDOT:CS 1:1 crosslinked film with the initial measurements in red, and the measurements following sample submersion in water in black.

film was dry, whereas the green plot shows the same sample whilst wet immediately following EIS. In the wet sample spectra, there was a rounded peak centred around 825 nm which indicated the presence of the PEDOT polaron. This suggested that EIS at 0 V (vs. Ag/AgCl) oxidised the film from the neutral undoped state to a more conducting state that was now accessible due swelling and/or to breakdown of bonds due to submersion in water for 3 days, creating larger pores allowing ion movement and thus ionic conductivity. The measurement was repeated after the sample air dried (figure 4.15, cyan spectrum) and the polaron peak centred around 825 nm was no longer visible. The shoulder seen in the spectrum for the undoped state centred around 510 nm started to appear in the spectrum suggesting that the sample was spontaneously reduced in air back towards the neutral undoped state. The mechanism of this reduction was not clear.

On the other hand, the crosslinked PEDOT:CS 1:2 film sample (figure 4.16) appeared to be more stable as the UV spectra from before and after the 3-day submersion in water appeared similar. The curved peak centred around 825 nm was present in the dry crosslinked PEDOT:CS 1:2 film samples both before

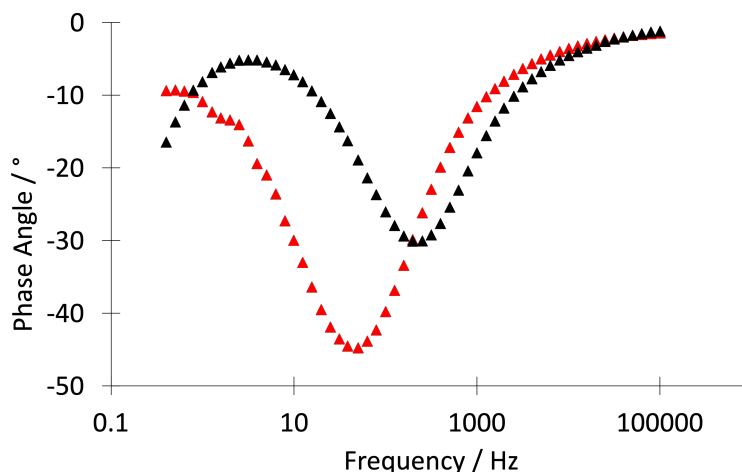


**Figure 4.14:** Phase angles plot produced from EIS data on PEDOT:CS 1:1 crosslinked film with the initial measurements in red, and the measurements following sample submersion in water in black.

and after the 3 day submersion in water. A slight increase in the absorbance for the peak centred around 510 nm was observed following the 3-day submersion in water. This suggested that there was an increase in neutral undoped PEDOT present in the sample. No measurements were taken on wet PEDOT:CS 1:2 samples.

From these data, it can be concluded that the crosslinked PEDOT:CS 1:1 films did not initially show ionic conductivity, unlike a typical conducting polymer that acts as an ionic-ohmic conductor. The EIS and UV data together suggested that the submersion of the PEDOT:CS crosslinked samples in water for 3 days improved the conductivity of the material and caused the material to act more like an ionic-ohmic conductor. This was likely due to swelling of the films themselves, or degradation of the crosslinking ester bonds in the CS, providing more flexibility in the samples leading to larger pores allowing movement of ions through the material. This explained the increase in OECT performance observed after the 3 days submersion in water.

On balance, the swelling of the film was the more likely reason for the changes observed in the OECT behaviour, EIS data, and UV spectra following 3-days of submersion in water. PEDOT:PSS-based transistor devices have been observed to have an increase in device performance due to swelling in the short-term followed by a decrease due to decohesion of the device [55]. Additionally, there were no observations of PEDOT:CS delamination or dissolution over the 3 day submersion period in any of the samples which implies little, if any, degradation of the actual material. Nevertheless, further examination of this behaviour is required in future. It is hypothesised that the increase in performance of the OECT devices observed here would be followed by a decrease as the PEDOT:CS film begins to degrade, delaminate, and dissolve into solution. Furthermore, future experiments should use more controlled conditions including temperature control (37 °C) and pH 7.4 buffered solutions to mimic basic physiological conditions.

The aim of the work in this thesis was to create a biocompatible, biodegradable, and mechanically appropriate OECT device that would be suitable for use in the CNS. Although experimentation with cell lines is required to prove that PEDOT:CS is truly biocompatible, literature evidence [168, 180] demonstrates that the choice of CS as a counter-ion to PEDOT is likely to fulfil the compatibility and

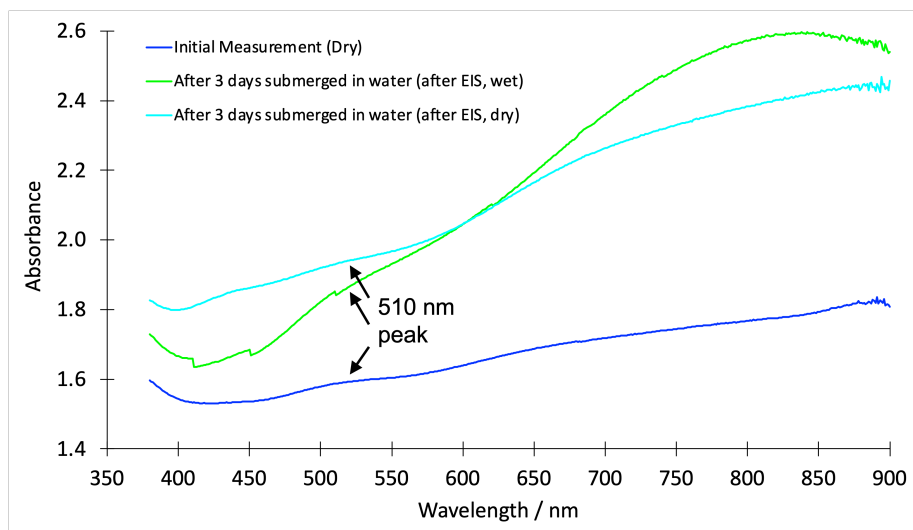


**Figure 4.15:** UV spectra of PEDOT:CS 1:1 crosslinked film with the initial data collected in dark blue, the spectrum of the sample following submersion in water whilst wet in green, and after the film had dried in cyan. The peak at 510 nm is labelled.

biodegradability requirements. EDC coupling was chosen due to the degradable ester bonds that form the crosslinks. The results and discussion presented in this section begin to explain how a PEDOT:CS OECT device behaves when submerged in water for a period of time. The changes seen in the behaviour of the PEDOT:CS OECTs and the changes in the UV and EIS data suggests some change PEDOT:CS itself, likely swelling of the film. To probe this in future and quantify the rate at which the PEDOT:CS degrades, further experimentation is required, such as measuring the water uptake of the films over time and tracking any chemical changes in the crosslinked films using IR spectroscopy, for example. Furthermore, the desired lifetime of a PEDOT:CS OECT device in the body will depend on its exact use. A short-term diagnostic tool for monitoring SCIs may be only required to function for a few days whereas a more long-term use may require functionality for weeks, months, or years. These considerations should be noted when conducting further work in future.

The PEDOT:CS based OECT requires further optimisation to improve device performance, but in addition, little attention has been paid thus far to the mechanical properties requirement. The work presented in chapter 5 addresses this through use of hydrogels.

### 4.3.5 Synapstor preparation

Having proved again that PEDOT:CS was a potential material offering biodegradability and biocompatibility for use in an OECT which in future could be useful in the treatment of SCIs, the use of PEDOT:CS in a synapstor device was explored. If a synapstor were developed that were able to interface directly with neurons, it could be used as an artificial synapse which could offer direct neuron to silicon communication technology. Such interfacing would be revolutionary in the treatment of injuries and diseases of the nervous system (for example, SCIs). A synapstor prepared from PEDOT:CS would benefit from the biocompatibility and degradability afforded by the use of the biomolecule counter-ion, opposed to the PSS counter-ion to PEDOT. The improved biocompatibility could offer improved cell-growth on the synapstor which could improve interfacing outcomes.

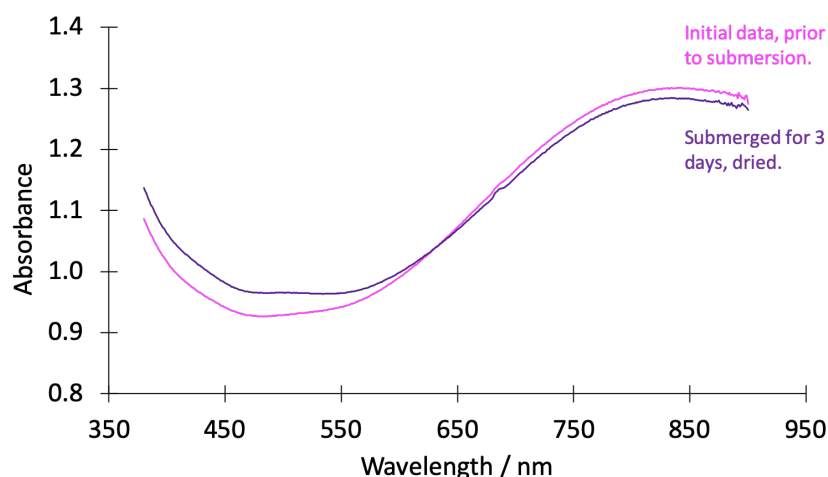


**Figure 4.16:** UV spectra of PEDOT:CS 1:2 crosslinked film with the initial data collected in pink and the spectrum of the sample following submersion in water after the film had dried in purple.

A method of preparing synapstors using laser ablation of thin films of PEDOT:PSS was reported in 2017 [131, 133]. The laser ablation technique was originally used to pattern gold films on poly(lactic-*co*-glycolic acid) substrates [206] to form interdigitating gold electrodes for a water-gated organic field-effect transistor. Outside of the scope of synapstors, this technique could be used in future to pattern electrodes onto the HA hydrogels discussed in chapter 5. For the synapstor devices, laser ablation was used to pattern PEDOT:PSS electrodes onto PDMS substrates [131, 133]. Equivalent experiments were undertaken on PEDOT:CS films as a first step towards creating a synapstor from an organic electronic material (PEDOT:CS) that offers a biocompatibility and biodegradability that PEDOT:PSS does not.

As described in chapter 3, PEDOT:CS films were not obtained using spin-casting. However, glass slides were used as the substrate in these experiments, not a polymeric surface such as PDMS. By eye, it appeared that a spin-coated thin film of PEDOT:CS had formed on the PDMS surface but was thought not be uniform as it appeared particulate in nature. Upon inspection under the microscope, no continuous film appeared to have formed, but there was a sparse distribution of PEDOT:CS particles across the surface. Although not ideal, this was considered sufficient to test the laser ablation technique.

Direct laser ablation with a computer-aided design-driven laser scan marker was used to pattern the spin-cast PEDOT:CS films on PDMS to create an electrode pattern in the PEDOT:CS film as seen in figure 4.17.

The laser ablation patterned the PEDOT:CS film (figure 4.18) Examination of the patterned areas of the film showed that the patterned electrodes were incomplete, due to the incomplete non-continuous nature of the films.

As suspected, due to poor film quality, no data were obtained for STP behaviour in the PEDOT:CS films. In future, these experiments should be repeated with drop-cast films of PEDOT:CS as these are known to be continuous. Synapstors offer a potential route to direct interfacing between the nervous system and man-made technologies. If these devices could be made from a biocompatible, biodegradable organic electronic material, it would offer an even wider range of possibilities.

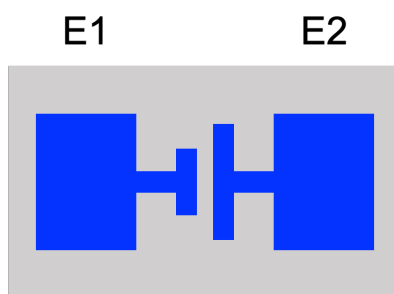


**Figure 4.17:** Schematic diagram of the electrode pattern produced by laser ablation - the grey colour indicates the areas of PDMS that were cleared of PEDOT:CS, and the blue areas indicate the PEDOT:CS electrodes. During STP testing, electrode E1 was where the displacement current was measured, and E2 was the electrode where the voltage pulses were applied.

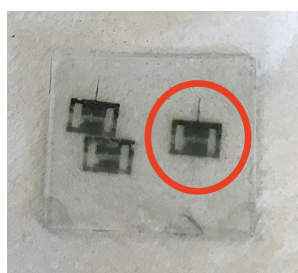


**Figure 4.18:** Photo of the PEDOT:CS film on PDMS substrate, post-laser ablation. The circled area shows a single patterned set of electrodes. The dark colour surrounding the electrodes shows where the laser ablated the PEDOT:CS film. These dark areas suggest that the laser power may have been too high, leading to scorch marks on the film.

#### 4.3.6 Lyophilisation of PEDOT:CS and PEDOT:HA

Another alternative use of PEDOT:CS to the planar OECT device presented in this thesis is to use the material in 3D scaffolds. Pitsalidis *et al.* [134] demonstrated that a 3D scaffold prepared from PEDOT:PSS could act as an electrochemical transistor for simultaneous cell culturing and monitoring purposes. This idea could be adapted for use in SCI treatment providing a bioelectronic approach as well as a cell based approach as a scaffold could be formed to the shape of a lesion. The scaffolds described in the paper were prepared from PEDOT:PSS and crosslinked using (3-glycidoxypropyl)-trimethoxysilane (GOPS) which leads to the formation of strong bonds between the GOPS and sulfonic acid groups of PSS [195]. This crosslinking technique would not be compatible with a biodegradable device as the crosslinks are not degradable, and the PEDOT:PSS material itself has been discussed at length in chapter 3 with regards to its biocompatibility. An EDC-crosslinked PEDOT:CS or PEDOT:HA scaffold would offer a degradable and biocompatible alternative to the PEDOT:PSS scaffolds described in the paper.

First, to show that it was possible to create PEDOT:CS scaffolds, GOPS-crosslinked PEDOT:CS and PEDOT:HA scaffolds were prepared. Although this method of crosslinking does not result in degradable crosslinks, it allowed PEDOT:CS and PEDOT:HA scaffolds to be prepared in a way analogous to the PEDOT:PSS scaffolds demonstrated by Pitsalidis *et al.* [134].

Mixtures of PEDOT:CS or PEDOT:HA aqueous dispersions with GOPS were pipetted into a multiwell-plate, lyophilised and annealed. The lyophilisation step acted to form the porous structure aimed for,

whilst the annealing step was necessary to trigger the GOPS crosslinking reaction in situ. In addition, some mixtures were prepared with ethylene glycol, GOPS, and PEDOT:biomolecule. This methodology proved generally successful for the samples containing the PEDOT:biomolecule aqueous suspension and GOPS alone, with no ethylene glycol (figure 4.19).

All of the samples containing no ethylene glycol, including all the PEDOT:CS ratios and PEDOT:HA, gave 3-dimensional scaffolds but the PEDOT:CS 1:1 and PEDOT:HA 1:1 appeared the sturdiest. They were spongy in appearance and were easy to handle without any evidence of disintegration. The PEDOT:CS 1:2 and 1:3 scaffolds (no ethylene glycol) were more delicate and some showed evidence of breakage when handled. The samples freeze-dried with ethylene glycol present in solution did not form 3-dimensional structures, but instead formed film-like layers over the base of the individual wells. The ethylene glycol did not play a role in the GOPS crosslinking process and was added to the samples to mimic the GOPS crosslinking methods used to form PEDOT:CS and PEDOT:HA films in work by Mantione *et al.* [168] who added the ethylene glycol to improve conductivity of the samples. The GOPS crosslinking method appeared to be compatible with the PEDOT:biomolecules producing sturdy and easy-to-handle scaffolds for both PEDOT:CS (1:1) and PEDOT:HA (1:1) samples when no ethylene glycol was present. The PEDOT:CS 1:2 and 1:3 samples containing GOPS only also produced scaffolds upon lyophilisation, but these were more delicate than the PEDOT:biomolecule 1:1 GOPS crosslinked scaffolds. As previously mentioned the GOPS crosslinking methodology is not compatible with the aim to create a biodegradable scaffold, therefore EDC-crosslinked scaffolds were prepared.

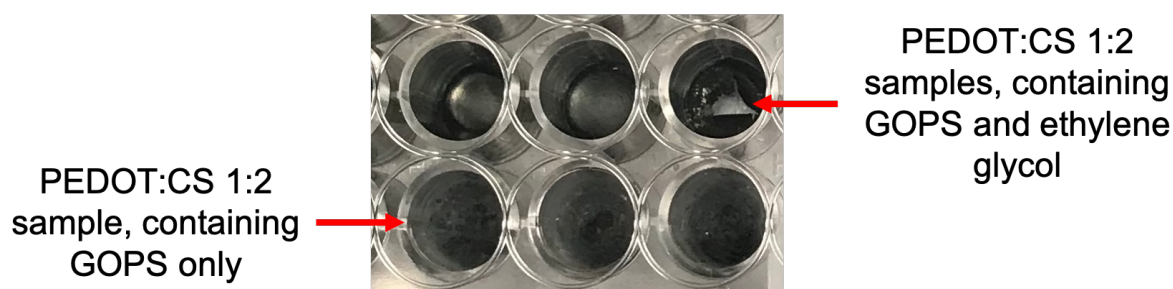


**Figure 4.19:** GOPS-crosslinked PEDOT:CS 1:2 samples - the samples containing ethylene glycol appeared film-like, whereas the samples containing GOPS only formed 3-dimensional scaffolds that appear light in colour in the image above.

PEDOT:CS (1:1) and PEDOT:HA (1:1) 2% (w/w) aqueous dispersions were freeze-dried using the same lyophilisation protocol as was used for the GOPS crosslinked samples. The structures of the resulting uncrosslinked PEDOT:CS and PEDOT:HA scaffolds appeared very different to those prepared using the GOPS crosslinking method. The one-step GOPS crosslinking method yielded sturdy scaffolds, whereas the uncrosslinked scaffolds (figure 4.20) were incredibly delicate and could not be easily handled. This was especially true for the PEDOT:CS samples which appeared more like a loose connected powder than a 3D scaffolds. It was noted that the PEDOT:HA uncrosslinked scaffolds had a layered structure to them which appeared to form a soft top ‘film’ layer with a more porous scaffold-like layer underneath and a fibrous layer at the base. This was unexpected and suggested that the lyophilisation parameters used may require tuning for the uncrosslinked PEDOT:CS and PEDOT:HA scaffolds compared to the GOPS crosslinked samples.

Additionally, both PEDOT:CS and PEDOT:HA freeze-dried samples were very hygroscopic and appeared to absorb water from the air leading to some scaffolds collapsing. This appeared to impact the PEDOT:CS

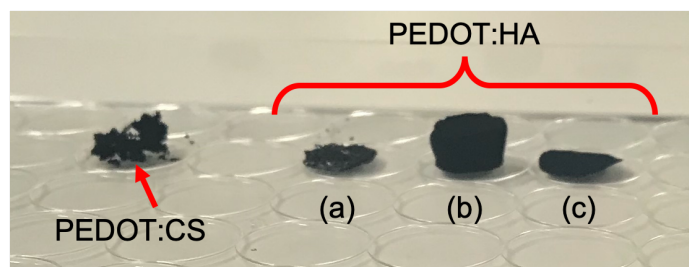


**Figure 4.20:** PEDOT:CS and PEDOT:HA freeze-dried samples for EDC-crosslinking. The PEDOT:HA samples formed three distinct layers upon freeze-drying which are labelled in the photo as (a) the fibrous base layer, (b) the scaffold-like centre layer, and (c) the soft film-like top layer.

samples more than the PEDOT:HA samples. This highlighted a potential incompatibility to the EDC-crosslinking step that involved submerging the samples in an ethanol-EDC solution mixture. If the water from the air made the samples collapse, there was the concern that the addition of solutions to the scaffolds would also trigger collapse. Following lyophilisation of PEDOT:CS and PEDOT:HA, a crosslinking mixture was prepared from EDC and an 75:25 ethanol:water mixture, and was pipetted over the individual PEDOT:CS and PEDOT:HA scaffolds in the wells. The scaffolds were left submerged for 24 hours. Upon returning to the samples after 24 hours, the majority of the samples had disintegrated and dissolved into the crosslinking mixtures. The PEDOT:HA samples had not completely dissolved, however when attempts were made to pipette the crosslinking mixture back out of the wells, the PEDOT:HA scaffolds broke apart.

It was clear from these results that the EDC-crosslinked scaffolds required further development. There are a number of variables that could be changed to improve sample quality; the first being the lyophilisation itself. The freeze-dried uncrosslinked PEDOT:CS and PEDOT:HA scaffolds were of poor quality with an unexpected layered structure and were very delicate to handle. This could be a result of incomplete drying during the lyophilisation process, so tuning the original freeze-drying protocol to involve a longer drying step could yield better scaffolds. Additionally, the EDC-crosslinking step itself could be varied with a greater concentration of EDC in the crosslinking mixtures to give more crosslinking within the structures increasing their stability.

In summary, these experiments demonstrate that the PEDOT:CS and PEDOT:HA suspensions can be used to form crosslinked scaffolds. The GOPS crosslinking method yielded sturdy and easy to handle scaffolds, whereas there were issues with the EDC-crosslinked samples which were more difficult to handle and did not form distinct scaffold structures. Despite the success with GOPS crosslinking, it does not offer the degradability conferred to EDC-crosslinked PEDOT:CS or PEDOT:HA samples. Through alteration of the lyophilisation and EDC coupling methods, it could be possible to create degradable EDC-crosslinked scaffolds from PEDOT:CS and PEDOT:HA. Such scaffolds could then be used as tubistor style devices that could offer an alternative route towards SCI treatment.

## 4.4 Summary and future work

The overarching aim of the work in this thesis was to create a biocompatible, biodegradable, and mechanically appropriate OECT device that would be suitable for use in the CNS. It was previously demon-

strated that the choice of CS as a counter-ion to PEDOT fulfils the compatibility and biodegradability requirements, and EDC-coupling was chosen due to the degradable ester bonds that form the crosslinks. PEDOT:CS 1:1 was demonstrated to function as the organic electronic material in an OECT in chapter 3. The aim of the work presented in this chapter was to develop and improve the performance of the PEDOT:CS OECT device and examine its degradation.

The use of interdigitating electrodes to improve device performance was attempted, and although no improvements were seen in the transconductances of PEDOT:CS 1:1 based OECTs, the ON/OFF ratios saw a two to three-fold increase compared to the original proof of concept data in chapter 3 (section 3.3.4). Additionally, these experiments proved once again that PEDOT:CS could be used in OECT devices which has not been seen in the literature prior to this work. Additionally, it was observed that a 6 week old PEDOT:CS 1:1 sample that had previously been tested and shown to demonstrate OECT behaviour no longer displayed such behaviour. This result showed that PEDOT:CS aqueous dispersions have a limited lifetime post-synthesis. The PEDOT:CS based OECTs require further optimisation to improve device performance. This could be achieved in future by more alternative electrode configurations, varying the EDC-crosslinking methodology, or making use of alternative crosslinking technologies, although this would have to be carefully considered with regards to degradation.

Further characterisation of the PEDOT:CS itself using UV spectroscopy and EIS was carried out to examine changes that occurred in the material following EDC-crosslinking. Crosslinking the PEDOT:CS films appeared to have caused a change in the doping state of the PEDOT evidenced by the presence of a band centred around 510 nm in the UV spectra for the crosslinked films that was not present in the uncrosslinked aqueous suspension samples. This band is typically attributed to undoped, neutral PEDOT, which would explain the increased sheet resistances upon crosslinking seen in chapter 3. The EIS results supported the findings of the UV spectroscopy as there was no ionic conductivity observed in the data indicating that the crosslinked PEDOT:CS 1:1 was present in its non-conducting undoped form.

Degradation experiments were carried out which acted to probe how the OECT behaviour of the PEDOT:CS-based devices changed following 3-days of submersion in water as one of the key requirements of the device was degradability. Concurrent experiments were run on crosslinked PEDOT:CS films so that they could be analysed using UV spectroscopy and EIS to examine any changes observed following the 3-day submersion in water. The OECT devices demonstrated a marked increase in performance with an up to five fold increase in maximum output current and increases in the maximum transconductances, whereas the ON/OFF ratios remained approximately similar. EIS and UV spectroscopy demonstrated that following the 3-day submersion in water the PEDOT was present in its doped conducting form with both ionic and electronic conductivity occurring within the film. The increase in device performance was suggested to be a result of increased swelling of the crosslinked film which lead to more facile ion diffusion, increasing the conductivity. This conclusion was supported by the EIS and UV spectroscopy data. Additionally, the increase in OECT device performance supported the assertion that the act of crosslinking the films in the first place decreased conductivity due to the formation of a tightly bound matrix. The swollen matrix allowed ionic conductivity that was not accessible prior to the 3-day submersion in water resulting in a recovery of conductivity and improved device performance. Further examination of this behaviour is required in future utilising more controlled conditions including temperature control (37 °C) and pH 7.4 buffered solutions to mimic basic physiological conditions. It is thought that the increase in performance of the OECT devices observed here would be followed by a decrease as the PEDOT:CS film begins to degrade, delaminate, and dissolve into solution. This has been shown to occur in PEDOT:PSS-based

transistor devices where an increase in device performance due to swelling in the short-term is observed, followed by a decrease in performance due to decohesion of the device [55]. Additionally, to understand the intertwining of the swelling of the PEDOT:CS films with the actual degradation of crosslinks, concurrent degradation experiments should be carried out on crosslinked PEDOT:CS films, as well as PEDOT:CS OECT devices. This would allow the swelling of the films to be probed over time. Chemical changes in the films could also be assessed to track degradation of the ester crosslinks via spectroscopic techniques such as nuclear magnetic resonance (NMR) spectroscopy.

Synapstors were tested, and it was concluded that the PDMS substrate used was inappropriate for spin-cast PEDOT:CS devices. There remains nevertheless the possibility that good quality synapstors may be achievable using a different film formation method such as drop-casting or a different substrate. Such developments are a possible separate thesis project.

The lyophilisation experiments showed that 3D crosslinked scaffolds can be formed from PEDOT:CS and PEDOT:HA. The GOPS crosslinked scaffolds were easy to handle and spongy in texture, whereas there was the requirement for further development of the EDC-crosslinked scaffolds. This success opens the door to tubistor devices [134], and the use of PEDOT:CS and PEDOT:HA scaffolds in the treatment of SCIs. Mechanical, electronic, degradation, and compatibility tests with cells would act as a starting point to move towards a biocompatible and biodegradable 3D transistor device, as an alternative to the planar devices investigated in the majority of this thesis.

An OECT based on PEDOT:CS has been successfully created which offers a biocompatibility and biodegradability that PEDOT:PSS devices do not. In the introduction to this thesis, one of the requirements of an implanted device such as the OECT developed here was that it must have appropriate mechanical properties. The mechanical properties of the OECT device have not been considered thus far. All the substrates used in testing would not be suitable for implantation in to the CNS as there would be a massive mismatch of moduli between the hard glass or quartz and the extremely soft tissues. The next step in developing this device further beyond improving the device performance is to create a substrate material that could be implanted in to the CNS providing a more mechanically appropriate surface on which the OECT could be prepared. The substrate would have to also be biocompatible and biodegradable to fulfil the other criteria of an implanted material and therefore CS and HA hydrogels were investigated. The preparation and characterisation of the CS and HA hydrogels is discussed in chapter 5. Alternatively, the lyophilisation experiments showed that 3D scaffolds could be prepared from PEDOT:CS and PEDOT:HA. If these scaffolds can be developed into fully realised 3D transistors or tubistors, these materials may also offer a more mechanically appropriate transistor device in future however this lies outside the scope of this project.

## Chapter 5

# Creating biocompatible, degradable, and soft hydrogels from biomolecules

### 5.1 Introduction

Spinal cord injuries (SCIs) are typically devastating and life changing events, resulting in paralysis leading to loss of function in limbs and many other related problems. There are a number of different treatment routes for SCIs including those that include electronic stimulation of the spinal cord, or bioelectronic implants [3–5]. There are also a number of approaches that do not include an electronic element, such as creating tissue scaffolds to encourage healing of damaged tissue naturally, or through the addition of stem cells [91, 93]. Hydrogels are often used in such cases. Hydrogels were introduced in chapter 1 as 3D crosslinked polymer networks that significantly swell in water. They are often used as biomaterials due to their high water contents, as well as the variation in materials and methods from which they can be synthesised [80, 81]. This wide range of materials and synthetic methods allow hydrogels to be designed with specific properties in mind, such as those required for biomaterials: biocompatibility, biodegradability, and appropriate mechanical properties.

Throughout this thesis, the main consideration has been creating a biocompatible, biodegradable organic electrochemical transistor (OECT) from PEDOT:CS or PEDOT:HA. These materials have been shown to fit the requirements of a bioelectronic device suitable for implantation into the human body, and more specifically the central nervous system (CNS). Thus far, all of the work on developing the PEDOT:CS/PEDOT:HA OECT device has taken place on glass (or similar) substrates, with little consideration of the mechanical properties of the device. Glass substrates would not be suitable for an OECT device designed for use in the CNS, due to its unsuitable mechanical properties. The elastic modulus of glass varies with manufacturing and materials used but typically it is around 70 GPa [78], compared to around 1 MPa [72, 73] for the spinal cord. Other bioelectronic devices and implants have used soft and more malleable substrates however there are issues with these materials as they are typically not biodegradable [60], which is not suitable for the requirements of the device discussed in this thesis. There is, therefore, a requirement to design a material that could be used as a substrate for the OECT devices previously reported in this thesis to make them suitable for implantation in the CNS, specifically the

spinal cord.

The aim of this work was to create a hydrogel that could be used in the spinal cord in conjunction with the OECT device based on PEDOT:CS or PEDOT:HA (chapters 3 and 4) that would fulfil the requirements of an implanted biomaterial, namely biocompatibility, appropriate mechanical properties, and biodegradability. As the substrate material typically makes up the majority of a device in comparison to the organic electronic material (OEM) [60], designing a hydrogel that fits these requirements is especially important. There are also the additional requirements of the hydrogel to be fairly easy to handle so that implantation would be as trivial as possible. Furthermore, the hydrogel has to be compatible with the OECT device and be able to act as the substrate effectively.

### 5.1.1 Hydrogels and their uses in the body

Hydrogels are three dimensional, crosslinked matrices that can swell in water by up to thousands of times their dry masses [80]. They are popular for use in and around the body due to their high water content. For example, hydrogel face masks as beauty treatments have become incredibly popular in recent years, and hydrogel wound dressings have been used since the 1950's for treating burns and other injuries [80, 88]. The use of hydrogels inside the body is popular and are useful for simulating natural biological structures [81].

Naturally derived materials are of significant interest to researchers for use as hydrogels due to their biocompatibility and biodegradability properties [81, 88]. They are especially popular for use in the CNS for their compatibility which can act to minimise immune responses that otherwise could lead to glial scar formation and related detrimental effects. For example, hyaluronic acid (HA) is a glycosaminoglycan that is found extensively throughout the ECM, especially in the ECM of the CNS [8], and is thus of interest to researchers studying hydrogels for use in the nervous system. It was used along with chondroitin sulfate (CS) in chapters 3 and 4 as an alternative counter ion to PSS in PEDOT complexes. Seidlits *et al.* [89] published a paper investigating the influence of the mechanical properties of a HA hydrogel on the differentiation of neuronal progenitor cells (NPCs) found in the nervous system. NPCs are able to differentiate into neurons, astrocytes, and oligodendrocytes, and have been shown to be a promising treatment option for SCIs. This work aimed to highlight the need to carefully control the mechanical properties of a hydrogel for use in the soft CNS, specifically in the context of cell differentiation however the broader message still applies. The hydrogel was prepared from various ratios of HA modified with methacrylate that was then freeze-dried (or lyophilised) prior to mixing with a photoinitiator in phosphate buffered saline (PBS). The mixtures were exposed to a broad range UV source to trigger crosslinking. The HA hydrogels were shown to fully degrade in hyaluronidase enzyme solutions over 6 to 24 hours depending on the level of methacrylation in the HA. This showed that these gels were both biocompatible and biodegradable. The hydrogels were mechanically tested and the elastic moduli were found to increase with increased methacrylation of the HA with the highest elastic modulus found to be  $5.1 \pm 0.4$  kPa (20:1 methacrylation), and the lowest modulus was  $3.0 \pm 0.4$  kPa (5:1 methacrylation). The lowest elastic modulus HA gel was found to have comparable mechanical properties to neonatal rat brain, and was shown to have the greatest level of NPC differentiation over a three week period. On the other hand, the highest modulus HA gel saw no significant differentiation of NPCs and could not support the cell cultures over the full three week period. This showed that the closer the mechanical properties of the hydrogel are to the native tissues, the better a support for cell growth and differentiation, clearly linking

mechanical properties to the biocompatibility of an implanted material. This work by Seidlits *et al.* [89] not only gave a clear example of the uses of a naturally derived material for use as a hydrogel, but also highlighted the three requirements of an implanted biomaterial described in the introduction chapter: biocompatibility, biodegradability, and appropriate mechanical properties.

Another example of a naturally derived material for use in the preparation of hydrogels is collagen. It is the main structural protein in the ECM of the connective tissues of most mammals [207], and thus is a popular material in biomaterial research [104, 207–212]. Collagen matrices with crosslinked CS attachments were prepared by Pieper *et al.* [90] via lyophilisation of collagen followed by EDC-crosslinking of the CS (more details on EDC-crosslinking in chapter 1). The collagen matrices are not strictly hydrogels but the techniques used to prepare them (freeze drying and EDC-crosslinking) can be applied to hydrogel synthesis. CS is also found throughout the ECM, and like HA, is a glycosaminoglycan. The work sought to establish a method of attaching CS to collagen matrices that could be used to improve outcomes of collagen based tissue scaffolds, as CS was attached in a way that was to mimic native ECM. CS and other glycoaminoglycans are found as markers in the ECM that help guide and determine cell attachment and differentiation.

Geissler *et al.* [91] created collagen based hydrogels to encourage and direct the differentiation of NPCs into oligodendrocytes. The hydrogels were prepared from mixtures of collagen I, laminin (a material present in the developing CNS thought to be involved in the differentiation and maturation of oligodendrocytes), and HA. The gels were found to have elastic moduli similar to that of the neonatal rat CNS. These hydrogels (some with NPCs and cell culture media to support cell growth) were implanted via injection into the sites of SCIs in rats. Over six weeks those with the hydrogel treatment displayed functional recovery, with greater significant functional recovery seen in the hydrogel-cell combination treatment. A control group of rats with SCIs were also prepared. These rats were injected with cell culture media only and saw no significant functional recovery, further demonstrating the value in the injectable hydrogel.

Injectable hydrogels are a popular approach to treating SCIs as the hydrogels can conform to the shape of a lesion or defect in the spinal cord and gel *in situ* [70, 92]. The injectable approach also removes the need for invasive surgeries that can be dangerous, which reduces the chance of further trauma and improves recovery times [70, 92]. For example, Gomes *et al.* [93] developed an injectable chemically modified gellan gum based hydrogel that was biocompatible and biodegradable. When modified with fibronectin-mimetic peptide GRGDS, the hydrogel, in combination with stem cells, promoted axonal and neurite regrowth during *in vitro* studies, and in a very promising development, showed improved motor responses in rats with SCIs.

Caicco *et al.* [94] described a HA-methyl cellulose injectable hydrogel for use in the spinal cord. The aim of the work was to develop a physically crosslinked hydrogel as a delivery system for therapeutic stem cells that could be used as a treatment for SCIs. The HA-methyl cellulose hydrogel was shown to gel within five minutes at physiological temperature, and the moduli could be controlled by the concentrations of the HA and methyl cellulose blend to give similar mechanical properties to the spinal cord (reported as 300 Pa here [94]). The hydrogel delivery system resulted in more evenly distributed cells and better cell viability than those delivered in saline solution, which in turn could lead to better outcomes in the use of cell therapies to treat SCIs. The hydrogel had the additional advantage of being biodegradable as HA is naturally occurring and enzymatically degradable. On the other hand, methyl cellulose cannot be broken

down by the human body as cellulase is not naturally occurring human enzyme. This means that to break down the methyl cellulose component of this hydrogel, another degradation route must be introduced into the body. Nevertheless, as the gelation of the HA-methyl cellulose mixture was triggered by temperature to form a physical hydrogel, meaning that no additional chemical bonding was introduced. The hydrogel maintained the natural degradation pathways of the HA component. Hardy *et al.* [92] also reported on an injectable hydrogel for use in the CNS. Instead of acting as a medium to disperse cells like the hydrogels developed by Caicco *et al.* [94], it was designed to act more like a tissue scaffold on which cells could proliferate post-gelation. The hydrogels were made up of linear poly(ethylene glycol) (PEG) terminated with aminoxy moieties with HA derivatives that displayed aldehydes, which could undergo *in situ* crosslinking through oxime-click chemistry. The compressive moduli of the hydrogels was reported to be between 2 and 12 kPa, comparable to the moduli of the CNS, and the gels were degradable via HA breakdown using hyaluronidase with a best case 40% mass loss over 25 days. In addition, the PEG-HA gels, with the addition of some collagen, were found to have high levels of cell seeding and viability of human stem cells. All of this evidence combined indicated that the PEG-HA gels were a feasible option for further development towards a treatment for a damaged CNS, including SCIs.

In the case of the aims of this project, an injectable hydrogel is unlikely to be useful as a substrate for a PEDOT:CS or PEDOT:HA based OECT, however the materials and crosslinking approaches are still relevant as they have clearly demonstrated success in the treatment of SCIs. As shown by the examples given, hydrogels are often used as a material to mimic the ECM when used in the CNS to encourage nerve regeneration and cell growth, whether it be an injectable or preformed hydrogel for implantation [70, 89–94]. Along with acting as a soft biodegradable substrate for the PEDOT:CS or PEDOT:HA-based OECT, the hydrogel component could also act as a material to encourage nerve regeneration in an SCI, working jointly with the OECT in a combination treatment for SCIs.

HA has been shown to be a popular material for use in hydrogels, especially in those intended for use in soft, delicate tissues such as in the CNS, as demonstrated by the previous examples and its popularity throughout the hydrogel literature [89, 91, 92, 94]. The popularity of HA and similar molecules in the field of soft hydrogels led to the decision to explore HA, as well as CS, as the material for the hydrogels presented in this thesis.

### **Conducting hydrogels for use in the nervous system**

There are a number of examples of hydrogels prepared from conductive materials. This differs from the approach taken in the research presented in this thesis where a conductive material is prepared on a non-conductive hydrogel substrate.

In the introduction to chapter 3, this was touched upon when discussing alternative counter-ions for PEDOT instead of PSS in the case of PEDOT:guar gum gels. Del Agua *et al.* [186] prepared PEDOT stabilised with guar gum which was then freeze dried to form a PEDOT:guar gum powder. The powder was then mixed with an ionic liquid (1-ethyl-3-methylimidazolium chloride), stirred at 100°C for three hours, and left to cool at room temperature. Although not strictly a hydrogel as an ionic liquid was used to swell the material instead of water, this example demonstrated that a PEDOT-based material could be used to form a gel and be conductive. The mechanical properties of the gel were assessed over a range of temperatures from room temperature up to 150 °C, and were found to be stable up to 80 °C with

elastic moduli between 40 and 100 kPa depending on the formulation used. These moduli are of the same order of magnitude to the elastic moduli of structures in the CNS. The authors suggested that this work acted as a proof of concept and in future, it could be used as a material in bioelectronics.

More recently in 2019, Liu *et al.* [213] published their findings following the development of a conductive hydrogel based on PEDOT:PSS. Firstly, a PEDOT:PSS ion gel was prepared by introducing an ionic liquid into the PEDOT:PSS using a similar method to the PEDOT:guar gum ion gel [186] previously mentioned. The ionic liquid was then removed from the ion gel and replaced with water via water exchange to give a hydrogel that was highly conductive ( $47.4 \pm 1.2 \text{ S cm}^{-1}$ ) and highly hydrated (85 % (w/w) water when swollen). Additionally, the Young's modulus of the hydrogel (by compression  $32 \pm 5.1 \text{ kPa}$ , by nanoindentation  $24 \pm 5.4 \text{ kPa}$ ) was comparable to that of nerve tissues. A UV-crosslinked dimethacrylate-functionalised perfluoropolyether (PFPE-DMA) elastomer was also prepared and tuned to have appropriate mechanical properties for use in nervous tissues and this was used as a dielectric material with the conductive hydrogel photolithographically micropatterned to form electrodes. The aqueous stability of the resulting device was found to be excellent both mechanically and electrochemically, and was biocompatible as the device triggered no significant immune response or cellular changes when implanted around the sciatic nerves of rats. Following device design optimisation, the authors successfully implanted the electronically conducting hydrogel device *in vivo* again around the sciatic nerve of rats and were able to stimulate movement in the feet and toes using low voltages of 50 mV. These experiments showed an alternative approach to introducing bioelectronics into the nervous system by using a conducting hydrogel as an electrode material.

These examples demonstrate that the combination of hydrogels and bioelectronics is an area of interest for researchers. Hydrogels prepared from conductive materials offer a route to creating mechanically appropriate, bioelectronic materials. This differs from the approach taken in the research presented in this thesis where the hydrogel forms the substrate for the PEDOT:biomolecule-based OECT. In future, it may be that a conductive hydrogel can be prepared from PEDOT:CS or PEDOT:HA, however this lies outside the scope of this project. Using the hydrogel as a substrate allows the PEDOT:CS to mimic the established geometries of an OECT allowing comparison between the established technology and a novel degradable device. Furthermore, a hydrogel substrate allows for flexibility in design for future devices where, for example, an electrode array for nervous system monitoring could be prepared on the hydrogel. Electrode arrays typically cover large areas meaning that a large surface area afforded by a hydrogel substrate would be advantageous.

### 5.1.2 Summary and requirements of hydrogels for use in the central nervous system

Hydrogels are of great interest to researchers in the field of biomaterials due to their intrinsic properties. The ability to absorb up to thousands of times their dry mass in water, thus providing a highly hydrated environment, and their porous structures make them ideal materials for providing surfaces on which cells can grow [80, 81]. The control given to the properties of a hydrogel through material and crosslinking type allows them to be designed to give the most desirable properties, including the three key properties of a biomaterial: biodegradability, biocompatibility, and appropriate mechanical properties.

The aim of the following experiments was to develop and characterise a hydrogel that would be suitable

for use in conjunction with a PEDOT:CS or PEDOT:HA based OECT. The hydrogel had to be biocompatible, biodegradable, and mechanically appropriate for use in the CNS. It is intended that the hydrogel could act as a soft substrate for the OECT, and in future could be developed into a fully realised device for the treatment of SCIs.

HA and CS are both glycosaminoglycans that have been previously used in hydrogel synthesis, and in the development of hydrogels for use in the CNS [89, 91, 92, 94, 100, 114, 115]. The fact they are naturally occurring throughout the human body makes them ideal candidates for the hydrogel being developed in this thesis as they are both biocompatible and biodegradable. EDC-crosslinking has been demonstrated as a method of crosslinking naturally occurring polymers and forming hydrogels [119, 120, 122, 125, 126]. It mediates the formation of ester crosslinks, which themselves are degradable [120]. Additionally, literature examples of CS and HA hydrogels have shown that they can be prepared to low moduli [89, 91, 92, 94], comparable to that of the CNS. Hydrogels of both types have been shown to encourage the differentiation and proliferation of neuronal cells which is important in the treatment of SCIs [70, 89, 91, 92, 94, 100, 114, 115]. For these reasons CS and HA were the choices of materials on which to base the hydrogels prepared by EDC-crosslinking presented in this thesis. It is also the reason that both the materials and crosslinking methods were chosen as the counter ion for the PEDOT:CS and PEDOT:HA materials discussed in earlier chapters of this thesis.

In this chapter, the preparation of CS and HA hydrogels will be described, and the swelling properties presented. The mechanical properties of the HA hydrogels were found to be tunable by the amount of EDC used in during their preparation, and the gels were found to have elastic moduli that were comparable to those of the spinal cord. The degradation profile of the HA hydrogels was also determined, and demonstrated that they were hydrolytically degradable under simulated physiological conditions. Finally, initial experiments combining HA hydrogels with PEDOT:CS are also reported.

## 5.2 Experimental methods

### 5.2.1 Materials

Chondroitin sulfate A sodium salt from bovine trachea, hyaluronic acid sodium salt from *Streptococcus equi*, ethanol, acetone, *N*-(3-Dimethylaminopropyl)-*N*'-ethylcarbodiimide hydrochloride, hydrochloric acid (ACS reagent grade, 37%) and phosphate buffered saline tablets were purchased from Merck (formerly Sigma Aldrich). Fisherbrand pH indicator paper sticks were obtained from Fisher Scientific. Deionised water was acquired from the laboratory purifier.

### 5.2.2 Synthesis of chondroitin sulfate and hyaluronic acid hydrogels by EDC-crosslinking

#### Single step casting method

A 0.6 % (w/w) CS or HA solution was prepared by dissolving CS or HA (0.03 g) in water (5.0 g, 0.28 mol). Six individual CS and six HA solutions were prepared. EDC was added to each of these solutions

and stirred. Three CS and three HA solutions were prepared with 0.03 g EDC, and another three of each solution type were prepared with 0.06 g EDC. The mixtures were cast into individual Petri dishes and allowed to air-dry for 2 to 4 days. The resulting films were peeled from the Petri dishes and submerged in water ( $3 \times$  five minutes) to rinse out any unreacted EDC and any by-products from the film.

### Establishing the most effective ethanol to water ratio

Experiments were undertaken to determine the most effective ethanol to water ratio for gel synthesis. CS and HA films were prepared from a 1 % (w/w) CS or HA solutions. CS or HA (0.05 g) was dissolved in water (5.0 g, 0.28 mol) and the solution was cast into a Petri dish and allowed to dry for 24 hours. The films were then cut to approximately 9 cm<sup>2</sup> squares. Three CS and three HA films were prepared for each ratio of ethanol to water.

For these experiments, individual mixtures of ethanol and water were prepared in the ratios given in table 5.1. EDC (0.05 g, 0.261 mmol) was then added to each individual ethanol-water mixture. This acted to maintain a constant amount (mol) of EDC available in each sample, no matter the volume of water. Three samples of each ethanol-water-EDC mixture were prepared for CS and three for HA. No EDC was added to the 100% ethanol samples as EDC is not soluble in ethanol.

**Table 5.1:** Preparations of mixtures of ethanol and EDC solutions in various ratios

Ratio of ethanol to EDC solution	Volume of ethanol / cm <sup>3</sup>	Volume of water / cm <sup>3</sup>
50:50	2.5	2.5
60:40	3.0	2.0
70:30	3.5	1.5
80:20	4.0	1.0
90:10	4.5	0.5
100:0	5.0	0.0

One CS or HA film was submerged in each EDC-ethanol mixture for 24 hours, noting any observations during this time. The films were then rinsed three times by submersion in water for five minutes, and air-dried for 24 hours.

Following this, the same experiment was then repeated with acetone instead of ethanol.

### EDC control experiments

Six CS and six HA films were prepared as outlined in the general method (section 5.2.3). Three CS and three HA films were submerged in 80:20 mixtures of ethanol and water, with no EDC present, and three more of each film were submerged in 80:20 mixtures of acetone and water for 24 hours. The films were then rinsed by submersion in water for ten minutes.

In a further control experiment, three CS and three HA films were prepared using the general method (section 5.2.3). Each film was submerged in individual 80:20 mixtures of acetone (4 cm<sup>3</sup>) and EDC solution (1 cm<sup>3</sup>, 0.26 mol dm<sup>-3</sup>) for 24 hours. The films were removed from the mixtures and rinsed by submersion in water ( $3 \times$  five minutes) and allowed to dry in air.

As a final control experiment, three CS and three HA films were prepared using the general method (section 5.2.3). Each film was submerged in an individual EDC solution ( $5 \text{ cm}^3$ ,  $0.26 \text{ mol dm}^{-3}$ ) and were observed.

### 5.2.3 General multi-step submersion method for hydrogel preparation

The method used to synthesise CS and HA hydrogels was based on methods by Tomihata *et al.* [120], using EDC-crosslinking. Firstly, CS or HA films were prepared from 1 % (w/w) solutions of CS or HA. The CS or HA solution ( $5 \text{ cm}^3$ ) was transferred into Petri dishes and slowly air-dried overnight in a heated cabinet. The films were then cut to approximately  $30 \text{ mm} \times 30 \text{ mm}$  squares and submerged in a 80:20 mixture of ethanol ( $4 \text{ cm}^3$ ) and EDC solutions ( $1 \text{ cm}^3$ ) of various concentrations for 24 hours. The films were then removed from the crosslinking reaction mixture and submerged in water for five minutes  $\times 3$  to rinse out any by-products and unreacted material.

Various EDC concentrations were examined and the solution components are listed in table 5.2 below.

**Table 5.2:** EDC solution concentrations and masses used in EDC-crosslinking of CS and HA films

Mass of EDC / g	Mass of water / g	Concentration of EDC solution / $\text{mol dm}^{-3}$
0.005	1.0	0.026
0.01	1.0	0.052
0.025	1.0	0.13
0.05	1.0	0.26
0.10	1.0	0.52
0.15	1.0	0.78
0.20	1.0	1.04
0.25	1.0	1.30

### 5.2.4 Infra-red spectroscopy

Fourier transform infra-red (FT-IR) spectra were recorded for the dry HA crosslinked films using a Thermo Scientific Nicolet iS10 FT-IR spectrometer fitted with a Golden Gate Diamond ATR accessory and each spectrum was averaged over 64 scans. A background spectrum in air was collected prior to collecting the spectra for the crosslinked HA films, and was subtracted from the HA film spectra by the software used to control the IR spectrometer.

### 5.2.5 Acidification of HA for film preparation

A 1 % (w/w) HA solution was prepared from HA (0.514 g) and water (51.4 g, 2.86 mol). A 0.05 M HCl solution was prepared from 37% HCl ( $0.8 \text{ cm}^3$ ) and water ( $200 \text{ cm}^3$ ).  $\text{HCl}_{(\text{aq})}$  (0.05 M) was added dropwise to the HA solution as it was magnetically stirred. The pH of the solution was carefully monitored using Fisherbrand pH indicator paper sticks. When the pH of the HA solution reached around 1 to 2, the mass of  $\text{HCl}_{(\text{aq})}$  added was recorded.

The acidified HA solution was distributed into Petri dishes using a syringe. Approximately 5.0 g was transferred into each Petri dish, and the solutions were left to air-dry for 24 hours.

The pH-altered HA films were crosslinked using the general method (section 5.2.3) in 80:20 ethanol:EDC solutions for 24 hours, and rinsed and dried.

## 5.2.6 Swelling properties of chondroitin sulfate and hyaluronic acid hydrogels

The dry mass of each of the sample hydrogels ( $m_d$ ) was recorded using a bench top balance prior to submersion in deionised water for 15 minutes. The wet hydrogels ( $m_w$ ) were then removed from the water and their mass immediately recorded. Following this, the wet hydrogels were then pressed dry with paper towel and the mass of the swollen hydrogel ( $m_s$ ) recorded. Three different measurements of swelling were made from these masses: the percentage water uptake of hydrogel (including water in pores),  $W_w$ , the percentage water uptake of hydrogel matrix itself (after drying with paper towel),  $W_s$ , and the degree of swelling,  $D$ , given by equations 5.1, 5.2, and 5.3, respectively.

$$W_w = 100 \times \frac{(m_w - m_d)}{m_w} \quad (5.1)$$

$$W_s = 100 \times \frac{(m_s - m_d)}{m_s} \quad (5.2)$$

$$D = \frac{m_s}{m_d} \quad (5.3)$$

## 5.2.7 Degradation experiments

The masses of dry HA hydrogels crosslinked with different concentrations of EDC solution were recorded and were then submerged in individual Petri dishes containing 0.01 M PBS (10 cm<sup>3</sup>) prepared from tablets warmed to 37 °C. This point was considered  $t = 0$ . The samples were sealed with parafilm and transferred in to an oven set at 37 °C for different time periods: 1 hour, 2, 3, 6, 24, 48, 72, and 96 hours. Following the intended time period, the HA hydrogels were removed from the PBS and dried in a heated cabinet overnight. The hydrogels were then rinsed by submersion in water (5 cm<sup>3</sup>, for 1 minute, three times), and returned to the heated cabinet to dry overnight again. Once completely dry, the masses of the HA hydrogels were recorded again. At least three samples per time point per EDC concentration underwent the degradation experiment.

The % change in mass ( $\Delta M$ ) was calculated using equation 5.4, where  $m_{t=0}$  is the mass of the hydrogel at  $t = 0$ , and  $m_t$  is the mass of the hydrogel at  $t$ .

$$\Delta M = 100 \times \frac{(m_{t=0} - m_t)}{m_t} \quad (5.4)$$

## 5.2.8 Mechanical testing

### Sample preparation

A strip of double-sided adhesive tape was attached to a Perspex block. The dry HA hydrogel film sample was cut to size so the entire film could fit easily on the double-sided tape (approximately 25 mm × 15 mm). The film was then stuck flat on the tape and weighted down at either end with paper clips. The paper clips were then further affixed to the Perspex block with masking tape. The set-up is shown in figure 5.1.

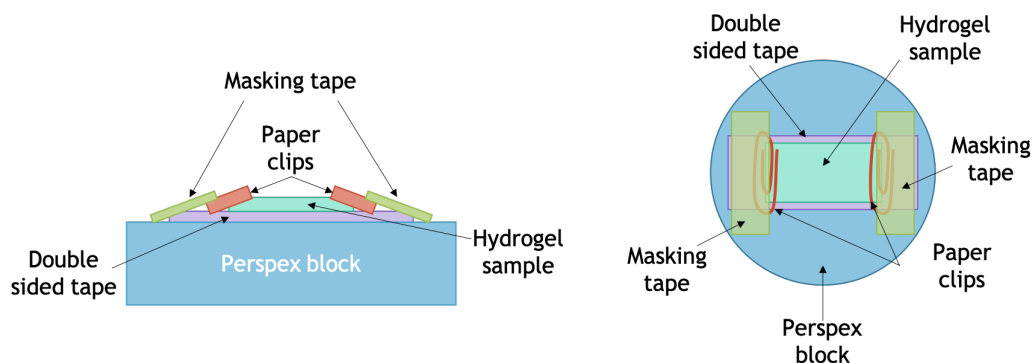


**Figure 5.1:** The sample set up for the mechanical testing of hydrogels.

The Perspex block with the sample attached was then submerged in a large beaker full of deionised water allowing the hydrogel to swell. The hydrogel was allowed to swell in the water for at least 15 minutes before beginning the mechanical testing, and the testing itself was carried out whilst the hydrogel was submerged in the water.

### Mechanical testing set up and parameters

The Stable Micro Systems Texture Analyser TA.Xtplus mechanical tester was used for mechanical testing of the hydrogels. The probe attachment used in these experiments was a cylindrical Delrin probe (10 mm diameter). This probe (attached to the arm of the tester) was lowered slowly into the beaker containing the water and submerged sample, and positioned approximately 2 to 8 mm above the hydrogel sample surface. A camera was positioned so that the sample surface and the probe could be easily seen. A sketch of the experimental set up is shown in figure 5.2.

Using the TEE32 software, the experiment parameters were entered as follows: pre-test speed 30 mm/min, test speed 15 mm/min, post-test speed 30 mm/min, return distance 0 mm, contact time 2 mins, trigger type AUTO, and trigger force 0.0 N. The trigger force determined the force at which data collection would begin, as all data from the beginning of each test were to be recorded, the trigger force was set to zero. The only parameter that was changed during the experiments was the applied force.

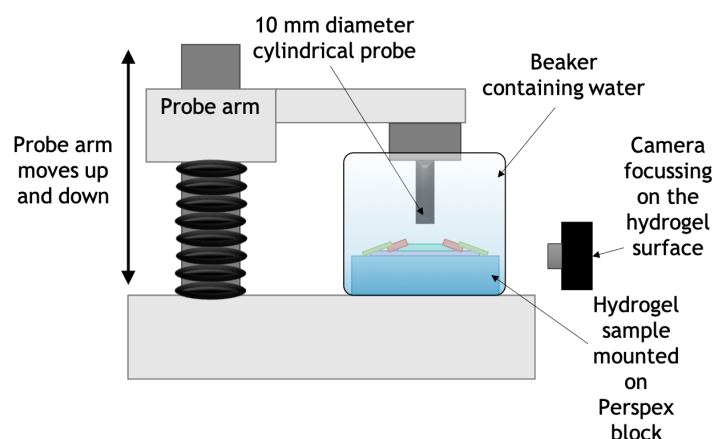


**Figure 5.2:** A sketch of the Stable Micro Systems Texture Analyser TA.Xtplus mechanical tester set up used to assess the mechanical properties of hydrogels.

### Data collection

Each test consisted of a slow approach to the surface of the hydrogel. When the probe was brought into initial contact with the surface of the hydrogel, the mechanical tester applied the set applied force to the hydrogel and held at this position for 2 minutes. After this, the probe returned to the original start position. Between each test, the beaker containing the sample was moved slightly to allow a different area of the hydrogel surface to be probed. During each test, a force-distance curve was recorded, as well as video capturing the contact area. The contact point, where the probe and the hydrogel made contact, was noted from the video.

The calculations used to obtain the elastic moduli of the hydrogels is outlined in section 5.3.4.

### 5.2.9 Combination of HA hydrogel with PEDOT:CS and PEDOT:HA

A HA hydrogel was prepared using the general method (section 5.2.3), and was crosslinked in an 80:20 ethanol:EDC solution mixture (total volume  $5 \text{ cm}^3$ ). The EDC solution was prepared to a concentration of  $0.782 \text{ mol dm}^{-3}$ . Once dry, the resulting HA gel was spread flat on the base of a Petri dish, and tightly taped down using masking tape leaving an area of HA gel exposed, forming a stencil (shown in figure 5.3). PEDOT:CS (1:1, 2 % aqueous dispersion) prepared using the methods described in chapter 3 was carefully drop-cast from a pipette using the minimum volume required to cover the exposed HA hydrogel and air-dried for 24 hours. When the sample was dry, the masking tape stencil was carefully pulled away from the HA hydrogel giving a HA hydrogel with a discreet square film of PEDOT:CS on top. The PEDOT:CS-HA hydrogel film was then crosslinked by submersion in an 80:20 ethanol:EDC solution ( $0.782 \text{ mol dm}^{-3}$ ) mixture (total volume  $5 \text{ cm}^3$ ) for 24 hours. The PEDOT:CS-HA hydrogel film was carefully removed from the crosslinking mixture and rinsed by submersion in water for five minutes. The rinsed film was then allowed to air-dry.

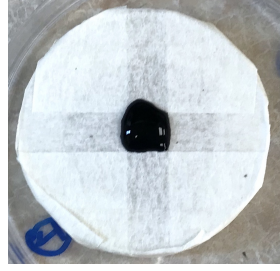


**Figure 5.3:** A masking tape stencil covers a HA hydrogel over which a small volume of PEDOT:CS aqueous dispersion has been drop-cast.

## 5.3 Results and discussion

As highlighted in the introduction to this chapter, hydrogels are highly compatible with the body with structures similar to those of the ECM. Hydrogels are of great interest to researchers for use in the CNS and the treatment of SCIs as they can be used as structures on which neural cells can differentiate and grow. It has been proven that both CS and HA hydrogels demonstrate this ability making them promising as materials on which to base the hydrogels required in this thesis.

The aim of this work on CS and HA hydrogels was to create a hydrogel that would fulfil the requirements of an implanted biomaterial. The hydrogel must be biocompatible, mechanically appropriate for the spinal cord, and biodegradable, as the device is not intended to be a permanent structure within the body. In future, this hydrogel may be used in the spinal cord in conjunction with the OECT device based on PEDOT:CS or PEDOT:HA (chapters 3 and 4). As the hydrogel is intended to be used as a substrate for an OECT that could be implanted in to the spinal cord, there is the additional requirement that the hydrogel must be compatible with the OECT device, as well as be fairly easy to handle so that implantation would be as trivial as possible.

Firstly, the synthesis of the hydrogels will be discussed, followed by characterisations of degradation and mechanical properties. Finally, initial explorations of the combination of a HA hydrogel with PEDOT materials will be presented, with a look towards future experiments.

### 5.3.1 Synthesis of chondroitin sulfate and hyaluronic acid hydrogels by EDC-crosslinking

EDC-crosslinking was chosen as the crosslinking method for the CS and HA hydrogels due to the nature of the ester crosslinks formed, as well as the ease of the synthesis methods. Ester bonds are hydrolytically degradable and thus fit the degradability requirement of the implanted device. Additionally EDC is a zero-length crosslinker, and so does not contribute chemically to the polysaccharides following crosslinking. That is to say that the only change that occurs to the inherently biocompatible CS or HA is the addition of extra ester bonds, and thus should have little effect on biocompatibility.

## Method development

The method used to synthesise the hydrogels was based on work by Tomihata *et al.* [120] who used EDC to crosslink HA and pectin. It was reported that HA and pectin could be crosslinked using EDC to form crosslinked films that were characterised using IR spectroscopy. Additionally, the swelling properties of the films were recorded, as well as some *in vivo* degradation data. A lot of research focuses on using three dimensional hydrogels to fill lesions in SCIs, however the aim of this work was to form a substrate material for an OECT device which is typically planar in geometry. The primary role of the hydrogel is to be a biocompatible, biodegradable, and mechanically appropriate support for the PEDOT:CS/PEDOT:HA OECT device for use in spinal cord, with a possible secondary role of providing a surface for cell growth and proliferation. A three dimensional structure would not necessarily be able to maintain the OECT geometry which would not fulfil the primary role of the hydrogel, despite perhaps being a more appropriate structure for cell growth and proliferation, aiding neuronal regrowth as an SCI treatment. A film hydrogel, on the other hand, would maintain the planar geometry of the OECT whilst still being appropriate for use in the spinal cord. Additionally, there is an advantage in having a soft thin film hydrogel to act as as it can conform to an uneven surface and bend more easily as to maximise surface area contact with damaged tissues whilst maintaining the planar geometry of the OECT.

Tomihata *et al.* [120] took two main approaches to creating HA crosslinked films: (1) single step synthesis where the HA and EDC were mixed and cast to form crosslinked films, and (2) multiple step synthesis via the submersion of HA films in a crosslinking mixture. The main method used in the experiments presented here was based on the multiple step synthesis, however the single step solution casting was attempted.

To create EDC-crosslinked HA films in a single step, the procedure introduced by Tomihata *et al.* [120] was adapted to create CS and HA hydrogel films. Tomihata *et al.* [120] prepared a mixture of HA and EDC in 80:20 ethanol:water. The mixture was stirred, then cast onto a glass plate and allowed to air-dry for 5 days at 25 °C. This resulted in a crosslinked HA film that was carefully peeled from the glass plate and dried further *in vacuo*.

CS or HA solutions were prepared, EDC added, and cast into Petri dishes. After drying for 2-4 days, the films were then peeled from the Petri dishes and rinsed. After the first 5-minute rinse, all the CS films had started to disintegrate and were not easy to handle, especially on removal from the water where some fully disintegrated into many small pieces. This was true for both EDC masses tested. In contrast to CS, this method resulted in crosslinked HA hydrogel films. The films were rinsed thrice in deionised water for five minutes each time and showed no evidence of disintegration but the films were very hydrated and difficult to handle. Upon repeating this experiment, however, the results were inconsistent with around half of the HA films dissolving and breaking apart on rinsing. The main drawback of this method was the inconsistency of results with the methodology appearing to work well for HA around half the time, but not working at all for CS. Occasionally, the CS films would not completely dry resulting in a hydrated, sticky substance that was not easy to handle. Additionally, the method took up to 4 days to yield the inconsistent results therefore, a multi-step submersion method was attempted. It was likely more time efficient, and later proved to be repeatable with consistent results.

The multiple step synthesis described by Tomihata *et al.* [120] is as follows; a HA solution was cast in a Petri dish and was left to air-dry to give a film. The HA film was then submerged in ethanol or acetone

mixed with water in various ratios, with EDC added for 24 hours. A rinse step followed crosslinking, and the films were dried. The role of the ethanol or acetone during crosslinking was important as it acted as a non-solvent. The HA films were water soluble, but were not soluble in ethanol or acetone. On the other hand, the EDC required for crosslinking was also insoluble in these organic solvents so water had to be present in the system for the EDC to dissolve. This led to the mixtures of organic 'non'-solvent and water with EDC added for the crosslinking of the HA films. It ensured the HA films did not dissolve, but allowed crosslinking to take place.

For the experiments undertaken here, the first stage in the multi-step synthesis was to prepare CS and HA films from solutions. This was fairly trivial, and was completed by slowly drying CS and HA 1 % (w/w) solutions for 24 hours in Petri dishes. It was noted that the CS films appeared more brittle than HA films and had a greater tendency to peel from the base of the Petri dishes in small pieces opposed to one discreet film.

Following film preparation, experiments were undertaken to determine the most effective ethanol to water ratio for synthesis. For these experiments, individual mixtures of ethanol and water were prepared in the ratios given in table 5.1. EDC (0.05 g, 0.261 mmol) was then added to each individual ethanol-water mixture. This acted to maintain a constant amount (mol) of EDC available in each sample, no matter the volume of water. No EDC was added to the 100% ethanol samples as EDC is not soluble in ethanol. There is evidence that EDC can hydrolyse in water [214]; however the ethanol-water-EDC mixtures were always used straight away and never stored, so the concentration of available EDC in these solutions was considered to be as prepared.

The CS films were observed to immediately dissolve on contact with the ethanol-water mixture (containing EDC) for the ratios 50:50, 60:40, and 70:30. This showed that the ethanol content in these samples was not great enough to counter the solvent effects of the water. By contrast, the CS films submerged in the 80:20, 90:10, and 100:0 ethanol:water ratio mixtures did not dissolve on contact. These CS films were submerged in the mixtures for 24 hours, carefully removed and rinsed in water. Washing the 80:20 ratio CS films resulted in the films becoming soft and more difficult to handle, however they did not dissolve which indicated successful crosslinking. The CS films from the 90:10 and 100:0 ratio samples were brittle and very delicate to handle. Additionally, during rinsing the edges of these 90:10 and 100:0 CS film samples dissolved in the water but some film remained suggesting some degree of successful crosslinking. All the CS films were air-dried for 24 hours. The 100% ethanol samples were not expected to show any crosslinking as EDC is not soluble in ethanol, thus the most likely explanation for the lack of immediate dissolution upon rinsing is that the CS film was fully swollen in ethanol. The film samples began to equilibrate with the water during rinsing, however were not soaked for long enough for the water to fully replace the ethanol within the matrix, thus some of the CS film was still in contact with the non-solvent, hence the non-dissolution. The HA films acted similarly to the CS films with the HA film samples submerged in 50:50 and 60:40 ethanol-water mixtures dissolving in around 20 minutes. On the other hand, the HA films submerged in the 70:30 ethanol:water mixtures became highly hydrated and began to break apart over the 24 hours leaving small pieces of crosslinked HA film instead of one larger film. The HA samples submerged in the 80:20, 90:10, and 100:0 ethanol-water mixtures containing EDC were left for 24 hours, and then removed and rinsed. The 100:0 HA samples all began to disintegrate on washing and appeared to start dissolving, and so were discarded, however the 80:20 and 90:10 samples were air-dried for 24 hours.

For both CS and HA films, the 80:20 and the 90:10 ethanol to water ratios gave the most promising results as there were no issues with dissolution for these samples. Tomihata *et al.* [120] were trying to create HA films with low levels of hydration and reported that 90:10 ethanol:water mixtures gave films with the least swelling. By contrast, the authors found that HA films crosslinked in 60:40 ethanol:water gave the most swollen gels, and the gels became less swollen when synthesised in mixtures with a greater ethanol content. During the experiments in this work, however, the CS and HA films dissolved in crosslinking mixtures in 60:40 ratios of ethanol to water, so could not be compared. The most appropriate crosslinking composition was decided based on the Tomihata *et al.* [120] findings, combined with observations made during the CS and HA gels preparation. The CS gels crosslinked in 90:10 ethanol:water showed some dissolution on rinsing and seemed more brittle and difficult to handle than the 80:20 samples. Furthermore, according to Tomihata *et al.* [120], HA films prepared in 80:20 ethanol:water mixtures demonstrated greater swelling than those prepared in 90:10 ethanol:water mixtures. It was therefore decided that the 80:20 ratio of ethanol to water was the most appropriate mixture composition for crosslinking the CS and HA films. For subsequent experiments, an EDC solution was prepared, instead of adding EDC to the mixtures, so that the concentration could be constant for each sample as the ratio of ethanol to EDC solution would not change from 80:20.

From these results, a general method (section 5.2.3) for preparing CS and HA was established utilising an 80:20 ethanol to EDC solution ratio as the crosslinking mixture.

### Control experiments

As a control experiment, additional samples were prepared so that it could be proven that the EDC was required to produce a crosslinked hydrogel under the experimental conditions. Three CS and three HA films were submerged in 80:20 mixtures of ethanol and water and three more of each film were submerged in 80:20 mixtures of acetone and water. No EDC was present in either mixture. After 24 hours, the CS and HA films were removed from the ethanol-water and acetone-water mixtures. All of the films were intact, however upon submersion in water for rinsing, the CS films immediately dissolved and the HA films dissolved within around ten minutes of submersion in water. This indicated that firstly EDC was required to crosslink the CS and HA films as crosslinked films would not dissolve in water so quickly. The acetone samples were used to demonstrate that even if an intact film of CS or HA was removed from the ethanol-water or acetone-water mixture after 24 hours, it could be shown that the ethanol was not



(a) Uncrosslinked HA film.



(b) Swollen HA film crosslinked in 80:20 ethanol:water.

**Figure 5.4:** HA films prepared from HA solutions, and crosslinked in ethanol:water mixtures that contained EDC.

active in the crosslinking as the acetone samples were also still intact.

EDC-crosslinking in the CS and HA films was via ester bonds, between carboxyl and hydroxyl groups. It could be suggested that the hydroxyl groups on the ethanol molecules could interfere with the esterification reaction mediated by the EDC. For this reason, further experiments using acetone as the non-solvent were performed to confirm that the ethanol played no role in crosslinking. Acetone was used in a similar way by Tomihata *et al.* [120] when synthesising HA crosslinked films as it does not contain hydroxyl groups or any other potentially reactive moieties. To confirm that ethanol did not play a part in the esterification reactions, CS and HA films were submerged in 80:20 mixtures of acetone and EDC solution for 24 hours. Following the 24 hour crosslinking period, the CS and HA films were removed from the mixtures and rinsed by submersion in water. Neither CS nor HA films showed any signs of dissolution during rinsing and thus crosslinking was considered to have occurred. This demonstrated that ethanol did not take part in or interfere with the EDC-crosslinking reaction.

As a final control experiment, a test was carried out to demonstrate the need for a non-solvent. CS and HA films were submerged in EDC solution and observed. It was expected that the CS and HA films would both dissolve in the EDC solution as they are soluble in water when not crosslinked, and this indeed occurred. The CS films dissolved immediately on contact with the EDC solution, and the HA films had broken apart in the first 2 minutes and completely dissolved within 15 minutes of submersion.

### **Varying EDC solution concentration**

Following the experiments to determine the ideal methodology to prepare the CS and HA films, the next step was to synthesise a range of crosslinked CS and HA hydrogels in the presence of various concentrations of EDC solution. By increasing or decreasing the concentration of EDC solution, it was expected that the amount of crosslinking ester bonds formed would increase or decrease respectively. This was expected to act as a way to control the characteristics of the CS or HA hydrogels as the degree of crosslinking in a hydrogel has been shown to be related to degradation and mechanical properties of a gel [121].

The method used followed the method developed in the previous section; a CS or HA film was prepared from a 1 % (w/w) CS or HA solution, and was submerged in a ethanol-EDC solution mixture in a 80:20 ratio for 24 hours. The EDC solutions were prepared to different concentrations as required. The crosslinked films were then removed from mixtures and rinsed three times for five minutes in deionised water, and air-dried.

CS hydrogels were synthesised but not fully characterised. It was observed that the CS gels were consistently more delicate and challenging to handle than those prepared from HA. It was especially true for the lowest EDC concentration CS hydrogels prepared in up to  $0.10 \text{ mol dm}^{-3}$  EDC solutions. (This became even more apparent during the swelling experiments later where the CS gels would begin to disintegrate and become stringy upon submersion in water.) By contrast, the HA gels maintained their film geometry throughout at all EDC concentrations. Equally, the CS gels prepared in greater than  $0.10 \text{ mol dm}^{-3}$  EDC solutions gave brittle hydrogels that broke into pieces on rinsing which was also problematic. This indicated that some crosslinking had occurred but it did not do so in an evenly distributed way. These small pieces could be collected but were not suitable for swelling tests or IR spectroscopy as the small sizes did not have enough mass to be reliably measured by the balance and the sample geometry was too small to fit the stand in the IR spectrometer. The HA hydrogels, however, were found to be robust

enough to be characterised.

IR spectroscopy was used as a simple characterisation tool to determine whether esterification had occurred in the HA films and whether the EDC concentration changes could be seen to change the amount of ester crosslinks within the matrices. CS hydrogels were not characterised by IR spectroscopy because the samples did not form discrete gels. EDC crosslinking mediated the formation of ester bonds between hydroxyl and carboxyl groups, therefore it was expected that there would a peak seen in the IR spectra at around  $1700\text{ cm}^{-1}$  of crosslinked HA films indicating the presence of ester bonds (specifically the ester carbonyl bond). Furthermore, as the EDC concentration was increased in crosslinking solutions, it was expected that the level of crosslinking bonds present in the hydrogels would also increase, signposted by decrease in transmittance for the ester peak in the IR spectra. A decrease in transmittance of the ester peak would indicate an increased absorption of IR radiation at that wavenumber, signifying greater quantities of ester bonds in the sample.

Figure 5.5 shows the IR spectrum of an uncrosslinked HA film in red. No specific peak can be seen at around  $1700\text{ cm}^{-1}$  for the uncrosslinked film, whereas a peak indicating the presence of ester bonds at  $1700\text{ cm}^{-1}$  is present in the stacked spectra for HA hydrogels crosslinked in EDC solutions, as highlighted in yellow on the figure. The % transmittance for the  $1700\text{ cm}^{-1}$  peak decreases with increasing EDC concentration demonstrating the increasing ester bonding in the hydrogels, and thus proving that ester crosslinking increases with increasing EDC concentration. A closer look at the  $1700\text{ cm}^{-1}$  peak is given in figure 5.6. The spectra in figures 5.5 and 5.6 are stacked and offset from each other by 5 % transmittance to aid visualisation of the peaks.

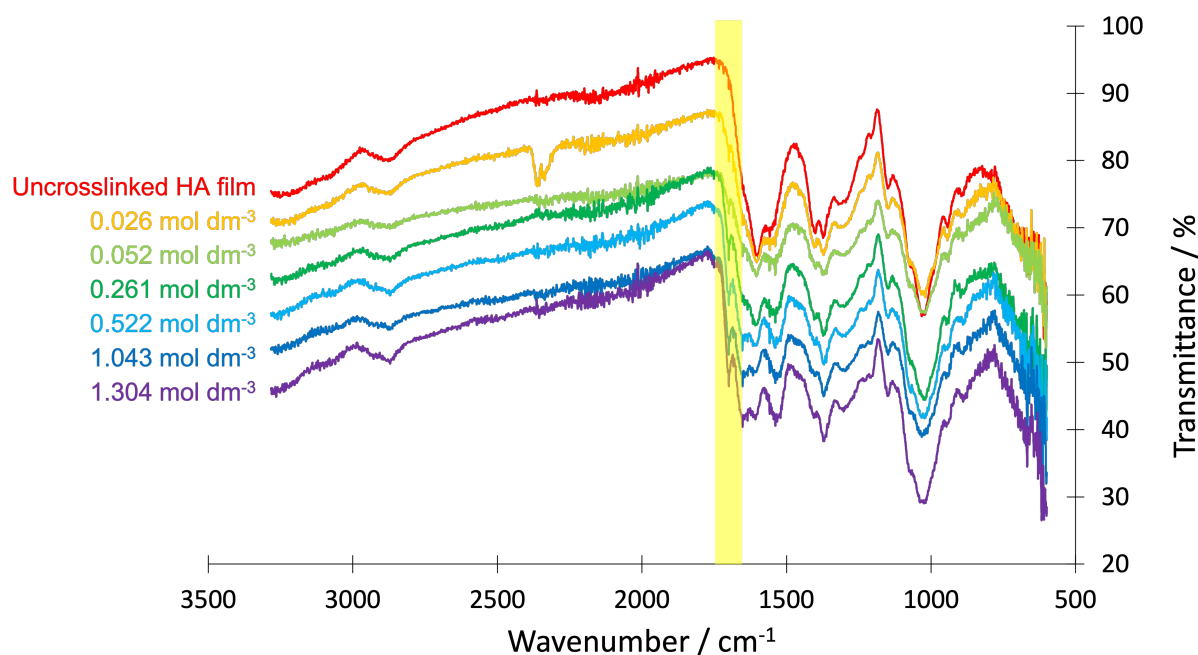


**Figure 5.5:** Stacked IR spectra of various HA hydrogels synthesised with different EDC solution concentrations as indicated by the labels on the spectra. The peak at  $1700\text{ cm}^{-1}$  highlighted in yellow is attributed to the ester carbonyl, confirming the presence of crosslinks in the HA films.

An ester carbonyl peak was also seen in crosslinked HA film IR spectra by Tomihata *et al.* [120] where they measured the  $1700\text{ cm}^{-1}$  peak intensity relative to a reference peak at  $2925\text{ cm}^{-1}$ . The relative ester

peak intensity increased with increasing EDC concentration, indicating that the level of crosslinking in the gels increased with EDC concentration. This comparison of peaks was completed for the HA crosslinked film spectra in figure 5.5 to quantitatively demonstrate the decrease in transmittance for the  $1700\text{ cm}^{-1}$  peak (and thus increase in ester bonding). The peak at  $2870\text{ cm}^{-1}$  was chosen as the reference peak as this was attributed to CH stretching that does not change during crosslinking. Figure 5.7 shows the decreasing peak transmittance (T) ratio with the increasing EDC concentration linearly when EDC concentration is plotted logarithmically as indicated by the trend line. Interestingly, a similar relationship was noted in the equivalent plots reported by Tomihata *et al.* [120] who observed a linear relationship in the peak ratios versus the EDC concentration on a logarithmic scale. This result further confirmed that increasing the EDC concentration during crosslinking, increased the level of ester bonds formed in the resulting hydrogel.

Additionally, it should be noted that there was no such peak present in the IR spectrum of an un-crosslinked HA film. This evidence demonstrated the presence of ester bonds in the crosslinked HA films and that the amount of crosslinks could be altered via changing the concentration of EDC solution during crosslinking. It also confirmed that ester bonds had formed, confirming that the crosslinking method gave rise to hydrolytically degradable bonds, which fulfils the biodegradability requirement discussed in more detail later.

### **Acidification of HA for film preparation**

Throughout the CS and HA hydrogel preparations so far, the CS and HA have been used straight from the bottle as the manufacturer provided. This means that both CS and HA were used in their sodium salt form. It was known that by altering the pH of the HA solutions, the protonation of the HA molecules could be changed with dissociation of the carboxylate groups occurring around pH 2 [215]. This had been observed to give HA solutions with physical gel-like properties and thus it was considered that for this work, performing a HA physical gel could give better quality crosslinked HA films. When preparing HA films, Tomihata *et al.* [120] did not alter the pH of the HA solutions.

Crosslinked, pH-altered HA films were prepared as outlined in section 5.2.5. The most notable observation made during the preparation was the sudden increase in viscosity that occurred as the pH reached 2. At this point, the HA solution became very gel-like in appearance and the magnetic stirrer often became stuck within the gel. Additionally, this caused challenges when casting the HA solution into Petri dishes. The very viscous HA solution was distributed around the Petri dish using a syringe as the material was resistant to simply pouring. Once dry, the pH-altered HA films appeared no different to the non-pH-altered films, and did not show any differences during crosslinking either. To determine whether the changes in pH prior to crosslinking had an effect on the resulting HA gel properties, swelling tests were carried out, and the results are given in the following section.

### **5.3.2 Swelling properties of CS and HA hydrogels**

The CS and HA hydrogels developed thus far were both based on molecules found native in the body and therefore biocompatible. The EDC-crosslinking method used had been demonstrated to form ester bonding within the gels meaning the crosslinks were hydrolytically degradable fulfilling another of the

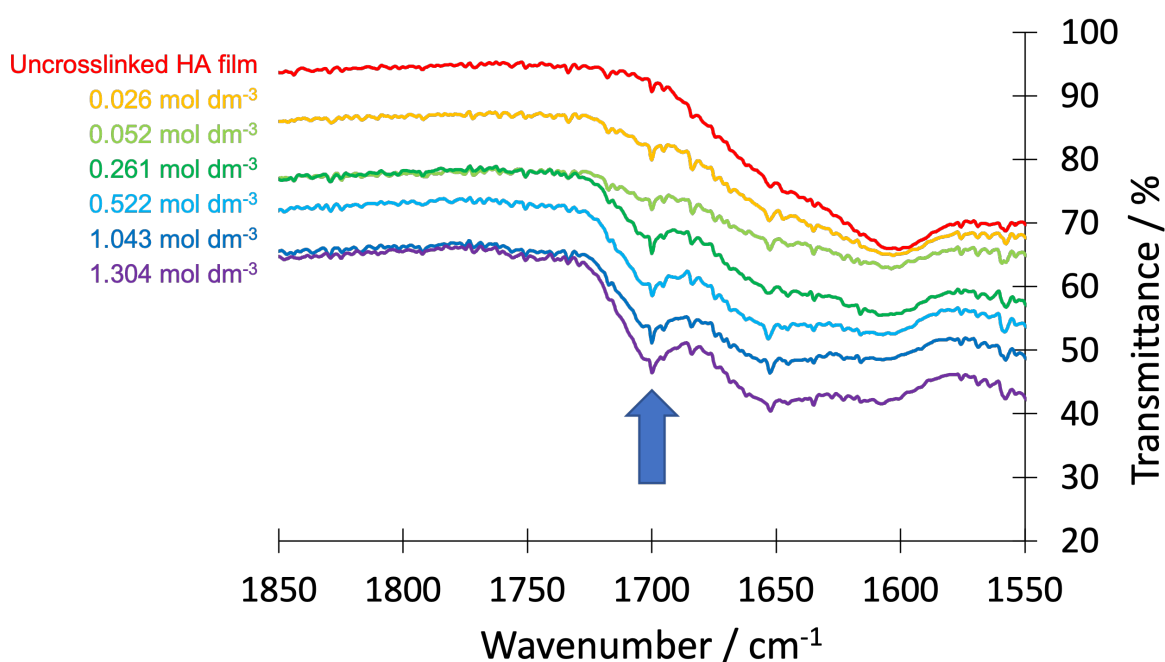


**Figure 5.6:** Stacked IR spectra of various HA hydrogels synthesised with different EDC solution concentrations as indicated by the labels on the spectra, focussing on the region between 1550 and 1850  $\text{cm}^{-1}$ . The peak at 1700  $\text{cm}^{-1}$  indicated by an arrow is attributed to the ester carbonyl, confirming the presence of crosslinks in the HA films.

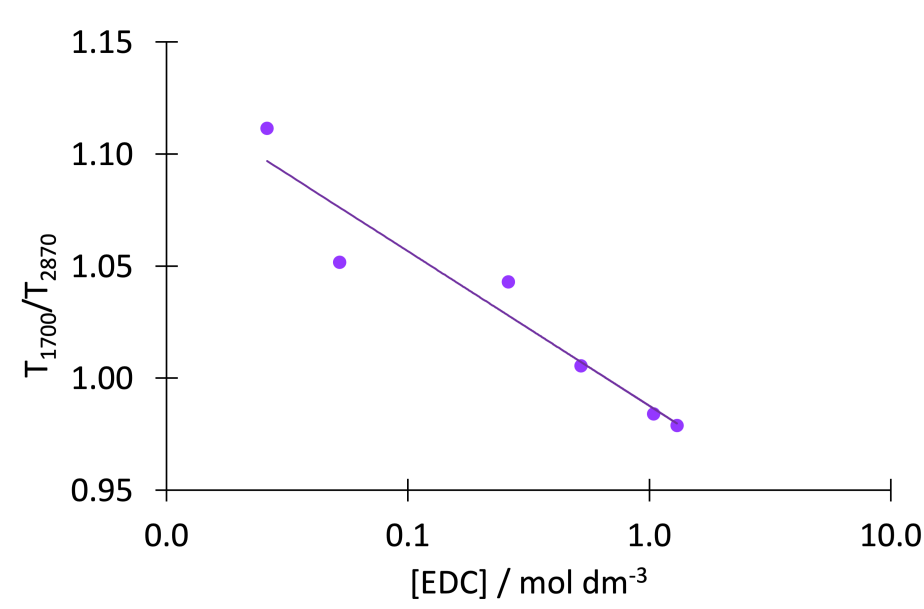
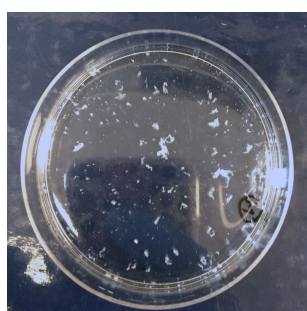


**Figure 5.7:** The ratios of the peak transmittance for the ester peak at 1700  $\text{cm}^{-1}$  to the reference peak at 2870  $\text{cm}^{-1}$  in the IR spectra of HA crosslinked gels in figure 5.5 in relation to the EDC solution concentration during crosslinking.

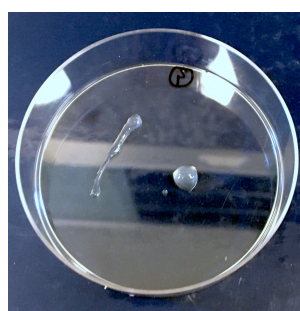
requirements of the hydrogel set out at the start of this chapter. Following this successful synthesis of both CS and HA hydrogels, the next step was to start to assess their properties. Many of the properties of hydrogels are related to the level of crosslinking within the matrix. Typically, greater crosslinking leads to a tighter matrix with smaller pores and a lesser capacity to swell. The degree of crosslinking also relates to the mechanical properties and degradation properties, as a more crosslinked hydrogel will often have a larger elastic modulus and take longer to degrade [121, 216].

As it had been shown that increased EDC concentration during crosslinking led to greater ester bonding in HA hydrogels, assessing the swelling behaviour of the hydrogels allowed examination of the effect different concentrations of EDC solution during crosslinking had on the resulting hydrogels properties. It also gave insight into how easy the hydrogels were to handle when swollen. Swelling experiments were undertaken on a limited number of CS hydrogels and HA hydrogels synthesised from HA solutions at neutral pH and at low pH (1-2).

A range of CS hydrogels were synthesised with different levels of EDC concentration in the crosslinking solutions. In a number of CS hydrogel syntheses, the hydrogel was observed to begin to disintegrate on contact with water during the rinse steps. These issues became more pronounced when attempting swelling experiments. In general, the CS hydrogel films were much harder to handle and of poorer quality than those made of HA. The CS gels tended to disintegrate submerging the films in the water for the swelling tests (figure 5.8a). Often the pieces of gel had to be carefully pulled out of the water and fell apart on doing so (figure 5.8b). This meant that it was unlikely that all of the hydrogel was collected back out of the water, and thus the wet and swollen masses recorded may be inaccurate.



(a) Fully disintegrated CS gel.



(b) Pieces of swollen CS gel following partial break up.

**Figure 5.8:** Disintegrating CS hydrogel samples during swelling tests.

For this reason, only limited data related to the swelling properties of CS hydrogels presented in figures 5.9 and 5.10. These results were considered to be a guide for comparison with the HA gels. Additionally, only low concentration EDC solution data were recorded as the CS gels crosslinked in the more concentrated EDC solutions disintegrated and the small pieces could not have their mass measured. This also meant that the gels were not fit for purpose as they did not form a discreet swollen film and were not able to stand up to manual handling (much like they would during implantation in to the body).

As seen in figures 5.9 and 5.10, the CS hydrogels were highly hydrated with the CS gels prepared with the lowest concentrations of EDC solution giving around 90 % water uptake. The hydration appeared to decrease with increasing EDC concentration as expected, however the range of EDC concentrations that successfully formed usable gels was limited so the swelling data obtained are also limited. As previously mentioned, the CS hydrogels were difficult to handle and often fell apart, so the characterisation of CS

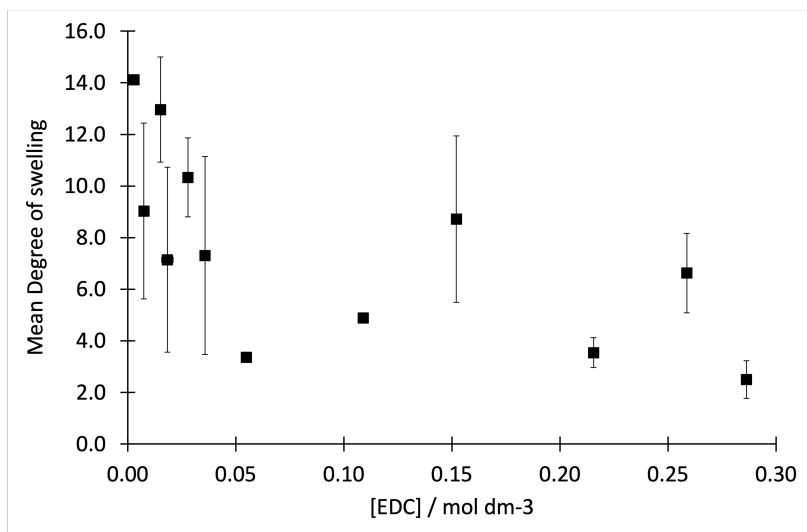


**Figure 5.9:** The degree of swelling calculated for CS hydrogels prepared in crosslinking mixtures containing various EDC concentrations, swollen in water.

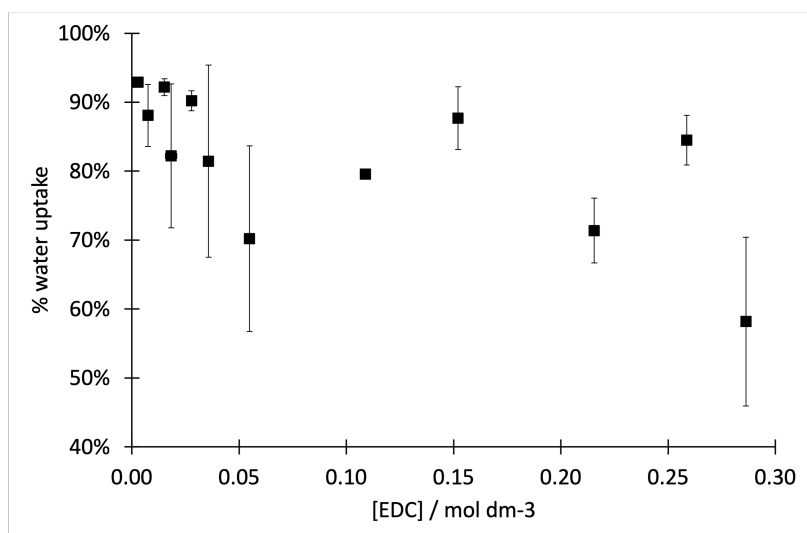


**Figure 5.10:** The water uptake calculated for CS hydrogels prepared in crosslinking mixtures containing various EDC concentrations, swollen in water.

hydrogels was not continued. Figures 5.9 and 5.10 show that there were large variations in the mean degree of swelling and water uptake (demonstrated by large error bars in the y-axis) which were attributed to loss of material during some swelling tests when CS films began to disintegrate on contact with water. The loss of different masses of CS film during swelling tests for equivalent EDC concentrations lead to large variations in the mean degree of swelling and water uptake.

Both types of HA gel (prepared with pH alteration and without) were tested to examine whether there were any significant differences between the two synthesis techniques beyond observations made in the previous section. Figures 5.11 and 5.12 show the mean degree of swelling and mean water uptake of the hydrogel ( $W_w$ ) and the hydrogel matrix itself ( $W_s$ ), respectively, for HA hydrogels synthesised in crosslinking mixtures containing different concentrations of EDC. The error bars refer to the standard deviation about the mean. From the figures it can be seen that especially for the HA hydrogels synthesised from HA solutions with the pH altered to 1 - 2, lower EDC concentrations during synthesis appeared to result in gels that demonstrated greater degrees of swelling and greater water uptake than those synthesised with greater concentrations of EDC. In future, further HA hydrogels should be prepared using EDC solutions at concentrations lower than  $0.20 \text{ mol dm}^{-3}$  to provide more data which could aid verification of this apparent trend. Nevertheless, these results fit the expected behaviour of the hydrogels. It was expected that HA hydrogels synthesised with greater concentrations of EDC present in the crosslinking solution would result in a larger number of crosslinks within the hydrogel network. A greater number of crosslinks would result in a tighter network that would not absorb as much water as a looser network hydrogel.

It can be seen in both the water uptake and the degree of swelling (figures 5.11 and 5.12) that there was larger variation about the mean within the HA hydrogels synthesised from HA solutions at pH 7 versus those synthesised from HA solutions that had their pH altered to pH 1 to 2. This is demonstrated by the much smaller error bars in both plots for the pH 1-2 HA hydrogels. It is suggested that when the pH of HA solutions was altered to pH 1-2, hydrogen bonded physical hydrogel structures were formed. This was supported by the change in viscosity observed on preparation of the pH altered HA solutions. This could lead to the EDC-crosslinking being more efficient as the molecules were already arranged in an ordered way leading to more consistent levels of crosslinking for the same EDC concentration than the pH 7 gels. This is supported by evidence from Gatej *et al.* [215] who stated that at around pH 2 carboxylate dissociation occurs giving rise to a large amount of intermolecular hydrogen bonding resulting in a physical hydrogel type structure. Both the pH 7 and pH 1-2 HA hydrogels were easy to handle when swollen and maintained a film like appearance.

These data on both the HA and CS films demonstrate that the swelling of the hydrogels can be controlled by the EDC content during the crosslinking reaction. The CS gels were too difficult to handle when swollen and thus were discarded and no further characterisation took place. The HA gels, on the other hand, maintained their film geometry when swollen. This is a good result that is important for their use as a biocompatible substrate for future bioelectronic devices. The HA hydrogels discussed in the rest of this thesis were not prepared from solutions in which an acid or base was added to alter its pH.

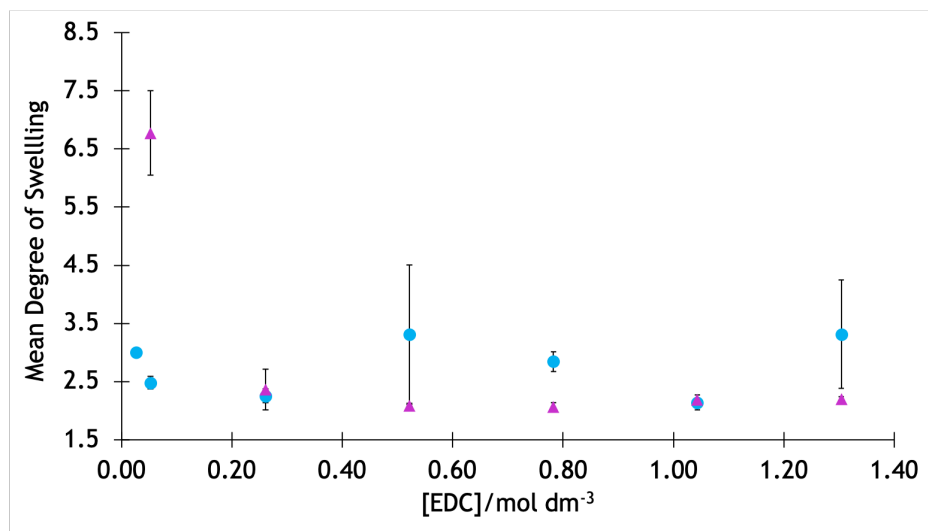


**Figure 5.11:** The degree of swelling measured for HA hydrogels prepared in various EDC solutions of different concentrations. The blue circles refer to HA hydrogels prepared from HA films without any pH alteration (pH 7), and the purple triangles are for those prepared from HA solutions altered to pH 1-2.

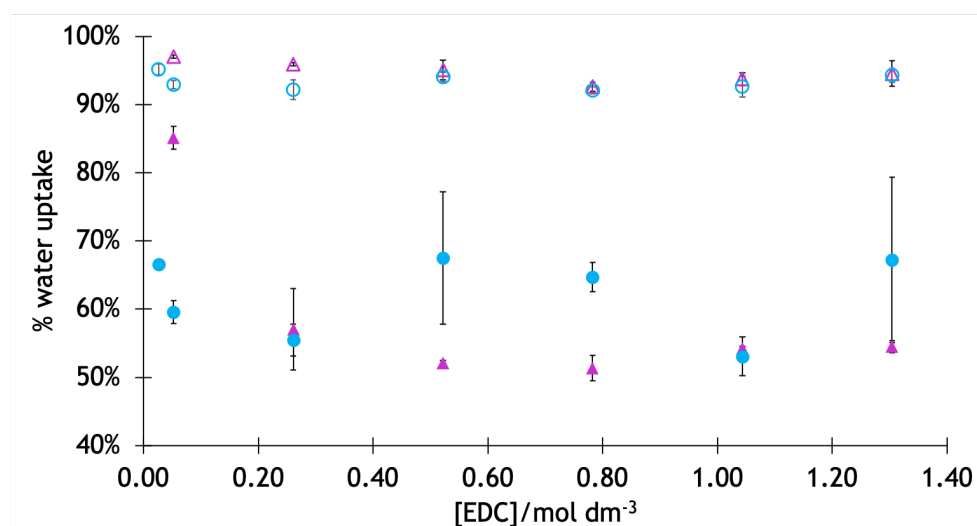


**Figure 5.12:** The mean water uptake measured for HA hydrogels prepared in various EDC solutions. As before, blue circles are for pH 7 HA samples, and purple triangles are for pH 1-2 HA samples. The unfilled points are for the mean % water uptake of the hydrogel ( $W_w$ ) and solid, filled points for the hydrogel matrix itself ( $W_s$ ).

### 5.3.3 Degradation of hyaluronic acid hydrogels

To assess how the hydrogels would degrade in the body, it was important to mimic physiological temperature and pH. This was achieved by undertaking the degradation experiments in PBS solutions (buffer solution that maintains a pH of 7.4) held at 37 °C. This work did not include enzymatic degradation studies. In reality, the body is a complex system in which the hyaluronase enzyme would be present. The degradation study presented here was to act as an indication of lifetime, and is a common practice in the field of biomaterial research [121, 216, 217]. In addition, strictly speaking, this work was not a biodegradation study, but a hydrolysis study as no biological activity, such as enzymatic degradation, was acting to break down the HA hydrogel.

A range of HA hydrogels crosslinked in the presence of a range of EDC concentrations were submerged in PBS at 37 °C, and stored in an oven at 37 °C to maintain the temperature of the buffer throughout the experiment. Prior to submersion the dry masses of the crosslinked HA films were recorded. At set time points throughout the experiments, crosslinked HA films were removed from the PBS and air-dried overnight, and the dry mass recorded. A white substance was observed on the surface of many of the gel samples, which were presumed to be salts from the PBS which had deposited during drying. For this reason, the crosslinked HA films were then carefully rinsed in deionised water and allowed to dry again. This removed the salty deposits from the HA hydrogels, and thus, the dry masses of the HA films were recorded again. By calculating the % mass lost of the gels at different time points, the degradation profiles could be plotted, as seen in figure 5.13. Each point on the graph represents the mean mass loss  $\pm$  standard deviation for at least three HA hydrogels crosslinked in a specific concentration of EDC solution, submerged in PBS solution at 37 °C for a set time period.

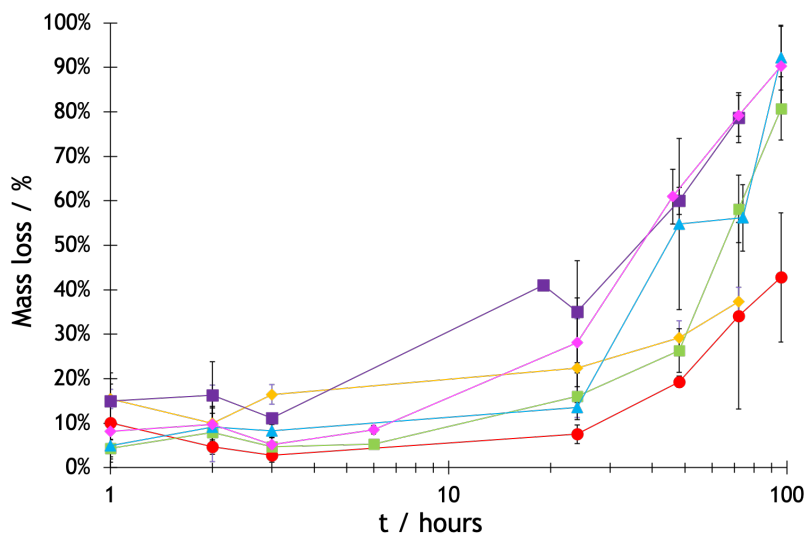


**Figure 5.13:** Degradation profiles of HA hydrogels crosslinked in mixtures containing EDC solutions of varied concentrations: 0.05 mol dm<sup>-3</sup> (red circles), 0.26 mol dm<sup>-3</sup> (yellow diamonds), 0.52 mol dm<sup>-3</sup> (green squares), 0.78 mol dm<sup>-3</sup> (blue triangle), 1.04 mol dm<sup>-3</sup> (purple square), and 1.30 mol dm<sup>-3</sup> (pink diamond).

From the results, it can be seen that after 96 hours the HA hydrogels crosslinked in EDC solutions of the following concentrations suffered almost 100% mass loss: 0.52 mol dm<sup>-3</sup> (green squares), 0.78 mol dm<sup>-3</sup> (blue triangle), 1.04 mol dm<sup>-3</sup> (purple square), and 1.30 mol dm<sup>-3</sup> (pink diamond). This meant that these gels had completely hydrolysed and the HA had dissolved back into the solution. On the other

hand, at the end of the 96 hour experiment, the lower concentrations of EDC solution HA gel samples,  $0.05 \text{ mol dm}^{-3}$  (red circles) and  $0.26 \text{ mol dm}^{-3}$  (yellow diamonds), had both reached around 30 to 40 % mass loss. This formed an unexpected trend as it appeared that the degradation time increased with increasing EDC concentrations in the crosslinking mixture.

The IR data collected on the HA gels post-synthesis confirmed the assertion that increasing EDC concentration in the crosslinking mixture resulted in increased ester bonding in the HA film samples. It was assumed that greater levels of crosslinking, associated with greater EDC concentrations, would lead to longer lasting HA hydrogels, however it seemed that the opposite was true. The HA hydrogels crosslinked in more concentrated EDC solutions appeared to degrade faster than those crosslinked in less concentrated EDC solutions. This was suggested to be a result of the random nature of the crosslinking process. The crosslinking in the HA hydrogels will be uneven throughout the films, leading to areas of greater and lesser crosslinking. As the gel degrades, it is likely that the action of degradation occurs at these more crosslinked regions since the ester crosslinks are the site of the hydrolysis reaction. These areas will swell substantially more, which in turn will disrupt the gel putting other regions under greater strain, accelerating degradation at these strained areas. Future researchers could use small-angle neutron scattering techniques to examine the structures of the crosslinked gels which could give insight into the validity of this hypothesis. Furthermore, if the degradation of the ester bonds were followed by FTIR spectroscopy, this could reveal a chemical origin for the unexpected degradation behaviour.

These results successfully demonstrate that the EDC-crosslinked HA hydrogels are degradable and undergo complete hydrolysis over a period of approximately four days, varying with the EDC concentration used in the crosslinking step. This lifetime may not be ideal for longer-term applications and could restrict the usefulness of the HA hydrogels within SCI treatments; for example, the e-dura device developed by Minev *et al.* [27] discussed in chapter 1 was implanted into the spinal cords of rats for 6 weeks for testing, which is significantly longer than the four day lifetime of the HA hydrogels presented here. Although not ideal for longer-term applications, the lifetime of the hydrogels could be appropriate for use as substrates for OECTs in short-term monitoring applications such as in one-off *in vivo* diagnostic testing or in bench-top cell culturing. It has previously been established that HA (and CS) hydrogels can be used as supporting structures for neuronal stem cells [70, 89, 91, 92, 94, 100, 114, 115]. Alternatively, other crosslinking methodologies could be explored in future to try and extend the HA gels lifetimes, however care must be taken as many crosslinking technologies in the literature are not degradable, and thus would not suit the biodegradation requirement established here. Further work should explore including amide bonding in EDC-crosslinked HA gels through the addition of a diamine to the crosslinking mixtures, or through the addition of another biocompatible molecule such as collagen. Amide bonding is resistant to simple hydrolysis but is degradable via enzyme action in the body [119, 120], and thus could fulfil the biodegradation criteria.

### 5.3.4 Mechanical properties of hyaluronic acid hydrogels

In the experimental techniques chapter (chapter 2), contact mechanics were introduced. Contact mechanics can be used to describe the deformation of solids in contact with each other, and can be used to determine areas of contact between two surfaces, depths of indentation, and elastic moduli. This approach was used to determine the elastic moduli of HA gels prepared in mixtures containing various concentrations of EDC solution. The aim of this was to determine whether the HA hydrogels had elastic

moduli that matched the elastic moduli of structures in the CNS, and to see whether varying the EDC concentration during crosslinking resulted in variation in the moduli.

To determine the elastic modulus of the HA hydrogels, force-distance plots were obtained using the mechanical tester (Stable Micro Systems Texture Analyser TA.Xtplus). The HA film samples were mounted on a Perspex block using double-sided tape and submerged in a beaker full of water for 15 minutes prior to testing to allow the gel to swell to an equilibrium level. The distance moved by the probe was recorded throughout the experiment (giving a force-distance plot) so that the depth of indentation into the gel could be obtained. Video capturing the point of contact was used in conjunction with the force-distance plots to determine the contact point between the gel and the probe. Each hydrogel was probed at three randomly chosen positions across the gel surface. At each of these three positions, the measurement was repeated three times. This gave a total of nine force-distance curves per hydrogel sample. An example of a typical force-distance curve for a HA hydrogel recorded by the mechanical tester can be seen in figure 5.14.

Figure 5.14 shows the approach of the probe to the submerged HA gel surface (1), followed by the contact point where the probe contacted the gel (2), determined from video. The force is applied shown by the indentation label (3) on the plot to the 2-minute hold (4). Following the 2-minute hold, the probe retracts (5) and moves away from the gel surface (6). It should be noted that an applied force appears in these force-distance plots as a negative force. The positive force shown as the probe retracts (5, in figure 5.14) is due to a force required to pull the probe from the test sample. This pull off force is discussed later in this section.

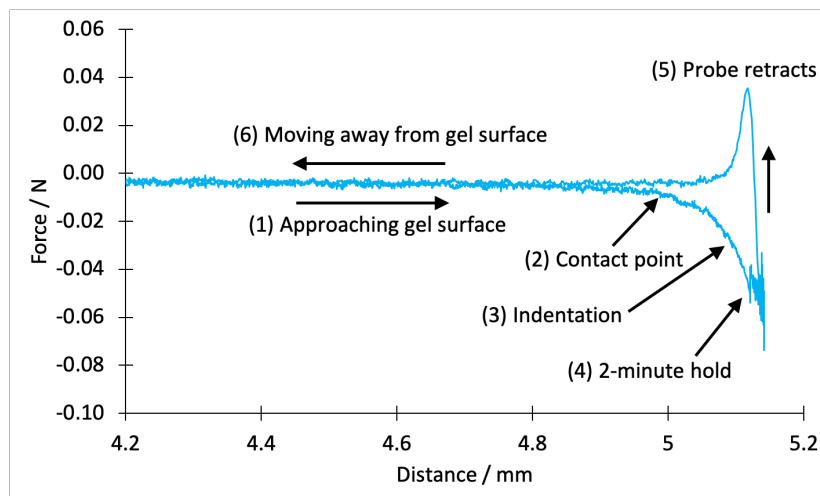


**Figure 5.14:** Force-distance plot obtained for a crosslinked HA hydrogel film with an applied force of 0.05 N. Each notable event is labelled and numbered in the order that they occur.

The elastic moduli of the HA hydrogels were calculated using principles of contact mechanics introduced in chapter 2. If it is assumed that the hydrogel can be described as an elastic half space, equation 5.5 can be used to calculate the reduced elastic modulus ( $E^*$ ) of the hydrogel when the hydrogel is indented with a cylindrical indenter. The reduced modulus can then be converted into the elastic modulus ( $E$ ) of the hydrogel sample using equation 5.6 [160], where  $\nu$  was the Poisson's ratio of the sample or indenter.

$$F = 2aE^*d \quad (5.5)$$

$$\frac{1}{E^*} = \frac{(1 - \nu_{sample}^2)}{E_{sample}} + \frac{(1 - \nu_{indenter}^2)}{E_{indenter}} \quad (5.6)$$

In the calculations for the reduced elastic modulus ( $E^*$ ), the normal force ( $F$ ) was the applied force by the mechanical tester, and the indentation depth ( $d$ ) was the calculated difference between the distance travelled by the probe at the contact point and the furthest distance travelled by the probe at the end of the 2-minute hold period. The radius of the indenting cylinder ( $a$ ) was 5 mm.

Equation 5.6 was rearranged to determine the elastic modulus of the sample hydrogels. The Poisson's ratio of the hydrogel ( $\nu_{sample}$ ) was assumed to be 0.5. This value is typical of hydrogels and assumes that the hydrogel follows rubber elasticity [158]. The elastic modulus ( $E_{indenter}$ ) and Poisson's ratio ( $\nu_{indenter}$ ) of the cylindrical Delrin probe were 3600 MPa and 0.35 respectively. The values for the cylindrical Delrin probe were obtained from the manufacturers of the mechanical tester (Stable Micro Systems), and the supplier of the Delrin material to the manufacturer (Ensinger). The elastic moduli of the HA hydrogels are shown in figure 5.15.

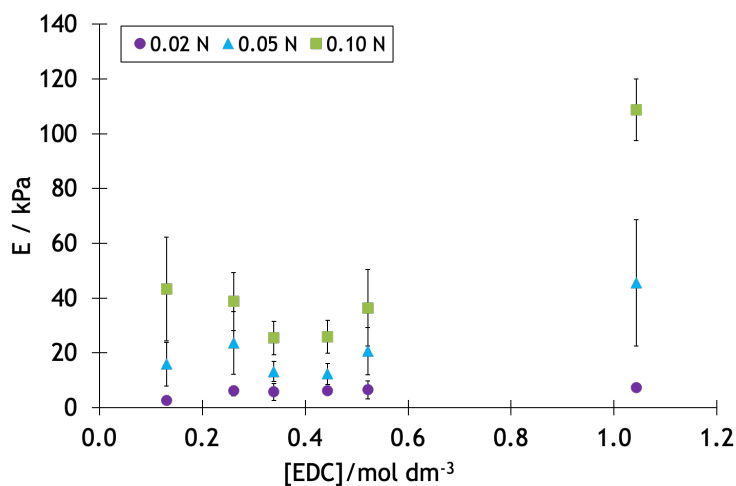


**Figure 5.15:** Plot of the elastic moduli of hyaluronic acid hydrogels as a function of the concentration of EDC solution during crosslinking. The data marked by the circle, triangle, and square markers refer to applied forces of 0.02 N, 0.05 N, and 0.10 N respectively. Each point is the mean elastic modulus with the minimum and maximum calculated elastic modulus for that EDC concentration indicated by the error bars.

This methodology of determining the elastic modulus through contact mechanics assumes non-adhesive contact, however as seen in the force-distance curve (figure 5.14) it appears that there is a force involved in detaching the probe from the surface of the HA hydrogel implying an attractive interaction. This could be a result of attractive interactions forming between the probe and water in the hydrated hydrogel following indentation. Within the hydrated hydrogel, there will be a large amount of hydrogen bonding between the water and the hydrogel. As the probe compresses the hydrated sample, water will be forced to move from the area of indentation. As the probe retracts, there may be some hydrogen bonding between the probe and the hydrogel leading to the apparent attractive interaction seen in figure 5.14. The pull-off force, however, is not always seen in the force-distance curves especially for the 0.02 N applied force experiments, as seen in the example force-distance curve in figure 5.16 where no positive force was recorded. This could be due to the force not being large enough to significantly displace water within

the hydrogel, thus giving no hydrogen bonding and no pull-off force. This could mean that the data for 0.02 N applied forces may not accurately indicate the elastic modulus of the swollen hydrogel matrix.

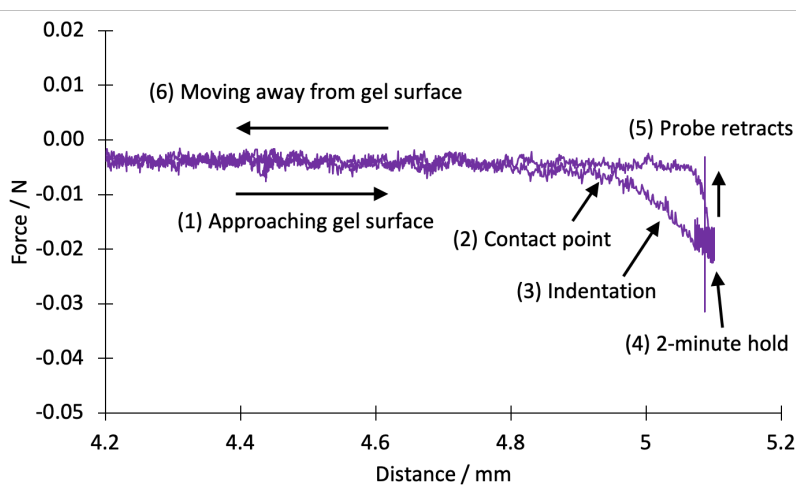


**Figure 5.16:** Force-distance plot obtained for a crosslinked HA hydrogel film with an applied force of 0.02 N. Each notable event is labelled and numbered in the order that they occur. The indentation of the hydrogel with the applied force of 0.02 N can be seen as the force becoming negative. In these force-distance curves, applied forces are seen as negative, and pull-off forces acting in the opposite direction are seen as positive.

Indentation methods to determine moduli are common in soft materials, however typically this is undertaken using a method such as AFM nano-indentation [158, 161]. There are limitations on using such a method as the hydrated nature of a swollen hydrogel is not usually compatible with AFM techniques [155, 161]. On the other hand, tensile testing on a universal mechanical test frame is also often used to characterise the elastic modulus of hydrogels [155] however these instruments would not be appropriate for the HA hydrogel characterisation due to the nature of the film geometry of the gels. Any method of elastic modulus determination for very soft materials is challenging with different methodologies yielding varied results for the same materials [155, 161].

The calculated elastic moduli of the HA gels prepared with a given EDC solution concentration differed with applied force (figure 5.15). This was especially apparent for the HA hydrogels prepared from EDC solutions of concentration  $1.04 \text{ mol dm}^{-3}$  where the error in each mean elastic modulus had no overlap for each applied force. The force applied to the soft gels could be too great, moving from probing elastic deformation to plastic deformation and thus giving inaccurate elastic moduli for the higher applied forces, making the data unreliable hence the inconsistency in calculated elastic moduli. To test this hypothesis, HA hydrogels were prepared for mechanical testing utilising 80:20 ethanol:EDC solution ( $0.26 \text{ mol dm}^{-3}$ ) mixtures. Instead of probing different locations across the surface of the HA hydrogels, repeated cycles of applied force were focused on one spot. If the applied force was probing elastic deformation, the HA hydrogel would spring back from deformation each time and the depth of indentation, and thus the elastic modulus calculated, would be constant. On the other hand, if plastic deformation were occurring, permanent deformation of the HA hydrogel would occur meaning that on each repeated probing cycle the depth of indentation would increase. The elastic moduli would however decrease in this case which would not explain the increased elastic modulus with increased applied force. Nevertheless, the experiments were carried out and the indentation depths and related elastic moduli are shown in figure 5.17.

The results of the repeated cycles of probing were inconclusive. At first glance, the repeated cycles of probing with 0.02 N and 0.05 N applied force appeared to yield more consistent depths of indentation and therefore elastic moduli, however the depth of indentation changes by 21.5% and -14.8% from cycle 1 to 10 respectively. The 0.10 N applied force experiment resulted in an increased depth of indentation from cycle 1 to 10 of 38.1%. This increase in depth of indentation can be seen in the figure to result in a diminished elastic modulus by cycle 10. This applied force of 0.10 N yielded the greatest change in depth of indentation from cycle 1 to 10 which could suggest that the force was too great to probe the elastic region of deformation for the gels and was in fact causing permanent plastic deformation. This suggestion would then imply that the 0.02 N force was also too great as there was an increase in indentation depth from cycle 1 to 10 by 21.5%. This would be inconsistent with 0.05 N forces resulting in a decreased indentation depth from cycle 1 to 10. Another consideration is that it is likely that the crosslinking is not consistent across the hydrogel yielding regions of high and low crosslinking densities. Repeated perturbation at a particular region on a hydrogel versus another on the same gel may give different results due to the heterogeneity of the crosslinking. This was outside the immediate scope of this experiment, however it could have led to the inconclusive results. In future experiments, 100 or more repeated probing cycles may be useful in identifying whether plastic deformation is being probed, and lead to more conclusive results.

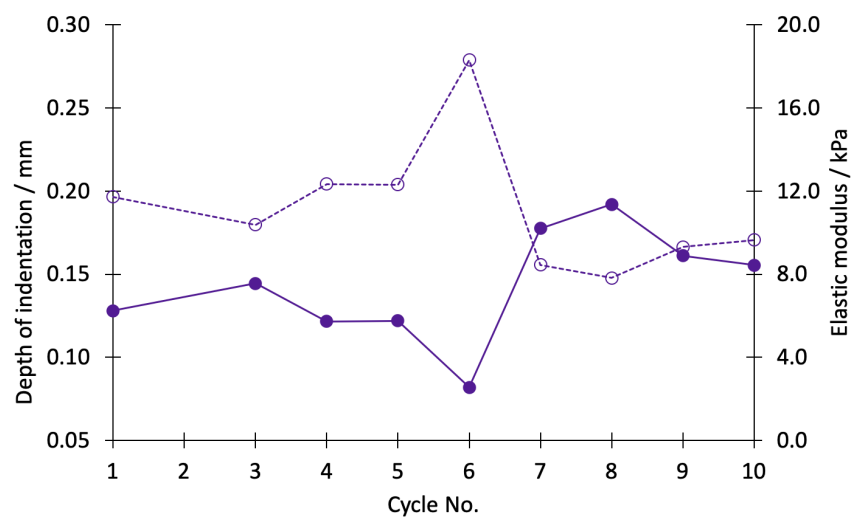
Figure 5.18 shows the elastic moduli calculated from just the 0.02 N and 0.05 N applied force data sets. The 0.10 N data set is not shown for clarity. Even with the highest applied force data not included on the plot, it can be seen that there was still a marked difference between the elastic moduli calculated from data from the two applied forces. This effect could be a result of the limitations of the assumptions used to calculate the elastic moduli.

It was hypothesised that the elastic moduli of the HA gels would increase with increased EDC concentration during crosslinking. Both the 0.02 N and 0.05 N applied force data shows increasing elastic modulus with increasing EDC concentration during crosslinking (figures 5.19 and 5.20).

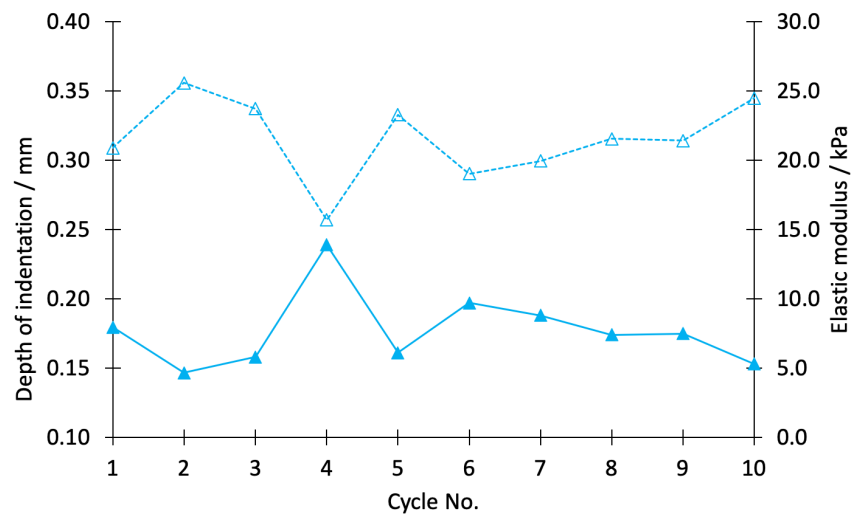
The elastic moduli of the HA gels were calculated using this method and were found to range from 2 to 50 kPa (figure 5.18) which were all within the range of previously reported elastic moduli for the CNS tissues (0.0003 - 1.40 MPa [70, 72-76]). This fulfilled the final criteria of the hydrogel to be mechanically appropriate for use in the CNS as well as biocompatible and biodegradable.

The characterisation of the HA hydrogels in this chapter has shown that by design they are degradable and mechanically appropriate for use in the CNS. It was shown that the HA hydrogels were hydrolytically degradable and that the elastic moduli of the gels were found to be appropriate for use in the CNS. Swelling, degradation, and mechanical properties all varied with EDC solution concentration used during preparation. By carefully choosing the EDC concentration upon crosslinking, a fine balance of properties could be achieved to fit the exact application of the hydrogel. Furthermore, the choice of HA as the material from which the hydrogels were formed began to fulfil the biocompatibility requirement. HA is naturally found in the human body, however, to prove the biocompatibility of the HA hydrogels definitively, further work involving direct exposure of the hydrogels to neural cell lines is required.

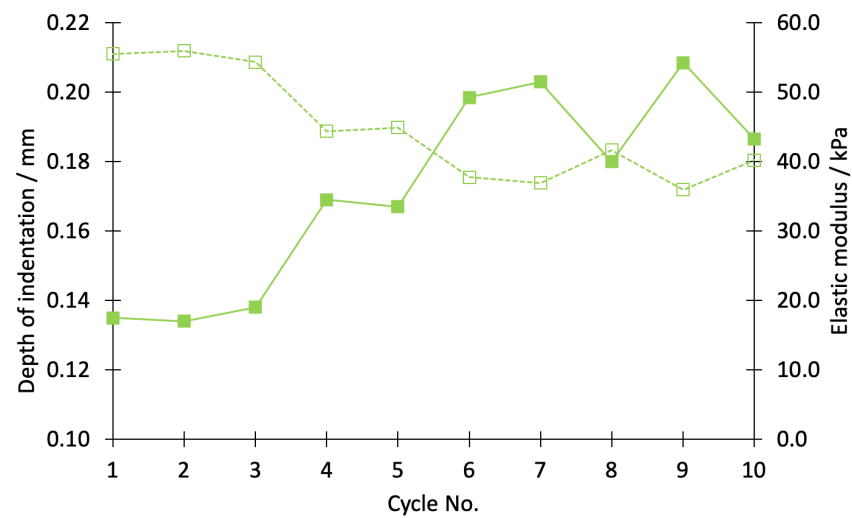
With the requirements fulfilled the next step was undertake some exploratory experiments on using the HA hydrogels as substrates for a bioelectronic device using PEDOT:CS or PEDOT:HA.



(a) 0.02 N applied force



(b) 0.05 N applied force



(c) 0.10 N applied force

**Figure 5.17:** Indentation depth and elastic moduli of HA gels undergoing multiple probing cycles under different applied forces. The depth of indentation is given by the solid filled points joined with a solid line, and the calculated elastic moduli are shown by the outlined points joined by the dashed line.

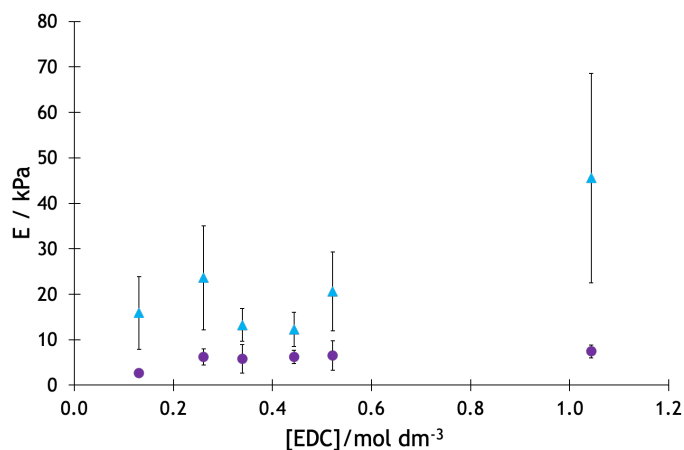


**Figure 5.18:** Plot of the elastic moduli of hyaluronic acid hydrogels as a function of the concentration of EDC solution during crosslinking without the 0.10 N applied force data. The data marked by the circle and triangle markers refer to applied forces of 0.02 N and 0.05 N respectively. Each point is the mean elastic modulus with the minimum and maximum calculated elastic modulus for that EDC concentration indicated by the error bars.

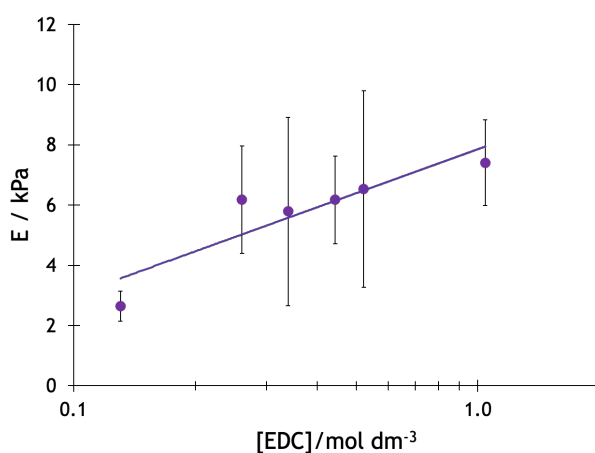


**Figure 5.19:** Plot of the elastic moduli of hyaluronic acid hydrogels as a function of the concentration of EDC solution during crosslinking, under 0.02 N of applied indentation force.

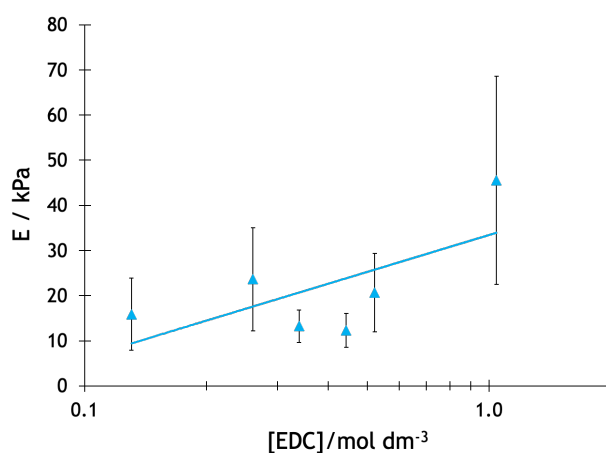


**Figure 5.20:** Plot of the elastic moduli of hyaluronic acid hydrogels as a function of the concentration of EDC solution during crosslinking, under 0.05 N of applied indentation force.

### 5.3.5 Combination of HA hydrogels with PEDOT:CS

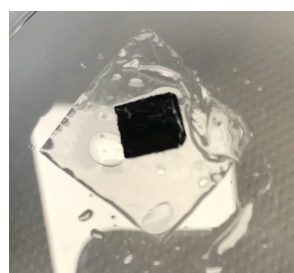
The aim of this work was develop a biocompatible and biodegradable hydrogel with mechanical properties that were comparable to that of the spinal cord. The HA hydrogels that were prepared meet these requirements, however the intended end use for these hydrogels was to act as a substrate for an OECT device based on PEDOT:CS. It was therefore necessary to assess the compatibility of the hydrogels with the organic electronic material and demonstrate that it was possible to cast a thin film of PEDOT:CS and graft it on to the HA hydrogel. In chapter 3 and 4, EDC-crosslinking was used to ensure that the PEDOT:CS and PEDOT:HA would not delaminate during testing in aqueous environments. This choice of crosslinking was due to considerations of degradation, and compatibility with the HA hydrogels, therefore could be used as a method to attach PEDOT:CS or PEDOT:HA to a crosslinked HA film.

As the OECT devices presented in the previous chapters were prepared from drop-cast PEDOT:CS or PEDOT:HA aqueous suspensions, drop-casting was also used to form a layer of PEDOT:CS on a HA crosslinked gel. Masking tape was used to form a stencil (figure 5.3) over which PEDOT:CS (1:1) aqueous suspension was drop-cast onto the HA hydrogel. This was so the PEDOT:CS film would form in a discreet area, as would be required in a real device.

Once the material was dry, the stencil was carefully peeled from the HA gel revealing a discreet square layer of PEDOT:CS. This PEDOT:CS was not crosslinked and if exposed to water, PEDOT:CS would come away from the HA hydrogel film and resuspend in the aqueous phase therefore an EDC-crosslinking step was performed. The HA film was already crosslinked, so was being exposed to EDC for a second time. The first crosslinking step was necessary as an uncrosslinked HA film would dissolve on contact with a PEDOT:CS aqueous dispersion due to the water contents. Following the crosslinking period, the HA crosslinked film with the PEDOT:CS layer was carefully removed from the ethanol-EDC solution mixture and submerged in water to rinse away any by-products or unreacted material. Additionally, this acted to test whether the PEDOT:CS had crosslinked. The PEDOT:CS layer and the HA hydrogel stayed together and intact during washing suggesting that the two had formed crosslinks (figure 5.21).



(a) Prior to crosslinking.



(b) Following crosslinking and rinsing.

**Figure 5.21:** HA hydrogel with PEDOT:CS drop-cast layer.

This experiment showed that EDC-crosslinking could be used to graft a PEDOT:CS film onto a HA hydrogel producing a biocompatible, degradable, and mechanically-appropriate prototype that forms the basis for the creation and characterisation of a full OECT device on a HA hydrogel in the future. This result opens up a range of possibilities for soft, degradable bioelectronic devices.

## 5.4 Summary and future work

The aim of this work was to develop a hydrogel that was biocompatible, biodegradable, and mechanically appropriate for use in the CNS, specifically in the spinal cord. The hydrogel has an intended end use as a substrate supporting materials in an OECT based on PEDOT:CS or PEDOT:HA, which could in future be developed towards a treatment for SCIs.

CS and HA were chosen as ideal candidates for the hydrogels as they are both molecules found throughout the human body and ECM, and thus inherently biocompatible. For this reason, both molecules have been previously used in hydrogel preparations for use in the CNS [70, 89, 91, 92, 94, 100, 114, 115]. CS and HA EDC-crosslinked hydrogels were prepared using a multi-step method based on work by Tomihata *et al.* [120]. The best methodology was established as preparing CS or HA films from solutions, and submerging them in an 80:20 mixture of ethanol and EDC solution, the concentration of which could be varied to alter the level of crosslinking within the gel. FTIR spectroscopy was used to prove the presence of ester crosslinks along with a simple rinse test which formed part of the synthetic route. FTIR spectroscopy also proved that the amount of ester bonding within crosslinked HA films increased with the concentration of EDC solution used in the crosslinking mixture. CS hydrogels prepared in this way were deemed inappropriate for the intended end use as they were incredibly delicate and would often start to break apart on contact with water, either during rinsing or swelling tests. As such, a limited number of CS hydrogels and a full range of HA hydrogels were fully characterised for their swelling properties, and were shown to demonstrate a lesser degree of swelling and % water uptake with increasing concentrations of EDC solution used during synthesis.

Following this, the degradation properties of the HA hydrogels were characterised. The choice of EDC-coupling to form ester crosslinks allowed facile hydrolysis which inherently fulfilled the degradation criteria of the hydrogels, as well as the fact HA is native to the human body and can undergo enzymatic degradation as such. The degradation of the HA hydrogels was shown to vary with concentration of EDC solution used during crosslinking, with gels prepared in the presence of greater concentrations of EDC hydrolysing faster than those with lower concentrations of EDC. This was the inverse of the expected trend and is thought to be a result of heterogeneous crosslinking across the film and strain caused by tight crosslinks. In general, the HA hydrogels had undergone complete hydrolysis within 4 days of submersion in PBS at 37 °C. This proved that the gels were degradable, thus fulfilling the criteria however for the intended end use may not be a long enough lifetime.

The HA hydrogels then underwent mechanical testing to determine whether the elastic moduli of the gels matched the elastic moduli of the spinal cord. The HA hydrogels underwent indentation testing using the Texture Analyser whilst swollen in water, and the elastic moduli calculated using contact mechanics. All of the HA hydrogels tested had elastic moduli in the range of 2 to 50 kPa, which were all within the range of elastic moduli reported in the literature for the CNS. The elastic moduli of the HA hydrogels appeared to increase with increasing EDC solution concentrations used during synthesis. This agreed with the hypothesis that increased EDC concentrations during gel preparation led to increased ester bonding within the gel which increased the elastic moduli of the hydrogel.

The degradation, swelling, and mechanical properties of the HA hydrogels were all shown to be tunable by varying the EDC solution concentration during crosslinking. This shows that by carefully choosing the EDC concentration during crosslinking an ideal balance can be struck between these three characteristics

to give the most appropriate HA hydrogel for the intended end use.

A simple prototype HA gel with a PEDOT:CS layer was developed as a first step towards a bioelectronic device based on the two materials. This showed that the EDC-crosslinking methodology was compatible with both materials in combination, not just separately as has been shown earlier in this thesis and this chapter.

There are many directions that this work could be taken in future. Although the choice of EDC-crosslinking led to facile synthesis and degradation, the lifetimes of the HA hydrogels were fairly short. This could restrict their usefulness in real applications within SCI treatment to short-term monitoring applications. Alternative crosslinking technologies could offer improvements, however the biocompatibility and biodegradability would have to be carefully considered. On the other hand, EDC-crosslinking could still be used but alterations to the methodology could be made. *N*-hydroxysuccinimide (NHS) is often used in concert with EDC to increase the efficiency of the coupling reaction, and thus could be used to increase the amount of crosslinking within the HA hydrogels [214]. There is also evidence that controlling the pH during EDC-crosslinking can yield better crosslinking [122, 124].

A 1996 paper by Hanthamrongwit [119] reported that CS could be crosslinked to collagen using EDC, and that this also was successful in the presence of a simple diamine. The author reported that the presence of 1,4-diaminobutane, also known as putrescine due to its pungent odour, increased the number of possible crosslinking opportunities by providing additional available reactive groups during crosslinking. Once a carboxylic acid group had been activated by EDC on the CS or collagen, it meant that amide bonds could form directly between collagen and CS, collagen and collagen, collagen and diamine, and CS and diamine. This was summarised in figure 1.26. Additionally, Tomihata *et al.* [120] added lysine and its methyl ester to ethanol-water-EDC reaction mixtures to try and include amide bonding in crosslinked HA films. This was thought to have been achieved as the presence of amide bonding was detected in the IR spectra of such crosslinked HA films. Additionally, *in vivo* degradation testing in rats yielded results showing that the HA films crosslinked in the presence of the lysine methyl ester fully degraded in around 14 days, whereas the lifetime of HA crosslinked films without the lysine additive degraded in around 7 days. This was attributed to the presence of amide bonds that are resistant to hydrolysis unlike ester bonds. These examples demonstrate that the addition of a diamine could introduce amide bonding into the CS and HA hydrogels prepared in this work, which could yield improved degradation times as amide bonds are not hydrolytically degradable, and degradation action would have to be exclusively through enzymatic action. One consideration, however, would be how to control the reactive sites for the diamine in the CS and HA. Ideally, following the activation of the carboxyl group by EDC on a molecule of CS or HA, a diamine such as 1,4-diaminobutane would react with the activated carboxyl to form an amide bond. This would, however, result in no crosslink as the bonded diamine would form a pendant group from backbone of the CS or HA and not be joined to another CS or HA molecule. This would be analogous to the collagen or CS reacting once with the diamine in the Hanthamrongwit [119] experiments, described by figure 1.26. A second EDC-activated carboxyl group on a CS or HA molecule would need to come into proximity of this dangling amine end group and react again to form a second amide bond for a crosslink to be formed. Careful control of the concentration of diamine would be required to limit the number of potential dangling ends in the CS or HA film.

Additionally, as the crosslinking in the HA films is not entirely uniform giving a heterogeneous gel, steps could be taken to prearrange the molecules in a way that gives a more homogeneous structure. For

example, a HA 3D porous scaffold structure could be prepared through lyophilisation which could then be crosslinked. This is how a number of collagen hydrogels and tissue scaffolds are prepared [83, 90, 111, 125] and could improve crosslinking efficiency in the resulting HA hydrogels.

As biocompatibility is a key requirement of the hydrogels prepared during this work, it would be foolish to not use the HA hydrogels in compatibility tests with cells to check whether there are initially any unexpected cytotoxic effects. It should be noted, however, that this is unlikely to be a risk considering HA is a native molecule found in the human body, crosslinked with hydrolysable bonds. Providing there are no issues with biocompatibility in terms of cytotoxicity, assessing the growth and proliferation of neural cells across the HA hydrogels would also provide insight into how the gel would perform as a scaffold material. This could be supplemented by similar cell line testing once a combination HA hydrogel and PEDOT:CS or PEDOT:HA OECT device has been realised.

To fully meet the criteria established at the beginning of this chapter, further development is required to fully realise a combination PEDOT:CS or PEDOT:HA OECT device on the HA hydrogels. It was shown that a layer of PEDOT:CS could be drop-cast onto a HA gel and crosslinked, however this does not make an OECT device. A method must be developed to include electrodes on the HA hydrogel. The electrodes themselves should be biocompatible and biodegradable, or at least biologically inert, and the way that they are included on the gel would need to be gentle enough to not destroy the HA gel. For example, laser ablation could be used to pattern polymeric electrodes onto the substrate surface [133] or photolithography could be used to prepare electrodes from the PEDOT:CS itself similar to the electrically conductive hydrogel reported on by Liu *et al.* [213]. Once successfully prepared in full, characterisation of swelling, degradation, and the mechanical properties of the HA hydrogel-OECT device would be required, in addition to electronic characterisation.

As has been previously discussed in chapter 4, synapstors are of interest for use within the CNS as they mimic the behaviour of biological synapses. This makes them potentially useful in the treatment of SCIs. Previously Giordani *et al.* [133] has shown that these synapstor devices can be prepared on PDMS substrates by laser ablating PEDOT:PSS thin films to form electrodes. If the HA hydrogels prepared here are robust enough to undergo the laser ablation process, these hydrogels may be suitable for use as biodegradable alternatives to PDMS substrates in such synapstor devices.

## Chapter 6

# Summary and future work

### 6.1 Summary

Presently, there is no known cure for SCIs. This is mostly due to the pathology of the injuries and the way the body minimises further damage through glial scar formation. There are a number of methods that medical professionals use to manage and minimise the extent of the damage during primary injury stage [2, 18, 20], as well as rehabilitation therapies to train patients to recover some function that was lost as a result of an SCI [2]. Rehabilitation physical therapies and virtual reality therapies can have successful outcomes with reductions in neuropathic pain reported in many patients [21]. Bioelectronic approaches have also been used to minimise pain in SCI treatments through electrical stimulation of the spinal cord [24]. Furthermore, electronic stimulation combined with physical training can produce even more impressive results with recovery of functionality in the limbs of paralysed test subjects [26], including allowing paralysed human patients to walk again unaided [5]. The e-dura device [27, 28], described in chapter 1, showed that a soft bioelectronic device could be used in direct interface with the spinal cord and allowed paralysed rats to regain functionality in non-functional hind-limbs. Such bioelectronic approaches, and specifically organic bioelectronics, are of great interest to researchers for the use in the treatment of SCIs and in the spinal cord in general [4, 29–33], as organic electronic materials offer a range of advantageous properties that traditional metallic electronic materials do not, such as lower elastic moduli and better biocompatibility. Unfortunately, one of the drawbacks of current bioelectronic technology for use in the central nervous system (CNS) is the lack of degradability and long term biocompatibility of the electronic materials within the devices [60]. In addition, many implants currently available on the market are hard and have mechanical mismatching with the soft tissues they interact with, thus there is a requirement for the design of soft, mechanically appropriate devices [218].

OECTs based on poly(3,4-ethylenedioxythiophene):poly(styrene sulfonate) (PEDOT:PSS) have been demonstrated to measure electrocardiographs of a human heartbeat [54], measure brain activity in rats [167], and there have been examples of devices mimicking the depressing and facilitating behaviour of biological synapses (synapstors) [13, 44, 128–133]. As OECTs transduce signals between ionic (ions in the electrolyte) and electronic currents (current flow through the organic electronic material), this often makes them the interface of choice for many between biological signals and manufactured electronics, making them a favoured bioelectronic device for many applications including for use in the CNS and

perhaps in the treatment of SCIs. This thesis aimed to present the development of a biocompatible, degradable, and mechanically appropriate organic electrochemical transistor (OECT) that begins to fulfil the basic requirements of an implanted device for use in the spinal cord.

As a first step towards developing this device, PEDOT:PSS alternatives were synthesised (chapter 3). PEDOT:PSS is the most popular organic electronic material for use in organic bioelectronic devices but has some drawbacks with regards to unknown long-term biocompatibility [168] and is not degradable [60]. PEDOT complexed with chondroitin sulfate (CS) or hyaluronic acid (HA) were prepared to offer a biocompatible and degradable material that demonstrated electronic conductivity and could be used in an OECT architecture (chapter 3). The use of these materials was novel in a transistor set up. The biocompatibility issues with PEDOT:PSS were mitigated by choosing CS and HA as alternative counterions for PEDOT as CS and HA are naturally occurring biomolecules within the human body [8, 95], specifically within the CNS [8, 96]. This also meant that *in vivo* degradation of CS and HA would occur via natural enzymatic pathways making the PEDOT:CS or PEDOT:HA degradable. In addition, previous research has shown that PEDOT:CS and PEDOT:HA complexes show greater cell adhesion and compatibility than PEDOT:PSS in viability studies [168, 180].

Drop-casting was used to prepare films of PEDOT:CS and PEDOT:HA for electronic testing and use in an OECT architecture. EDC-coupling was used to crosslink the films and was advantageous towards degradation as the crosslinks formed were ester bonds which are hydrolytically degradable. It was demonstrated that PEDOT:CS and PEDOT:HA were conductive, however there were large variations in the data sets. Uncrosslinked PEDOT:CS samples consistently showed the lowest sheet resistances with the lowest sheet resistance of  $4.7 \text{ k}\Omega\text{cm}^{-1}$  which was similar to sheet resistances recorded for PEDOT:PSS by Jonsson *et al.* [198]. The act of crosslinking was also seen to increase the sheet resistance of the PEDOT:CS and PEDOT:HA film samples by  $31 \times$  and  $20000 \times$ , respectively. The increase in sheet resistance was suggested to be due to the change in film structure upon crosslinking [195], with the crosslinking step forming a tighter matrix in the PEDOT:biomolecule films than an uncrosslinked film leading to lower levels of ionic conductivity, and thus higher sheet resistances.

To probe the changes in sheet resistance in the PEDOT:CS films upon crosslinking, UV spectroscopy and electrochemical impedance spectroscopy (EIS) was utilised to examine the electronic behaviours of PEDOT:CS films (chapter 4). Crosslinking the PEDOT:CS films appeared to have caused a change in the doping state of the PEDOT evidenced by the presence of a band centred around 510 nm in the UV spectra for the crosslinked films that was not present in the uncrosslinked aqueous suspension samples. This band is typically attributed to undoped, neutral PEDOT, which would explain the increased sheet resistances upon crosslinking. The EIS data supported the findings of the UV spectroscopy as it appeared that the crosslinked PEDOT:CS 1:1 was present in its non-conducting undoped form. Additionally, EIS data supported the assertion that the crosslinking step resulted in a more tightly bound PEDOT:CS matrix that sterically limited the ability of ions to diffuse through the structure as no ionic conductivity was seen in the Nyquist plots generated by EIS.

A PEDOT:CS 1:1 based OECT was developed, offering a biocompatibility and biodegradability that PEDOT:PSS devices do not. The OECT demonstrated a maximum transconductance of  $50.5 \mu\text{S}$  and these initial measurements provided a proof of concept for using PEDOT:CS in an OECT and acted as a starting point for optimisation. The use of interdigitating electrodes to improve device performance was attempted, and although no improvements were seen in the transconductances of PEDOT:CS 1:1 based

OECTs, the ON/OFF ratios saw a two to three-fold increase compared to the original proof of concept data in chapter 3. These experiments proved once again that PEDOT:CS could be used in OECT devices which has not been seen in the literature prior to this work.

By design, the PEDOT:CS films in the OECT were degradable, thus degradation experiments were carried out which examined how the transconductive behaviour of the devices changed following 3-days of submersion in water. The OECTs demonstrated a marked increase in performance with an up to five fold increase in maximum output current and increases in the maximum transconductances, whereas the ON/OFF ratios remained approximately similar. The increase in device performance was suggested to be a result of increased swelling of the crosslinked film which lead to more facile ion diffusion, increasing the conductivity. This conclusion was supported by the EIS data that showed following the 3-day submersion in water both ionic and electronic conductivity was occurring within the film. Ionic conductivity was not observed prior to the submersion in water. Additionally, the UV spectroscopy showed that the PEDOT was present in its doped conducting form. It was thought that the increase in performance of the OECT devices observed here would be followed by a decrease as the PEDOT:CS film begins to degrade, delaminate, and dissolve into solution. This has been shown to occur in PEDOT:PSS based transistor devices where an increase in device performance due to swelling in the short term is observed, followed by a decrease in performance due to decohesion of the device however the PEDOT:PSS itself does not degrade [55].

Attempts were made to prepare synapstors from PEDOT:CS, however success was limited by poor PEDOT:CS film formation. Furthermore, lyophilisation experiments were performed on PEDOT:CS and PEDOT:HA aqueous suspensions to form 3D crosslinked scaffolds as a step towards developing the materials into tubistors [134]. The GOPS-crosslinked scaffolds were easy to handle and spongy in texture, however the crosslinking bonds formed are not degradable. On the other hand, EDC-crosslinked scaffolds would offer degradable crosslinks but there was the requirement for further development of these scaffolds as the methodology used to crosslink the scaffolds caused them to collapse.

All the substrates used in OECT testing would not be suitable for implantation in to the CNS as there would be a massive mismatch of moduli between the hard glass or quartz and the extremely soft tissues. This was overcome by developing CS and HA hydrogels which offered biocompatibility, biodegradability, and had appropriate mechanical properties for use in the CNS (chapter 5). CS and HA EDC-crosslinked hydrogels were prepared using a multi-step method based on work by Tomihata *et al.* [120]. The concentration of EDC solution during crosslinking could be varied to alter the level of crosslinking within the gel. IR spectroscopy was used to prove the presence of ester crosslinks along with a simple rinse test which formed part of the synthetic route. IR spectroscopy also proved that the amount of ester bonding within crosslinked HA films increased with the concentration of EDC solution used in the crosslinking mixture. CS hydrogels prepared using the EDC-crosslinking methodology were deemed inappropriate for the intended end use as they were incredibly delicate and would often start to break apart on contact with water.

The degradation of the HA hydrogels was examined and was shown to vary with concentration of EDC solution used during crosslinking, with gels prepared in the presence of greater concentrations of EDC hydrolysing faster than those with lower concentrations of EDC. This was the inverse of the expected pattern and is thought to be a result of heterogeneous crosslinking across the film and strain caused by tight crosslinks. Nevertheless, in general, the HA hydrogels had undergone complete hydrolysis within

4 days of submersion in PBS at 37 °C. This proved that the gels were degradable, thus fulfilling the criteria, however the experiment did not consider enzymatic degradation that would occur *in vivo*.

Mechanical testing was performed on the HA hydrogels to determine whether the elastic moduli of the gels matched the elastic moduli of the spinal cord. The HA hydrogels underwent indentation testing using the Texture Analyser whilst swollen in water, and the elastic moduli calculated using contact mechanics. All of the HA hydrogels tested had elastic moduli in the range of 2 to 50 kPa, which were all within the range of elastic moduli reported in the literature for the CNS (0.0003 - 1.40 MPa [70, 72–76]). The elastic moduli of the HA hydrogels appeared to increase with increasing EDC solution concentrations used during synthesis. This agreed with the hypothesis that increased EDC concentrations during gel preparation lead to increased ester bonding within the gel which increased the elastic moduli of the hydrogel. The swelling, degradation, and mechanical testing results all demonstrated that the properties of the HA hydrogels were tunable by varying the EDC solution concentration during crosslinking. This showed that by carefully choosing the EDC concentration during crosslinking an ideal balance can be struck between these three characteristics to give the most appropriate HA hydrogel for the intended end use.

As the HA hydrogels were to act as a substrate for a PEDOT:CS based OEET, a prototype HA gel with a grafted PEDOT:CS layer was developed as a first step towards a bioelectronic device based on the two materials. This showed that the EDC-crosslinking methodology was compatible with both materials simultaneously. This result forms the basis of a fully degradable OEET device that meets the basic requirements of an implanted biomaterial, and opens up a range of opportunities for other fully degradable devices for use in the medical field.

## 6.2 Future Work

The work presented in this thesis paves the way for PEDOT:biomolecule usage in OEETs for bioelectronic applications. The HA hydrogels provide a biocompatible, degradable, and mechanically appropriate surface on to which PEDOT:CS can be grafted meaning that a wholly degradable and soft device is possible in future. There are, however, improvements that are required to device performance to fully optimise PEDOT:CS for use in an OEET. For example, changing the design of the electrodes used to increase the  $W/L$  ratio or adding additives such as ethylene glycol for improved conductivity are areas of interest that could maximise output currents and transconductances in OEET devices based on PEDOT:CS. Alternative crosslinking technologies or varying the EDC-crosslinking methodology could also lead to changes in PEDOT:CS film conductivity, although this would have to be carefully considered with regards to degradation. Further understanding the changes that occur during PEDOT:CS crosslinking using EDC-coupling would also aid further optimisation of the device. NMR spectroscopy could be used to identify the chemical changes that occur during crosslinking. Such data would be useful to compare with UV spectroscopy and EIS data which previously showed that there was a decrease in doping levels in the PEDOT:CS films upon crosslinking and there was a lack of ionic conductivity. NMR spectroscopy would allow future researchers to identify if there were any chemical changes in the samples that contributed to the change in doping level. Moreover, NMR spectroscopy could be used to follow degradation in the crosslinked PEDOT:CS film samples by identifying peaks that were attributed to the ester crosslinks. More closely controlled conditions including temperature control (37 °C) and pH 7.4 buffered solutions

to mimic basic physiological conditions would also be advantageous in future degradation experiments. Longer term experiments would also reveal whether the initial increase in performance of the PEDOT:CS OECTs observed in the experiments would be followed by a decrease as the PEDOT:CS film begins to degrade, delaminate, and dissolve into solution, as expected [55]. By running concurrent degradation experiments on PEDOT:CS film samples as well as actual OECTs, the swelling of films could be observed over time whilst being analysed by UV spectroscopy and EIS. This would aid understanding of the role swelling of the PEDOT:CS films has with regards to the actual degradation of crosslinks in the matrix.

The HA hydrogels that were developed and reported on in thesis did fulfil the requirements of a biomaterial: biocompatibility, degradability, and mechanically appropriate. The lifetimes of the HA hydrogels were seen to be around 4 days which may be appropriate for short term applications but if the hydrogel is required to remain intact in the body for longer, the EDC-crosslinking method presented in this thesis would not suffice. NHS is often used in concert with EDC to increase the efficiency of the coupling reaction, and thus could be used to increase the amount of crosslinking within the HA hydrogels [214]. There is also evidence that controlling the pH during EDC-crosslinking can yield better crosslinking [122, 124]. More crosslinks could improve lifetimes, whilst maintaining the biocompatibility and biodegradability offered by EDC-crosslinking. It was also suggested in chapter 5 that utilising a diamine during EDC-crosslinking would introduce amide bonding into the HA hydrogels which could extend their lifetimes [119, 120]. Amide bonds are not hydrolytically degradable but the HA remains enzymatically degradable thus still providing a degradation route. Furthermore, amide bonds are common throughout biological systems thus the biocompatibility of the HA hydrogels would be maintained. On the other hand alternative crosslinking technologies could offer improvements to the lifetime making the hydrogels more appropriate for real applications within SCI treatments. The biocompatibility and biodegradability of any alternative crosslinking method would have to be carefully considered.

The ease with which the PEDOT:CS drop-cast film was successfully grafted to the HA hydrogels was a promising result in the development of a fully functional soft, degradable, and biocompatible OECT device. To achieve this goal in future, a method must be developed to include electrodes on the HA hydrogel. The electrodes themselves should be biocompatible and biodegradable, or at least biologically inert, and the way that they are included on the gel would need to be gentle enough to not destroy the HA hydrogel. For example, laser ablation could be used to pattern polymeric electrodes onto the substrate surface [133] or photolithography could be used to prepare electrodes from the PEDOT:CS itself, similar to the electrically conductive hydrogel reported on by Liu *et al.* [213].

For a material or device to be considered for implantation, it must demonstrate biocompatibility first through compatibility testing with cells to check whether there are any unexpected cytotoxic effects. For the device proposed in this thesis, assessing the growth and proliferation of neural cells across the HA hydrogels would also provide insight into how the gel would perform as a scaffold material. Additionally, similar cell line testing on PEDOT:CS films and the HA hydrogel-PEDOT:CS OECT would not only allow the biocompatibility of the materials to be assessed but also allow characterisation of the interactions and interfacing possible between the electronic device and the biological nerve cells.

As touched upon earlier in the thesis, synapstors, although originally designed for neuromorphic computing applications, are of interest for use in the CNS as they mimic the behaviour of biological synapses which could be incredibly powerful in the treatment of SCIs. The experiments presented in this thesis showed that the spin-cast film formation of PEDOT:CS dispersions on polydimethylsiloxane (PDMS)

was not compatible with the laser ablation technique used to prepare these synapstor devices [133], however there are experiments that could be performed allowing this issue to be overcome. If HA hydrogels prepared by EDC-crosslinking are robust enough to undergo the laser ablation process, these hydrogels may be suitable for use as biodegradable alternatives to the PDMS substrates. Furthermore, drop-cast films of PEDOT:CS could be used in the laser ablation technique as oppose to spin-cast films. In this case, if the short-term plasticity (STP) characterisation were successful and a synapstor prepared from PEDOT:CS, the device would offer a potential route to direct interfacing between the nervous system and synthetic technologies.

Beyond specific experiments to improve the properties of the PEDOT:CS OECT and the HA hydrogels, the research described in this thesis forms the basis for a biocompatible, biodegradable, and mechanically appropriate device that could be developed further to be used in the CNS and for the treatment of SCIs. The degradable OECT has other potential applications, not limited to use in the CNS. A simple degradable OECT such as the device proposed in this thesis could be adapted as a short term diagnostic tool. The OECT could act as a sensor if calibrated to detect medically relevant compounds (e.g. as glucose levels in suspected diabetics). The device could be implanted in the body and require no removal procedure due to its degradability. Biodegradable devices are of particular interest in the wider organic bioelectronic research area for sustainability reasons with degradable devices offering a route to minimise polluting electronic waste [60].

# Bibliography

- (1) J. S. Pincock and A. L. Terrill, *Spinal Cord Series and Cases*, 2020, **6**, 7.
- (2) C. S. Ahuja, J. R. Wilson, S. Nori, M. R. N. Kotter, C. Druschel, A. Curt and M. G. Fehlings, *Nature Reviews Disease Primers*, 2017, **3**, 17018.
- (3) R. Van Den Brand, J. Heutschi, Q. Barraud, J. DiGiovanna, K. Bartholdi, M. Huerlimann, L. Friedli, I. Vollenweider, E. M. Moraud, S. Duis, N. Dominici, S. Micera, P. Musienko and G. Courtine, *Science*, 2012, **336**, 1182–1185.
- (4) A. Jonsson, Z. Song, D. Nilsson, B. A. Meyerson, D. T. Simon, B. Linderoth and M. Berggren, *Science Advances*, 2015, **1**, e1500039.
- (5) F. B. Wagner, J. B. Mignardot, C. G. Le Goff-Mignardot, R. Demesmaeker, S. Komi, M. Capogrosso, A. Rowald, I. Seáñez, M. Caban, E. Pirondini, M. Vat, L. A. McCracken, R. Heimgartner, I. Fodor, A. Watrin, P. Seguin, E. Paoles, K. Van Den Keybus, G. Eberle, B. Schurch, E. Pralong, F. Becce, J. Prior, N. Buse, R. Buschman, E. Neufeld, N. Kuster, S. Carda, J. von Zitzewitz, V. Delattre, T. Denison, H. Lambert, K. Minassian, J. Bloch and G. Courtine, *Nature*, 2018, **563**, 65–93.
- (6) P. Brodal, *The Central Nervous System : Structure and Function*, Oxford University Press USA - OSO, New York, 4th edn., 2003.
- (7) T. A. Woolsey, J. Hanaway and M. H. Gado, *The Brain Atlas : A Visual Guide to the Human Central Nervous System*, John Wiley & Sons, Incorporated, New York, 4th edn., 2017.
- (8) A. Wilkinson, A. McCormick and N. Leipzig, *Synthesis Lectures on Tissue Engineering*, 2011, **3**, 1–112.
- (9) C. Solaro, E. Trabucco and M. Messmer Uccelli, *Current Neurology and Neuroscience Reports*, 2013, **13**, 320.
- (10) B. C. Lim and M. N. Rasband, *Current Biology*, 2020, **30**, R326–R328.
- (11) R. S. Zucker and W. G. Regehr, *Annual Review of Physiology*, 2002, **64**, 355–405.
- (12) L. F. Abbott and W. G. Regehr, *Nature*, 2004, **431**, 796–803.
- (13) P. Gkoupidenis, N. Schaefer, B. Garlan and G. G. Malliaras, *Advanced Materials*, 2015, **27**, 7176–7180.
- (14) L. Grassner, A. Grillhösl, C. J. Griessenauer, C. Thomé, V. Bühren, M. Strowitzki and P. A. Winkler, *Journal of Neurotrauma*, 2018, **35**, 403–410.
- (15) B. B. Lee, R. A. Cripps, M. Fitzharris and P. C. Wing, *Spinal Cord*, 2014, **52**, 110–116.

- (16) S. L. James, A. Theadom, R. G. Ellenbogen, M. S. Bannick, W. Montjoy-Venning, L. R. Lucchesi, N. Abbasi, R. Abdulkader, H. N. Abraha, J. C. Adsuar, M. Afarideh, S. Agrawal, A. Ahmadi, M. B. Ahmed, A. N. Aichour, I. Aichour, M. T. E. Aichour, R. O. Akinyemi, N. Akseer, F. Alahdab, A. Alebel, S. A. Alghnam, B. A. Ali, U. Alsharif, K. Altirkawi, C. L. Andrei, M. Anjomshoa, H. Ansari, M. G. Ansha, C. A. T. Antonio, S. C. Y. Appiah, F. Ariani, N. G. Asefa, S. W. Asgedom, S. Atique, A. Awasthi, B. P. Ayala Quintanilla, T. B. Ayuk, P. S. Azzopardi, H. Badali, A. Badawi, S. Balalla, A. Banstola, S. L. Barker-Collo, T. W. Bärnighausen, N. Bedi, M. Behzadifar, M. Behzadifar, B. B. Bekele, A. B. Belachew, Y. A. Belay, D. A. Bennett, I. M. Bensenor, A. Berhane, M. Beuran, A. Bhalla, S. Bhaumik, Z. A. Bhutta, B. Biadgo, M. Biffino, A. Bijani, N. Bililign, C. Birungi, S. Boufous, A. Brazinova, A. W. Brown, M. Car, R. Cárdenas, J. J. Carrero, F. Carvalho, C. A. Castañeda-Orjuela, F. Catalá-López, Y. Chaiah, A. P. Champs, J.-C. Chang, J.-Y. J. Choi, D. J. Christopher, C. Cooper, C. S. Crowe, L. Dandona, R. Dandona, A. Daryani, D. V. Davitoui, M. G. Degefa, G. T. Demoz, K. Deribe, S. Djalalinia, H. P. Do, D. T. Doku, T. M. Drake, M. Dubey, E. Dubljanin, Z. El-Khatib, R. Ofori-Asenso, S. Eskandarieh, A. Esteghamati, S. Esteghamati, A. Faro, F. Farzadfar, M. H. Farzaei, S.-M. Fereshtehnejad, E. Fernandes, G. T. Feyissa, I. Filip, F. Fischer, T. Fukumoto, M. Ganji, F. G. Gankpe, A. K. Gebre, T. T. Gebrehiwot, K. E. Gezae, G. Gopalkrishna, A. C. Goulart, J. A. Haagsma, A. Haj-Mirzaian, A. Haj-Mirzaian, R. R. Hamadeh, S. Hamidi, J. M. Haro, H. Hassankhani, H. Y. Hassen, R. Havmoeller, C. Hawley, S. I. Hay, M. I. Hegazy, D. Hendrie, A. Henok, D. T. Hibstu, H. J. Hoffman, M. K. Hole, E. Homaie Rad, S. M. Hosseini, S. Hostiuc, G. Hu, M. A. Hussen, O. S. Ilesanmi, S. S. N. Irvani, M. Jakovljevic, S. Jayaraman, R. P. Jha, J. B. Jonas, K. M. Jones, Z. Jorjoran Shushtari, J. J. Jozwiak, M. Jürisson, A. Kabir, A. Kahsay, M. Kahssay, R. Kalani, A. Karch, A. Kasaeian, G. M. Kassa, T. D. Kassa, Z. Y. Kassa, A. P. Kengne, Y. S. Khader, M. A. Khafaie, N. Khalid, I. Khalil, E. A. Khan, M. S. Khan, Y.-H. Khang, H. Khazaie, A. T. Khoja, J. Khubchandani, A. A. Kiadaliri, D. Kim, Y.-E. Kim, A. Kisa, A. Koyanagi, K. J. Krohn, B. Kuate Defo, B. Kucuk Bicer, G. A. Kumar, M. Kumar, R. Lalloo, F. H. Lami, V. C. Lansingh, D. O. Laryea, A. Latifi, C. T. Leshargie, M. Levi, S. Li, M. L. Liben, P. A. Lotufo, R. Lunevicius, N. B. Mahotra, M. Majdan, A. Majeed, R. Malekzadeh, A.-L. Manda, M. A. Mansournia, B. B. Massenburg, K. K. V. Mate, M. M. Mehndiratta, V. Mehta, H. Meles, A. Melese, P. T. N. Memiah, W. Mendoza, G. Mengistu, A. Meretoja, T. J. Meretoja, T. Mestrovic, T. Miazgowski, T. R. Miller, G. Mini, A. Mirica, E. M. Mirrakhimov, B. Moazen, M. Mohammadi, M. Molokhia, L. Monasta, S. Mondello, M. Moosazadeh, G. Moradi, M. Moradi, M. Moradi-Lakeh, M. Moradinazar, S. D. Morrison, M. M. Moschos, S. M. Mousavi, S. Murthy, K. I. Musa, G. Mustafa, M. Naghavi, G. Naik, F. Najafi, V. Nangia, B. R. Nascimento, I. Negoi, T. H. Nguyen, E. Nichols, D. N. A. Ningrum, Y. L. Nirayo, P. S. Nyasulu, F. A. Ogbo, I.-H. Oh, A. Okoro, A. T. Olagunju, T. O. Olagunju, P. R. Olivares, S. S. Otstavnov, M. O. Owolabi, M. P. A, S. Pakhale, A. R. Pandey, K. Pesudovs, G. D. Pinilla-Monsalve, S. Polinder, H. Poustchi, S. Prakash, M. Qorbani, A. Radfar, A. Rafay, A. Rafei, A. Rahimi-Movaghar, V. Rahimi-Movaghar, M. Rahman, M. A. Rahman, R. K. Rai, F. Rajati, U. Ram, D. L. Rawaf, S. Rawaf, R. C. Reiner, C. Reis, A. M. N. Renzaho, S. Resnikoff, S. Rezaei, S. Rezaeian, L. Roever, L. Ronfani, G. Roshandel, N. Roy, G. M. Ruhago, B. Saddik, H. Safari, S. Safiri, M. A. Sahraian, P. Salamati, R. d. F. Saldanha, A. M. Samy, J. Sanabria, J. V. Santos, M. M. M. Santric Milicevic, B. Sartorius, M. Satpathy, K. Savuon, I. J. C. Schneider, D. C. Schwebel, S. G. Sepanlou, H. Shabaninejad, M. A. A. Shaikh, M. Shams-Beyranvand, M. Sharif, M. Sharif-Alhoseini, S. M. Shariful Islam, J. She, A. Sheikh, J. Shen, K. N. Sheth, K. Shibuya, M. S. Shiferaw, M. Shigematsu, R. Shiri, I. Shiue, H. Shoman, S. Siabani, T. J. Siddiqi,

- J. P. Silva, D. G. A. Silveira, D. N. Sinha, M. Smith, A. M. Soares Filho, S. Sobhani, M. Soofi, J. B. Soriano, I. N. Soyiri, D. J. Stein, M. A. Stokes, M. B. Sufiyan, B. F. Sunguya, J. E. Sunshine, B. L. Sykes, C. E. I. Szoeki, R. Tabarés-Seisdedos, B. J. Te Ao, A. Tehrani-Banihashemi, M. G. Tekle, M.-H. Temsah, O. Temsah, R. Topor-Madry, M. Tortajada-Girbés, B. X. Tran, K. B. Tran, L. Tudor Car, K. N. Ukwaja, I. Ullah, M. S. Usman, O. A. Uthman, P. R. Valdez, T. J. Vasankari, N. Venketasubramanian, F. S. Violante, F. W. S. Wagnew, Y. Waheed, Y.-P. Wang, K. G. Weldegewergs, A. Werdecker, T. Wijeratne, A. S. Winkler, G. M. A. Wyper, Y. Yano, M. Yaseri, Y. J. Yasin, P. Ye, E. M. Yimer, P. Yip, E. Yisma, N. Yonemoto, S.-J. Yoon, M. G. Yost, M. Z. Younis, M. Yousefifard, C. Yu, Z. Zaidi, S. B. Zaman, M. Zamani, Z. M. Zenebe, S. Zodpey, V. L. Feigin, T. Vos and C. J. L. Murray, *The Lancet Neurology*, 2019, **18**, 56–87.
- (17) J. W. McDonald and C. Sadowsky, *The Lancet*, 2002, **359**, 417–425.
- (18) K. Venkatesh, S. K. Ghosh, M. Mullick, G. Manivasagam and D. Sen, *Cell and Tissue Research*, 2019, **377**, 125–151.
- (19) T. T. Roberts, G. R. Leonard and D. J. Cepela, *Clinical Orthopaedics and Related Research*®, 2017, **475**, 1499–1504.
- (20) M. G. Fehlings and R. G. Perrin, *Spine*, 2006, **31**, 28–35.
- (21) P. D. Austin and P. J. Siddall, *The Journal of Spinal Cord Medicine*, 2019, **0**, 1–11.
- (22) A. R. C. Donati, S. Shokur, E. Morya, D. S. F. Campos, R. C. Moioli, C. M. Gitti, P. B. Augusto, S. Tripodi, C. G. Pires, G. A. Pereira, F. L. Brasil, S. Gallo, A. A. Lin, A. K. Takigami, M. A. Aratanha, S. Joshi, H. Bleuler, G. Cheng, A. Rudolph and M. A. L. Nicoletis, *Scientific Reports*, 2016, **6**, 30383.
- (23) D. Cizkova, A. N. Murgoci, V. Cubinkova, F. Humenik, Z. Mojzisoava, M. Maloveska, M. Cizek, I. Fournier and M. Salzet, *Neurochemical Research*, 2020, **45**, 134–143.
- (24) Q. Huang, W. Duan, E. Sivanesan, S. Liu, F. Yang, Z. Chen, N. C. Ford, X. Chen and Y. Guan, *Neuroscience Bulletin*, 2019, **35**, 527–539.
- (25) D. R. Gater, D. Dolbow, B. Tsui and A. S. Gorgey, *NeuroRehabilitation*, 2011, **28**, ed. T. Gentry, 231–248.
- (26) A. Ievins and C. T. Moritz, *Physiology*, 2017, **32**, 391–398.
- (27) I. Minev, P. Musienko, A. Hirsch, Q. Barraud, N. Wenger, E. Moraud, J. Gandar, M. Capogrosso, T. Milekovic, L. Asboth, R. Torres, N. Vachicouras, Q. Liu, N. Pavlova, S. Duis, A. Larmagnac, J. Voros, S. Micera, Z. Suo, G. Courtine and S. Lacour, *Science*, 2015, **347**, 159–163.
- (28) G. Schiavone, F. Fallegger, X. Kang, B. Barra, N. Vachicouras, E. Roussinova, I. Furfaro, S. Jiguet, I. Seáñez, S. Borgognon, A. Rowald, Q. Li, C. Qin, E. Bézard, J. Bloch, G. Courtine, M. Capogrosso and S. P. Lacour, *Advanced Materials*, 2020, **32**, 1906512.
- (29) K. Feron, R. Lim, C. Sherwood, A. Keynes, A. Brichta and P. Dastoor, *International Journal of Molecular Sciences*, 2018, **19**, 2382.
- (30) D. Simon, E. Gabrielsson, K. Tybrandt and M. Berggren, *Chemical Reviews*, 2016, **116**, 13009–13041.
- (31) J. Rivnay, S. Inal, A. Salleo, R. M. Owens, M. Berggren and G. G. Malliaras, *Nature Reviews Materials*, 2018, **3**, 17086.
- (32) H. von Holst, *Biochimica et Biophysica Acta (BBA) - General Subjects*, 2013, **1830**, 4345–4352.

- (33) M. D. Ferro and N. A. Melosh, *Advanced Functional Materials*, 2018, **28**, 1704335.
- (34) J. Rivnay, R. Owens and G. Malliaras, *Chemistry of Materials*, 2014, **26**, 679–685.
- (35) L. Torsi, M. Magliulo, K. Manoli and G. Palazzo, *Chemical Society Reviews*, 2013, **42**, 8612.
- (36) L. Kergoat, B. Piro, M. Berggren, G. Horowitz and M. Pham, *Analytical and Bioanalytical Chemistry*, 2012, **402**, 1813–1826.
- (37) T. Someya, Z. Bao and G. G. Malliaras, *Nature*, 2016, **540**, 379–385.
- (38) M. Tanese, L. Torsi, N. Cioffi, L. Zotti, D. Colangiuli, G. Farinola, F. Babudri, F. Naso, M. Giangregorio, L. Sabbatini and P. Zambonin, *Sensors and Actuators B: Chemical*, 2004, **100**, 17–21.
- (39) S. Inal, J. Rivnay, A.-O. Suiiu, G. G. Malliaras and I. McCulloch, *Accounts of Chemical Research*, 2018, **51**, 1368–1376.
- (40) D. Wang, V. Noël and B. Piro, *Electronics*, 2016, **5**, 9.
- (41) T. Cramer, A. Campana, F. Leonardi, S. Casalini, A. Kyndiah, M. Murgia and F. Biscarini, *Journal of Materials Chemistry B*, 2013, **1**, 3728–3741.
- (42) S. K. Sailapu, E. Macchia, I. Merino-Jimenez, J. P. Esquivel, L. Sarcina, G. Scamarcio, S. D. Minter, L. Torsi and N. Sabaté, *Biosensors and Bioelectronics*, 2020, **156**, 1–7.
- (43) T. Cramer, B. Chelli, M. Murgia, M. Barbalinardo, E. Bystrenova, D. M. De Leeuw and F. Biscarini, *Physical Chemistry Chemical Physics*, 2013, **15**, 3897–3905.
- (44) S. Desbief, M. di Lauro, S. Casalini, D. Guerin, S. Tortorella, M. Barbalinardo, A. Kyndiah, M. Murgia, T. Cramer, F. Biscarini and D. Vuillaume, *Organic Electronics: physics, materials, applications*, 2016, **38**, 21–28.
- (45) H. S. White, G. P. Kittlesen and M. S. Wrighton, *Journal of the American Chemical Society*, 1984, **106**, 5375–5377.
- (46) M. Moser, J. F. Ponder, A. Wadsworth, A. Giovannitti and I. McCulloch, *Advanced Functional Materials*, 2019, **29**, 1807033.
- (47) D. Khodagholy, J. Rivnay, M. Sessolo, M. Gurfinkel, P. Leleux, L. H. Jimison, E. Stavrinidou, T. Herve, S. Sanaur, R. M. Owens and G. G. Malliaras, *Nature Communications*, 2013, **4**, 1–6.
- (48) I. Gualandi, M. Marzocchi, E. Scavetta, M. Calienni, A. Bonfiglio and B. Fraboni, *Journal of Materials Chemistry B*, 2015, **3**, 6753–6762.
- (49) A. Elschner, S. Kirchmeyer, K. Reuter, W. Lovenich and U. Merker, *PEDOT principles and applications of an intrinsically conductive polymer*, CRC Press, Boca Raton, First edit, 2011.
- (50) A. V. Volkov, K. Wijeratne, E. Mitiraka, U. Ail, D. Zhao, K. Tybrandt, J. W. Andreasen, M. Berggren, X. Crispin and I. V. Zozoulenko, *Advanced Functional Materials*, 2017, **27**, 1700329.
- (51) Y. Wen and J. Xu, *Journal of Polymer Science, Part A: Polymer Chemistry*, 2017, **55**, 1121–1150.
- (52) S. Kirchmeyer and K. Reuter, *Journal of Materials Chemistry*, 2005, **15**, 2077.
- (53) E. Bihar, Y. Deng, T. Miyake, M. Saadaoui, G. G. Malliaras and M. Rolandi, *Scientific Reports*, 2016, **6**, 2–7.
- (54) A. Campana, T. Cramer, D. T. Simon, M. Berggren and F. Biscarini, *Advanced Materials*, 2014, **26**, 3874–3878.

- (55) F. Hempel, J. K.-Y. Y. Law, T. C. Nguyen, W. Munief, X. Lu, V. Pachauri, A. Susloparova, X. T. Vu and S. Ingebrandt, *Biosensors and Bioelectronics*, 2017, **93**, 132–138.
- (56) M. Vert, Y. Doi, K. Hellwich, M. Hess, P. Hodge, P. Kubisa, M. Rinaudo and F. Schué, *Pure and Applied Chemistry*, 2012, **84**, 377–410.
- (57) F. O'Brien, *Materials Today*, 2011, **14**, 88–95.
- (58) Y. Zhong and R. Bellamkonda, *Journal of the Royal Society Interface*, 2008, **5**, 957–975.
- (59) L. Nair and C. Laurencin, *Progress in Polymer Science*, 2007, **32**, 762–798.
- (60) V. R. Feig, H. Tran and Z. Bao, *ACS Central Science*, 2018, **4**, 337–348.
- (61) A. D. McNaught and A. Wilkinson, *IUPAC Compendium of Chemical Terminology*, ed. M. Nič, J. Jiráť, B. Košata, A. Jenkins and A. McNaught, IUPAC, Research Triangle Park, NC, 2nd edn., 2009.
- (62) C.-C. Chiu, Y. Liou and J. Yung-Der, *Thin Solid Films*, 1995, **260**, 118–123.
- (63) G. N. Kamm and G. A. Alers, *Journal of Applied Physics*, 1964, **35**, 327–330.
- (64) J. Y. Rho, T. Y. Tsui and G. M. Pharr, *Biomaterials*, 1997, **18**, 1325–1330.
- (65) H. H. Bayraktar, E. F. Morgan, G. L. Niebur, G. E. Morris, E. K. Wong and T. M. Keaveny, *Journal of Biomechanics*, 2004, **37**, 27–35.
- (66) X. Wang, X. Chen, P. Hodgson and C. Wen, *Transactions of Nonferrous Metals Society of China*, 2006, **16**, s744–s748.
- (67) L. Di Landro, G. Sala and D. Olivieri, *Polymer Testing*, 2002, **21**, 217–228.
- (68) S. Diridollou, F. Patat, F. Gens, L. Vaillant, D. Black, J. M. Lagarde, Y. Gall and M. Berson, *Skin Research and Technology*, 2000, **6**, 214–221.
- (69) P. G. Agache, C. Monneur, J. L. Leveque and J. De Rigal, *Archives of Dermatological Research*, 1980, **269**, 221–232.
- (70) B. Niemczyk, P. Sajkiewicz and D. Kolbuk, *Journal of Neural Engineering*, 2018, **15**, 051002.
- (71) A. Tamura, S. Hayashi, K. Nagayama and T. Matsumoto, *Journal of Biomechanical Science and Engineering*, 2008, **3**, 263–274.
- (72) L. Bilston and L. Thibault, *Annals of Biomedical Engineering*, 1996, **24**, 67–74.
- (73) E. Mazuchowski and L. Thibault, Summer Bioengineering Conference, Sonesta Beach Resort, Key Biscayne, FL, USA. 2003, pp. 1–2.
- (74) H. Ozawa, T. Matsumoto, T. Ohashi, M. Sato and S. Kokubun, *Journal of Neurosurgery: Spine*, 2004, **1**, 122–127.
- (75) R. Oakland, R. Hall, R. Wilcox and D. Barton, *Proceedings of the Institution of Mechanical Engineers, Part H: Journal of Engineering in Medicine*, 2006, **220**, 489–492.
- (76) G. Chang, T. Hung and W. Feng, *Journal of Biomechanical Engineering*, 1988, **110**, 115–122.
- (77) T.-K. Hung and G.-L. Chang, *Journal of Biomechanical Engineering*, 1981, **103**, 43–47.
- (78) T. Rouxel and J.-C. Sangleboeuf, *Journal of Non-Crystalline Solids*, 2000, **271**, 224–235.
- (79) B. Slaughter, S. Khurshid, O. Fisher, A. Khademhosseini and N. Peppas, *Advanced Materials*, 2009, **21**, 3307–3329.
- (80) A. Hoffman, *Advanced Drug Delivery Reviews*, 2012, **64**, 18–23.

- (81) J. Hunt, R. Chen, T. van Veen and N. Bryan, *Journal of Materials Chemistry B*, 2014, **2**, 5319–5338.
- (82) K. B. Neeves, A. J. Sawyer, C. P. Foley, W. M. Saltzman and W. L. Olbricht, *Brain Research*, 2007, **1180**, 121–132.
- (83) N. Davidenko, J. Campbell, E. Thian, C. Watson and R. Cameron, *Acta Biomaterialia*, 2010, **6**, 3957–3968.
- (84) S. C. Owen, S. A. Fisher, R. Y. Tam, C. M. Nimmo and M. S. Shoichet, *Langmuir*, 2013, **29**, 7393–7400.
- (85) J. Kopecek, *Journal of Polymer Science Part A: Polymer Chemistry*, 2009, **47**, 5929–5946.
- (86) M. Dreifus and L. Klenka, *Ceskoslovenska oftalmologie*, 1959, **15**, 95–101.
- (87) P. C. Nicolson and J. Vogt, *Biomaterials*, 2001, **22**, 3273–3283.
- (88) E. Caló and V. Khutoryanskiy, *European Polymer Journal*, 2015, **65**, 252–267.
- (89) S. K. Seidlits, Z. Z. Khaing, R. R. Petersen, J. D. Nickels, J. E. Vanscoy, J. B. Shear and C. E. Schmidt, *Biomaterials*, 2010, **31**, 3930–3940.
- (90) J. Pieper, T. Hafmans, J. Veerkamp and T. van Kuppevelt, *Biomaterials*, 2000, **21**, 581–593.
- (91) S. A. Geissler, A. L. Sabin, R. R. Besser, O. M. Gooden, B. D. Shirk, Q. M. Nguyen, Z. Z. Khaing and C. E. Schmidt, *Journal of Neural Engineering*, 2018, **15**, 025004.
- (92) J. Hardy, P. Lin and C. Schmidt, *Journal of Biomaterials Science, Polymer Edition*, 2015, **26**, 143–161.
- (93) E. Gomes, S. Mendes, H. Leite-Almeida, J. Gimble, R. Tam, M. Shoichet, N. Sousa, N. Silva and A. Salgado, *Biomaterials*, 2016, **105**, 38–51.
- (94) M. Caicco, T. Zahir, A. Mothe, B. Ballios, A. Kihm, C. Tator and M. Shoichet, *Journal of Biomedical Materials Research - Part A*, 2013, **101 A**, 1472–1477.
- (95) S. Carney and H. Muir, *Physiological Reviews*, 1988, **68**, 858–910.
- (96) T. Laabs, D. Carulli, H. M. Geller and J. W. Fawcett, *Current Opinion in Neurobiology*, 2005, **15**, 116–120.
- (97) S. Haylock-Jacobs, M. Keough, L. Lau and V. Wee Yong, *Autoimmunity Reviews*, 2011, **10**, 766–772.
- (98) K. T. Dicker, L. A. Gurski, S. Pradhan-Bhatt, R. L. Witt, M. C. Farach-Carson and X. Jia, *Acta Biomaterialia*, 2014, **10**, 1558–1570.
- (99) S. Sahoo, C. Chung, S. Khetan and J. Burdick, *Biomacromolecules*, 2008, **9**, 1088–1092.
- (100) L. Karumbaiah, S. F. Enam, A. C. Brown, T. Saxena, M. I. Betancur, T. H. Barker and R. V. Bellamkonda, *Bioconjugate Chemistry*, 2015, **26**, 2336–2349.
- (101) J. Pieper, *Biomaterials*, 1999, **20**, 847–858.
- (102) S. Vasvani, P. Kulkarni and D. Rawtani, *International Journal of Biological Macromolecules*, 2020, **151**, 1012–1029.
- (103) Boots UK, *Boots.com*, 2020.
- (104) S. Federico, U. Nöchel, C. Löwenberg, A. Lendlein and A. T. Neffe, *Acta Biomaterialia*, 2016, **38**, 1–10.

- (105) S. Park, H. Lee, K. Lee and H. Suh, *Biomaterials*, 2003, **24**, 1631–1641.
- (106) D. Zhu, H. Wang, P. Trinh, S. C. Heilshorn and F. Yang, *Biomaterials*, 2017, **127**, 132–140.
- (107) D. Uebelhart, E. J. Thonar, P. D. Delmas, A. Chantraine and E. Vignon, *Osteoarthritis and Cartilage*, 1998, **6**, 39–46.
- (108) Y. H. Lee, J.-H. Woo, S. J. Choi, J. D. Ji and G. G. Song, *Rheumatology International*, 2010, **30**, 357–363.
- (109) M. C. Hochberg, J. Martel-Pelletier, J. Monfort, I. Möller, J. R. Castillo, N. Arden, F. Berenbaum, F. J. Blanco, P. G. Conaghan, G. Doménech, Y. Henrotin, T. Pap, P. Richette, A. Sawitzke, P. du Souich and J.-P. Pelletier, *Annals of the Rheumatic Diseases*, 2016, **75**, 37–44.
- (110) S. Bryant, K. Davis-Arehart, N. Luo, R. Shoemaker, J. Arthur and K. Anseth, *Macromolecules*, 2004, **37**, 6726–6733.
- (111) H. Cao and S. Xu, *Journal of Materials Science: Materials in Medicine*, 2008, **19**, 567–575.
- (112) J. W. S. Hayami, S. D. Waldman and B. G. Amsden, *European Polymer Journal*, 2015, **72**, 687–697.
- (113) J. Yang, M. Shen, H. Wen, Y. Luo, R. Huang, L. Rong and J. Xie, *Carbohydrate Polymers*, 2020, **230**, 115650.
- (114) A. Conovaloff and A. Panitch, *Journal of Neural Engineering*, 2011, **8**, 056003.
- (115) C. Liu, L. Fan, J. Xing, Q. Wang, C. Lin, C. Liu, X. Deng, C. Ning, L. Zhou, L. Rong and B. Liu, *Biomaterials Science*, 2019, **7**, 1995–2008.
- (116) A. Takahashi, Y. Suzuki, T. Suhara, K. Omichi, A. Shimizu, K. Hasegawa, N. Kokudo, S. Ohta and T. Ito, *Biomacromolecules*, 2013, **14**, 3581–3588.
- (117) S.-Y. Choh, D. Cross and C. Wang, *Biomacromolecules*, 2011, **12**, 1126–1136.
- (118) C. Highley, G. Prestwich and J. Burdick, *Current Opinion in Biotechnology*, 2016, **40**, 35–40.
- (119) M. Hanthamrongwit, W. Reid and M. Grant, *Biomaterials*, 1996, **17**, 775–780.
- (120) K. Tomihata and Y. Ikada, *Journal of Biomedical Materials Research Part A*, 1997, **37**, 243–251.
- (121) C. N. Grover, R. E. Cameron and S. M. Best, *Journal of the Mechanical Behavior of Biomedical Materials*, 2012, **10**, 62–74.
- (122) P. F. Gratzner and J. M. Lee, *Journal of Biomedical Materials Research*, 2001, **58**, 172–179.
- (123) Thermo Fisher Scientific, *Carbodiimide Crosslinker Chemistry*, 2017.
- (124) M. Collins and C. Birkinshaw, *Journal of Applied Polymer Science*, 2007, **104**, 3183–3191.
- (125) L. Olde Damink, P. Dijkstra, M. van Luyn, P. van Wachem, P. Nieuwenhuis and J. Feijen, *Biomaterials*, 1996, **17**, 765–773.
- (126) F. Li, M. Ducker, B. Sun, F. G. Szele and J. T. Czernuszka, *Acta Biomaterialia*, 2020, **112**, 122–135.
- (127) D. Mantione, I. del Agua, A. Sanchez-Sanchez and D. Mecerreyes, *Polymers*, 2017, **9**, 354.
- (128) F. Alibart, S. Pleutin, D. Guérin, C. Novembre, S. Lenfant, K. Lmimouni, C. Gamrat and D. Vuillaume, *Advanced Functional Materials*, 2010, **20**, 330–337.
- (129) F. Alibart, S. Pleutin, O. Bichler, C. Gamrat, T. Serrano-Gotarredona, B. Linares-Barranco and D. Vuillaume, *Advanced Functional Materials*, 2012, **22**, 609–616.

- (130) S. Desbief, A. Kyndiah, D. Guérin, D. Gentili, M. Murgia, S. Lenfant, F. Alibart, T. Cramer, F. Biscarini and D. Vuillaume, *Organic Electronics*, 2015, **21**, 47–53.
- (131) M. Di Lauro, M. Berto, M. Giordani, S. Benaglia, G. Schweicher, D. Vuillaume, C. A. Bortolotti, Y. H. Geerts and F. Biscarini, *Advanced Electronic Materials*, 2017, **3**, 1700159.
- (132) P. Gkoupidenis, N. Schaefer, X. Strakosas, J. A. Fairfield and G. G. Malliaras, *Applied Physics Letters*, 2015, **107**, 263302.
- (133) M. Giordani, M. Berto, M. Di Lauro, C. A. Bortolotti, M. Zoli and F. Biscarini, *ACS Sensors*, 2017, **2**, 1756–1760.
- (134) C. Pitsalidis, M. P. Ferro, D. Iandolo, L. Tzounis, S. Inal and R. M. Owens, *Science Advances*, 2018, **4**, eaat4253.
- (135) S. Khopkar, *Basic Concepts of Analytical Chemistry*, New Academic Science, Tunbridge Wells, UK, 3rd edn., p. 2008.
- (136) B. H. Stuart, *Infrared Spectroscopy : Fundamentals and Applications*, John Wiley & Sons, Incorporated, Chichester, UK, 1st edn., 2004.
- (137) P. Larkin, *Infrared and Raman Spectroscopy : Principles and Spectral Interpretation*, Elsevier, Amsterdam, The Netherlands, 2011.
- (138) A. Sakamoto and S. Ochiai, *Introduction to Experimental Infrared Spectroscopy : Fundamentals and Practical Methods*, ed. M. Tasumi, John Wiley & Sons, Incorporated, Chichester, UK, 1st edn., 2014.
- (139) Merck, *IR Spectrum Table & Chart*, 2020.
- (140) F. S. Rocha, A. J. Gomes, C. N. Lunardi, S. Kaliaguine and G. S. Patience, *The Canadian Journal of Chemical Engineering*, 2018, **96**, 2512–2517.
- (141) G. R. Chatwal and S. K. Anand, *Spectroscopy : Atomic and Molecular*, Himalaya Publishing House Pvt. Ltd., Mumbai, India, 2008.
- (142) T. P. Kaloni, P. K. Giesbrecht, G. Schreckenbach and M. S. Freund, *Chemistry of Materials*, 2017, **29**, 10248–10283.
- (143) I. Zozoulenko, A. Singh, S. K. Singh, V. Gueskine, X. Crispin and M. Berggren, *ACS Applied Polymer Materials*, 2019, **1**, 83–94.
- (144) T. A. Yemata, Y. Zheng, A. K. K. Kyaw, X. Wang, J. Song, W. S. Chin and J. Xu, *RSC Advances*, 2020, **10**, 1786–1792.
- (145) V. F. Lvovich, *Impedance Spectroscopy : Applications to Electrochemical and Dielectric Phenomena*, John Wiley & Sons, Incorporated, Hoboken, New Jersey, 2012.
- (146) M. E. Orazem and B. Tribollet, *Electrochemical Impedance Spectroscopy*, John Wiley & Sons, Incorporated, Hoboken, New Jersey, 2nd edn., 2017.
- (147) Gamry Instruments, *Basics of Electrochemical Impedance Spectroscopy*, 2020.
- (148) E. P. Randviir and C. E. Banks, *Analytical Methods*, 2013, **5**, 1098–1115.
- (149) R. Green, R. Hassarati, J. Goding, S. Baek, N. Lovell, P. Martens and L. Poole-Warren, *Macromolecular Bioscience*, 2012, **12**, 494–501.
- (150) M. ElMahmoudy, S. Inal, A. Charrier, I. Uguz, G. G. Malliaras and S. Sanaur, *Macromolecular Materials and Engineering*, 2017, **302**, 1600497.

- (151) S. Carli, M. Bianchi, E. Zucchini, M. Di Lauro, M. Prato, M. Murgia, L. Fadiga and F. Biscarini, *Advanced Healthcare Materials*, 2019, **1900765**, 1900765.
- (152) M. Grossi and B. Riccò, *Journal of Sensors and Sensor Systems*, 2017, **6**, 303–325.
- (153) M. Ohring, *Engineering Materials Science*, Academic Press, Inc., San Diego, CA, 1st edn., 1995.
- (154) M. M. Saunders, *Synthesis Lectures on Biomedical Engineering*, 2015, **54**, 1–275.
- (155) M. L. Oyen, *International Materials Reviews*, 2014, **59**, 44–59.
- (156) G. N. Greaves, A. L. Greer, R. S. Lakes and T. Rouxel, *Nature Materials*, 2011, **10**, 823–837.
- (157) R. S. Lakes, *Annual Review of Materials Research*, 2017, **47**, 63–81.
- (158) Y. Zhu, Z. Dong, U. C. Wejinya, S. Jin and K. Ye, *Journal of Biomechanics*, 2011, **44**, 2356–2361.
- (159) I. N. Sneddon, *International Journal of Engineering Science*, 1965, **3**, 47–57.
- (160) B. Riccardi and R. Montanari, *Materials Science and Engineering A*, 2004, **381**, 281–291.
- (161) J. D. Kaufman and C. M. Klapperich, *Journal of the Mechanical Behavior of Biomedical Materials*, 2009, **2**, 312–317.
- (162) F. Louwet, L. Groenendaal, J. Dhaen, J. Manca, J. Van Luppen, E. Verdonck and L. Leenders, *Synthetic Metals*, 2003, **135-136**, 115–117.
- (163) M. Berggren and A. Richter-Dahlfors, *Advanced Materials*, 2007, **19**, 3201–3213.
- (164) J. Liu, M. Agarwal and K. Varahramyan, *Sensors and Actuators B: Chemical*, 2008, **135**, 195–199.
- (165) S. K. Kanakamedala, H. T. Alshakhouri, M. Agarwal and M. A. Decoster, *Sensors and Actuators, B: Chemical*, 2011, **157**, 92–97.
- (166) E. Bihar, S. Wustoni, A. M. Pappa, K. N. Salama, D. Baran and S. Inal, *npj Flexible Electronics*, 2018, **2**, 1–8.
- (167) W. Lee, D. Kim, J. Rivnay, N. Matsuhisa, T. Lonjaret, T. Yokota, H. Yawo, M. Sekino, G. G. Malliaras and T. Someya, *Advanced Materials*, 2016, **28**, 9722–9728.
- (168) D. Mantione, I. del Agua, W. Schaafsma, J. Diez-Garcia, B. Castro, H. Sardon and D. Mecerreyes, *Macromolecular Bioscience*, 2016, **16**, 1227–1238.
- (169) M. Asplund, H. von Holst and O. Inganäs, *Biointerphases*, 2008, **3**, 83–93.
- (170) M. Asplund, T. Nyberg and O. Inganäs, *Polymer Chemistry*, 2010, **1**, 1374.
- (171) J. Cameron and P. J. Skabara, *Materials Horizons*, 2020, DOI: 10.1039/C9MH01978B.
- (172) H. Okuzaki and M. Ishihara, *Macromolecular Rapid Communications*, 2003, **24**, 261–264.
- (173) U. Lang, N. Naujoks and J. Dual, *Synthetic Metals*, 2009, **159**, 473–479.
- (174) D. Tahk, H. H. Lee and D.-Y. Khang, *Macromolecules*, 2009, **42**, 7079–7083.
- (175) E. Dauzon, A. E. Mansour, M. R. Niazi, R. Munir, D.-M. Smilgies, X. Sallenave, C. Plesse, F. Goubard and A. Amassian, *ACS Applied Materials & Interfaces*, 2019, **11**, 17570–17582.
- (176) L. V. Kayser and D. J. Lipomi, *Advanced Materials*, 2019, **31**, 1806133.
- (177) C. Vallejo-Giraldo, A. Kelly and M. Biggs, *Drug Discovery Today*, 2014, **19**, 88–94.
- (178) M. J. Donahue, A. Sanchez-Sanchez, S. Inal, J. Qu, R. M. Owens, D. Mecerreyes, G. G. Malliaras and D. C. Martin, *Materials Science and Engineering: R: Reports*, 2020, **140**, 100546.
- (179) E. M. Thaning, M. L. M. Asplund, T. A. Nyberg, O. W. Inganäs and H. von Holst, *Journal of Biomedical Materials Research Part B: Applied Biomaterials*, 2010, **93B**, 407–415.

- (180) M. Asplund, E. Thaning, J. Lundberg, A. C. Sandberg-Nordqvist, B. Kostyszyn, O. Inganäs and H. Von Holst, *Biomedical Materials*, 2009, **4**, 045009.
- (181) A. Harris, P. Molino, A. Paolini and G. Wallace, *Electrochimica Acta*, 2016, **197**, 99–106.
- (182) A. R. Harris, P. J. Molino, A. G. Paolini and G. G. Wallace, *Synthetic Metals*, 2016, **222**, 338–343.
- (183) Y. Ner, M. Invernale, J. Grote, J. Stuart and G. Sotzing, *Synthetic Metals*, 2010, **160**, 351–353.
- (184) M. Horikawa, T. Fujiki, T. Shirosaki, N. Ryu, H. Sakurai, S. Nagaoka and H. Ihara, *Journal of Materials Chemistry C*, 2015, **3**, 8881–8887.
- (185) D. G. Harman, R. Gorkin, L. Stevens, B. Thompson, K. Wagner, B. Weng, J. H. Chung, M. In Het Panhuis and G. G. Wallace, *Acta Biomaterialia*, 2015, **14**, 33–42.
- (186) I. Del Agua, D. Mantione, N. Casado, A. Sanchez-Sanchez, G. G. Malliaras and D. Mecerreyes, *ACS Macro Letters*, 2017, **6**, 473–478.
- (187) S. Wang, S. Guan, Z. Zhu, W. Li, T. Liu and X. Ma, *Materials Science and Engineering C*, 2017, **71**, 308–316.
- (188) J. L. Hutter and J. Bechhoefer, *Review of Scientific Instruments*, 1993, **64**, 1868–1873.
- (189) D. Nečas and P. Klapetek, *Central European Journal of Physics*, 2012, **10**, 181–188.
- (190) T. M. Althagafi, Ph.D. Thesis, University of Sheffield, 2017.
- (191) S. Hayashi, *Polymer-Plastics Technology and Engineering*, 1988, **27**, 61–91.
- (192) S. Wang, S. Guan, J. Wang, H. Liu, T. Liu, X. Ma and Z. Cui, *Journal of Bioscience and Bioengineering*, 2017, **123**, 116–125.
- (193) C. B. Nielsen, A. Giovannitti, D.-T. Sbircea, E. Bandiello, M. R. Niazi, D. A. Hanifi, M. Sessolo, A. Amassian, G. G. Malliaras, J. Rivnay and I. McCulloch, *Journal of the American Chemical Society*, 2016, **138**, 10252–10259.
- (194) J. Rivnay, P. Leleux, M. Ferro, M. Sessolo, A. Williamson, D. A. Koutsouras, D. Khodagholy, M. Ramuz, X. Strakosas, R. M. Owens, C. Benar, J.-M. Badiet, C. Bernard and G. G. Malliaras, *Science Advances*, 2015, **1**, e1400251.
- (195) A. Håkansson, S. Han, S. Wang, J. Lu, S. Braun, M. Fahlman, M. Berggren, X. Crispin and S. Fabiano, *Journal of Polymer Science, Part B: Polymer Physics*, 2017, **55**, 814–820.
- (196) D. Mantione, I. Del Agua, W. Schaafsma, M. Elmahmoudy, I. Uguz, A. Sanchez-Sanchez, H. Sardon, B. Castro, G. Malliaras and D. Mecerreyes, *ACS Applied Materials and Interfaces*, 2017, **9**, 18254–18262.
- (197) R. D. Deegan, O. Bakajin, T. F. Dupont, G. Huber, S. R. Nagel and T. A. Witten, *Nature*, 1997, **389**, 827–829.
- (198) S. K. M. Jönsson, J. Birgerson, X. Crispin, G. Greczynski, W. Osikowicz, A. W. Denier van der Gon, W. R. Salaneck and M. Fahlman, *Synthetic Metals*, 2003, **139**, 1–10.
- (199) L. H. Jimison, A. Hama, X. Strakosas, V. Armel, D. Khodagholy, E. Ismailova, G. G. Malliaras, B. Winther-Jensen and R. M. Owens, *Journal of Materials Chemistry*, 2012, **22**, 19498–19505.
- (200) L. V. Lingstedt, M. Ghittorelli, H. Lu, D. A. Koutsouras, T. Marszalek, F. Torricelli, N. I. Crăciun, P. Gkoupidenis and P. W. M. Blom, *Advanced Electronic Materials*, 2019, **5**, 1800804.
- (201) R. A. Bressan and J. A. Crippa, *Acta Psychiatrica Scandinavica*, 2005, **111**, 14–21.

- (202) M. Giordani, M. Sensi, M. Berto, M. Di Lauro, C. A. Bortolotti, H. L. Gomes, M. Zoli, F. Zerbetto, L. Fadiga and F. Biscarini, *Advanced Functional Materials*, 2020, **30**, 2002141.
- (203) H. Heuer, R. Wehrmann and S. Kirchmeyer, *Advanced Functional Materials*, 2002, **12**, 89–94.
- (204) E. Nasybulin, S. Wei, M. Cox, I. Kyymissis and K. Levon, *The Journal of Physical Chemistry C*, 2011, **115**, 4307–4314.
- (205) R. Gangopadhyay, B. Das and M. R. Molla, *RSC Adv.*, 2014, **4**, 43912–43920.
- (206) A. Campana, T. Cramer, P. Greco, G. Foschi, M. Murgia and F. Biscarini, *Applied Physics Letters*, 2013, **103**, DOI: 10.1063/1.4818549.
- (207) Z. Saddiq, J. Barbenel and M. H. Grant, *Journal of Biomedical Materials Research Part A*, 2009, **89A**, 697–706.
- (208) E. E. Antoine, P. P. Vlachos and M. N. Rylander, *Tissue Engineering - Part B: Reviews*, 2014, **20**, 683–696.
- (209) S. Rhee, J. Puetzer, B. Mason, C. Reinhart-King and L. Bonassar, *ACS Biomaterials Science & Engineering*, 2016, **2**, 1800–1805.
- (210) L. Racine, A. Guliyeva, I. Wang, V. Larreta-Garde, R. Auzély-Velty and I. Texier, *Macromolecular Bioscience*, 2017, **17**, 1–11.
- (211) Z. Cai, Y. Gan, C. Bao, W. Wu, X. Wang, Z. Zhang, Q. Zhou, Q. Lin, Y. Yang and L. Zhu, *Advanced Healthcare Materials*, 2019, **8**, 1900013.
- (212) C. F. Marques, G. S. Diogo, S. Pina, J. M. Oliveira, T. H. Silva and R. L. Reis, *Journal of Materials Science: Materials in Medicine*, 2019, **30**, DOI: 10.1007/s10856-019-6234-x.
- (213) Y. Liu, J. Liu, S. Chen, T. Lei, Y. Kim, S. Niu, H. Wang, X. Wang, A. M. Foudeh, J. B. Tok and Z. Bao, *Nature Biomedical Engineering*, 2019, **3**, 58–68.
- (214) K. Nam, T. Kimura and A. Kishida, *Macromolecular Bioscience*, 2008, **8**, 32–37.
- (215) I. Gatej, M. Popa and M. Rinaudo, *Biomacromolecules*, 2005, **6**, 61–67.
- (216) A. Martínez, M. Blanco, N. Davidenko and R. Cameron, *Carbohydrate Polymers*, 2015, **132**, 606–619.
- (217) Z. Yang, S. Best and R. Cameron, *Advanced Materials*, 2009, **21**, 3900–3904.
- (218) K. Liu, H. Tran, V. R. Feig and Z. Bao, *MRS Bulletin*, 2020, **45**, 96–102.

# Appendix A

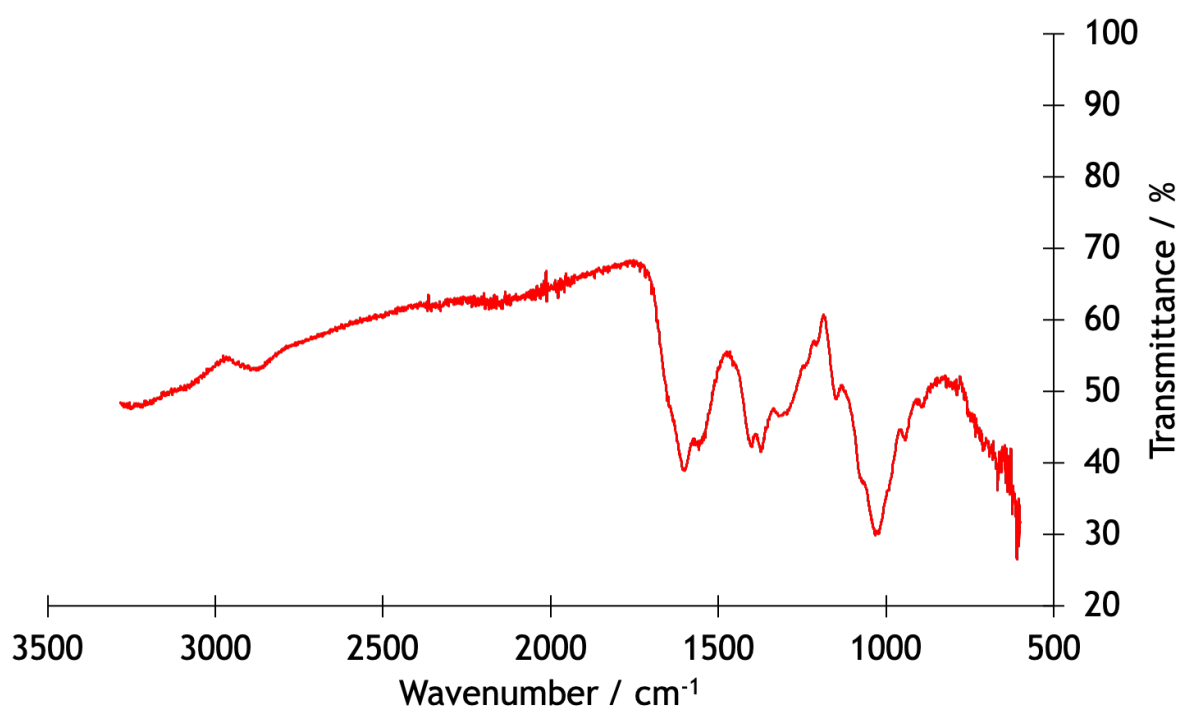
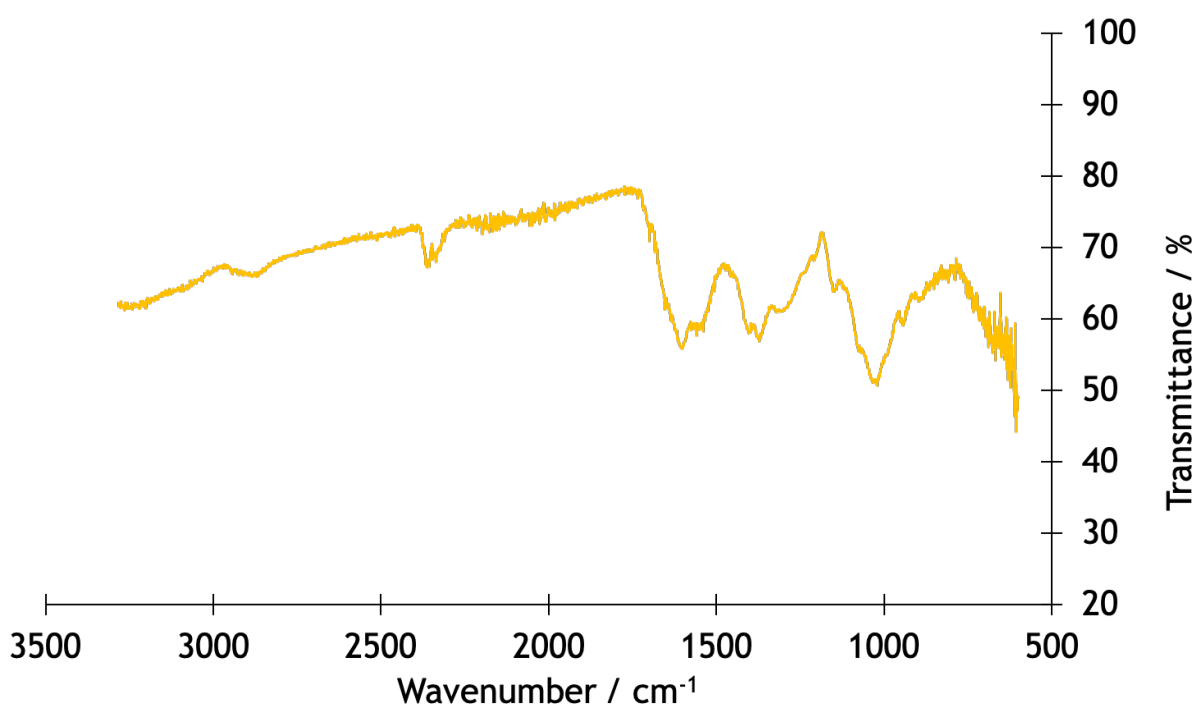
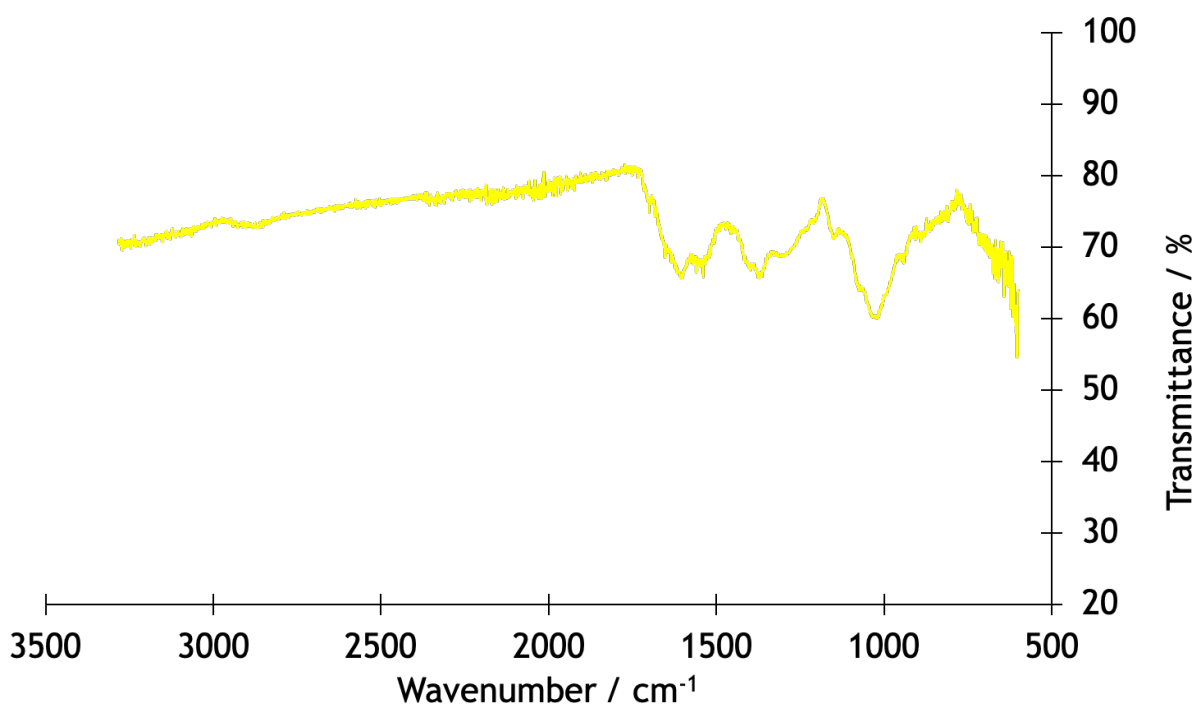


Figure 6.1: IR spectra of uncrosslinked HA film.



**Figure 6.2:** IR spectra of HA hydrogel, crosslinked in 0.026 mol dm<sup>-3</sup> EDC solution.



**Figure 6.3:** IR spectra of HA hydrogel, crosslinked in 0.052 mol dm<sup>-3</sup> EDC solution.

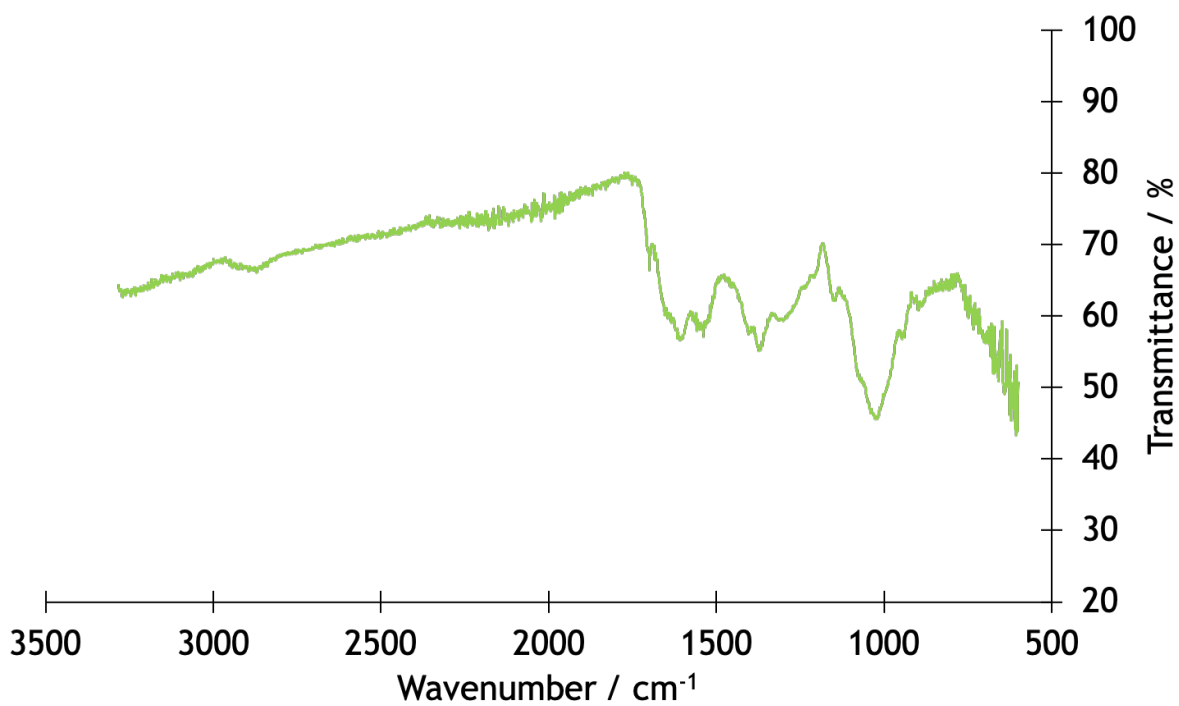


**Figure 6.4:** IR spectra of HA hydrogel, crosslinked in 0.26 mol dm<sup>-3</sup> EDC solution.

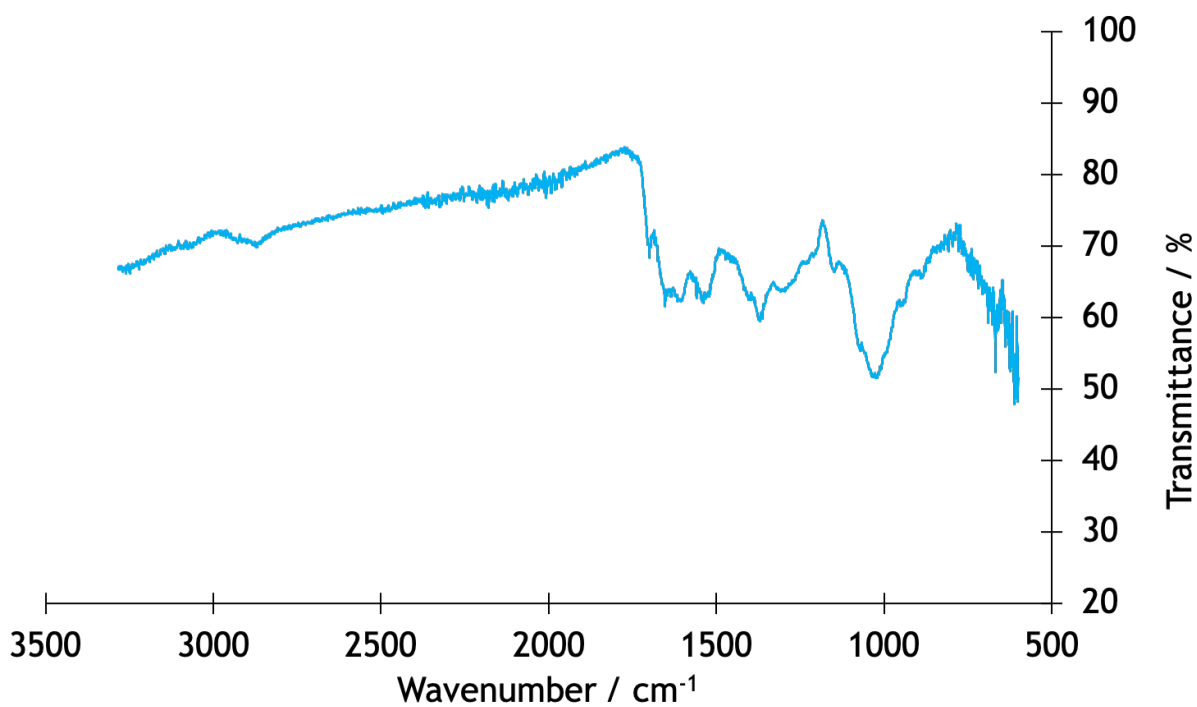


**Figure 6.5:** IR spectra of HA hydrogel, crosslinked in 0.52 mol dm<sup>-3</sup> EDC solution.

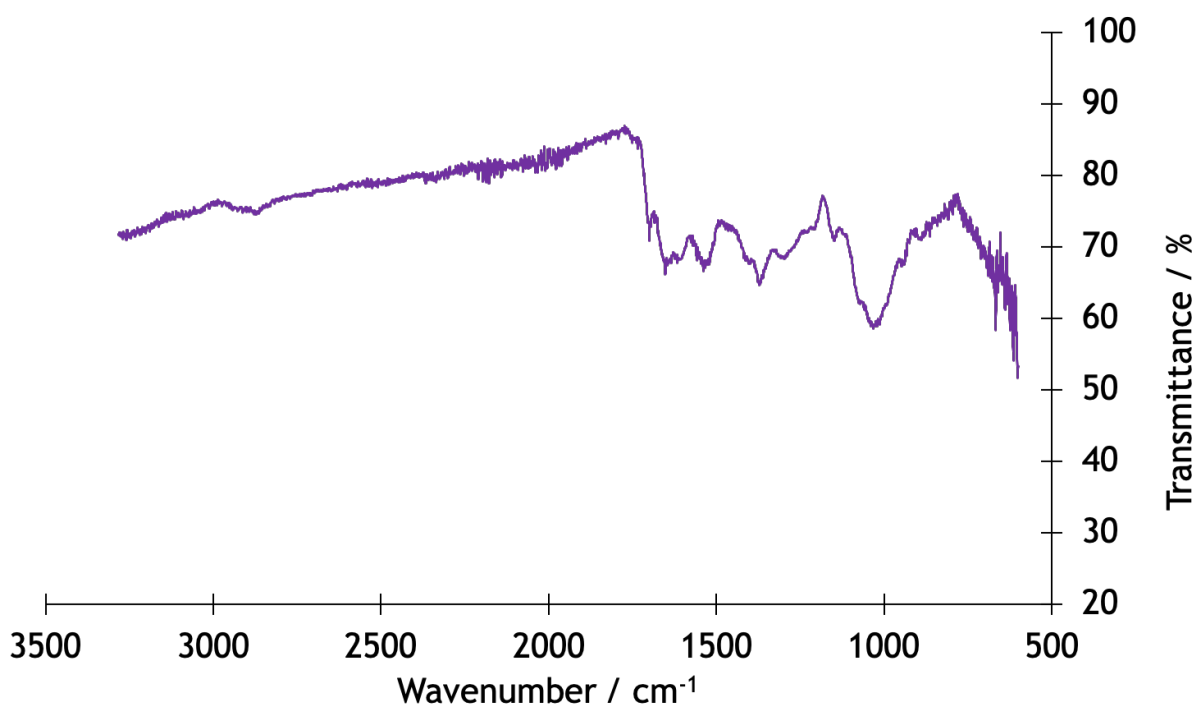


**Figure 6.6:** IR spectra of HA hydrogel, crosslinked in 1.0 mol dm<sup>-3</sup> EDC solution.

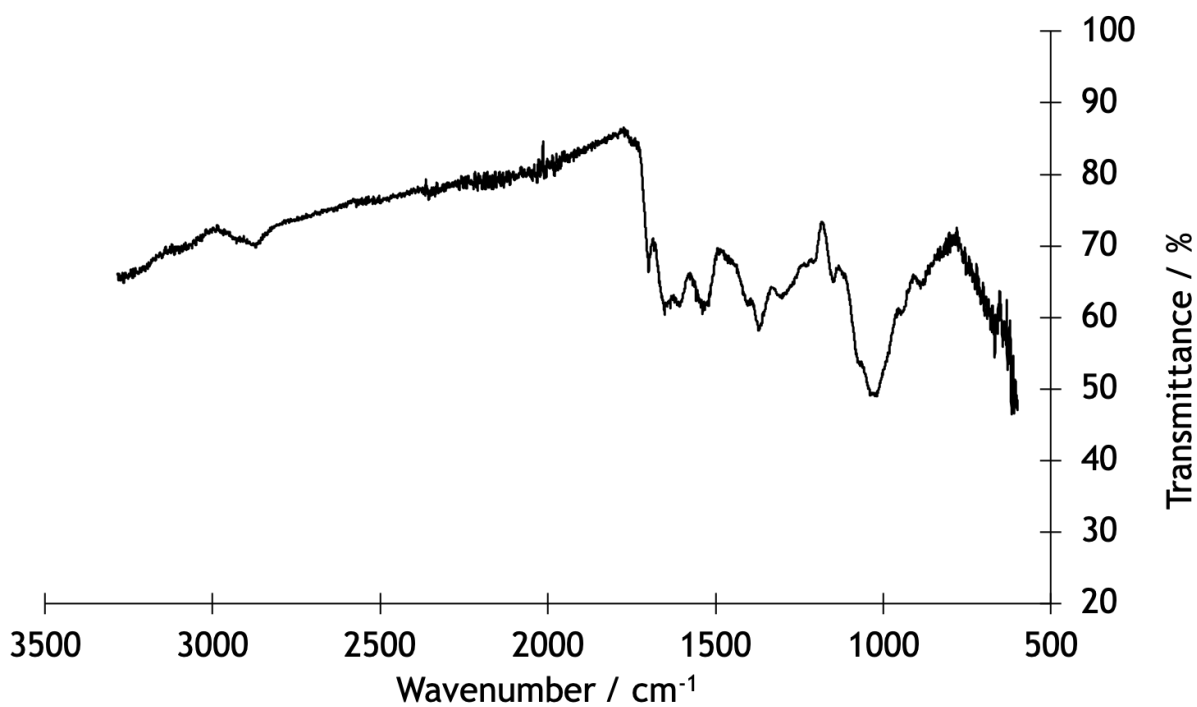


**Figure 6.7:** IR spectra of HA hydrogel, crosslinked in 1.3 mol dm<sup>-3</sup> EDC solution.